

Mechanisms and Prevention of Lead Sulphide (PbS) Scale Deposition in Multiphase Systems

William Keogh

Submitted in accordance with the requirements for the degree of
Doctor of Philosophy

The University of Leeds
School of Mechanical Engineering

July 2019

The candidate confirms that the work submitted is his own, except where work which has formed part of jointly-authored publications has been included. The candidate confirms that appropriate credit has been given where reference has been made to the work of others

This copy has been supplied on the understanding that it is copyright material and that no quotation from the thesis may be published without proper acknowledgement

Acknowledgements

I would like to express a huge thank you to Professor Anne Neville for both giving me the opportunity to work with her, and for granting me such a large degree of autonomy in how I approached this project. I'll be eternally grateful to Dr Thibaut Charpentier for not only having seemingly inexhaustible time and patience whenever I needed direction or someone to bounce ideas off, but for injecting a sense of fun into the whole process with which I could not have done without.

A sincere thank you to Equinor, Total and ConocoPhillips for funding the ASSESS project and providing critical feedback that helped shape both the project and my thesis.

I would also like to thank the technical and administrative staff at the University of Leeds for their contribution and advice: Mick, Jordan, Andrew, Paul, Fiona and Judith. Also, thanks to the members of the scale group for their continued technical contributions.

Finally, I'd like to thank my family and friends for all the love and support over the last few years.

Abstract

The deposition of mineral scale poses a major challenge in the oil and gas industry, where flow assurance issues can result in significant operating costs and well downtime.

This study aimed to analyse the mechanisms of precipitation and deposition for a range of scale types (calcium carbonate, barium sulphate and lead sulphide) in simple and complex systems. Whilst traditionally, studies looking to mitigate mineral scaling have investigated precipitation and deposition in single phase brines, the introduction of a light oil phase to induce multiphase conditions in this study was representative of processes occurring within oilfield production systems.

A rig that enabled the propagation of turbulent, multiphase, emulsion-forming flow within a H₂S environment was designed and constructed in order to assess the interaction of bulk colloids at the oil-water interface and consequently the mechanism by which they deposited upon surfaces. Characterisation of solid stabilised Pickering emulsions took place through optical microscopy and cryo-scanning electron microscopy (cryo-SEM). As a secondary objective, the mitigation efficacy of a number of anti-fouling coatings was assessed under a range of scaling conditions, with physiochemical characteristics inherent to the surfaces that prevented initial deposition identified. Fluoropolymers, diamond-like-carbon (DLC) and sol-gel coatings, were found to be the most promising anti-fouling substrates and as such were assessed for potential application into oilfield systems and equipment. Scaling severity was measured through mass gain analysis and SEM of surface crystals to establish morphology and coverage. The relationship between coating wettability and scale adhesion was explored using atomic force microscopy (AFM), where the interfacial forces acting upon hydrophilic and hydrophobic tips when in contact with a cleaved [001] galena face.

Results showed that whilst attractive hydrophobic force had a bearing on PbS deposition on hydrophobic surfaces in single phase, the presence of a light oil phase in multiphase systems was pre-dominant in determining scaling likelihood upon surfaces. The oil wetting of hydrophobic surfaces was seen to largely prevent the deposition of bulk precipitated scale, with a relationship found between the thermodynamics of precipitation of a species and the degree of accuracy to which scaling could be predicted upon surfaces of varying wettability.

Table of Contents

Chapter 1 Introduction.....	1
1.1 Oil and gas: Evolution and Production	1
1.2 Oilfield mineral scaling	4
1.3 Scale deposition in oil/water (o/w) systems.....	5
1.4 Objectives	6
Chapter 2 Literature review of scale nucleation and deposition mechanisms	8
2.1 Inorganic scaling	8
2.2 Conventional scales.....	10
2.2.1 Calcium carbonate (CaCO ₃)	11
2.2.2 Barium sulphate (BaSO ₄).....	12
2.3 Unconventional sulphide scales.....	14
2.3.1 Lead sulphide (PbS)	16
2.3.2 Crystal structure of PbS	16
2.4 Mineral nucleation and crystallisation	18
2.4.1 Supersaturation	18
2.4.2 Induction time	19
2.4.3 Nucleation.....	20
2.4.4 Primary nucleation	21
2.4.5 Secondary nucleation	26
2.4.6 Crystal nucleation and growth mechanisms.....	27
2.5 Importance of pH in CO ₂ and H ₂ S dissociation	32
2.5.1 CO ₂ dissociation	33
2.5.2 H ₂ S dissociation.....	34
2.5.3 pH vs. electron activity (Eh)	34
2.5.4 IEP of galena and PbS charge.....	35
2.5.5 Nanoparticle agglomeration.....	38
2.6 Factors influencing scale precipitation	38
2.6.1 CaCO ₃ and BaSO ₄	38

2.6.2 PbS	41
2.6.3 Crystal co-precipitation	42
2.6.4 CaCO ₃ and PbS co-precipitation likelihood in oilfield	42
2.6.5 Influence of ionic impurities on crystal precipitation and growth ..	43
2.6.6 Occlusion co-precipitation.....	43
2.7 Factors affecting scale deposition.....	44
2.7.1 Flow pattern and turbulence	44
2.7.2 Agglomerate/particle size.....	44
2.7.3 Solution pH	44
2.7.4 Substrate topography and roughness	45
2.7.5 Substrate surface energy/wettability	45
2.8 Factors affecting scale adhesion.....	47
2.8.1 Substrate surface energy/wettability	48
2.8.2 Agglomerate/particle size.....	48
2.8.3 Surface charges between bodies.....	48
2.8.4 Substrate topography and roughness	49
2.8.5 Substrate pre-scaling.....	50
2.9 Forces governing attraction and adhesion between surfaces	50
2.9.1 DLVO forces	50
2.9.2 Non-DLVO forces	52
2.9.3 Oxidation of galena.....	53
2.10 Scaling in multiphase flow.....	54
2.10.1 Flow dynamics and emulsion types	54
2.10.2 Adsorption of particles at a liquid-liquid interface.....	55
2.10.3 Desorption of particles from a liquid-liquid interface	56
2.10.4 Crystal growth at liquid-liquid interfaces	58
2.11 Multiphase emulsions.....	58
2.11.1 Emulsion stability	58
2.11.2 Emulsion inversion.....	60
2.11.3 Role of the multiphase in functionalisation and co-precipitation.	61
2.12 Mineral scale mitigation.....	62

2.12.1 Chemical – Scale Inhibitors and Dispersants.....	62
2.12.2 Mechanical – Anti-fouling surfaces	64
2.12.3 ASSESS program	65
2.12.4 Scale removal	67
2.13 Summary of Literature.....	67
Chapter 3 Materials and Methods	69
3.1 Anti-fouling surface characterisation	69
3.1.1 Water contact angle	69
3.1.2 Substrate hardness.....	71
3.1.3 Surface roughness.....	72
3.2 Anti-fouling surfaces	72
3.2.1 Coating characteristics	73
3.2.2 Coating selection	75
3.3 Mineral scaling tests	76
3.3.1 Carbonate and sulphate scaling tests.....	76
3.3.2 Modifications to equipment for sulphide tests	76
3.3.3 Sulphide scaling tests	77
3.3.4 Scaling rig.....	79
3.3.5 Hydrodynamic conditions.....	81
3.3.6 System limitations	82
3.4 Brine compositions.....	82
3.5 Saturation ratio (SR) calculation	85
3.5.1 PbS.....	85
3.5.2 CaCO ₃ and BaSO ₄	86
3.6 Multiphase experiments	87
3.6.1 PbS and PbS/CaCO ₃ emulsion inversion	87
3.6.2 PbS and PbS/CaCO ₃ w/ polymeric inhibitor.....	88
3.6.3 PbS pre-precipitation	88
3.7 Post-experimental analysis	89
3.7.1 Surface scaling	89
3.7.2 Bulk particle characterisation	91

3.7.3 Emulsion characterisation.....	92
3.8 Interfacial forces governing PbS adhesion.....	95
3.8.1 Atomic Force Microscopy.....	96
3.8.2 Mineral galena characterisation	98
3.8.3 AFM tip hydrophobisation	102
3.8.4 AFM solution preparation.....	102
3.8.5 AFM force curve measurements.....	103
Chapter 4 Scale Behaviour and Deposition in Single Phase Flow: Calcium Carbonate (CaCO₃), Barium Sulphate (BaSO₄) and Lead Sulphide (PbS) Systems	106
4.1 CaCO ₃ deposition	106
4.2 BaSO ₄ deposition.....	108
4.3 PbS deposition.....	110
4.4 PbS characterisation.....	113
4.4.1 Mineral galena and synthetic PbS differences.....	116
4.5 PbS adhesion.....	116
4.5.1 AFM force curve analysis.....	116
4.5.2 Topography of galena.....	117
4.5.3 Interfacial forces in PbS deposition.....	117
4.6 PbS/CaCO ₃ single phase.....	119
4.7 Chapter Summary	121
4.7.1 Chapter Highlights	125
Chapter 5 Scale Behaviour and Deposition in Multiphase Flow: Simple Calcium Carbonate (CaCO₃), Barium Sulphate (BaSO₄) and Lead Sulphide (PbS) Systems	126
5.1 CaCO ₃ in a multiphase (o/w) emulsion	126
5.2 BaSO ₄ deposition in a multiphase (o/w) emulsion	129
5.3 PbS deposition in a multiphase (o/w) emulsion.....	131
5.4 PbS pre-precipitation.....	134
5.5 PbS emulsion characterisation.....	135
5.6 PbS emulsion viscosity	138
5.7 PbS emulsion thermal stability	139

5.8 PbS emulsion inversion.....	140
4.1 PbS deposition (w/o) emulsion.....	142
5.9 Chapter summary	143
5.9.1 Deposition mechanisms in multiphase systems.....	143
5.9.2 Predicting scale deposition in multiphase flow.....	147
5.9.3 Chapter Highlights	149
Chapter 6 Scale Behaviour and Deposition in Multiphase Flow: Complex Lead Sulphide (PbS)/Calcium Carbonate (CaCO₃) Systems.....	151
6.1 PbS/CaCO ₃ deposition (o/w) emulsion	151
6.2 PbS/CaCO ₃ emulsion characterisation	154
6.3 PbS pre-precipitation (o/w emulsion)	158
6.4 PbS/CaCO ₃ emulsion inversion	159
6.5 PbS/CaCO ₃ deposition (w/o emulsion)	159
6.6 Chapter summary	162
6.6.1 PbS occlusion in CaCO ₃ at the o-w interface.....	162
6.6.2 PbS/CaCO ₃ emulsion behaviour.....	164
6.6.3 Chapter Highlights	166
Chapter 7 Influence of Poly(2-acrylamido-2-methyl-1-propanesulfonic acid) (PAMPS) on PbS precipitation and deposition in single and multiphase systems.....	167
7.1 PAMPS adsorption on PbS/galena	167
7.2 PAMPS functionalised PbS adhesion	169
7.3 PbS deposition in single phase – 50 mg/L PAMPS.....	171
7.4 PbS deposition in o/w multiphase – 50 mg/L PAMPS.....	173
7.5 PbS deposition in o/w multiphase – 500 mg/L PAMPS.....	175
7.6 PbS deposition in o/w multiphase – 5000 mg/L PAMPS.....	177
7.6.1 PbS/PAMPS emulsion rheology	179
7.6.2 Emulsion behaviour at the coating interface	180
7.7 Influence of PAMPS on PbS deposition.....	180
7.7.1 Multiphase system - 0 mg/L PAMPS	180
7.7.2 Multiphase system - 500 mg/L PAMPS	181

7.8 PbS/CaCO ₃ deposition in o/w multiphase – 50 mg/L PAMPS.....	182
7.9 Chapter Summary	185
7.9.1 Chapter Highlights	187
Chapter 8 Conclusion	188
8.1 Attachment and adhesion of PbS to anti-fouling surfaces.....	188
8.2 Light oil phase influence on mineral scale behaviour and Pickering emulsion formation.....	189
8.3 PbS deposition in multiphase systems.....	191
8.4 Chemical inhibition of PbS scale	193
8.5 Ranking of surfaces for field application	194
Chapter 9 Future work	196
9.1 Laboratory-based testing	196
9.2 Assessment of field trial samples	198

Table of Figures

Figure 1.1 Maturation of oil through burial of biomass that transforms into kerogen (diagenesis) and eventually fossil fuels (catagenesis) (5)	2
Figure 1.2 Schematic showing the progression of oil production from primary to tertiary recovery. *IOR, improved oil recovery; EOR, enhanced oil recovery (7).....	3
Figure 1.3 Formation-water brine chemistry assumed to have carbonate and sulphate scaling potential on mixing with injected water (8)	3
Figure 1.4 The global cost of scale divided into regions (13)	4
Figure 2.1 Calcium carbonate scale build-up (34).....	11
Figure 2.2 Schematic representation of the carbonic system (36)	12
Figure 2.3 Illustration of seawater injection and influence on reservoir temperature (40)	13
Figure 2.4 The biochemical pathway of dissimilatory sulphate reduction in SRB (44)	14
Figure 2.5 Sulphide scale deposits from the North Sea Central Graben fields (38).....	16
Figure 2.6 Crystal lattice structure of PbS (33).....	17
Figure 2.7 Molecular illustration of water interacting with a galena surface (33)	18
Figure 2.8 Pathways via which nucleation can occur (35).....	20
Figure 2.9 Homogeneous nucleation – mechanism of bulk growth (25).....	21
Figure 2.10 Heterogeneous nucleation – surface nucleation (25).....	21
Figure 2.11 Free energy diagram for nucleation – existence of a ‘critical nucleus’ (35).....	23
Figure 2.12 Interfacial tension at boundaries between phases (35)	26
Figure 2.13 Schematic illustration of different stages of the crystal growth in solution. Growth units adsorb to the surface or directly attach to kink positions. After adsorption to the surface, it migrates across the surface up to the step, where it incorporates into the crystal lattice (84)	28
Figure 2.14 small nanocrystallites are produced responsible for aggregative growth; secondary particles which are monocrystalline due to a	

recrystallization step, where at high levels of supersaturation the presented growth mechanism dominates (31)	29
Figure 2.15 Schematic illustration of the nucleation and growth process of nanocrystals in solution: nuclei develop from monomers before the growth of nanocrystals via the aggregation of nuclei (87)	30
Figure 2.16 Schematic showing the formation of PbS nanoparticles (88) ...	31
Figure 2.17 Bjerrum plots of pH vs mole fraction of a) H ₂ CO ₃ ; and b) H ₂ S species concentration at 25°C.....	32
Figure 2.18 Persistency-field Eh-pH diagram for galena in the presence of sulphate and carbonate ion species at 0.1 activity (98).....	35
Figure 2.19 pH vs. zeta-potential for unoxidised galena (101)	36
Figure 2.20 Schematic representation of the electric double layer (EDL) (103)	37
Figure 2.21 Pressure vs. calcite (SI) at 200 and 250°F (93 and 121°C).....	38
Figure 2.22 Absolute salinity vs. calcite SR where red line 25°C and blue 40°C (106).....	39
Figure 2.23 pH vs CaCO ₃ solubility (107).....	39
Figure 2.24 Temperature vs. BaSO ₄ solubility (27)	40
Figure 2.25 NaCl concentration vs. BaSO ₄ solubility (108)	40
Figure 2.26 PbS solubilities at 25 to 300°C, 1- 5 m NaCl at pH 4 and mS(r) = 0.001 (29).....	41
Figure 2.27 pH vs. solubility of metal sulphide species (110).....	42
Figure 2.28 a) Heterogeneous nucleation and crystal arrangement on asperities; b) Migration of homogeneous particles from the bulk phase to the substrate and crystal arrangement on asperities (131)	45
Figure 2.29 Schematic energy versus distance profiles of the DLVO interaction. The actual magnitude of the energy <i>W</i> is proportional to the particle size (radius) or interaction area (between two planar surfaces) (103)	51
Figure 2.30 Evolution of a cleaved galena surface with time in an oxidised aqueous environment (152)	53
Figure 2.31 Illustrations of types of multiphase pipe flow; a) very fine dispersion of oil in water; b) dispersion of oil in water; c) oil in water churn flow (154).....	55

Figure 2.32 Particle position at an o-w interface based on wettability	56
Figure 2.33 Influence of contact angle and particle size on the energy required for desorption from the o-w interface (162)	57
Figure 2.34 Solid particles stabilized at the interface in an o/w Pickering emulsion.....	59
Figure 2.35 a) Ostwald ripening where small drops shrinking and larger drops swelling as molecules transfer from the small to larger drops; b) if there are not sufficient particles present formed drop surfaces limited coalescence occurs (167)	60
Figure 2.36 Particles arranged an o-w interface where half of the colloid is functionalised from particles within the aqueous phase (172)	61
Figure 2.37 Chemical structure of PAMPS (177)	63
Figure 3.1 Sessile drop with fitted contour (202)	70
Figure 3.2 Schematic of a scratch test (204)	71
Figure 3.3 Substrates post-scratch test a) DLC; b) F3	72
Figure 3.4 DLC film cross-section showing graphical representation of amorphous carbon structure (210)	74
Figure 3.5 PTFE film cross-section and chemical representation of fluorocarbon structure (213)	74
Figure 3.6 SEM cross-section of silica-based sol gel coating and chemical structure of typical branched network (217)	75
Figure 3.7 Photograph of multiphase scaling rig with H ₂ S injection capability and seawater (SW) delivery vessel	79
Figure 3.8 Schematic of multiphase scaling rig with H ₂ S injection capability and seawater (SW) delivery vessel	79
Figure 3.9 Solidworks TM images of main reaction vessel a) lid top; b) lid bottom; main vessel	81
Figure 3.10 Extraction of PbS Pickering emulsion from post-experiment reaction vessel to vial using a digital pipette	93
Figure 3.11 Agitation of recovered emulsion in 30 ml vial before recording of emulsion stabilisation time	93
Figure 3.12 Schematic of AFM equipment (227).....	96
Figure 3.13 Illustration of force curve example sample displacement vs. force (104).....	97

Figure 3.14 Mineral galena (229)	98
Figure 3.15 2 x 2 μm tapping mode image of cleaved galena [001] face to determine topography and RMS roughness.....	99
Figure 3.16 PAMPS coverage on galena after 30 min adsorption time in 50 mg/L PAMPS 0.5 M KCl solution.....	100
Figure 3.17 PAMPS coverage on galena after 120 min adsorption time in 50 mg/L PAMPS 0.5 M KCl solution.....	100
Figure 3.18 Inverse goniometer cell for oil-galena-water contact angle measurements	101
Figure 3.19 FE-SEM image of Si_3N_4 tip where R was determined to be 32.5 ± 10 nm	103
Figure 4.1 Photographs of samples – CaCO_3 single phase conditions	107
Figure 4.2 SEM images – CaCO_3 single phase conditions	107
Figure 4.3 Water contact angle vs. mass gain – CaCO_3 single phase conditions	108
Figure 4.4 Photographs of samples – BaSO_4 single phase conditions.....	109
Figure 4.5 SEM images – BaSO_4 single phase conditions.....	109
Figure 4.6 EDX analysis of REF coupon showing extensive presence of Sr, likely incorporated into the BaSO_4 lattice	110
Figure 4.7 Water contact angle vs. mass gain – BaSO_4 single phase conditions	110
Figure 4.8 Photographs of samples – PbS single phase conditions.....	111
Figure 4.9 SEM images – PbS single phase conditions	112
Figure 4.10 Water contact angle vs. mass gain – PbS single phase conditions	113
Figure 4.11 Post-experiment – PbS single phase conditions	114
Figure 4.12 TEM images of precipitated PbS crystals.....	115
Figure 4.13 X-Ray Diffraction spectra of PbS nanoparticles	116
Figure 4.14 AFM contact mode image of cleaved galena [001] face – RMS roughness of 503 pm.....	117
Figure 4.15 Force curve approach – a) Untreated Si_3N_4 tip - hydrophilic and galena substrate; b) Si_3N_4 (OTS treated) tip - hydrophobic and galena substrate	118

Figure 4.16 Force curve retraction – a) Untreated Si ₃ N ₄ tip - hydrophilic and galena substrate; b) Si ₃ N ₄ (OTS treated) tip - hydrophobic and galena substrate	119
Figure 4.17 Photographs of samples – PbS/CaCO ₃ single phase conditions	120
Figure 4.18 SEM images – PbS/CaCO ₃ single phase conditions.....	120
Figure 4.19 Water contact angle vs. mass gain – PbS/CaCO ₃ single phase conditions	121
Figure 4.20 Truncated octahedron crystal morphology; a) Illustration; b) Imaged from PbS/CaCO ₃ single phase systems	124
Figure 5.1 Photographs of samples – CaCO ₃ multiphase conditions	127
Figure 5.2 SEM images – CaCO ₃ multiphase conditions	128
Figure 5.3 Water contact angle vs. mass gain – CaCO ₃ multiphase conditions	128
Figure 5.4 Photographs of samples – BaSO ₄ multiphase conditions	129
Figure 5.5 SEM images – BaSO ₄ multiphase conditions	130
Figure 5.6 Water contact angle vs. mass gain – BaSO ₄ multiphase conditions	131
Figure 5.7 Photographs of samples – PbS multiphase conditions	132
Figure 5.8 SEM images – PbS multiphase conditions.....	132
Figure 5.9 SEM images – PbS multiphase conditions.....	133
Figure 5.10 Water contact angle vs. mass gain – PbS multiphase conditions	133
Figure 5.11 Photographs of samples – PbS multiphase conditions (pre-precipitated)	134
Figure 5.12 Water contact angle vs. mass gain – PbS multiphase conditions (pre-precipitated).....	134
Figure 5.13 Oil, emulsion and brine phase separation: a) PbS emulsion after shaking; b) separation of oil phase (40 seconds) and significant migration of PbS particles from water to o/w interface after approximately 220 seconds	135
Figure 5.14 PbS stabilised oil droplets in o/w Pickering emulsion.....	136
Figure 5.15 Cryo-SEM of oil droplet with PbS nanoparticles at o-w interface; EDX highlighting oil droplet and PbS species	136

Figure 5.16 Cryo-SEM image of PbS arrangement at o-w interface; TEM image shows size and shape of PbS.....	137
Figure 5.17 Main image shows inverted sessile drop of oil on galena in aqueous solution where oil CA was $132.1 \pm 1.8^\circ$; thumbnail displays water contact angle on galena in air where water CA was $47.9 \pm 0.6^\circ$	138
Figure 5.18 Shear rate vs. viscosity of o/w PbS Pickering emulsion at shear values of 0 - 2 Pa	139
Figure 5.19 Thermal stability of a PbS Pickering emulsion – Conductivity vs. Temperature.....	140
Figure 5.20 PbS multiphase system – a) o/w emulsion at < 0.75 oil phase fraction; b) w/o emulsion at > 0.75 oil phase fraction	141
Figure 5.21 Particle laden droplet coalescing with uncoated droplet. The time between each photograph (top left to bottom right) was reported to be 0.5 ms (269).....	142
Figure 5.22 Anti-fouling coupons in a multiphase PbS system (80:20 o:w ratio)	142
Figure 5.23 Water contact angle vs. mass gain in a multiphase PbS system (o:w 80:20 ratio)	143
Figure 5.24 Oil droplet state in-situ within turbulent system. Oil wetting of hydrophobic surfaces by free excess oil and impaction of hydrophilic surfaces by PbS stabilised oil droplets	144
Figure 5.25 A liquid droplet coated with hydrophobised beads and impacted upon a hydrophobic surface where $t = -0.2, 1, 2.2, 4.8$. Scale bars in each image are 2 mm long (274)	145
Figure 5.26 SEM of deposition pattern on DLC coupon in a o/w multiphase PbS system	146
Figure 5.27 Water droplet state in-situ within turbulent system. Oil wetting of hydrophobic surfaces by bulk oil and impaction of hydrophilic surfaces by PbS stabilised water droplets.....	147
Figure 6.1 Anti-fouling coupons in a multiphase PbS/CaCO ₃ system (5:95 o:w ratio)	152
Figure 6.2 SEM of deposited PbS/CaCO ₃ complexes on anti-fouling coupons (5:95 o:w ratio)	152

Figure 6.3 SEM and EDX of deposited PbS/CaCO ₃ complexes (REF coupon) – o:w 5:95 ratio.....	153
Figure 6.4 Water contact angle vs. mass gain in a multiphase PbS/CaCO ₃ system (o:w 5:95 ratio)	153
Figure 6.5 Optical microscope images of PbS/CaCO ₃ stabilised oil droplet	154
Figure 6.6 Cryo-SEM of PbS/CaCO ₃ complexes at o-w interface; EDX shows centralised PbS within calcite structures	155
Figure 6.7 Cryo-SEM of PbS/CaCO ₃ complexes at o-w interface	156
Figure 6.8 PbS/CaCO ₃ complexes at the o-w droplet interface.....	157
Figure 6.9 XRD of dried PbS/CaCO ₃ co-precipitate emulsion.....	158
Figure 6.10 SEM and EDX of deposited PbS/CaCO ₃ complexes after pre-precipitation and dosing of PbS agglomerates – o:w 5:95 ratio.....	158
Figure 6.11 PbS/CaCO ₃ system – a) o/w emulsion at < 0.5 oil phase fraction; b) w/o emulsion at > 0.5 oil phase fraction	159
Figure 6.12 Anti-fouling coupons in a multiphase PbS/CaCO ₃ system (60:40 o:w ratio)	160
Figure 6.13 SEM of deposited PbS/CaCO ₃ complexes on anti-fouling coupons (60:40 o:w ratio)	160
Figure 6.14 SEM and EDX of deposited PbS/CaCO ₃ complexes (REF coupon) – o:w 60:40 ratio.....	161
Figure 6.15 Water contact angle vs. mass gain in a multiphase PbS/CaCO ₃ system (o:w 60:40 ratio)	161
Figure 6.16 Growth of calcite around occluded PbS agglomerates at an o-w interface	164
Figure 6.17 a) PbS arrangement at oil droplet interface – high packing fraction; b) PbS/CaCO ₃ arrangement at oil droplet interface – low packing fraction	165
Figure 7.1 a) 2 x 2 µm area of PAMPS functionalised galena analysed through contact mode topography; b) respective phase image.....	168
Figure 7.2 Main image - inverted sessile drop of oil on PAMPS functionalised galena in aqueous solution where oil CA is 151.4 ± 3.3°; Thumbnail - water contact angle on PAMPS functionalised galena in air where water CA is 29.5 ± 2.4°.....	169

Figure 7.3 Force curve upon approach – a) Untreated Si ₃ N ₄ tip and PAMPS functionalised galena substrate; b) Si ₃ N ₄ (OTS treated) tip and PAMPS functionalised galena substrate	170
Figure 7.4 Force curve upon retraction – a) Untreated Si ₃ N ₄ tip and PAMPS functionalised galena substrate; b) Si ₃ N ₄ (OTS treated) tip and PAMPS functionalised galena substrate	171
Figure 7.5 Photographs of samples – PbS single phase conditions - 50 mg/L PAMPS.....	172
Figure 7.6 Water contact angle vs. mass gain in a single phase PbS system – 50 mg/L PAMPS.....	172
Figure 7.7 Photographs of samples – PbS multiphase conditions - 50 mg/L PAMPS.....	174
Figure 7.8 PbS multiphase system - 50 mg/L PAMPS a) Post-experimental emulsion after agitation; b) Separation into stable 3-phase emulsion after 60 seconds; c) Optical microscope image of oil droplet (x20 mag)	174
Figure 7.9 Water contact angle vs. mass gain in a multiphase PbS system – 50 mg/L PAMPS.....	175
Figure 7.10 Photographs of samples – PbS multiphase conditions - 500 mg/L PAMPS.....	175
Figure 7.11 Water contact angle vs. mass gain in a multiphase PbS system – 500 mg/L PAMPS.....	176
Figure 7.12 500 mg/L PAMPS inhibitor a) Post-experimental emulsion after agitation; b) Separation into stable Winsor type III emulsion after 24 hours; c) Optical microscope image of oil droplets (x20 mag).....	177
Figure 7.13 Photographs of samples – PbS multiphase conditions - 5000 mg/L PAMPS.....	177
Figure 7.14 Water contact angle vs. mass gain in a multiphase PbS system – 5000 mg/L PAMPS.....	178
Figure 7.15 5000 mg/L PAMPS a) Post-experimental emulsion after agitation; b) Separation into stable Winsor type III emulsion after 24 hours; c) Optical microscope image of oil droplets (x20 mag).....	178
Figure 7.16 Viscosity of PbS Pickering emulsions with concentrations of 0, 500 and 5000 mg/L under ramping shear rate	179

Figure 7.17 PbS multiphase systems - 0 mg/L PAMPS a) SEM image of PbS deposition on REF coupon; b and c) EDX images of Pb and S respectively	180
Figure 7.18 PbS multiphase systems - 500 mg/L PAMPS a) SEM image of PbS deposition on REF coupon; b and c) EDX images of Pb and S	181
Figure 7.19 a) EDX spectra of PbS deposit on REF coupon - 0 mg/L PAMPS; b) EDX spectra of PbS deposit on REF coupon - 500 mg/L PAMPS	182
Figure 7.20 Photographs of samples - multiphase PbS/CaCO ₃ system (5:95 o:w ratio) - 50 mg/L PAMPS inhibitor	183
Figure 7.21 SEM images of deposits on anti-fouling surfaces in a multiphase PbS/CaCO ₃ system (o:w 5:95 ratio) - 50 mg/L PAMPS	183
Figure 7.22 SEM and EDX of deposited PbS/CaCO ₃ complexes - 50 mg/L PAMPS inhibitor (DLC coupon) – o:w 5:95 ratio	184
Figure 7.23 Water contact angle vs. mass gain in a multiphase PbS/CaCO ₃ system (o:w 5:95 ratio) - 50 mg/L PAMPS	184

Tables

Table 2.1 Common mineral scales in oilfields and variables affecting solubility *TDS = total dissolved solids.....	9
Table 2.2 Characterisation of oilfield scales examined in this study (30-33)	10
Table 2.3 Types of multiphase pipe flow (154).....	54
Table 2.4 ASSESS coating types and characteristics	66
Table 3.1 Anti-fouling coatings tested	73
Table 3.2 Solution composition	78
Table 3.3 Proportion of solution mixed to form acetate buffer	78
Table 3.4 Hydrodynamic conditions at coupon interface in single phase conditions	82
Table 3.5 Brine A - CaCO ₃ forming brine composition and SR _{initial}	83
Table 3.6 Brine B - BaSO ₄ forming brine composition and SR _{initial}	83
Table 3.7 Brine C - PbS forming brine composition and SR _{initial}	84
Table 3.8 Brine D - PbS and CaCO ₃ forming brine concentration and SR _{initial}	84
Table 3.9 Variation in PbS solubility with NaCl concentration and pH *m _{S(r)} is total reduced sulphide concentration.....	85
Table 3.10 Calculation of Brine C and D saturation ratio.....	86
Table 3.11 Emulsion type and o:w ratios for scaling systems	88
Table 5.1 Relationship between salt, SR and CA vs. mass gain correlation	148
Table 7.1 PbS zeta-potential at 0 and 50 mg/L concentration.....	169

Publications

Keogh, W., Charpentier, T., Neville, A., O'Brien, A., Eroini, V., Olsen, J. H., Baraka-Lokmane, S. (2017, April 27). "*Evaluation of Anti-Fouling Surfaces for Prevention of Lead Sulfide Scaling in Single and Multiphase Conditions*". NACE International 2017

W. Keogh, A. Neville, M. Huggan, V. Eroini, JH Olsen, FM Nielsen, S. Baraka-Lokmane, E. Bourdelet, JA Ellingsen, O. Bache, and T. Charpentier. "*Deposition of Inorganic Carbonate, Sulfate, and Sulfide Scales on Antifouling Surfaces in Multiphase Flow*". Energy & Fuels 2017

Keogh, W., Boakye, G. O., Neville, A., Charpentier, T., Olsen, J. H., Eroini, V., ... Bourdelet, E. (2018, July 20). "*Lead Sulfide (PbS) Scale Behavior and Deposition as a Function of Polymeric Sulfide Inhibitor Concentration in Multiphase*". NACE International 2018

Keogh, W., Charpentier, T., Eroini, V., Olsen, J. H., Nielsen, F. M., Baraka-Lokmane, S., Neville, A. (2018, June 20). "*Insights into the Mechanism of Lead Sulfide PbS Fouling and The Influence of Light Distillate Fraction*". Society of Petroleum Engineers 2018

W. Keogh, A. Neville, Q. Liu, L.Feng, V. Eroini, JH Olsen, FM Nielsen, S. Baraka-Lokmane, E. Bourdelet, JA Ellingsen, O. Bache, D. Harbottle and T. Charpentier. "*Study of Lead Sulfide Scaling in Multiphase Systems and Co-precipitation in the Presence of Calcium Carbonate*". Journal of Petroleum Science and Engineering 2020

Nomenclature

o/w: oil-in-water

w/o: water-in-oil

Eh: electron activity

Å: angstrom

k: Boltzmann constant

T: absolute temperature

K_{sp}: solubility product

t_T : relaxation time

t_n : time required for the formation of a nucleus

t_g : is the time required for the nucleus to grow to a detectable size

r : radius of particle

ΔG : overall excess free energy

ΔG_s : the sum of the surface excess free energy

ΔG_v : volume free energy

r_{crit} : critical nucleus

v_l : molecular volume of the liquid

σ : is the surface tension

S: supersaturation

J: nucleation rate

K: kinetic prefactor

ΔG^* : change in Gibbs free energy required to form a critical cluster of the new phase from the supersaturated phase

v_A : rate of molecule attachment to the critical cluster per unit of surface

J: total flux of monomers passing through a spherical plane with radius x

D: diffusion coefficient

C: concentration at distance x

Δ : distance from the particle surface to the bulk concentration of monomers within solution

C_b : bulk concentration of monomers within solution and C_i is the concentration of monomers at the solid/liquid interface

K_1 : 1st equilibrium constant

K_2 : 2nd equilibrium constant

m_F : mass of the fluid

m_P : mass of the particle

U_F : fluid velocity

p : pressure

\dot{m}_d : mass deposition rate

v : molecular volume

C_3 : proportionality constant

h : shape factor

F_{el} : electrostatic force

F_{vdW} : van der Waals force

F_{cap} : capillary force

F_{chem} : forces due to chemical bonds

W_A : work of adhesion/free energy of adhesion

F_I : coulombic attraction

α : factor to correct for the polarization of the particle

q : particle charge

F_{ad} : adhesion force

A_H : Hamaker constant

D_0 : minimum distance between sphere and asperity

C_L : microscopic property of two interacting atoms depending on the strength of interaction between the two bodies

h : height of the particle centre of mass above the interface

p_c : capillary pressure

R_1 and R_2 : principal radii of curvature

Re : Reynolds number

U_{cyl} : surface velocity at cylinder

a_i : activity
 m_i : molality
 F_{HB} : hydrophobic force
 D_0 : decay length of hydrophobic interaction
 F_{adh} : adhesion force
 S_a : average roughness
 S_{ku} : sharpness

HT/HP: high temperature/high pressure
FW: formation water
SW: seawater
TDS: total dissolved solids
SRB: sulphate reducing bacteria
MVT: Mississippi Valley Type
SSSV: sub-surface-safety valve
NTU: Nephelometric Turbidity Units
CNT: classical nucleation theory
ACC: amorphous calcium carbonate
TPC: three-phase contact
BSE: back-scatter electron imaging
IOR: improved oil recovery
EOR: enhanced oil recovery
RMS roughness: root mean squared roughness
SEM: scanning electron microscopy
EDX: energy dispersive x-ray
TEM: transmission electron microscopy
PSD: particle size distribution
OTS: octadecyltrichlorosilane
JTC: jumps to contact

WLI: white light interferometry

DE: displacement energy

IEP: iso-electric point

EDL: electrical double layer

SR: saturation ratio

IAP: ion activity product

α : size of individual growth units

σ : surface tension

$\Delta\mu$: chemical potential

γ : interfacial tension

γ_{o-w} : interfacial tension at the o-w interface

γ_i : activity coefficient

γ_{cl} : interfacial energy between crystalline phase/liquid

γ_{sl} : interfacial energy between solid phase/liquid

γ_{cs} : interfacial energy between crystalline phase/solid

θ : contact angle

λ : microscale

τ : wall shear stress

ϵ_0 : permittivity of free space

γ^{LW} : dispersive forces

γ^{AB} : Lewis acid-base forces

ρ : atoms per millimetre of the particle

Chapter 1

Introduction

Energy underpins modern society, with increasing global demand not only a by-product of an exponentially growing population, but also the expanding carbon footprint of individuals who in this age routinely travel internationally, embrace digitalisation and buy more products than ever before. As of 2018, around 80% of the world's energy is derived from fossil fuels, with demand for petrochemicals set to increase by 60% by 2040 as the requirement for fuels and plastics increases.(1) Ensuring that oil and gas can be produced as efficiently and exhaustively as possible is therefore of critical importance.

The complexities associated with the recovery of oil and gas from deep reservoirs that are increasingly difficult to survey, drill and produce, combined with the extreme temperatures and pressures and potential for souring result in a host of production issues. Harsh conditions can exacerbate mineral scaling, corrosion, failure risk in piping and equipment, and presence of toxic H₂S gas downhole and topside. This work aims to contribute to the prevention of mineral scaling on downhole equipment through the application of anti-scaling surfaces, with a particular focus on scaling in sour environments.

1.1 Oil and gas: Evolution and Production

Production, accumulation and preservation of un-degraded organic matter are required for the existence of petroleum source rocks. Organic matter is material comprised of organic molecules in monomeric or polymeric form derived from the organic part of organisms. Organic matter is synthesised by living organisms before being deposited and preserved in sediments, and depending on further geological events, may be transformed into petroleum-like compounds.(2)

Sedimentary organic matter comprises largely of the elements carbon (C) and hydrogen (H) with additional heteroatoms present, mainly nitrogen (N), sulphur (S) and oxygen (O).(3) Given appropriate environmental conditions, diagenesis and catagenesis can convert the sedimentary organic matter to petroleum over time scales of tens of millions of years. 'Diagenesis' is defined as the chemical reactions that occur in the first few thousand years after burial at temperatures less than 50°C, with catagenesis of the deeply buried

sediments then occurring, undergoing abiotic chemical reactions at heightened temperatures and pressures. Cooking conditions of the organic matter ultimately determines the chemical composition of the maturation products, with slow burial and low geothermal gradients generating a different suite of petroleum hydrocarbons than fast burial with high gradients.(4) Figure 1.1 shows the oil maturation process, whereby 300 to 400 million years ago, dead marine plants and animals and came to rest on the seafloor, with their organic material buried under layers of both porous sedimentary rock and impermeable cap rock e.g. shale.(5) Prolonged exposure of the biomass to heat and pressure then resulted in the formation of oil or gas formation.

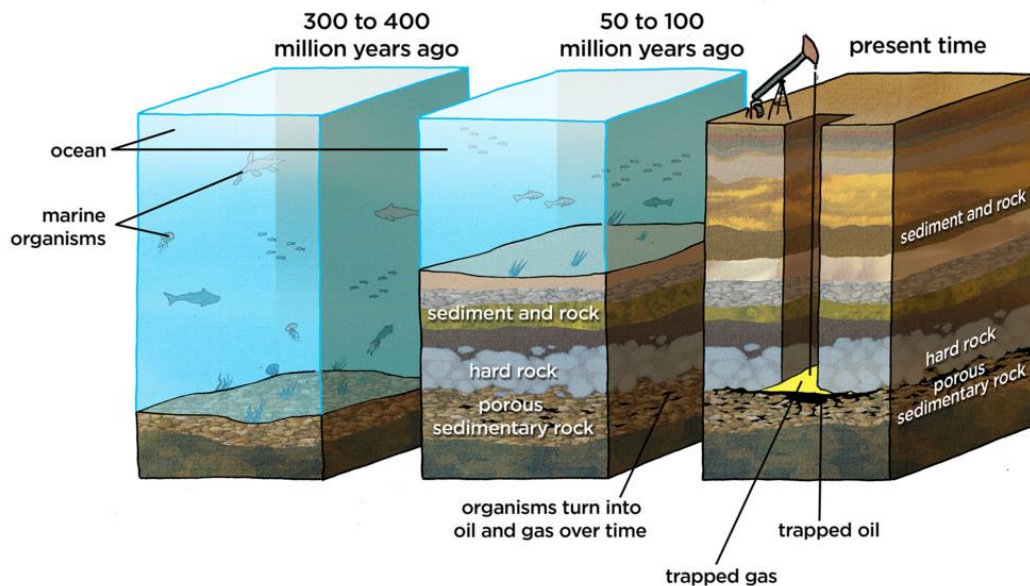


Figure 1.1 Maturation of oil through burial of biomass that transforms into kerogen (diagenesis) and eventually fossil fuels (catagenesis) (5)

Primary oil recovery is defined as the oil and gas produced by natural reservoir forces, with the majority of petroleum reservoirs containing sufficient energy and internal pressures to push oil and gas to the surface when first penetrated by a drill bit.(6) Figure 1.2 displays the typical stages of oil production from primary to tertiary recovery.(7)

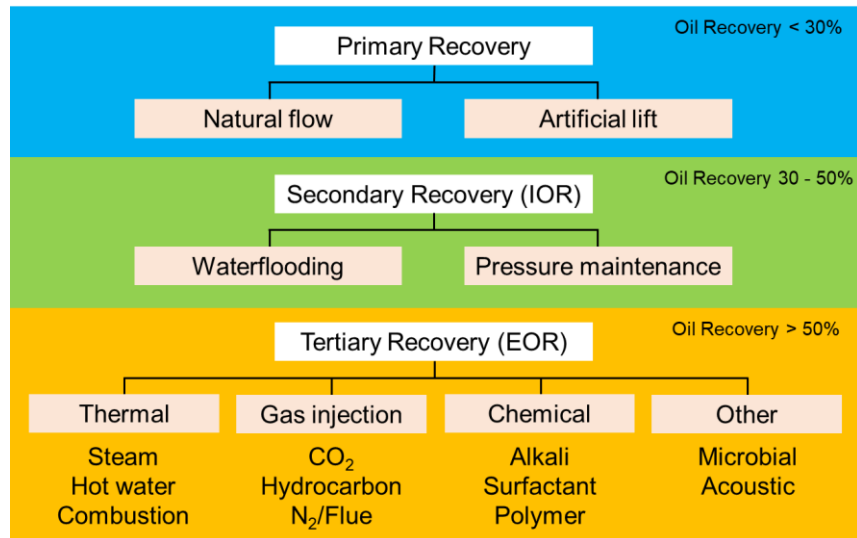


Figure 1.2 Schematic showing the progression of oil production from primary to tertiary recovery. *IOR, improved oil recovery; EOR, enhanced oil recovery (7)

Once natural flow of produced oil and gas has diminished, improved and enhanced oil recovery is initiated.

The injection of sea-water into offshore oil-bearing reservoirs to maintain reservoir pressure and as a secondary recovery method is a well-established operation. During the early stages of production, formation water is produced prior to injection brine breakthrough. However, carbonate and sulphide scales are still potential challenges to production before secondary recovery through injection if formation water is already saturated with the appropriate ions, with sulphate scales being dependent on the onset of injection brine. Figure 1.3 shows the point at which seawater is injected into reservoir as a secondary recovery method and the subsequent effect on produced water-cut.(8)

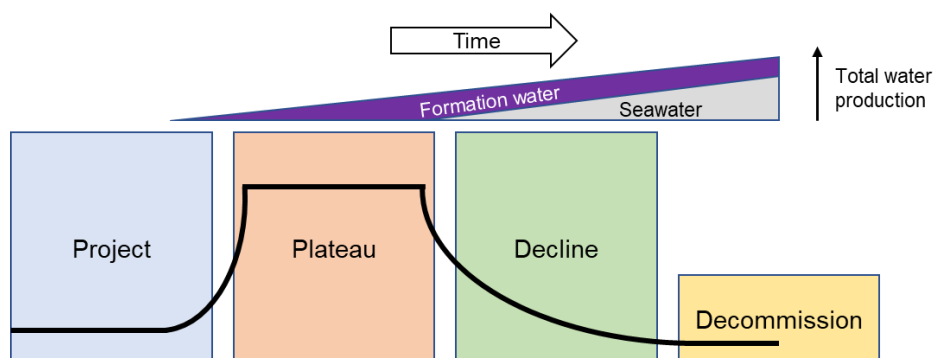


Figure 1.3 Formation-water brine chemistry assumed to have carbonate and sulphate scaling potential on mixing with injected water (8)

1.2 Oilfield mineral scaling

The initial accumulation and consequent build-up of insoluble inorganic mineral scales has plagued flow streams since the inception of industrial processes that utilise aqueous solutions (9-11). In oil and gas production, the disruption of the chemical equilibrium of produced water as a consequence of physical changes induced by the drilling process can lead to the crystallisation of scales around the wellbore, in the production tubing and in processing equipment topside. The implications of scale build-up are severe, where blocking of flow in pipes, impediment of moving parts in valves and fouling of pumps and tanks can lead to the eventual need to replace equipment and components and a significant cost and loss of time.(11, 12) The global cost of scale worldwide each year per millions of dollars is displayed in Figure 1.4 based on region.(13)

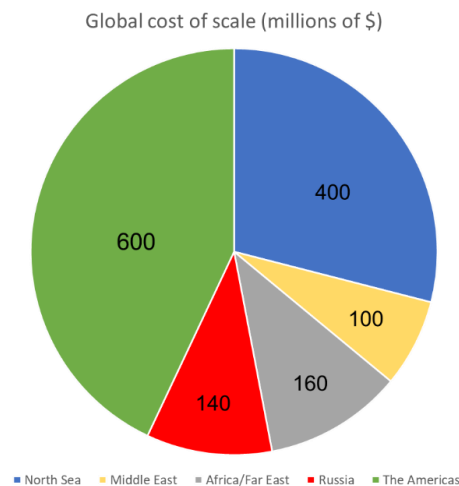


Figure 1.4 The global cost of scale divided into regions (13)

The attempt to mitigate problematic crystallisation has often utilised both chemical inhibitors in the form of routine and reactionary treatments, as well as mechanical cleaning. Sulphates have typically been removed by both milling and jetting, where coiled tubing, gel sweeps, a motor and saw-tooth mills are used. CaCO_3 is softer than BaSO_4 and can be more easily removed through acid treatments, e.g. hydrochloric acid (HCl) jetting, though this can promote other flow assurance issues such as asphaltenes, corrosion, emulsion formation and potential sand production. Whilst sulphides are able to be removed with acid treatments, PbS is typically the hardest to dissolve due to its very low solubility and as such inhibitors may be the most effective

form of mitigation. Whilst carbonate and sulphate scales can be inhibited through chemical means, inhibitors effective at combating the precipitation of sulphides are required in significantly higher dosages (12, 14, 15)

Whilst inhibitors are largely effective in systems where water chemistry and conditions are predictable, they are expensive to design, synthesise and deploy, and as such, the use of anti-fouling surfaces as a more affordable and permanent means to prevent crystallisation has become commonplace.(16-18) Whilst often used in conjunction with chemical treatment methods, surfaces with specific physiochemical traits are able to prolong the operational lifetime of process integral equipment before costly scale removal methods or replacement is required.

1.3 Scale deposition in oil/water (o/w) systems

While significant literature has been published on the efficacy of anti-fouling surfaces in single phase aqueous systems, there is very limited published work that has explored fouling within oil-in-water (o/w) systems. Multiphase flow, where an immiscible light oil and aqueous phase constitute a process stream is standard in petroleum production and processing, where recovery of the energy-rich organic phase is the objective. This work aims to demonstrate the previously unreported and profound effect that the presence of a light oil phase can have on the behaviour and deposition of mineral scales commonly found in oilfield systems in parallel with anti-scaling surfaces.

Whilst studies looking at the precipitation and build-up of conventional carbonate and sulphate scales in oil producing wells have been around since the inception of oil and gas drilling, the unwelcome build-up of uncommon sulphide scales in producing wells is a relatively recent phenomenon. Precipitation of sulphides is largely prompted by high temperature/high pressure (HT/HP) conditions that foster the proliferation and growth of bacteria, able to reduce sulphate ions into reactive sulphide species that then readily react with heavy metal cations such as iron (Fe^{2+}), zinc (Zn^{2+}) and lead (Pb^{2+}).⁽¹¹⁾ As a consequence of the target minerals' low solubility combined with the extremely challenging conditions downhole, the chemical inhibition of sulphides poses a difficult exercise. High inhibitor concentrations need to be maintained in the near-wellbore region in order to prevent crystallisation of highly insoluble scales, whilst contending with the inevitable degradation of certain inhibitor types at exceedingly high temperatures.^(19, 20) Therefore, as

a result of the challenges associated with chemical inhibition of sulphide species, the role of anti-fouling surfaces in preventing both excessive operating expenditure and loss of production as a result of sulphide scale build-up is significant.

An experimental apparatus was designed and constructed that was able to reproduce tailored scaling conditions in a turbulent multiphase system. Whilst previous sulphide scaling experiments have engineered the spontaneous precipitation of sulphide scales through the mixing of two incompatible brines, the set-up described within uses the dissociation rate of $\text{H}_2\text{S}_{(g)}$ into formation water (FW) brine to represent the gradual precipitation expected in producing HT/HP wells.(21-23) Due to the highly toxic nature of $\text{H}_2\text{S}_{(g)}$, the design of a system that was able form a multiphase emulsion due to high shear and propagate turbulence upon anti-fouling samples, all within an anaerobic vessel, was complex in nature. It, for the first time, enabled the mechanism of sulphide scaling in multiphase systems to be investigated, with comparisons drawn between against the nature of carbonate and sulphate scaling under similar conditions on a range of different surfaces. Inevitably, field case studies and analysis of produced waters reveal a level of complexity from three-phase (water-oil-solid) interactions under changing conditions that cannot be replicated in the laboratory. Tests illuminating the complex association of sulphide and carbonate scale species in multiphase conditions however aimed to show the synergistic influence of co-precipitation as well as the significance of an o-w interface in scaling mechanics.

1.4 Objectives

The primary objective of this study was to elucidate the mechanism of mineral precipitation and deposition in both single phase and upon introduction of a light oil phase within a scaling brine through design and construction of a novel scaling rig. The significance of anti-fouling coating characteristics was then assessed under flow conditions representative of those downhole, where emulsification of the bulk oil and water components and turbulence at the depositing interface were propagated.

Secondary to this investigation, the nature of PbS deposition and scaling in a multiphase system was explored, whereby particle stabilised Pickering emulsions adhered to surfaces after impaction contingent on their wettability at the interface. The relationship between the saturation ratio of a precipitating

mineral salt and the reliance on substrate wettability with regard to scaling tendency was also explored. Complex scaling systems were investigated where commonly occurring CaCO_3 and PbS were precipitated in tandem, with the presence of an oil-water interface of great significance.

Finally, the influence of polymeric sulphide inhibitor on PbS precipitation and emulsion behaviour was examined in conjunction with the effect of inhibitor addition on the degree of scale deposition upon various anti-fouling surfaces.

This thesis is structured as follows:

Chapter 4 explores the nature of carbonate, sulphate and sulphide scale deposition and the use of anti-fouling surfaces in order to mitigate its problematic nucleation, adhesion and build-up on surfaces.

Chapter 5 goes on to examine the role of the oil phase in scaling upon a range of anti-fouling surfaces

Chapter 6 further reflects sour oilfield conditions, where carbonate and sulphide forming brines are precipitated in tandem to assess the effects of co-precipitation

Chapter 7 investigates the influence on addition of sulphonated polymer, commonly a component of metal sulphide chemical inhibitors, on the deposition of scales on surfaces in multiphase systems

Chapter 2

Literature review of scale nucleation and deposition mechanisms

Mineral scale formation defined simply is the precipitation of sparingly soluble inorganic salts from aqueous solutions.(11) It poses a stubborn problem in a number of industries and processes, where crystalline solids are able form in solution and grow on surfaces that once compromised either reduce efficiency or completely halt production outputs. Within the oil industry, severe flow assurance and scaling issues arise from decreasing temperature and pressure of formation water (FW) during production, and consequent changes in water chemistry and solubility; or the incompatible mixing of FW with injected seawater (SW). Scales can block pores in the near-wellbore that can result in formation damage, or deposit on equipment in the well that affects functionality.(11)

This Chapter provides a background to the fundamental literature detailing carbonate, sulphate and sulphide scaling, as well as the influence of a light oil phase with respect to deposition. A focus on the ultimate mitigation of such scales required investigation into possible prevention through application of surfaces bearing a wide-range of characteristics in conjunction with chemical inhibitors that are traditionally utilised to prevent scale formation in oilfield systems.

2.1 Inorganic scaling

Mineral scale species are prone to precipitate out of solution as a consequence of their low solubility, where the solubility ratio (K_{sp}) is the solute concentration at which the flux of ions to and from the surface of a crystal is equal. Minerals with a low solubility ratio consequently require a lower solute concentration in solution in order to precipitate and grow.(24)

The most common form of scale, CaCO_3 , forms during primary production in a process known as auto-scaling, whereby the environmental changes in temperature and pressure of the formation water ultimately prompt reduced solubility that leads to crystallisation. CaCO_3 scale can lead to production issues and even blockage in relatively short periods of time.(12) Alternatively, mineral scaling can be caused by mixing of incompatible injection and formation waters during secondary recovery processes. Seawaters are rich

in sulphate (SO_4^{2-}) anions, while formation waters contain divalent cations such as Ba^{2+} , Sr^{2+} and Ca^{2+} ; and as a result of fluid mixing in the near wellbore, combined ion concentrations can surpass the solubility limits leading to crystallisation. Calcium sulphate (CaSO_4) scale has a higher propensity to form in limestone formations, with barium sulphate (BaSO_4) and strontium sulphate (SrSO_4) more likely to form in sandstone formations. Sulphate scales are difficult to remove chemically and near impossible to remove mechanically.(25)

Another adverse side effect of seawater injection is that it can prompt the reduction of SO_4^{2-} anions to sulphide species e.g. HS^- , in a process known as souring, while simultaneously exacerbating the proliferation of the sulphate reducing bacteria (SRB) that are responsible for the reduction reaction. Not only does the presence of sulphide species prompt vastly increased corrosion rates and provide potentially toxic release of gas topside, it can react with metal cations found as part of production equipment and naturally in formation waters, to form metal sulphide corrosion products e.g. FeS , and precipitates e.g. PbS and ZnS respectively.(26)

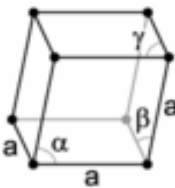

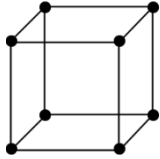
Table 2.1 shows a number of insoluble scales that have a propensity to form and cause operational issues in oilfield production systems. While variables such as temperature and total dissolved solids (TDS) almost uniformly influence scale solubility and precipitation likelihood, they do so in different ways, e.g. whilst CaCO_3 solubility decreases with temperature, BaSO_4 solubility will increase up to approximately 100°C . Numerous external variables can affect solubility of scales and hence scaling likelihood, as seen in Table 2.1.(12, 27-29)

Table 2.1 Common mineral scales in oilfields and variables affecting solubility *TDS = total dissolved solids

Mineral	Chemical formula	Primary variables
Calcium carbonate	CaCO_3	p CO_2 , Temp, TDS, pH
Barium sulphate	BaSO_4	Temp, Pressure
Calcium sulphate	CaSO_4	Temp, Pressure, TDS
Strontium sulphate	SrSO_4	Temp, Pressure, TDS
Lead sulphide	PbS	pH, H_2S conc., Temp, TDS

The control and management of scale downhole is therefore difficult, particularly where multiple scaling species have the potential to precipitate in different regions of the production tubing from the near-wellbore to topside, as each responds uniquely to specific removal methods. Table 2.2 shows the three basic forms of scale investigated in this study.(30-33)

Table 2.2 Characterisation of oilfield scales examined in this study (30-33)

	Calcite (CaCO₃)	Barite (BaSO₄)	Galena (PbS)
Crystal system			
Morphology	Rhombohedral	Orthorhombic/Diamond Spherical/Rhombohedral Rectangular/Spindle	Cubic
Axis system	$a = b = c$ $\alpha = \beta = \gamma$ $\neq 90^\circ$	<i>Dependent on morphology</i>	$a = b = c$ $\alpha = \beta = \gamma$ $= 90^\circ$
Other polymorphs	Aragonite and vaterite	None	None

2.2 Conventional scales

Crystalline CaCO₃ and BaSO₄ deposits can coat downhole completion equipment, the near wellbore and tubulars, requiring physical or mechanical removal to maintain flow from the reservoir if proactive mitigation methods have not been successfully carried out.(25) Figure 2.1 shows an example of CaCO₃ build-up in a pipe, where significant narrowing of the functional pipe diameter leads to substantial loss of performance and even failure.(34)

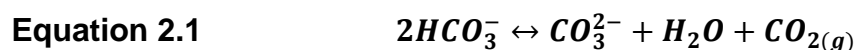


Figure 2.1 Calcium carbonate scale build-up (34)

2.2.1 Calcium carbonate (CaCO₃)

CaCO₃ commonly occurs in three polymorphic forms: calcite, aragonite and vaterite (in order of decreasing thermal stability), whilst barite is the only polymorph of barium sulphate. Calcite, the most stable state of CaCO₃ has a cubic or rhombohedral morphology, whilst barite morphology varies significantly based on levels of supersaturation.(31, 35)

CaCO₃ fouling is endemic in oilfield systems, as formation water containing both bicarbonate (HCO₃⁻) and calcium (Ca²⁺) ions is prone to form precipitate simply as a result of pressure changes during production. The release of carbon dioxide (CO₂) gas from the aqueous phase as a result of pressure reduction prompts the evolution of carbonate (CO₃²⁻) as seen in Equation 2.1, resulting in a rise in pH and consequent precipitation (Equation 2.2).(11)



Le Chatelier's principle determines in which direction Equation 2.1 shifts, where any imposed changes in concentration, volume, pressure or temperature will push the equilibrium to counteract the change.(12) A schematic representation of the carbonic system can be seen in Figure 2.2.(36)

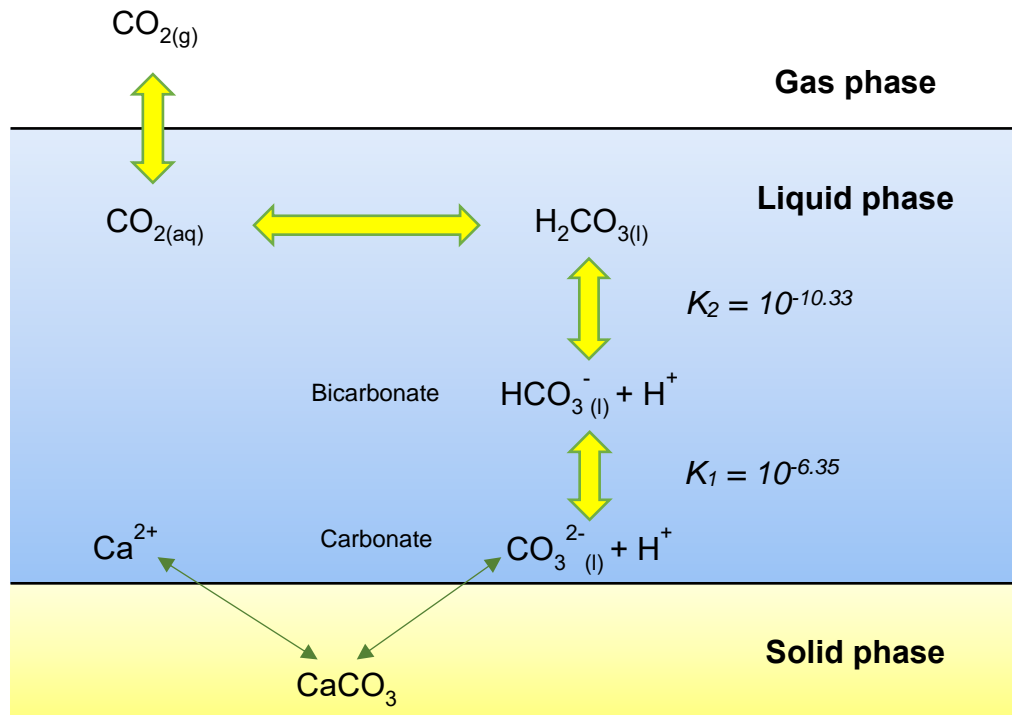


Figure 2.2 Schematic representation of the carbonic system (36)

Build-up of carbonate scales can occur rapidly upon downhole surfaces and equipment, leading to significant production downtime and potential well failure.(12) Whilst the formation of BaSO_4 scale, like metal sulphides, is prompted by the injection of sulphate containing seawater, CaCO_3 can precipitate during the primary recovery phase, a process referred to as auto-scaling. The additional reduction of CaCO_3 solubility with increased temperature when CO_2 is present dictates that precipitation can occur anywhere in the production tubing, with case studies showing precipitation of CaCO_3 species from both near the wellbore to the topside.(37, 38)

2.2.2 Barium sulphate (BaSO_4)

BaSO_4 is the most insoluble of the sulphate scales and consequently one of the hardest to control, forming when formation water and injected seawater mix during secondary recovery, often in the near-wellbore region of producing wells, as seen in Equation 2.3:(11)



In oil wells and reservoirs within the North Sea, barite is the dominant scaling mineral, estimated to cause \$1.4 billion per annum in operating costs for removal and unscheduled downtime. Barite is also able to incorporate radioactive ions such as radium into its lattice that poses a safety risk to offshore workers.(39)

Figure 2.3 shows a basic illustration of seawater injection, where seawater injection results in cooling of the reservoir in proximity to the injection point.(40)

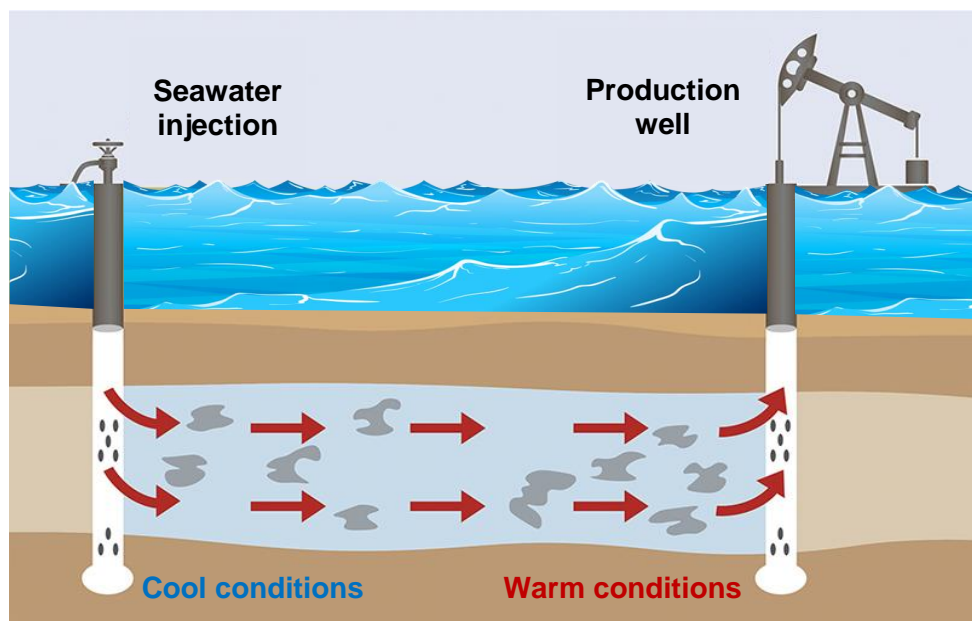


Figure 2.3 Illustration of seawater injection and influence on reservoir temperature (40)

Before injection, seawater is treated through filters to remove SO_4^{2-} anions to firstly prevent the precipitation of Ba^{2+} and Sr^{2+} salts, and secondly for souring control to mitigate the proliferation of sulphate reducing bacteria (SRB) within the reservoir and consequent production of sulphide species. It is extremely hard to control bacterial outbreaks in the reservoir as even if only a small fraction of bacteria survive they can act as a seed and later proliferate.(12) SRB can survive up to pressures of 52 bar but reach reductive efficiency at approximately 27 bar.(40) Most strains however are not particularly resistant to temperature, where most common SRB cannot grow at temperatures above 317 K, with some strains able to function at approximately 343 K.(40) Whilst extreme HT/HP reservoirs can reach temperatures of up to 533 K, injection of seawater results in reservoir cooling around the injector wellbore, as seen in

Figure 2.3, that provides conditions under which SRB can potentially thrive. As such the effect is twofold, where injected seawater results in a temperature downhole that may lead to the multiplication of undesirable SRB, as well as provide a trace amount sulphates (after nanofiltration membrane systems can reduce concentration to 40 mg/L) that can then nevertheless be reduced to sulphide species.(41) It is also possible that injected seawater can contain strains of SRB that lie dormant until under highly anoxic conditions downhole, where O_2 concentration is less than 0.5 mg/L. SO_4^{2-} reduction consequently occurs under anoxic conditions, at which electron activity (Eh) of the water downhole is between 0 and -300 mV.(40, 42, 43) The biochemical mechanism occurring within a SRB can be seen in Figure 2.4.(44)

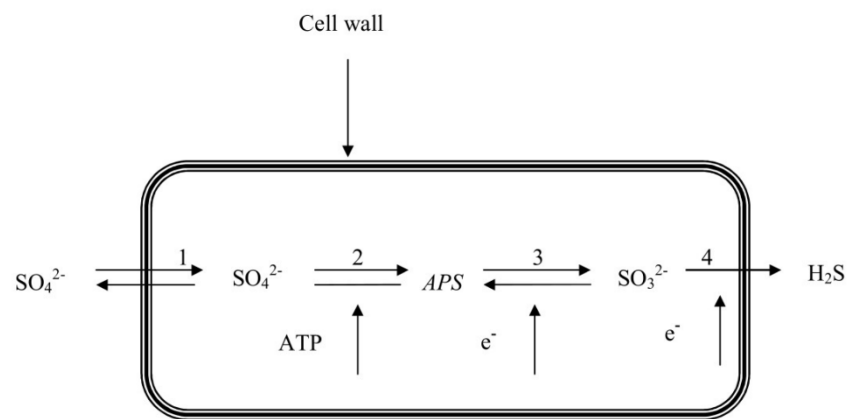


Figure 2.4 The biochemical pathway of dissimilatory sulphate reduction in SRB (44)

Aqueous H_2S released as a product of SRB (Figure 2.4) dissociates into sulphide species before reacting readily with metal cations present in the formation water to form insoluble metal sulphide scales.

The presence of H_2S can exacerbate the formation of other sulphide scales, increase corrosion risk, pose a danger for workers at topside due to its toxicity and reduce the value of oil and gas.(12)

2.3 Unconventional sulphide scales

Though less common than carbonate and sulphate scales, build-up and deposition of metal sulphide scales on downhole equipment and production tubing can negatively affect the flow and production of oil.(12) Lead and zinc

sulphide scaling has become a concern in a number of North Sea oil and gas fields, rich in both evolved hydrogen sulphide (H₂S) gas and formation metal ions.(45) Sulphide ore deposits of lead and zinc, known as Mississippi Valley Type (MVT) deposits, are commonly observed in Devonian to Permian and Cretaceous to Tertiary formations.(46) As a result, cations of lead and zinc are found naturally in many formation waters in HT/HP fields due to mineral dissolution of these ores over millions of years. Dependent on pH, sulphide (S²⁻) and/or bi-sulphide (HS⁻) anions form when hydrogen sulphide (H₂S) gas present in the reservoir diffuses into formation water, and consequently dissociates. Anions are highly susceptible to precipitate into sulphide scales when reacted with aqueous metal cations such as lead (Pb²⁺) and zinc (Zn²⁺), present in formation waters.(11) Injected water used for pressure support can also enrich seawater with heavy metal ions from the formation.(14) Evolution of H₂S gas or 'souring' of reservoirs can occur through both microbiological and geochemical means; a consequence of the decomposition of organic matter, increased activity of sulphate reducing bacteria (SRB) and chemical reactions resulting from seawater injection, respectively.(47) The dissociation of H₂S to its constituent bi-sulphide anions in water at pH levels expected in sour systems where pH values are typically between 5 – 7, can be seen in Equation 2.4.(48, 49)



Lead cations (Pb²⁺) in produced water react readily with sulphide ions (S²⁻) to form PbS (galena) in Equation 2.5.



Concentrations of dissolved aqueous H₂S in the produced water of North Sea oil wells have been recorded at levels as high as 55 ppm during production, yet it has been reported that concentrations as low as 2 ppm are sufficient to prompt formation of sulphide scale.(12, 50) Precipitation of PbS crystals and the location at which they adhere to surfaces of production equipment or tubing is reported to be based upon changes in temperature, water chemistry, pH and residence time; in addition to the oil composition, characteristics and water-cut.(14) As with conventional carbonate and sulphate scales, build-up

of sulphide scale debris can contribute to damage and malfunction of downhole equipment such as sub-surface safety valves (SSSV), consequently compromising well integrity, which can in turn lead to considerable unscheduled downtime.(50)

2.3.1 Lead sulphide (PbS)

PbS is the most insoluble of all the sulphide scales that form downhole and as such is almost impossible to remove through chemical means. Wet PbS scale deposits (Figure 2.5), found commonly in HT/HP wells in the North Sea, have been reported to be a build-up of black, non-porous, fine grained scale that is particularly hard and brittle; and as a consequence is not easily removed.(38, 50)



Figure 2.5 Sulphide scale deposits from the North Sea Central Graben fields
(38)

2.3.2 Crystal structure of PbS

The cubic structure of PbS is represented in Figure 2.6a & b, where a slab view and top view of the lattice is shown respectively.(33) Values in Figure 2.6a are representative of the bond lengths in angstroms (\AA) between Pb and S, where the average value of the three-interacting axial Pb-S bond lengths is 2.813 \AA .(33)

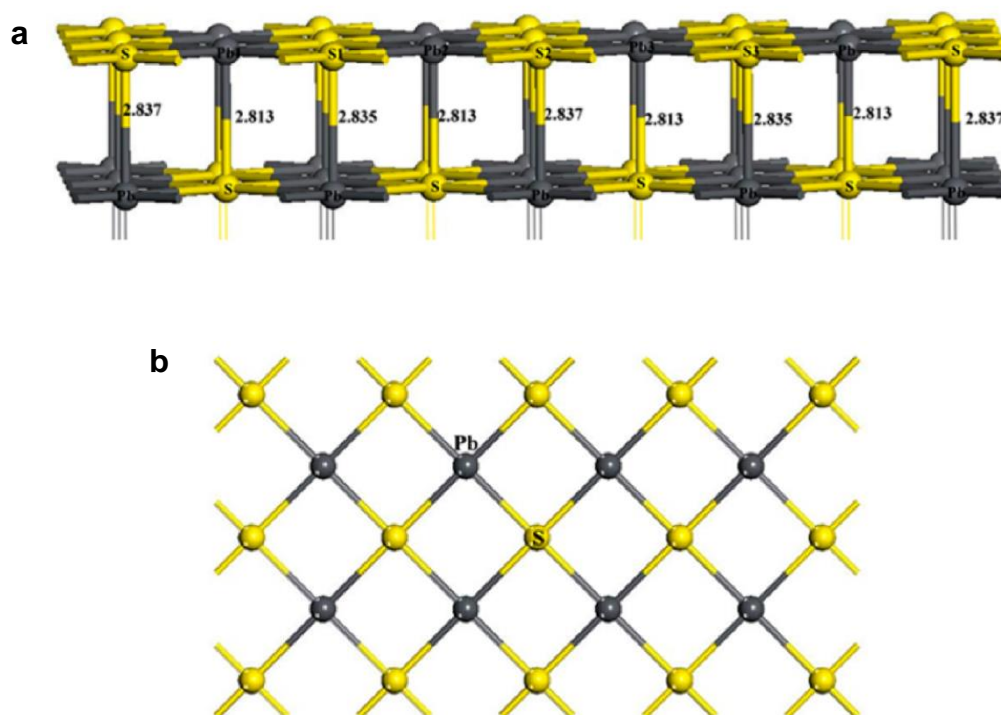


Figure 2.6 Crystal lattice structure of PbS (33)

PbS is a stoichiometric compound, with homogeneity in the region $\text{PbS}_{0.9995-1.0005}$ and crystallises in a cubic morphology, where the space group is $Fm\bar{3}m$ with a lattice constant of $a = 0.59362$.(51)

Water adsorption upon the hydrophobic galena surface is primarily through strong hydrogen bonds formed between water H atoms and surface S atoms. Two-dimensional hydrogen bonding of a water monolayer on the PbS surface strengthens S – H bonding; though as three-dimensional hydrogen bonding is stronger than S – H bonding the interaction of water and the galena surface is weakened (Figure 2.7). As such, unoxidised galena water contact angle is predicted to lie between 48 - 52°.(33)

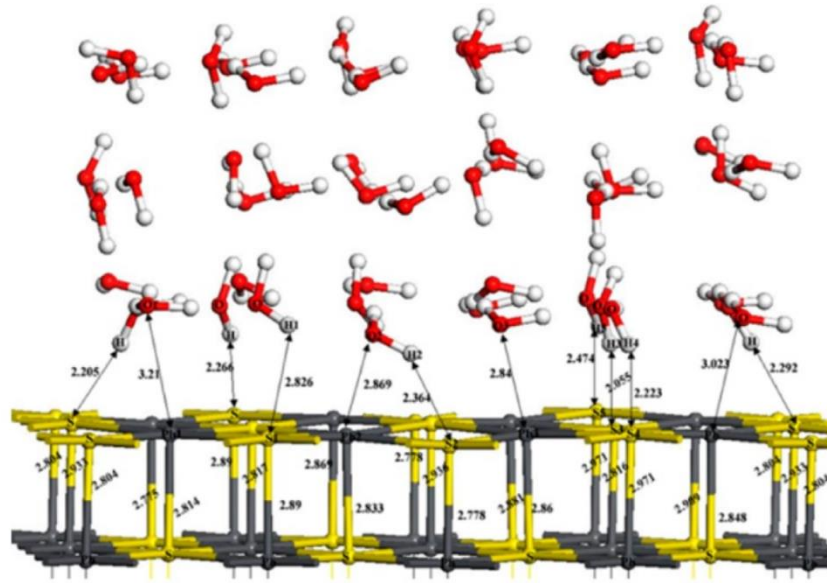


Figure 2.7 Molecular illustration of water interacting with a galena surface (33)

2.4 Mineral nucleation and crystallisation

2.4.1 Supersaturation

The likelihood of the precipitation of a specific mineral is contingent on the saturation ratio (SR), defined as the difference in chemical potential between a molecule in solution and that in the bulk of the crystal phase.(52) Following the rules of thermodynamics, this can be given by Equation 2.6.

Equation 2.6
$$\Delta\mu = kT \ln SR$$

Where $\Delta\mu$ is the difference in chemical potential, k is the Boltzmann constant, T is the absolute temperature, and SR the saturation ratio. When $\Delta\mu > 0$ the solution is supersaturated.(52)

A saturated solution is in thermodynamic equilibrium with the solid phase at a specified temperature. A state of supersaturation is required for crystallisation, with two classes of supersaturated solutions being defined as ‘labile’ and ‘metastable’ by Ostwald to determine spontaneous nucleation would or would not occur respectively.(35, 53)

- 1) Stable (unsaturated) where crystallisation is impossible

- 2) Metastable (supersaturated), where spontaneous crystallisation is improbable. If a crystal seed were placed in a metastable solution, growth would occur at its surface.
- 3) Unstable or labile (supersaturated) where spontaneous crystallisation is probable, but not inevitable

These states that determine the likelihood of initial crystallisation can be quantified and represented as the initial saturation ratio ($SR_{Initial}$), allowing scaling power to be defined. Water is supersaturated with respect to calcium carbonate if the ion activity product (IAP) for Ca^{2+} and CO_3^{2-} exceeds the $CaCO_3$ solubility product. A solution's scaling tendency (or saturation ratio), is calculated through a ratio of the IAP (ion activity product) and K_{sp} (solubility product) for $CaCO_3$.(54) $SR_{Initial}$ for $CaCO_3$ is defined in Equation 2.7 below:
(55)

Equation 2.7
$$SR_{Initial} = \frac{(IAP Ca^{2+})(IAP S^{2-})}{(K_{sp} CaCO_3)}$$

Where at:

$SR < 1$: Scale formation is impossible due to under-saturation and the solution is likely to dissolve any deposit.

$SR = 1$: Scale formation and dissolution rate are equal under equilibrium. There is no nucleation and any seeds added to a solution neither dissolve or increase in size.

$SR > 1$: The solution is supersaturated with scale formation thermodynamically possible and likely to occur.(56)

2.4.2 Induction time

Induction time is the time which elapsed between the moment of mixing between two incompatible brines within a supersaturated solution and the first appearance of crystals or turbidity.(57) It is influenced by the degree of supersaturation, state of agitation, presence of impurities, viscosity, etc. Mullin (58) defined the induction time (Equation 2.8) as:

Equation 2.8
$$t_i = t_T + t_n + t_g$$

Where t_T is the relaxation time (s), t_n is the time required for the formation of a nucleus (s); and t_g is the time required for the nucleus to grow to a detectable size (s).(58)

2.4.3 Nucleation

Given that the saturation ratio is sufficient, nucleation occurs and is defined as the series of atomic or molecular processes by which the atoms or molecules of a reactant phase rearrange into a cluster of the product large enough as to have the ability to grow to a macroscopically larger size.(58) Primary nucleation is described as ‘nucleation in systems that do not contain crystalline matter, and secondary nucleation when ‘nuclei are generated in the vicinity of crystals already present in supersaturated solution’. Primary nucleation can be classified as either homogeneous and heterogeneous, relating to spontaneous precipitation within the bulk phase and nucleation induced by a foreign surface respectively.(35) Figure 2.8 demonstrates the modes of nucleation.(35)

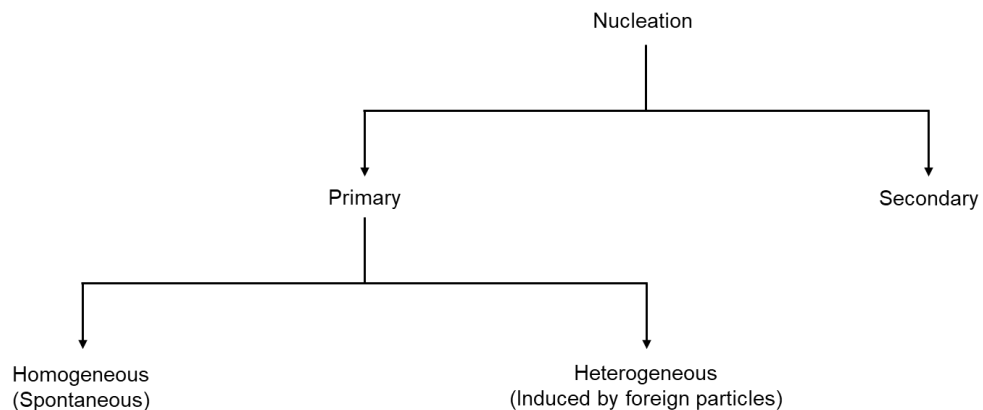


Figure 2.8 Pathways via which nucleation can occur (35)

The nature of oil production provides not only a multiphase system where high TDS brine containing scale forming species are present but tubing and equipment that provide sites at which crystals can either nucleate or adhere from solution.

2.4.4 Primary nucleation

Scale can adhere to surfaces via two different mechanisms from a supersaturated solution. Homogeneous nucleation occurs within the bulk phase deposits and adheres to a surface (Figure 2.9), whereas heterogeneous nucleation characterises crystallisation directly onto a surface, as seen in Figure 2.10.(25)

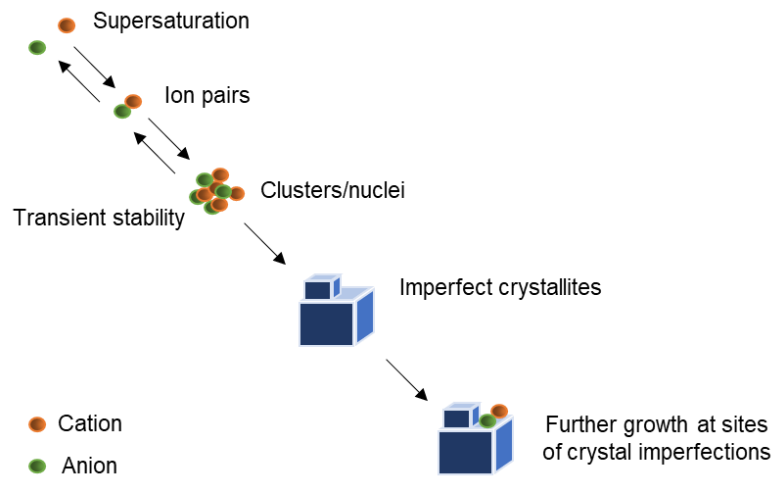


Figure 2.9 Homogeneous nucleation – mechanism of bulk growth (25)

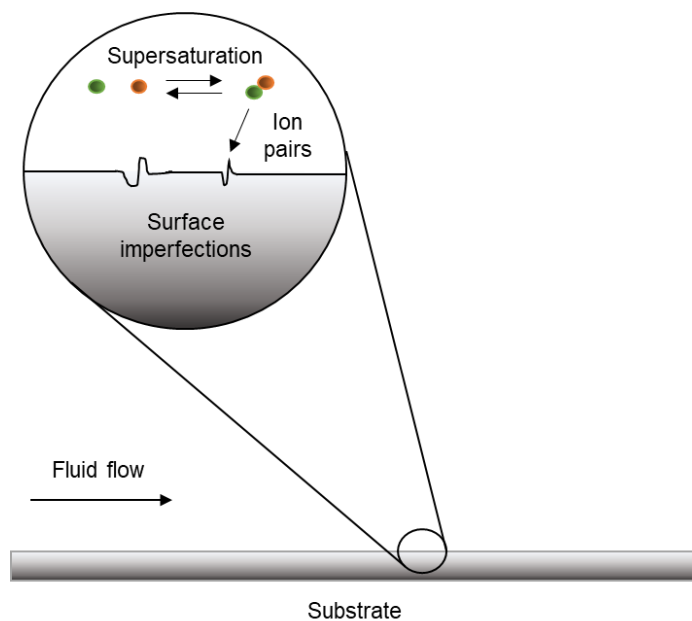
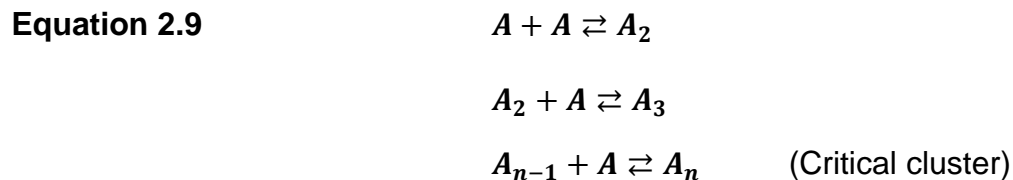


Figure 2.10 Heterogeneous nucleation – surface nucleation (25)

The precipitation and growth of inorganic mineral scales can proceed via both heterogeneous surface nucleation and homogeneous bulk nucleation mechanisms. Homogeneous precipitation is the predominant process given a sufficiently high degree of supersaturation; largely determined by the compound solubility, ionic species concentration, temperature, pH or the influence of foreign inhibiting species.(59, 60)

2.4.4.1 Homogenous nucleation

The exact details of formation of a stable crystal nucleus within a homogeneous fluid is not known with any degree of certainty. Not only are constituent molecules required to coagulate and resist the tendency to re-dissolve but become orientated into a fixed lattice. The number of molecules in a stable lattice can vary from ten to several thousand, yet a stable nucleus is unlikely to result from simultaneous collision of the required number of molecules, as this would be an extremely rare occurrence. It is likely to result due to a sequence of bimolecular additions according to the scheme shown in Equation 2.9.(35)



Where A is representative of a single molecule and A_n the number of molecules required to construct a critical cluster. Further molecular additions to the critical cluster results in nucleation and subsequent growth of the nucleus, with short chains forming initially and eventually building up a crystalline lattice structure.(35)

Classical nucleation theory is based on condensation of a vapour to a liquid, with free energy changes associated with the process of homogeneous nucleation. The overall excess free energy (ΔG), is the sum of the surface excess free energy (ΔG_s) and volume free energy (ΔG_v), shown in Equation 2.10. Equation 2.11 shows the overall excess free energy between a small solid particle of solute and the solute in solution.(35)

Equation 2.10

$$\Delta G = \Delta G_s + \Delta G_v = 4\pi r^2 \gamma + \frac{4}{3}\pi r^3 \Delta G_v$$

Equation 2.11

$$\frac{d\Delta G}{dr} = 8\pi r \gamma + 4\pi r^2 \Delta G_v = 0$$

Where r is the radius of the particle assumed to be spherical (m), γ the interfacial tension (mN/m) between the developing crystalline surface and the supersaturated solution in which it is located. The surface free energy (ΔG_s) can be described as the excess free energy between the surface of the particle and the bulk of the particle (also described as the interfacial energy), and the volume free energy (ΔG_v) as the excess free energy between a very large particle ($r = \infty$) and the solute in solution.(35)

The two terms, ΔG_s and ΔG_v are of opposite signs and depend differently on r , so the free energy ΔG passes through a maximum, as can be seen in Figure 2.11 as indicated by the dotted line. This maximum value, indicated by ΔG^* (or ΔG_{crit}) corresponds to the critical nucleus, r_c , and for a spherical cluster is obtained by maximising Equation 2.10, setting $\frac{d\Delta G}{dr} = 0$ results in Equation 2.11.(35)

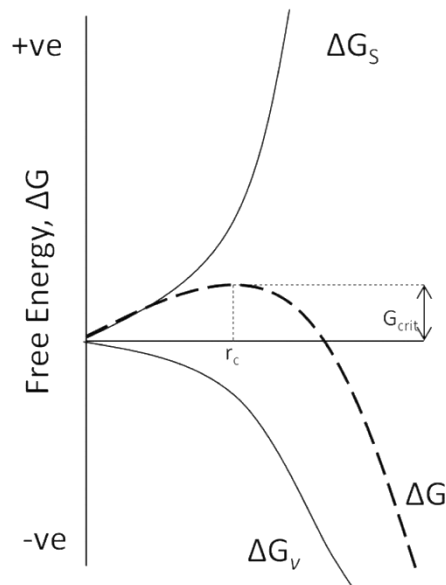


Figure 2.11 Free energy diagram for nucleation – existence of a ‘critical nucleus’ (35)

The critical size, represented by Equation 2.12, is the minimum size of a stable nucleus.(35, 61)

Equation 2.12
$$r_{crit} = \frac{2\sigma v_l}{kT \ln S}$$

where v_l is the molecular volume of the liquid (L), σ is the surface tension (mN/m) and S the supersaturation.

Behaviour of a newly created crystalline lattice in a supersaturated solution depends on its size and can either grow or re-dissolve. However, the process necessarily results in a decrease in the free energy of the particle. Particles smaller than r_{crit} will dissolve or evaporate as a liquid in a supersaturated vapour, as this is the only way the particle can achieve a reduction in its free energy. Similarly, particles larger than r_{crit} will continue to grow.(35)

According to classical nucleation theory (CNT) described by Volmer (62), given a suitably high saturation ratio the reduction of the required critical ion cluster size and consequent lowering of activation energy barrier enables spontaneous nucleation of crystals within the bulk phase.(54) Based on the kinetics of homogeneous precipitation, at sufficiently high saturation ratios nucleation rate occurs at such speed to be considered spontaneous, with the number of nuclei formed increasing linearly with induction time (63). Spontaneous homogeneous nucleation, whereby the rate of crystal nucleation is greater than that of crystal growth, results in formation of small particles with narrow size distributions. Cubic PbS crystals precipitated in the bulk phase have been reported to range from 20-100 nm, as a result of the remarkably high initial saturation ratio and nucleation rate allowing formation of thermodynamically stable nanometric particles.(19, 64-66)

Following classical nucleation theory (CNT), nucleation rate (J) can be defined as the number of clusters formed per unit time and per unit volume in a supersaturated system. Given the high supersaturation of PbS and the assumption that only primary nucleation is taking place, the nucleation rate of homogeneous nucleation can be predicted in Equation 2.13.(61, 67)

Equation 2.13
$$J = K \exp\left(-\frac{\Delta G^*}{kT}\right)$$

Where K is the kinetic prefactor, ΔG^* is the change in Gibbs free energy required to form a critical cluster of the new phase from the supersaturated phase, k is the Boltzmann constant ($J.K^{-1}$) and T is the temperature (K).

Very low solubility of PbS in distilled water where $K_{sp} = 3 \times 10^{-28} \text{ mol}^2 \text{ dm}^{-6}$ at 25°C ; pH 7, results in an SR_{Initial} value of approximately 1.7×10^{19} when Ionic Activity Product (IAP) concentrations of reactants and pH values typically seen in oilfield systems are applied experimentally.(68)

2.4.4.2 Heterogeneous nucleation

The rate of nucleation of mineral species within a solution can be affected by the presence of impurities within a system that act as a nucleation inhibitor in one case, and as a nucleation accelerator in another. Many cases of spontaneous (homogeneous) nucleation are found to have been induced in some way, and it is accepted that true homogeneous nucleation is a rare event. A supercooled system can be seeded unknowingly by the presence of atmospheric dust which may contain 'active' particles known as hetero-nuclei.(35)

The presence of a suitable foreign body or surface can induce nucleation at degrees of super-cooling lower than those required for spontaneous nucleation. Overall free energy change associated with the formation of a critical nucleus under heterogeneous conditions, $\Delta G'_{crit}$, must be less than the corresponding free energy change ΔG_{crit} , associated with homogeneous nucleation as seen in Equation 2.14.(35)

Equation 2.14
$$\Delta G'_{crit} = \phi \Delta G_{crit}$$

Where ϕ = less than unity

Interfacial tension, γ (mN/m), is an important factor in determining the nucleation rate, as can be seen in Young's equation (Equation 2.15).

Equation 2.15
$$\cos\theta = \frac{\gamma_{sl} - \gamma_{cs}}{\gamma_{cl}}$$

Interfacial energy is dependent on three phases in contact; being denoted by γ_{cl} (crystalline phase/liquid), γ_{sl} (solid/liquid) and γ_{cs} (crystalline phase/solid).

The contact angle, θ , between the crystalline deposit and the foreign solid surface corresponds to the angle of wetting in liquid-solid systems. This is shown in Equation 2.15 and illustrated in Figure 2.12.(35, 69)

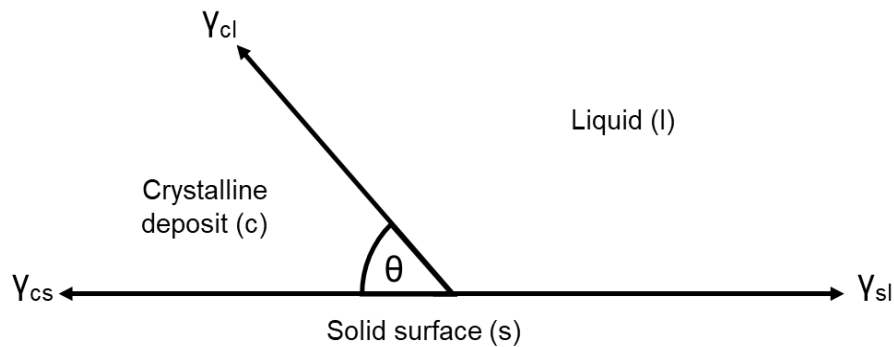


Figure 2.12 Interfacial tension at boundaries between phases (35)

When θ lies between 0 and 180° , $\phi < 1$; therefore: $\Delta G'_{crit} < \Delta G_{crit}$

In the case of complete affinity/hydrophilicity (complete wetting), θ is equal to 0° , ϕ is also 0 and consequently the free energy of nucleation $\Delta G'_{crit}$ is also equal to 0. Conversely, if θ is equal to 180° , this corresponds to complete non-wetting in liquid-solid systems.

2.4.5 Secondary nucleation

Secondary nucleation is defined as the formation of new crystals from those that are already present in solution, and requires a SR that is substantially lower than that needed for primary nucleation.(70)

Three different mechanisms have been described, where abrasion is the removal of small parts of the crystal; attrition the disintegration of the crystal into two dissimilarly sized parts; and fracture the fragmentation of the crystal into two parts similar in size.(71) Industrial crystallizers often undergo secondary nucleation by way of attrition, a result of the high speed of moving parts and the brittle nature of crystalline materials.(72) Impingement of downhole mineral scale build-up by solids in a high flow-rate producing stream may also lead to attrition in a context specific to this work. Secondary nucleation has also been shown to occur in natural environments e.g. saline spring waters, basaltic caves etc. and biomineralization, where secondary

nucleation in sea urchin spicules propagates from one particle to the next transforming from amorphous calcium carbonate (ACC) to calcite.(73-75)

2.4.6 Crystal nucleation and growth mechanisms

Crystallisation growth of a crystal can be categorised in two ways: the process of transporting materials and assembly/interface kinetics. Free energy (G) is consumed in both processes where at constant temperature and pressure, chemical potential is expended. Transport of ions is controlled via diffusion, where material is transported to the crystal interface down a chemical potential gradient before transformation from liquid to solid occurs. Solidification occurs via the incorporation of an atom into the crystal lattice when the solute concentration is in excess within solution. During the process of solidification an atom or molecule may need to break bonds with solvent molecules, known as desolvation.(76, 77)

Crystal growth occurs from a supersaturated solution when the flux of the molecules attaching to the surface exceeds that of those detaching. Solubility, as previously stated, is the concentration at which the flux of ions to and away from the surface is equal and is dependent on solute concentration (activity). As such, more highly soluble crystals have a higher growth rate in solution when compared to sparingly soluble crystals, even at identical supersaturation.(78)

Crystal surfaces become roughened at higher temperatures, resulting in a multitude of kink sites from which growth can occur in the normal direction through incorporation of atoms or molecules, known as normal growth. If a crystal surface is faceted however, atoms require a kink site, usually located along steps on the surface in order to crystallise. As such, growth occurs forward along the surface of the crystal, advancing laterally in steps and hence is referred to as lateral growth.(77)

2.4.6.1 CaCO₃ nucleation and growth mechanisms

The thermodynamic solubility product for CaCO₃ ($K_{sp} = 3.8 \times 10^{-9}$) is relatively high when compared to that of metal sulphides at ambient temperature and neutral pH, resulting in low levels of supersaturation that leads to heterogeneous crystallisation induced by surfaces, impurities and phase boundaries.(57, 79-81) The extensive growth of calcite crystals at supersaturations typically seen in oilfields during production and topside processing may be explained by the presence of many small crystallites on

the growing face, exhibiting rough surfaces with a multitude of kink-and-step sites.(82)

For calcite, layer growth occurs, whereby anions incorporate into the growing lattice, followed by cations, with the rate-limiting step the movement of ions from preferred adsorption sites to those critical for growth.(83) On a flat crystal face growth proceeds in two stages, whereby building units transfer to the surface from the solution before incorporation into the crystal lattice as seen in Figure 2.13. Incorporation can include adsorption to the surface, step and surface diffusion, the slowest step determining the calcite growth rate.(84)

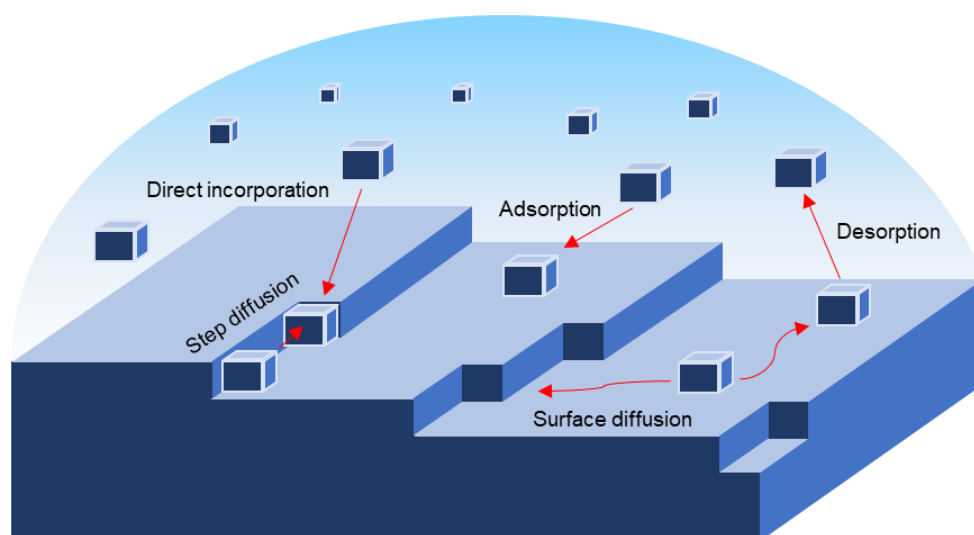


Figure 2.13 Schematic illustration of different stages of the crystal growth in solution. Growth units adsorb to the surface or directly attach to kink positions. After adsorption to the surface, it migrates across the surface up to the step, where it incorporates into the crystal lattice (84)

Typically, there are three mechanisms of calcite crystal growth: continuous growth, surface nucleation and spiral growth. In continuous growth units incorporate directly with no surface diffusion step on a crystal with rough faces. Surface nucleation is the dominant growth mechanism on flat crystal faces, with screw dislocation occurring when defects are present.(84)

2.4.6.2 BaSO₄ nucleation and growth mechanisms

Kowacz et al. showed through AFM study Ba²⁺ ion incorporation to be the rate-limiting step in two-dimensional nucleation when thermodynamic force

was constant, where the mechanism for barite growth was governed by the kinetics of Ba^{2+} attachment.(85)

Judat and Kind (31), described the aggregation and ripening of $BaSO_4$ nanoparticles that had nucleated and grown in solution at high supersaturations.(31, 86) Highly-ordered, self-assembled aggregation of barium sulphate nano-crystallites resulted in a monocrystalline structure after re-crystallisation or ripening, whereby smaller crystals dissolve in favour of bigger crystals as a dependence of solubility on the surface curvature. As such, the growth model predicted at high saturations is a two-step process reliant on aggregation and ripening, whilst traditional molecular growth plays a big role at lower supersaturations. Figure 2.14 shows the proposed mechanism of $BaSO_4$ growth at high supersaturations.(31)

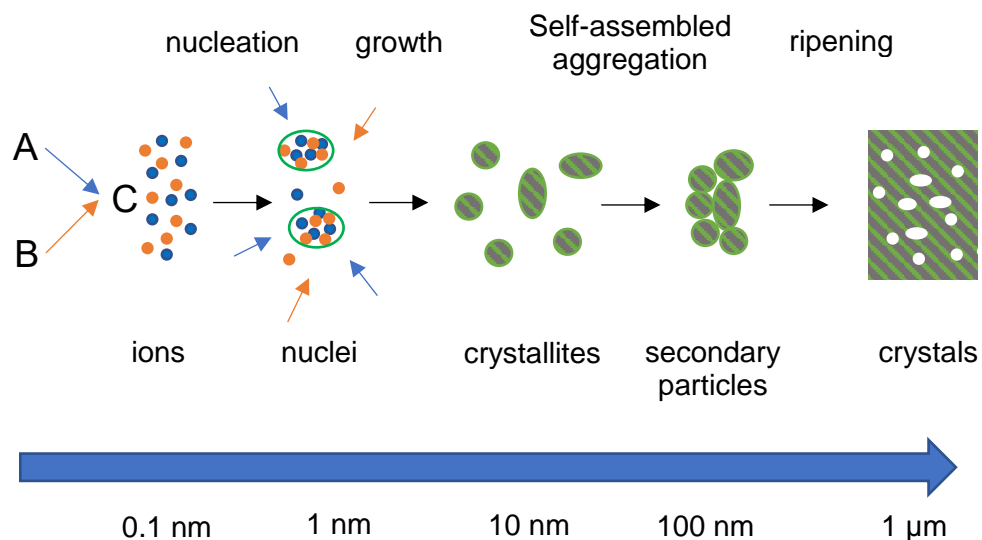


Figure 2.14 small nanocrystallites are produced responsible for aggregative growth; secondary particles which are monocrystalline due to a recrystallization step, where at high levels of supersaturation the presented growth mechanism dominates (31)

2.4.6.3 PbS nucleation and growth mechanisms

The exceedingly high supersaturation for PbS results in the spontaneous precipitation of particles within the homogeneous bulk phase. Following CNT, the growth of nanoparticles is contingent on two separate mechanisms: the surface reaction and diffusion of the monomer to the surface. Fick's first law can be rewritten to accommodate nanoparticle growth within solution:

Equation 2.16

$$J = \frac{4\pi D r (r + \delta)}{\delta} (C_b - C_i)$$

Where r is particle radius (m); J the total flux of monomers passing through a spherical plane ($\text{mol m}^{-2} \text{s}^{-1}$) with radius x (m); D the diffusion coefficient (m^2/s); C the concentration (mol/m^3) at a distance x (m); δ is the distance from the particle surface to the bulk concentration of monomers within solution (m); C_b is the bulk concentration of monomers within solution and C_i is the concentration of monomers at the solid/liquid interface.

The LaMer mechanism defines rapid nanoparticle precipitation in a supersaturated medium as a process of three stages, where nucleation and crystal growth stages are defined, represented in Figure 2.15, where time is plotted as a function of monomer concentration. (87, 88) Firstly, there is an increase in the concentration of free monomers in solution, followed by ‘burst-nucleation’, where nucleation rate is effectively infinite, until stalling due to the expiration of free Pb^{2+} and S^{2-} monomers. Finally, post-nucleation growth occurs through diffusion of monomers through the solution.

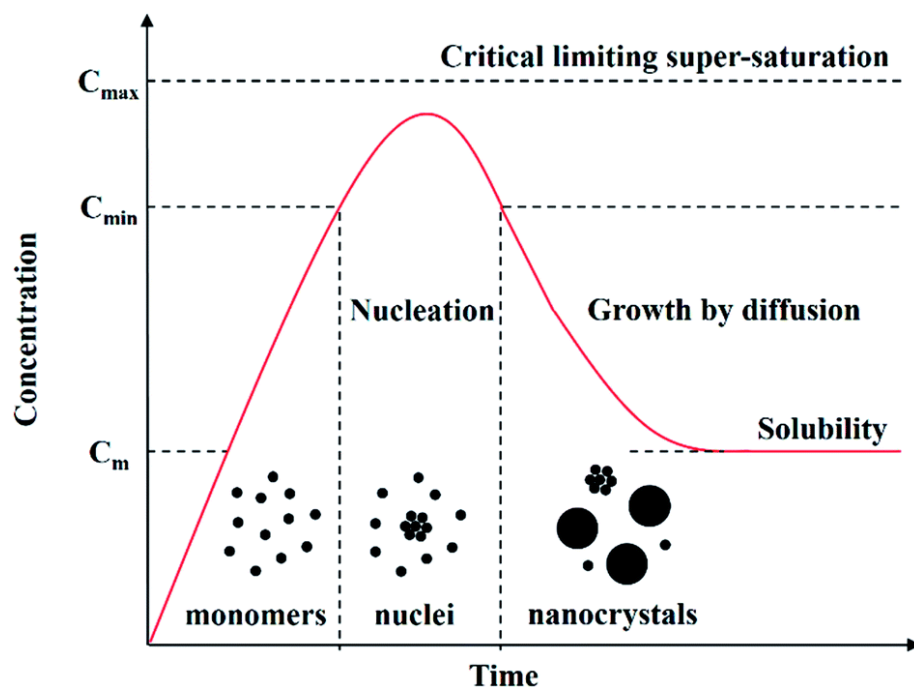


Figure 2.15 Schematic illustration of the nucleation and growth process of nanocrystals in solution: nuclei develop from monomers before the growth of nanocrystals via the aggregation of nuclei (87)

Nucleation and growth mechanisms described in Figure 2.15 are illustrated in Figure 2.16 for the nucleation and formation of PbS nanoparticles, where free ions form nuclei that then coalesce and grow to form nanoparticles. (88, 89)

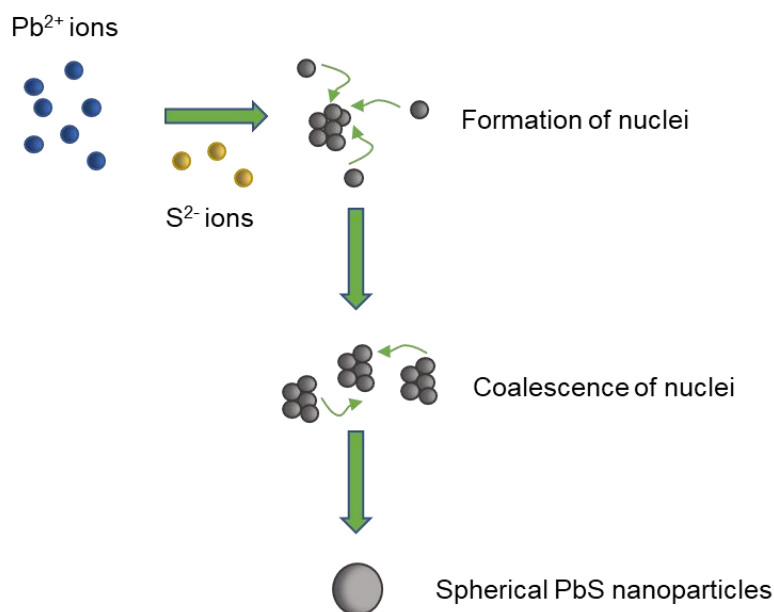


Figure 2.16 Schematic showing the formation of PbS nanoparticles (88)

Kinetic investigations however have shown that Ostwald ripening may be the predominant growth mechanism for PbS nanoparticles after the early stages of crystal formation and nucleation, occurring at times beyond 0.5 s in experiments performed by Brazeau and Jones.(90) Ostwald ripening was particularly significant at temperatures up to 298 K, with temperatures above 303 K seeing the onset of oriented attachment between two particles.(90)

Conventional scales are far more soluble than PbS in water, with solubility products (K_{sp}) of $3.8 \times 10^{-9} \text{ mol}^2 \text{ dm}^{-6}$ and $1.1 \times 10^{-10} \text{ mol}^2 \text{ dm}^{-6}$ at 25°C for CaCO_3 and barium sulphate BaSO_4 respectively.(91, 92) As the saturation ratios of CaCO_3 and BaSO_4 are approximately 19 orders of magnitude lower than PbS given an identical ionic activity product (IAP), the thermodynamic driving force for nucleation to occur is significantly lower compared to that of PbS. In systems prone to CaCO_3 and BaSO_4 scaling, the presence of a foreign surface within a system is likely to induce nucleation at degrees of supercooling lower than those required for homogeneous nucleation, resulting in increased heterogeneous nucleation.(35) In conventional scaling systems with a significantly lower SR_{initial} than is likely within sulphide systems, crystal

growth is likely to occur by way of Ostwald ripening mechanism, with a significantly higher critical nucleus size and hence nucleation barrier.(35) Average crystal size was therefore expected to be significantly higher for CaCO_3 and BaSO_4 crystals than those of PbS , where the growth rate of highly soluble crystals is significantly higher than those that are sparingly soluble.(78)

2.5 Importance of pH in CO_2 and H_2S dissociation

pH is an integral parameter with regards to determining the mole fraction of aqueous species concentration at equilibrium within a system saturated by carbon dioxide (CO_2) or hydrogen sulfide (H_2S). Dissociation of molecules in the aqueous phase results in formation of anionic species that react readily with metal cations present within the formation brine, which then precipitate as solid scales. It can be seen from the Bjerrum plots in Figure 2.17 for $\text{CO}_{2(\text{aq})}$ and $\text{H}_2\text{S}_{(\text{aq})}$ species, derived from the dissociation constants in Equation 2.19, Equation 2.21 and Equation 2.23, Equation 2.25 respectively that a higher pH favors oxidation, promoting higher fractions of reacting anions and moving precipitation reactions seen in Equation 2.18 and Equation 2.22 to the right.

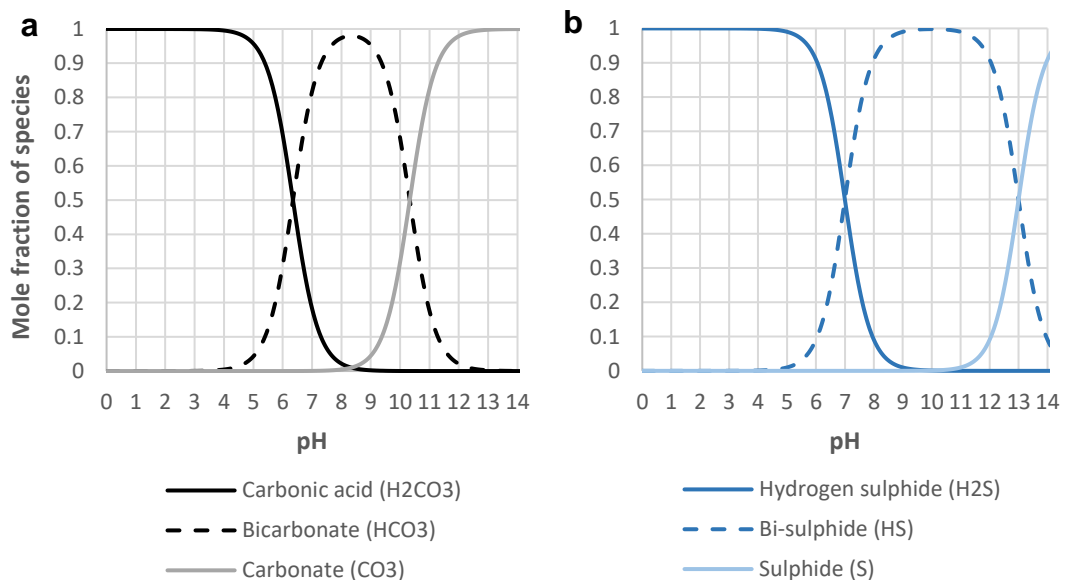


Figure 2.17 Bjerrum plots of pH vs mole fraction of a) H_2CO_3 ; and b) H_2S species concentration at 25°C

Saturation of CO_{2(g)} and/or H₂S_(g) in an aqueous system leads to lowering of a pH neutral solution or brine through formation of HCO₃⁻ and HS⁻ anions respectively through protonation. The pH of formation water in even the most acidic of sour producing wells rarely falls below pH 5, allowing for the limited presence of reacting HS⁻ anions.(49)

2.5.1 CO₂ dissociation

Upon dissolution of CO_{2(g)} into water, CO_{2(aq)} reacts with water to form carbonic acid.(93)



Carbonic acid is a weak acid that then dissociates as follows:



For which the dissociation constant (K₁) at 25°C and 1 bar is:

Equation 2.19
$$K_1 = \frac{a_{HCO_3^-} a_{H^+}}{a_{H_2CO_3^*}} = 10^{-6.35}$$

Bicarbonate then dissociates according to:



For which the dissociation constant (K₂) at 25°C and 1 bar is:

Equation 2.21
$$K_2 = \frac{a_{CO_3^{2-}} a_{H^+}}{a_{HCO_3^-}} = 10^{-10.33}$$

2.5.2 H₂S dissociation

Upon dissolution of H₂S_(g) into water, H₂S_(aq) dissociates as follows:(94, 95)



For which the dissociation constant (K₁) at 25°C and 1 bar is:

Equation 2.23
$$K_1 = \frac{a_{HS^-} a_{H^+}}{a_{H_2S}} = 10^{-7}$$

Bi-sulphide then dissociates according to:



For which the dissociation constant (K₂) at 25°C and 1 bar is:

Equation 2.25
$$K_2 = \frac{a_{CO_3^{2-}} a_{H^+}}{a_{HCO_3^-}} = 10^{-13}$$

Based on case studies of sour wells, pH values of produced water routinely lie between pH 5-7, meaning there is typically a mix of H₂CO₃/HCO₃⁻ and H₂S/HS⁻ present and available for reaction in oilfield systems.

2.5.3 pH vs. electron activity (Eh)

pH vs. Eh curves show the stability of a mineral species with respect to the activity of hydrogen ions (pH) and the activity of electrons (Eh). Environments such as those near the wellbore or in reservoirs are isolated from the atmosphere and hence largely free of oxygen, where operators aim to maintain levels of dissolved O₂ below 50 ppb.(42, 96) Under anoxic conditions 'redox potential' is approximately -100 mV, required for the proliferation of SRB's and bacterial reduction of sulphates present in seawater to HS⁻.(97)

From a pH vs. Eh curve for PbS in Figure 2.18, it is clear that under downhole conditions between pH 5 – 7 and anoxic conditions where Eh is approximately

-0.1 V, solid PbS is the product. At pH 5.2 under which experiments were conducted, it can be seen that increased electron activity to an Eh value of 0.2 V results in oxidation of the galena surface and the formation of anglesite (PbSO₄). (98)

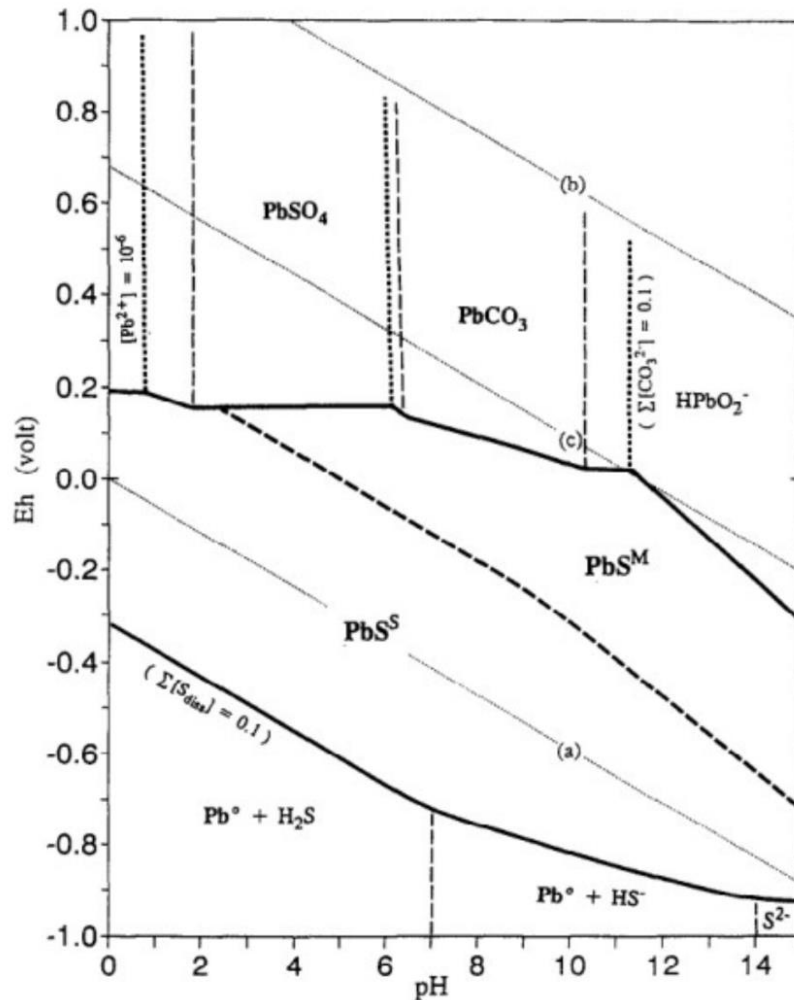


Figure 2.18 Persistency-field Eh-pH diagram for galena in the presence of sulphate and carbonate ion species at 0.1 activity (98)

2.5.4 IEP of galena and PbS charge

Given that PbS is formed at pH 5.2 under anoxic conditions, the particle charge can be calculated based on the pH of the solution from pH vs. zeta potential curves, shown in Figure 2.19.

Studies have reported the I.E.P. of naturally occurring galena to reside between a pH of 2.5 and 3 when unoxidized, with synthetic galena yielding a I.E.P value of approximately 2.1. (99, 100). This conforms with the expectation

that at pH values typically seen in oilfield systems of 5 - 7, precipitated PbS will carry a slight negative charge, determined from Figure 2.19 to be between -15 and -5 mV for ground unoxidised galena.(101)

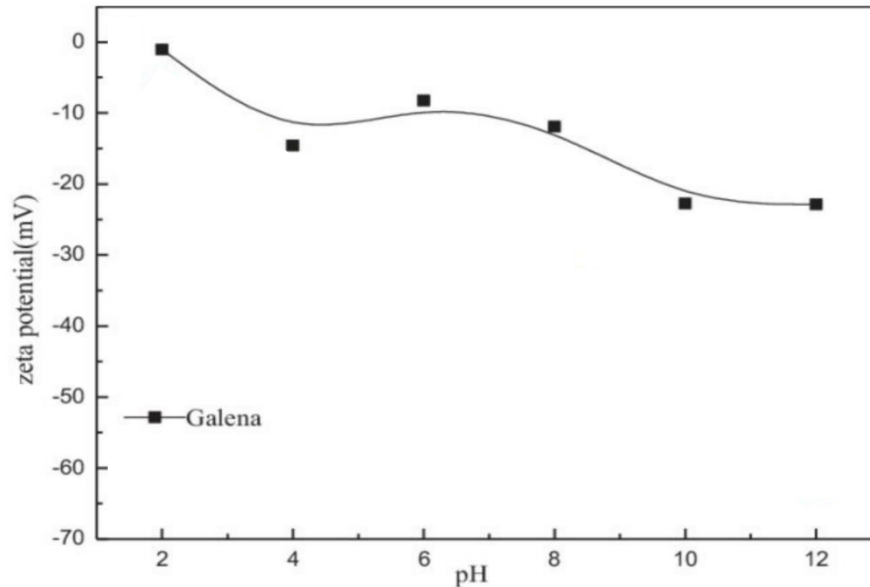


Figure 2.19 pH vs. zeta-potential for unoxidised galena (101)

Particles in aqueous solution tend to carry surface charges that are a consequence of surface group ionisation, ion adsorption or charge exchange mechanism.(102) Counter-ions from solution sustain an electrically neutral charge when balanced with co-ions at the particle surface and are firmly bound via a Coulomb force within the Stern layer. The electric potential decreases linearly with distance from the particle surface, with counter-ions moving freely within the diffuse layer, as seen in Figure 2.20.(103, 104)

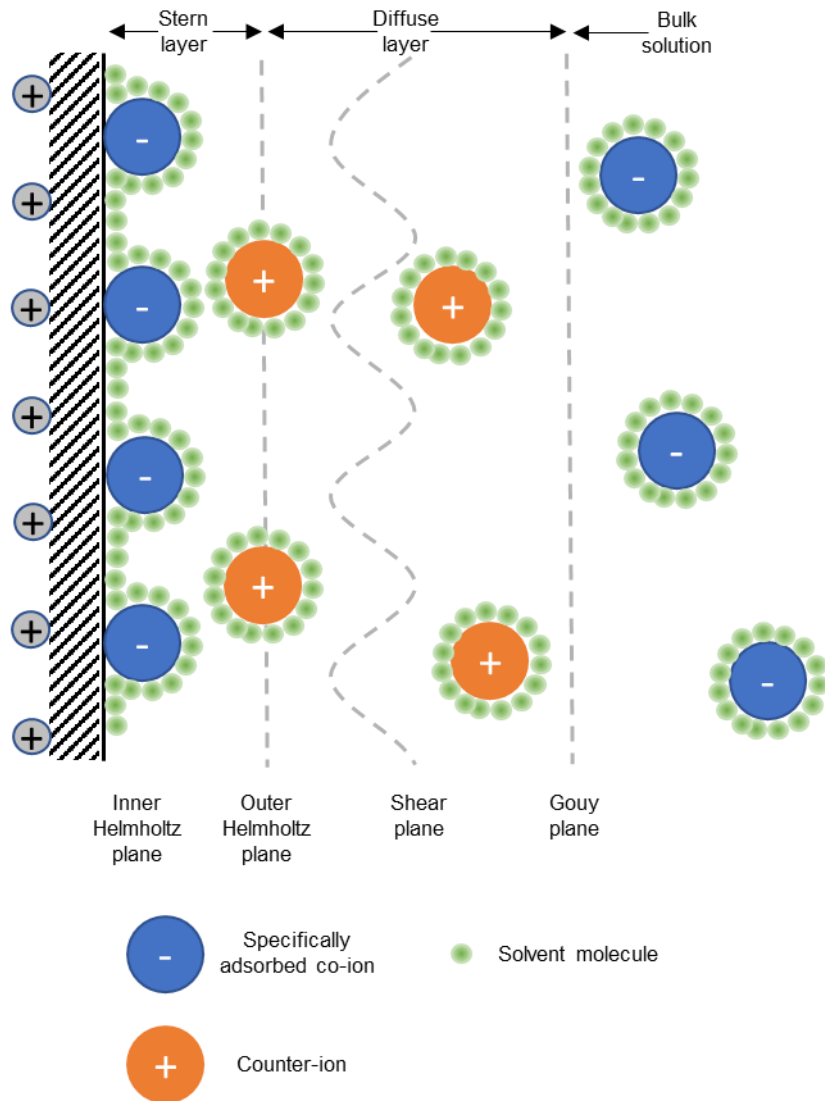


Figure 2.20 Schematic representation of the electric double layer (EDL)
(103)

The electrical double layer (EDL) of two interacting colloids overlaps upon approach, where osmotic pressure is generated due to variation of the ionic concentration within the gap and the bulk solution. Between two surfaces carrying a similar surface charge the EDL force is repulsive, increasing in magnitude with surface potential.(104)

Introduction of an electrolyte e.g. KCl to aqueous solution has been reported to lead to compression and increased capacitance of the Stern layer within the EDL as a result of the increasing of osmotic pressure on the outer-Helmholtz plane (OHP). This in turn leads to an increase surface charge density and consequent decrease in zeta-potential.(105)

2.5.5 Nanoparticle agglomeration

It is commonly understood that colloidal solutions with a zeta-potential between -20 and +20 mV, as is the case with galena and PbS nanoparticles at pH 5 - 7, display limited electrostatic repulsion. This consequently leads to dominance of the vdW attractive force between particles and colloids and the formation of large PbS agglomerates.(104)

2.6 Factors influencing scale precipitation

A multitude of physical factors can influence scaling tendency of specific minerals in oilfield systems, playing a role in the thermodynamics and kinetics of precipitation, and hence the location and severity of scaling.

2.6.1 CaCO₃ and BaSO₄

CaCO₃ precipitation is largely dependent on pressure, with calcite scaling increasing in severity as pressure reduces higher up the well, as can be seen in Figure 2.21.(12) The influence of temperature isn't quite as prominent as seen with other conventional scales e.g. BaSO₄, where an increase in temperature slightly increases scaling index of calcite, where solubility is reduced.

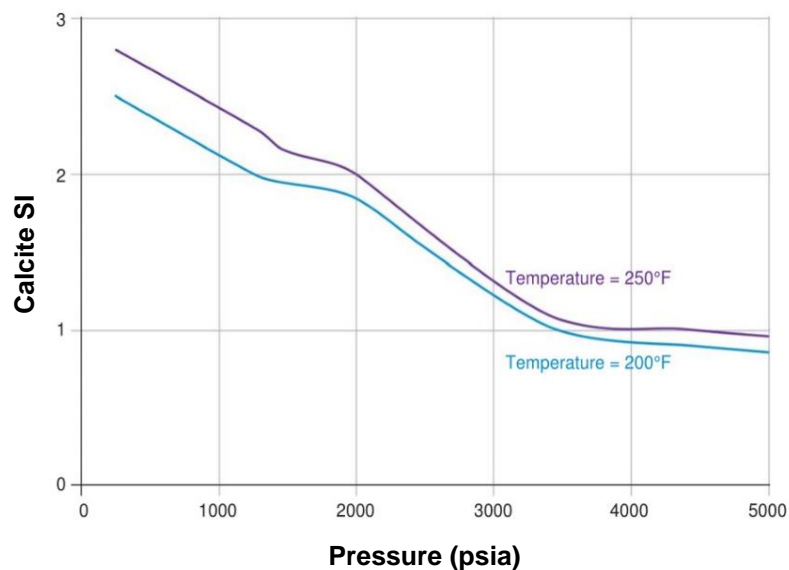


Figure 2.21 Pressure vs. calcite (SI) at 200 and 250°F (93 and 121°C)

Figure 2.22 shows the effect of absolute salinity on calcite supersaturation, where the presence of Na, Mg, Ca and K ions collectively increases supersaturation at temperatures of 25 and 40°C, highlighted in red and blue respectively.(106)

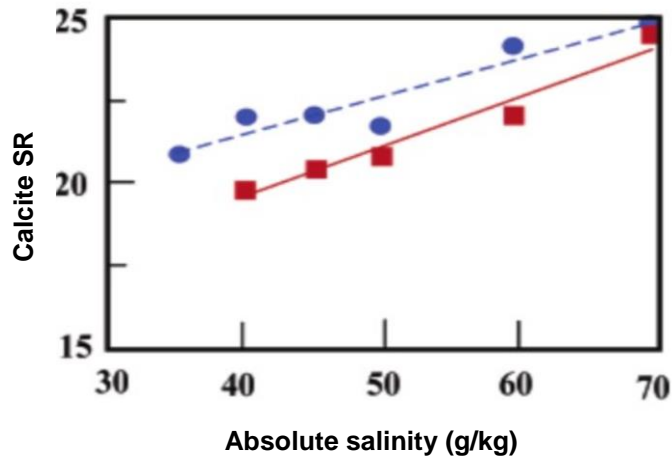


Figure 2.22 Absolute salinity vs. calcite SR where red line 25°C and blue 40°C (106)

Changes in pressure as produced water proceeds up the tubing induces the formation of CO₂ gas from the aqueous phase, where the reduction in HCO₃⁻ concentration results in a general pH increase. As pH increases the solubility of calcite is reduced, as seen in Figure 2.23.(107)

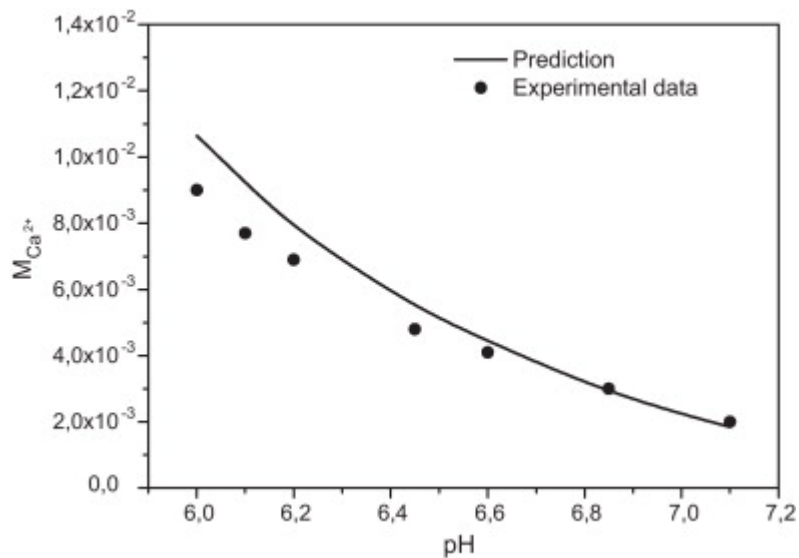


Figure 2.23 pH vs CaCO₃ solubility (107)

The solubility of BaSO₄ can be seen to significantly decrease as temperature is reduced, prompting precipitation as temperature is reduced from the wellbore to topside (Figure 2.24).(27)

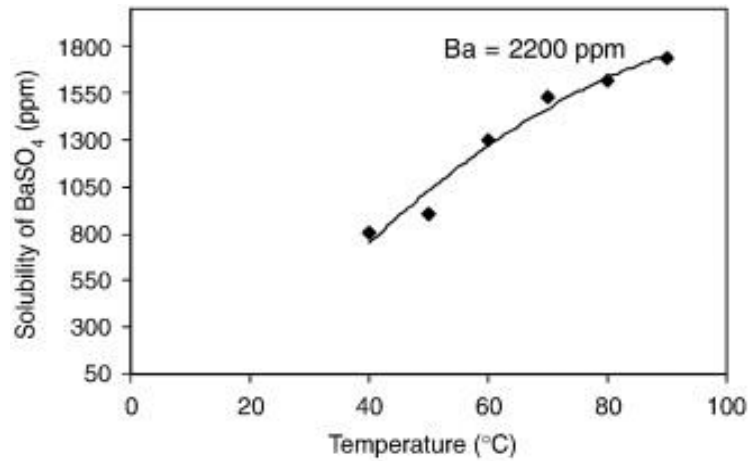


Figure 2.24 Temperature vs. BaSO₄ solubility (27)

Yuan and Templeton (108) show the effect of electrolyte concentration on BaSO₄ solubility at several different temperatures, where solubility increases as NaCl concentration in solution is increased (Figure 2.25).(108)

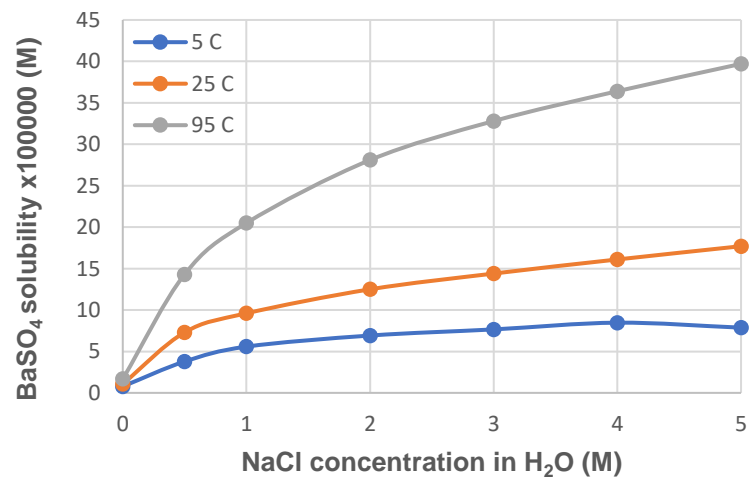


Figure 2.25 NaCl concentration vs. BaSO₄ solubility (108)

2.6.2 PbS

The typically low solubility of PbS is significantly increased by high free chloride (Cl^-) ion concentration, high temperature and low pH, that can result in precipitation high in the production tubing as opposed to the wellbore under more extreme conditions. (29, 38, 109) Figure 2.26 shows the influence of both temperature and NaCl concentration on PbS solubility, where solubility increases with temperature and electrolyte concentration. (29)

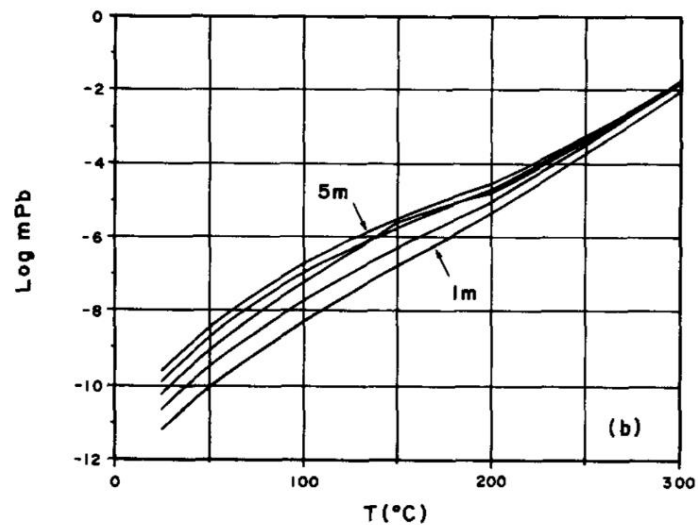


Figure 2.26 PbS solubilities at 25 to 300°C, 1- 5 m NaCl at pH 4 and $mS(r) = 0.001$ (29)

Figure 2.27 shows the influence of pH on a number of sulphide species commonly found in sour systems, where solubility decreases linearly with an increase in pH for PbS and ZnS. PbS is the most insoluble of the sulphide species, followed by ZnS, where FeS the most soluble when pH is constant. (110)

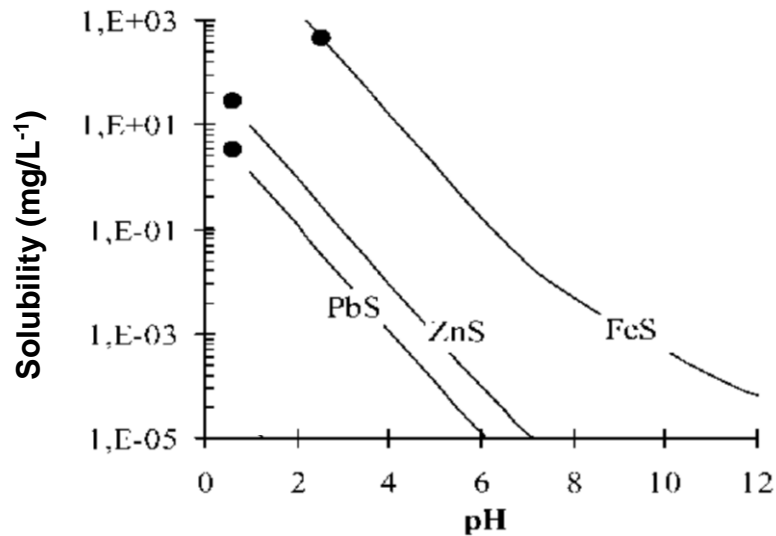


Figure 2.27 pH vs. solubility of metal sulphide species (110)

2.6.3 Crystal co-precipitation

Co-precipitation of crystal species can occur in a number of forms. Surface adsorption amounts to the adsorption of foreign ionic species that are otherwise soluble onto the face of a uniform crystal. Mixed crystal formation however involves the incorporation of a foreign ion into the crystal lattice, replacing that of the original crystal structure, often resulting in disruption and alteration of layer growth.(111, 112)

The formation of crystal complexes and films as a consequence of occlusion co-precipitation, otherwise known as mechanical entrapment, is well documented, occurring when an impurity is trapped inside a growing crystal. It typically occurs under high supersaturations where the crystal is growing rapidly.(113-115)

2.6.4 CaCO₃ and PbS co-precipitation likelihood in oilfield

Case studies have shown precipitation of PbS and CaCO₃ species can occur both near the wellbore and higher up the production tubing.(37, 38) PbS precipitation tendency is significantly influenced by temperature, salinity and pH, and as such is analysed on a well-by-well basis through both custom modelling techniques and fouling analysis after equipment recovery.(38, 116) The likelihood therefore of co-precipitation occurring is high, where the spontaneous precipitation of barely soluble PbS towards the wellhead occurs in tandem with CaCO₃ crystallisation.

2.6.5 Influence of ionic impurities on crystal precipitation and growth

Chen et al.(117) highlight the influence of commonly occurring formation water brine cation Mg^{2+} on the precipitation of $CaCO_3$ crystals, where the presence of Mg^{2+} inhibits scale formation, prolongs induction time and adsorbs onto the roughened surface of the more prevalent calcite polymorph.(117) It is theorised that Mg^{2+} either adsorbs at the lattice site, preventing the transfer of $CaCO_3$ units at the growing interface, or adsorbs more generally on the crystal surface.(118)

Additionally, de Leeuw shows that calcite growth can be severely impeded by the presence of other metal cations at step edges, where Fe^{2+} and Sr^{2+} cations, in addition to Mg^{2+} , with inhibition increasing with increasing cation concentration.(119)

Growth forms and surface morphology of KCl crystals have been shown to be variable based on the concentration of Pb^{2+} ions in solution. Adsorption of $PbCl_2$ crystallites along the steps of growth layers reduces the advancing velocity of the growing face in perpendicular directions, resulting in a morphology change from cubic to octahedral. Further growth results in the development of 'hoppered' or pyramidal structures upon the [111] face, with higher Pb^{2+} concentrations resulting in the emergence of 'hoppered' growth layers on the [100] face.(120)

2.6.6 Occlusion co-precipitation

Occlusion co-precipitation methods are implemented widely in industry, from remediation and entrapment of gold (Au) and silver (Ag) nanoparticle contaminants within water systems through co-precipitation with $CaCO_3$,(121) to PbS nanoparticles functioning as nucleation sites to promote the formation of perovskite lattice structures to improve performance in solar cells.(122)

Perhaps the best example of solid occlusion within calcite at an interface is the calcification of organic sites on a membrane as part of the process of avian eggshell mineralisation. These organic structures promote the nucleation and stabilisation of ACC that is then converted into more a stable calcite structure. As described by Reddy et al.(123), the principle of high local supersaturation prompting crystallisation at the solid-liquid interface can be applied, in this case where sulphate groups on the organic sites concentrate Ca^{2+} ions promoting the nucleation of calcium carbonate.(123, 124)

2.7 Factors affecting scale deposition

2.7.1 Flow pattern and turbulence

Highly turbulent flow rates have been shown to result in increased mass transport of scaling ions and solutes to substrates and pre-deposited crystals, that can increase crystal growth and exacerbate secondary nucleation.(125)

The relative particle-fluid velocity (U_R) can be used to show how turbulence can enhance diffusional growth rates (Equation 2.26).(126)

Equation 2.26
$$\bar{U}_R^2 = 2\left(1 - \left(\frac{m_F}{m_P}\right)\right)^2 \frac{\bar{U}_f^2}{\lambda^2 p^2}$$

Where m_F is the mass of the fluid (g), m_P is the mass of the particle (g), U_F is fluid velocity (cm/s), λ is microscale (s) and p is pressure (dynes/sq. cm).

2.7.2 Agglomerate/particle size

The size of depositing colloids and agglomerates in the turbulent flow can influence the likelihood of deposition or settling. For small colloidal particles that have precipitated homogeneously in the bulk phase, deposition is primarily due to Brownian diffusion whereas relatively large particles or agglomerates are deposited on the surface as a result of inertial effects.(127) Therefore, the effect of interfacial surface forces on the particle transport to the channel surface is stronger for smaller particles.(128)

2.7.3 Solution pH

pH can have a significant bearing on mineral solubility and hence supersaturation, that may determine the predominant pathway for nucleation in solution as well as surface growth rates etc. For PbS forming solutions at low pH values or small saturation ratios, fewer particles are grown but at a higher growth rate. In experimental run times of 24 hours at room temperature where PbS concentration was 3.5 mg/L at pH 1.45 results in the heterogeneous precipitation of cubic crystals of approximately 10 μm in diameter.(129)

Additionally, the charge of a particle or substrate is heavily related to pH, often influencing colloidal stability of a system and interfacial forces between two surfaces, as seen in Figure 2.19.

2.7.4 Substrate topography and roughness

Increased roughness results in an increase in the number of potential nucleation sites, where the energy required for heterogeneous nucleation is reduced in valleys or on peaks.(130) Cheong et al.(131) describe the heterogeneous nucleation of crystals from the tips of surface asperities, where adhesion is far more persistent than that of crystals that have migrated from the bulk solution to the substrate surface, as shown in Figure 2.28 where heterogeneous and homogeneous nucleation are compared as a function of surface structure.

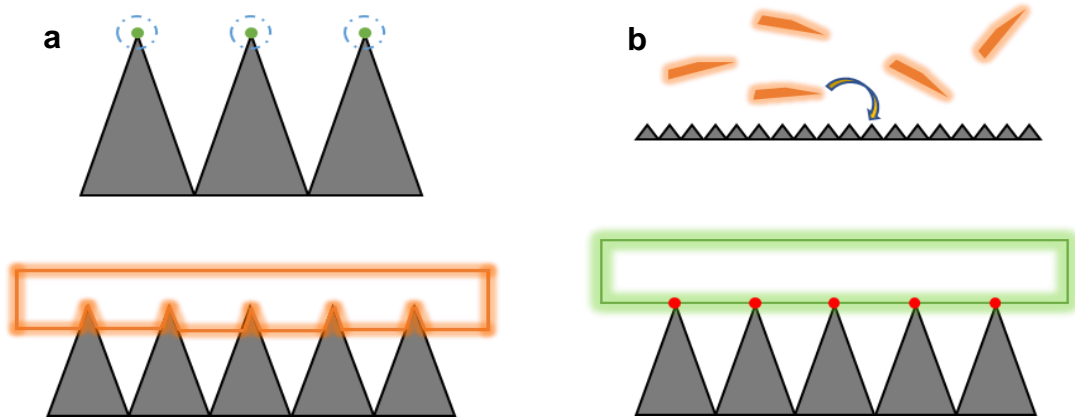


Figure 2.28 a) Heterogeneous nucleation and crystal arrangement on asperities; b) Migration of homogeneous particles from the bulk phase to the substrate and crystal arrangement on asperities (131)

Migration of particles from the bulk phase onto substrates results in a comparatively low adhesion strength when compared to crystals that have precipitated heterogeneously due to reduced contact area of the crystal to the substrate.

2.7.5 Substrate surface energy/wettability

Heterogeneous surface nucleation, from the point of view of the substrate is influenced by a number of variables including wettability, chemical composition and structure, rendering it difficult to quantify the precise effect of wettability on single phase scaling. The contact angle can be regarded as a measure of the affinity between a deposit and a substrate, whereby large contact angles of the crystal with the solid substrate are indicative of lower affinity and vice versa.(69)

Mass deposition rate (\dot{m}_d) during the induction period is shown by Equation 2.27:

$$\text{Equation 2.27} \quad \dot{m}_d = C_3 \exp \left[-\frac{16\pi}{3} \frac{\gamma_{cl}^3 v^2}{k_B^3 T^3 \ln^2(c/c_3)} \right]$$

Where v is molecular volume (cm^3/mol), k_B is the Boltzmann constant and C_3 is a proportionality constant, c is the concentration of the precipitating material at the bulk and at the surface and γ_{cl} the interfacial free energy (mJ/m^2) between the solid crystal and the liquid. The interfacial energies at the boundary of a three-phase contact point where a crystal is contacting a nucleus in solution have a massive bearing on the adhesive forces between the two surfaces, covered in Section 2.4.4.2.

Whilst surface nucleation is strongly influenced by the interfacial free energy between the substrate and liquid phase (γ_{sl}), surface structure and roughness can also affect scaling tendency.(69) Chevalier (132) shows that after increasing wettability through UV/O₃ treatment of polyethylene for a 10-minute period scaling density is drastically lowered, whereas similar UV/O₃ treatment of glass results in significant CaCO₃ scaling, where water contact angles were 20° and 0° respectively. Polyethylene did not promote a specific crystal orientation, whereby any CaCO₃ adsorbing to the surface had to compete with substrate-solution interactions e.g. EDL. On glass however, UV/O₃ treatment prompted changes in the surface structure that bought about specific crystal orientation resulting in high densities.(132)

Dependent on salinity, the supersaturation ratio of CaCO₃ at 40°C and pH 8 needs to be between 20 and 25 in order for homogeneous nucleation to start to occur, according to studies carried out by Marion et al.(133) In most producing wells, this value is only likely to be reached gradually, if at all, when undergoing pressure and pH changes that coincide with production of produced water from the wellbore to the topside. As such, heterogeneous nucleation is the more thermodynamically feasible scaling pathway for CaCO₃ crystallisation as supersaturation is reached. This is the case for other scales such as BaSO₄, where a reduction in temperature towards the topside is often the catalyst for reduced solubility and consequent precipitation.(27)

Ions are often reported to condense as ACC and later transform into crystalline CaCO₃. In single phase systems the hydrophobic surface may also encourage the formation of CaCO₃ - substrate bonds over that of solution -

substrate bonds due to a reduction in wettability, and hence decreased net surface free energy of the CaCO₃ solution - substrate system. The relationship between substrate - solution (sub/sol), CaCO₃ - solution interface (CaCO₃/sol) and CaCO₃ - substrate interface (CaCO₃/sub) is given in Equation 2.28.(132)

Equation 2.28
$$\gamma_{net} = \gamma_{CaCO_3/sol} + h(\gamma_{CaCO_3/sub} - \gamma_{sub/sol})$$

Where h is a shape factor and γ is the interfacial free energy (mJ/m²).

2.8 Factors affecting scale adhesion

Adhesion is defined by Wu (134) as the state in which two dissimilar bodies are held together by interfacial contact where mechanical work is transferred across the interface, or in other words, ‘the mechanical forces necessary to separate two materials.(134, 135)

At the nanoscale, surface forces play a significant role in adhesion. The Derajun, Landau, Verwey, Overbeek (DLVO) theory can be used to describe the adhesion force between colloids and surfaces in solution in terms of attractive van der Waals forces and repulsive forces that result from EDL interactions. Other interfacial forces that constitute the extended DLVO model are hydrogen bonding, the steric interaction, structural forces, hydrophobic interactions and hydration pressure for example.(136, 137)

Adhesion of two surfaces within an aqueous medium can be summarised as the combination of a number of forces, as described by Equation 2.29.(102)

Equation 2.29
$$F_{ad} = F_{el} + F_{vdW} + F_{cap} + F_{chem}$$

Where F_{el} is the electrostatic force, F_{vdW} is the van der Waals force, F_{cap} the capillary force and F_{chem} forces due to chemical bonds. High concentrations of divalent ions in high TDS solutions e.g. produced water adsorb to surfaces consequently diminishing the influence of repulsive electrostatic force and surface charges.(138)

2.8.1 Substrate surface energy/wettability

The work of adhesion/free energy of adhesion (W_A) in a liquid between two solid surfaces is related to the surface free energies of a system and is given by Equation 2.30, derived from the Young-Dupre equation.(69)

Equation 2.30
$$W_A = \gamma_{sl} + \gamma_{cl} - \gamma_{sc} = \gamma_{cl}(1 + \cos\theta)$$

Where γ_{sl} is the solid-liquid interfacial energy, γ_{cl} the crystal-liquid interfacial energy and γ_{sc} the solid-crystal interfacial energy.

The surface energy is typically expressed as the sum of the components, where dispersive (γ^{LW}) and Lewis acid-base (γ^{AB}) forces are combined to describe total surface energy in Equation 2.31.(69)

Equation 2.31
$$\gamma_{sl} = \gamma_{sl}^{LW} + \gamma_{sl}^{AB}$$

The contact angle of a drop on a liquid surface gives an indication of the adhesion due to the relationship between contact angle and bonding strength between a liquid and a surface.(139) Typically, a lower contact angle results in a stronger bond to the substrate surface.

2.8.2 Agglomerate/particle size

Though adhesive forces between particles and substrates generally increase with particle size the influence of turbulent flow results in a higher rate of removal of large objects.(140) Simply, larger particles or agglomerates are more likely to have stronger adhesion to a substrate but are less likely to remain adhered due to the physical effects of turbulence. The influence of interfacial forces on the adhesion of two surfaces e.g. a mineral scale colloid and a substrate, is described in greater detail in Section 2.9.

2.8.3 Surface charges between bodies

Based on the net charge of particles and substrates, electrostatic attraction of two oppositely charged surfaces can enhance the deposition and adhesion of particles from the bulk phase to a substrate. Coulombic attraction (F_I) between particles in contact with a grounded metal plate can be given by Equation 2.32:

Equation 2.32

$$F_I = \alpha \frac{q^2}{16\pi\epsilon_0 R^2}$$

where α is a factor to correct for the polarization of the particle, q and R are the charge (C) and radius (m) of the particle respectively, and ϵ_0 is the permittivity of free space.(104)

Fluoropolymer coatings such as Teflon™ acquire charge as a result of the accumulation of OH⁻ and H₃O⁺ ions at the substrate surface. The higher affinity of OH⁻ at the surface compared to H₃O⁺ results in an iso-electric point of approximately pH_{iep} 3.7 in KCl solution, where the surface carries a net negative charge above this point.(141) Given that a particle carrying a net positive charge e.g. silica, comes into contact with a Teflon™ substrate at a neutral pH, the electrostatic force will contribute to the attraction between the two surfaces and ultimately enhance the adhesive force. Conversely, the interaction of two similarly charged surfaces will result in an electrostatic repulsion force, limiting the likelihood of deposition and consequent adhesion.

2.8.4 Substrate topography and roughness

Increased roughness of a substrate often increases the density of hooking sites promoting an interlocking. Keysar et al.(142) demonstrate the enhanced nucleation of calcite on a rough surface leads to a stronger bond as more crystallites are created linking the substrate to the crystalline deposit. This leads to a more compact and dense structure that has a higher tensile adhesion strength that increases linearly with increasing roughness.(142) Conversely, the adhesion of individual particles often diminishes with increased substrate roughness, though the *rms* value is not a good predictor of adhesive behaviour due to the complex nature and multitude of roughness parameters, e.g. kurtosis, asperity spacing, peak/trough height etc.(143)

The influence of surface roughness on adhesion force (F_{ad}) can be described mathematically by the modified Rumpf model suggested by Rabinovich et al. (144) based on hemispherical asperities in Equation 2.33.

Equation 2.33

$$F_{ad} = \frac{A_H R}{6D_0} \left[\frac{1}{1+(R/1.48 \text{ rms})} + \frac{1}{(1+1.48 \text{ rms}/D_0)^2} \right]$$

Where rms is root mean squared roughness, A_H is the Hamaker constant, D_0 is the minimum distance between sphere and asperity (interatomic spacing) and R is the particle radius.

2.8.5 Substrate pre-scaling

Pre-scaling of a surface compromises the anti-fouling characteristics of the substrate and provides scope for additional growth in supersaturated solutions, nucleation points from which secondary nucleation can occur and hooking points that promote homogeneous adhesion of scales and other impurities from the bulk.(145)

2.9 Forces governing attraction and adhesion between surfaces

2.9.1 DLVO forces

The (Derjaguin, Landau, Verwey, and Overbeek (DLVO) theory considers both the effects of vdW attraction and EDL repulsion and is used to explain the interaction of colloids. Figure 2.29 displays the high and low interaction potentials that occur between two similarly charged particles in a 1:1 electrolyte solution under the influence of both vdW and EDL force. At small enough distances, the vdW attraction will always exceed the EDL repulsion as it is a power-law interaction, whereas EDL interaction energy remains finite as D approaches 0.(146) Ionic concentration can be increased in order to reduce the EDL repulsion and reduce the energy barrier resulting in loss of stability and aggregation in colloidal systems.(103)

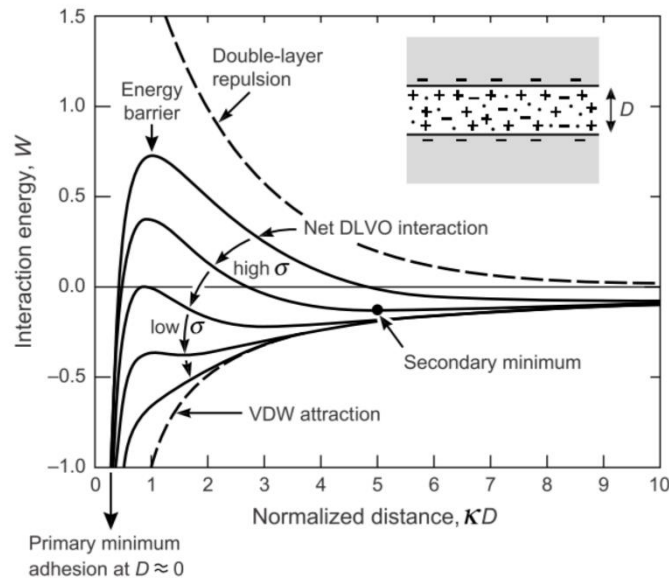


Figure 2.29 Schematic energy versus distance profiles of the DLVO interaction. The actual magnitude of the energy W is proportional to the particle size (radius) or interaction area (between two planar surfaces) (103)

2.9.1.1 van der Waals (vdW)

vdW forces are the sum of attractive or repulsive forces between atoms that arise from intermolecular interactions within any medium, dependent on both the geometry and physical and chemical properties of two bodies. (103, 136) Van der Waals forces include three different types of atomic interactions, where the Debye and Keesom interactions are based on electrostatic mechanisms, and London dispersion forces that are created by induced dipoles arising from electronic polarisation of interacting atoms. vdW forces act over relatively short distances between atoms and are proportional to the inverse of the 6th power of the intermolecular distances. (103, 147)

In calculating the Hamaker constant, the Lifshitz theory gives the vdW interaction energy as a function of macroscopic electrodynamic properties, such as refractive indices and dielectric permittivity of the interacting media. Given that these properties are higher in the medium than that of the two objects (e.g. scale crystal and substrate), the vdW value will be attractive and the Hamaker constant positive. (103, 104)

Hamaker constants provide scales for the vdW forces of between various particles within media and is given by:

Equation 2.34

$$A = \pi^2 C_L \rho_1 \rho_2$$

Where C_L is a microscopic property of two interacting atoms depending on the strength of interaction between the two bodies, and ρ the atoms per millimetre of the particle.(104)

2.9.2 Non-DLVO forces**2.9.2.1 Hydrophobic interaction**

Rabinovich and Derajun (104) showed that the range of attractive force could be significantly increased through hydrophobisation of a surface. A number of possible theories have been put forward as the sole cause or effects that contribute to the phenomena of the hydrophobic interaction:

- 1) Changes in the structure of the water in the thin layer between hydrophobic surfaces compared to the structure of bulk water;
- 2) Capillary force due to cavitation near hydrophobic surfaces
- 3) Hydrodynamic fluctuations at a hydrophobic surface/water interface;
- 4) Dipole-dipole or dipole-charge interactions (electrostatic phenomena)
- 5) Dipole interactions associated with the large domains of ordered hydrocarbon chains
- 6) Capillary bridging of nanobubbles attached on hydrophobic surfaces

It is likely that while all may in small part contribute to the attractive effect, is the primary factor contributing to the long-range interaction.(6)

2.9.2.2 Hydration forces

The hydration or 'structural' force is exponentially repulsive force and can be attributed to the energy required to remove water of hydration from the surface due to strong charge-dipole, dipole-dipole or H-bonding interactions.(148, 149) Hydration forces arise when strong binding of water molecules to surfaces containing hydrophilic groups produces repulsion or are prevented from desorbing as two interacting surfaces approach each other. Adsorbed

cations retain some of their water of hydration upon binding with the surface, with dehydration leading to a repulsive hydration force.(104) Hydration force strength can be ordered as follows: $Mg^{+2} > Ca^{+2} > Li^{+} > Na^{+} > K^{+} > Cs^{+}$.(146, 150)

2.9.3 Oxidation of galena

Oxidation of the PbS or galena surface and the subsequent formation of a uniform layer of Pb-deficient PbS, would have resulted in increased hydrophobicity. Experiments by Lei (151) showing the electrochemical treatment of cleaved galena indicate that oxidation of the surface through increasing of the surface potential to 0 V caused a sharp rise in contact angle to 79°, forming a hydrophobic, sulphur-rich layer, the formation of which can be seen in Equation 2.35.(103)



Lead oxide compounds such as PbO and Pb₃O₄ were predicted to only be stable within basic solution and do not form in solutions where pH < 8.9.(152)

From Figure 2.30, oxidative dissolution of a galena surface can be seen at pH 5.8, where oxygen incorporates into the PbS lattice alongside sulphate species such as thio-sulphate, sulphites and anglesite (PbSO₄). (152)

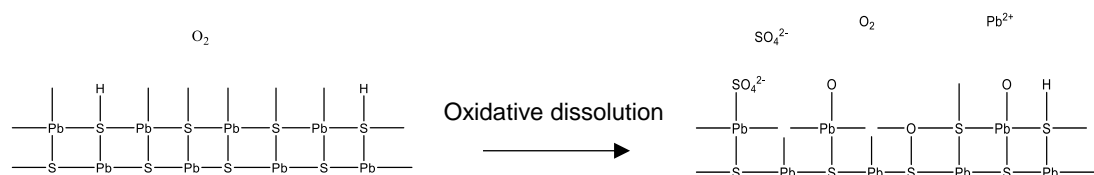


Figure 2.30 Evolution of a cleaved galena surface with time in an oxidised aqueous environment (152)

The [001] galena surface reacts in oxygen-saturated solutions to form phases that cover the surface, where partial oxidation occurs at the interface resulting in accumulation and re-dissolving at a slower rate than galena.(152, 153)

2.10 Scaling in multiphase flow

2.10.1 Flow dynamics and emulsion types

Flores et al.(154) identified six flow patterns in vertical tubing in which oil and water flowed upwards, three where oil was the continuous phase and three where oil was the dispersed phase, as seen in Table 2.3.

Table 2.3 Types of multiphase pipe flow (154)

From Figure 2.31	o/w based	w/o based
a	Very fine dispersion of oil in water <i>(vfd o/w)</i>	Very fine dispersion of water in oil <i>(vfd w/o)</i>
b	Dispersion of oil in water (<i>d o/w</i>)	Dispersion of water in oil (<i>d w/o</i>)
c	Oil in water churn flow (<i>o/w cf</i>)	Water in oil churn flow (<i>w/o cf</i>)

Churn flow often occurs at low to moderate velocities and is characterised by irregularly shaped droplets. Increasing the flow velocity will result in a dispersion of droplets and globules, with the sphericity and mono-dispersity of the dispersed phase increasing at higher velocities as droplet size decreases. As the flow rate of the continuous phase increases so too do turbulent forces, causing breakage forces to dominate which results in a non-slip state and a very fine dispersion, where very small droplets are dispersed across the entire pipe section.(154) It is worth noting that in terms of basic multiphase flow, behaviour between oil or water dominated flow patterns is largely similar, with the phase ratio dominating the role of the dispersed phase. Very fine dispersion, dispersion and churn flow for an o/w system can be seen in Figure 2.31 respectively.(154, 155)

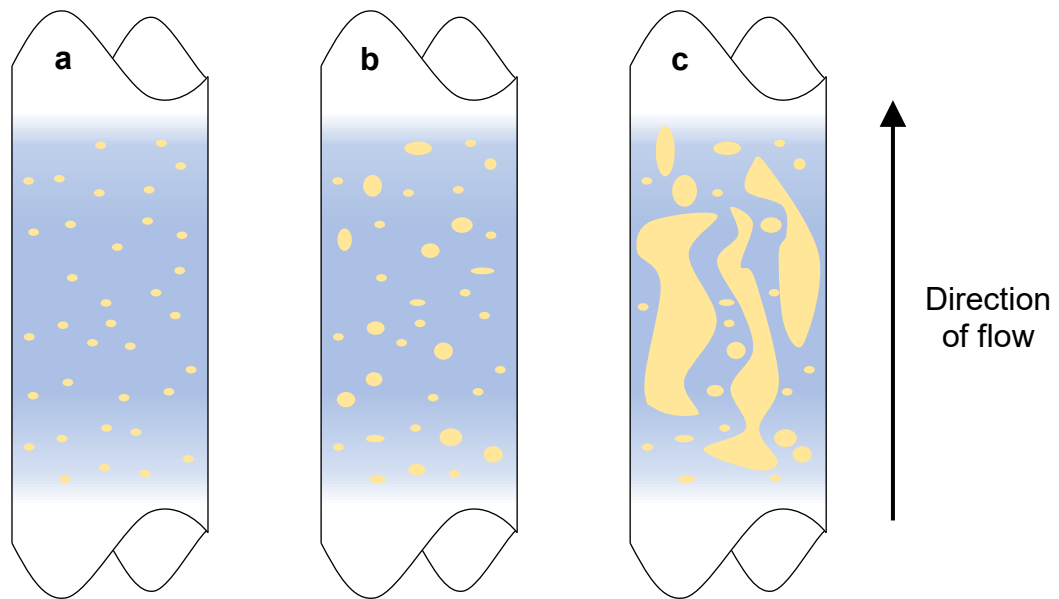


Figure 2.31 Illustrations of types of multiphase pipe flow; a) very fine dispersion of oil in water; b) dispersion of oil in water; c) oil in water churn flow (154)

Experiments carried out in this study worked under the assumption that due to the low viscosity of the oil from light oil or gas condensate wells upon which the sulphide tests were based, and the high pressure nature of the reservoirs from which petroleum was being produced resulting in high flow velocities, very fine dispersions of either w/o or o/w were produced (dependent on water-cut). It is feasible that later in the life of the producing reservoir, reduction in pressure will lead to the formation of either dispersed flow or churn flow regimes.(154, 155)

2.10.2 Adsorption of particles at a liquid-liquid interface

Particles will bind to a liquid-liquid interface under equilibrium conditions in order to minimise system energy, their position determined by the contact angle that is described by Young's law (Equation 2.15).(156) Arrangement, position and adsorption strength of solid particles at an o-w interface is reliant on a myriad of factors including particle charge and wettability; particle size and shape, the dielectric discontinuity between water and oil as a result of ionic strength, and particle roughness.(157)·(158-160) Positions at the o-w interface based on partially hydrophilic and partially hydrophobic particles can be seen in Figure 2.32.

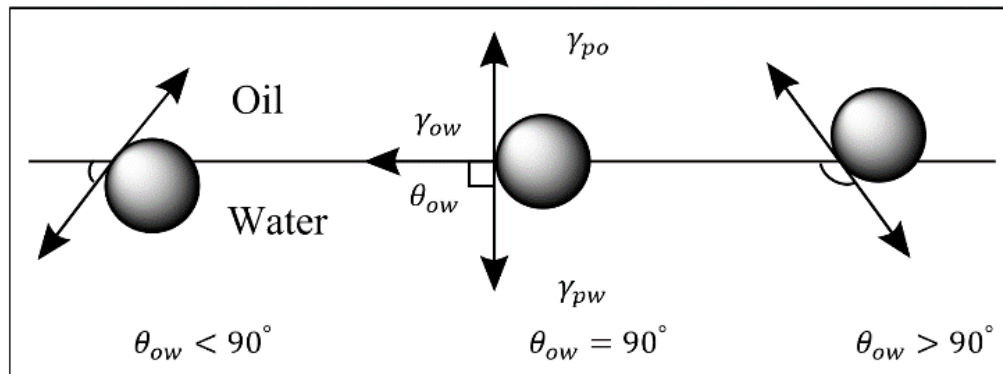


Figure 2.32 Particle position at an o-w interface based on wettability

Large particles have higher contact area with the oil and water phases either side of the interface, and as such possess a higher desorption energy, where energy required for removal for stabilised particles of 1-10 μm is approximately 10^8 - 10^9 $k_B T$. Figure 2.33 shows the relationship between particle size and contact angle at the o-w interface and the energy required to desorb that particle into its respective phase.(161)

Partially-wetted solid particles are held together in a layer at the o-w interface by attractive interactions such as capillary forces, with both intermolecular dispersion and electrostatic repulsion further influencing wetting and stability.(157)

2.10.3 Desorption of particles from a liquid-liquid interface

The energy required for desorption of a particle from an interface is displayed in Figure 2.33, where the water contact angle and size of the particle are key parameters.(162)

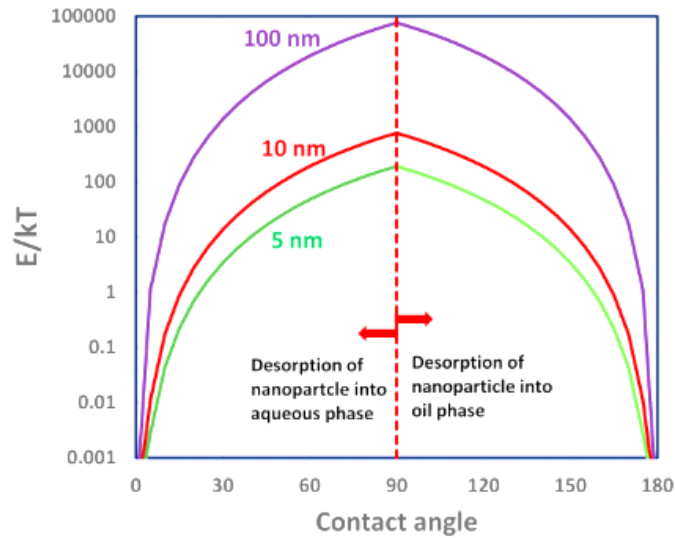


Figure 2.33 Influence of contact angle and particle size on the energy required for desorption from the o-w interface (162)

The free energy of desorption (ΔG_w) is given in Equation 2.36 and contact angle (θ) of a spherical particle at a fluid-fluid interface is given by Equation 2.37.(163)

Equation 2.36
$$\Delta G_w = \pi R^2 \gamma_{o-w} (1 - \cos(\theta))^2$$

Equation 2.37
$$\theta = \cos^{-1} \left(\frac{h}{R} \right)$$

Where γ_{o-w} is the interfacial tension (mN/m) at the o-w interface, h is the height of the particle centre of mass above the interface (m), and R the particle radius (m).(164) When θ is equal to 90° , the proportion of the particle volume wetted within each phase across the interface is identical.(164) The partially hydrophobic nature of PbS where water contact angle is equal to $48 - 52^\circ$ results in the adsorption of particles at the o-w interface, though predominantly within the aqueous phase, favouring formation of an o/w emulsion given identical phase volume fractions.(33, 165)

2.10.4 Crystal growth at liquid-liquid interfaces

Reddy et al.(123) showed that strontium carbonate (SrCO_3) can be grown at the interface of two immiscible liquid solutions, where stearic acid molecules would adsorb at the o-w interface, enabling in an enhancement of the metal cation concentration at the interface and a subsequent rise in local supersaturation. CO_3^{2-} anions free in solution then readily react with Sr^{2+} ions at the interface leading to the formation of SrCO_3 .(123)

2.11 Multiphase emulsions

Emulsions are defined as a mixture of two or more immiscible liquids, with crude oil and water a pertinent example that is able to form both an oil-in-water (o/w) or water-in-oil (w/o) emulsion, where oil and water form droplets as the dispersed phase respectively. The type of emulsion formed is dependent on the volume fraction of the oil and water and the nature of the emulsifier.(166)

2.11.1 Emulsion stability

Emulsion stability is regarded as the capacity of the emulsion to maintain its properties over time. Instability can occur through flocculation, creaming and coalescence, where droplets attract to form flocs, rise to the top of the emulsion and combine to form larger droplets respectively. Surfactants are commonly used to stabilise emulsions resulting in droplets that do not change significantly in size with time that usually have a mean diameter of approximately 1 μm . However, solid particles or agglomerates are also a viable means of emulsification and have an ability to stabilise droplets within an emulsion without the formation of a monolayer, whereby much larger droplet diameters are possible.(157, 166)

Emulsions stabilised by solid particles as opposed to surfactants are referred to as Pickering emulsions, with current applications including drug delivery, food production and mesoporous materials.(157) Their novelty stems from the irreversible attachment of particles at the o-w interface, as seen in Figure 2.34.(157)

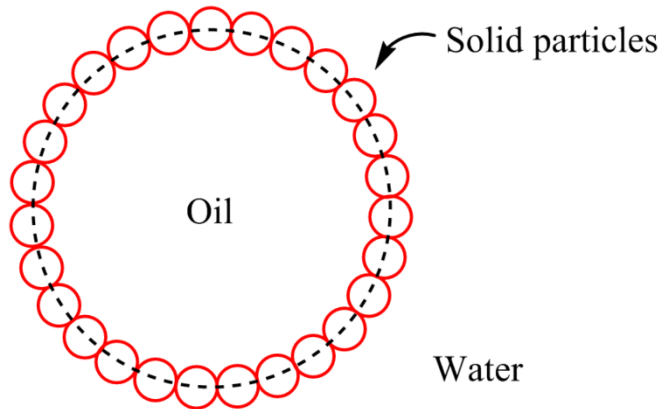


Figure 2.34 Solid particles stabilized at the interface in an o/w Pickering emulsion

Where surfactants generally cover emulsified droplets uniformly, particles and agglomerates at the interface of Pickering emulsion droplets have been reported to show incomplete coverage. In an o/w emulsion with a dense monolayer, the relationship between droplet diameter and the mass ratio of the dispersed phase to solid particles can be given by Equation 2.38.(157)

Equation 2.38
$$\text{Droplet diameter} = \frac{6}{\rho_{oil}\alpha_{solid}} \frac{M(oil)}{M(solid)}$$

Where ρ_{oil} and α_{solid} represents the interfacial area covered per mass of solid particles. This linear relationship however is not maintained with the introduction of a higher oil fraction whilst particle mass is kept constant.(157, 167)

As the ratio of solid particles decreases, a smaller interfacial area of the droplet can be stabilised, resulting in larger droplet sizes and higher emulsion polydispersity. Agitation of the emulsion results in the formation of small droplets that coalesce when left to settle, with ripening halted by the interfacial area reaching the area at which coverage is deemed to be full by solid particles. As such, a stable coarse emulsion is formed after 'limited coalescence', where free oil is released. This results in the formation of a 'Winsor type III' emulsion where the particle stabilised component is sandwiched between excess oil and water layers.(157, 168, 169)

2.11.2 Emulsion inversion

Particle wettability plays a significant role in determining the dispersed and continuous phases in Pickering emulsions. Particles with an $\theta_w > 90^\circ$ will favour the formation of an o/w Pickering emulsion and stabilising particles with an $\theta_w < 90^\circ$ favour w/o emulsion arrangement. Pickering emulsion stability is at its highest however when contact angle is 90° , demonstrated in Figure 2.33. As such, phase inversions can be triggered by both particle properties and water and oil phase ratios.(157)

Destabilisation and inversion of emulsions typically occurs through coagulation followed by coalescence of droplets. However, in Pickering emulsions the rigid coating formed by partially-wet solid particles acts against this coalescence, with a persistent emulsion forming between excess oil and water phases, termed a 'Winsor – type III' emulsion.(170) Reorganisation of surface materials required for liquid droplets to coalesce is prevented by a physical barrier; the mechanical strength of the droplet deriving from aggregation of solid particles at the surface.(157) When the dispersed phase of an emulsion is increased, or solid particle mass per system droplet volume is decreased, mass transfer of oil occurs between the dispersed oil phase in o/w emulsions. Mass transfer of oil between stabilised droplets of different sizes is referred to as Ostwald ripening where the external phase acts as the transfer medium. Additionally, coalescence refers to merging of similarly sized droplets but is based on the direct contact. Figure 2.35 shows Ostwald ripening and coalescence in images a and b respectively.(167)

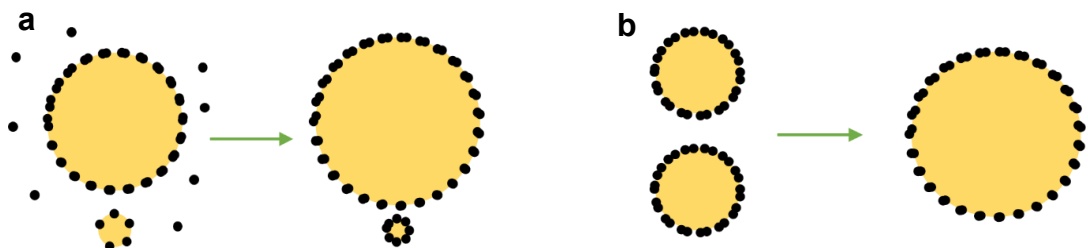


Figure 2.35 a) Ostwald ripening where small drops shrinking and larger drops swelling as molecules transfer from the small to larger drops; b) if there are not sufficient particles present formed drop surfaces limited coalescence occurs (167)

Increasing of the oil fraction to particle mass ratio reduces the influence of the mechanical barrier preventing coalescence, where droplets not only become

enlarged but are deformed as they are forced into closer proximity, decreasing in stability prior to coalescence and Ostwald ripening.(165) Catastrophic phase inversion then occurs after sufficient shifting of the system to its lowest energy state.(167)

While conversely in oilfield systems it is likely that oil fraction is likely to decrease over the production life of the reservoir, the principle should hold true for w/o emulsions. Water-cut is initially low and a steady increase in produced water results in larger solid stabilised droplets as water-cut increases before inversion to an o/w emulsion occurs.

2.11.3 Role of the multiphase in functionalisation and co-precipitation

Janus particles are colloids that are customised specifically to have two or more distinct physical properties, allowing themselves to arrange at interfaces where one hemisphere is hydrophilic and the other hydrophobic in character.(171) Modification of particle surfaces can be achieved through partial contact with reactive media, whereby reacting molecules or particles are dissolved in the first medium (the second being inert) before attaching to pre-cursor Janus particles stabilised at the liquid-liquid interface as illustrated in Figure 2.36.(172)

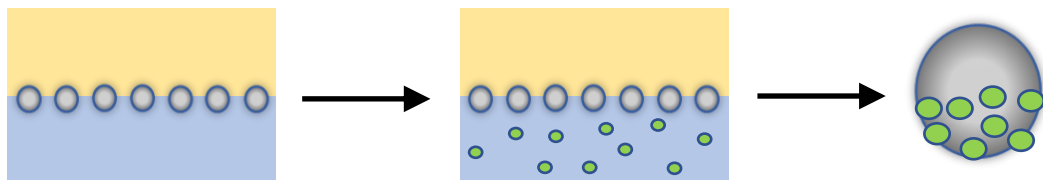


Figure 2.36 Particles arranged at an o-w interface where half of the colloid is functionalised from particles within the aqueous phase (172)

This process demonstrates how interfacially stabilised colloids can act as nucleation or attachment points for attachment of reacting molecules, secondary nucleation or occlusion growth.

2.12 Mineral scale mitigation

2.12.1 Chemical – Scale Inhibitors and Dispersants

The primary function of an oilfield scale inhibitor is to prevent/inhibit crystal growth at threshold concentrations. Inhibitor molecules adsorb at active growth sites, resulting in a reduction in the driving force towards crystallisation and subsequent growth. Morphology, tendency to agglomerate and the potential of the electrical double layer of the growing nucleons are also altered.(173)

Nucleation inhibition involves disruption of the thermodynamic stability of growing nucleons during homogeneous nucleation, with endothermic adsorption of inhibitors at crystal embryos causing an increase in critical radius for crystallisation.(173)

Crystal growth retardation occurs through blocking the growth processes of crystals for homogeneous crystal growth. Inhibitors are irreversibly adsorbed at active growth sites, blocking growth at these points.(173)

Polymeric inhibitors, utilised in the removal of heavy metal cations from aqueous solutions, are commonly implemented in industrial applications such as wastewater treatment, as well as chemical inhibition of inorganic scale growth in oilfield systems.(19, 174) The amphiphilic nature of the polymeric sulphide inhibitor allows both inhibition of crystal nucleation through cation complexation, and growth retardation after adsorption upon crystalline surfaces.(175) Water-soluble polymers also behave as surfactants and are used in a multitude of applications related to emulsion stabilization; such as gene and drug delivery, detergents, ceramics etc. In oil and gas production, chemically enhanced oil recovery (CEOR) is driven by adsorption of viscosity enhancing polymers at the o/w interface, with performance influenced by aqueous pH, block structure and length, and concentration.(176)

Figure 2.37 displays poly(2-acrylamido-2-methyl-1-propanesulfonic acid) or PAMPS, a high MW sulphonated polymer that is commonly used as a thickener for cleaning agents, a friction reducing agent, a lubricant as well as a mineral scale remover.(177-179)

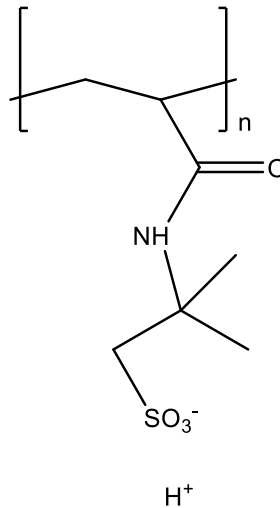


Figure 2.37 Chemical structure of PAMPS (177)

2.12.1.1 PAMPS inhibition mechanism

Dietschz et al. (178) conclude that not only does the sulphonated PAMPS molecule inhibit nucleation through cation complexation but interacts with crystallites already present in solution through adsorption onto the surface. The high supersaturation of barely soluble salts e.g. PbS, at concentrations found in produced waters, is likely to result in the precipitation of solids from solution and hence both PAMPS complexation and adsorption mechanisms are likely to occur.

2.12.1.2 Squeeze treatments

Industrial scale inhibitor squeeze treatments are carried out to deliver inhibitor into the reservoir, maintaining downhole inhibitor concentration above a pre-set threshold and dependent on the field can be required every few days up to over a year. Directly after treatment in producing wells, the localised inhibitor concentration around the point of injection can reach extremely high levels, before displacement further into the reservoir.(12)

Continuous downhole chemical injection coupled with squeeze treatments is routine in a number of wells, in particular those with CaCO₃ scales that build-up in the production tubing as opposed to the reservoir. Constant inhibitor delivery is able to prolong squeeze lifetimes.(12)

2.12.1.3 Biocidal treatment of SRB

SRB, responsible for numerous problems in oil and gas production due to the production of corrosive/reactive H₂S, are treated through regular application of biocides.(180-182) A complication surrounding the treatment of such bacteria is that protective biofilms are able to grow on the surfaces of tubing or in the reservoir formation.(183)

2.12.1.4 Nitrate reducing bacteria (NRB)

The introduction of nitrates into the reservoir within injected water as part of secondary recovery is another viable means of reducing souring. Nitrate reducing bacteria (NRB) are able to out-compete SRB, with nitrate able to provide more energy than sulphate when used as a bacterial electron acceptor. The treatment of sour reservoirs through continuous injection of nitrate salt has been shown to lead to suppression of SRB and hence results in the gradual sweetening of the reservoir.(184)

2.12.2 Mechanical – Anti-fouling surfaces

Previous research in the area of mineral scale prevention has predominantly focused on chemical inhibition, or physical removal through acid chemical treatment combined with mechanical methods.(12) (22, 185, 186) As an alternative to batch injection or reactionary mechanical techniques, the use of anti-fouling coatings has been proposed as a way to drastically reduce the initial deposition and build-up of inorganic scales on surfaces. This paper investigates a number of proposed anti-fouling coatings with diverse physiochemical characteristics. The wettability of anti-scaling surfaces, particularly in multiphase conditions, has been shown to be of particular importance with regards to the degree of inorganic scales deposited.(187)

Hydrophilic and hydrophobic coatings are starting to become more widely applied on downhole coatings, though there is limited consensus on which are the most effective. Fluoropolymers, sol-gels, diamond-like-carbon and others are applied industrially, all of which have different characteristics that can influence the propensity of scale to form under different conditions, shown in Table 3.1.

Four properties are key when assessing the suitability of coatings for anti-fouling purposes in downhole applications:

- 1) *Wettability and surface energy* are strong determinants of both crystal nucleation propensity (Section 2.7.5) and the wetting behaviour of both water and oil in multiphase systems
- 2) *Roughness* has a bearing on both nucleation and adhesion likelihood, and whilst increased roughness generally increases hooking sites and adhesion strength of deposits, wettability can be tuned through the design of 'self-cleaning' surfaces e.g. lotus-leaf (188)
- 3) *Durability* is of paramount importance in ensuring that any applied coating maintains its functionality over long periods of time. A lack of resilience to chemical and physical wear e.g. impingement, will result in damage or removal of the coating, compromising its anti-fouling characteristics leading to undesirable fouling
- 4) *Application feasibility* takes into account the price and the difficulty of machining the coating onto complex geometries e.g. SSSV

Whilst the scaling mitigation potential of both anti-fouling surfaces and inhibitors has been investigated extensively on an individual basis, particularly for conventional scales, this work is the first on their combined efficacy in sulphide forming multiphase processes.(19, 131, 185, 189) As operators become increasingly intent on applying anti-fouling coatings onto downhole equipment to prevent the deposition and build-up of scales, understanding the synergy (or lack thereof) between chemical and surface mitigation techniques is critical.

2.12.3 ASSESS program

The ASSESS (AntiScale Surface Engineering Solutions) program aimed to develop anti-fouling coatings for application in sub-surface safety valves (SSSV). Build-up of mineral scales within the well can deposit and build-up on the inner wall and spring cavities of the SSSV, obstructing the sliding sleeve and forcing open the flapper controlling the valve mechanism. This then results in the SSSV being stuck open, and the well being shut-in, consequently halting production.(16)

A number of coatings with anti-fouling properties, ranging from rough hydrophobic fluoropolymer based to ultra-smooth hydrophilic surfaces, underwent scaling tests in complex environments to determine the characteristics of a coating that prevent initial deposition of scale onto a

surface. Examples of coating types with varying physiochemical parameters can be seen in Table 2.4.

Table 2.4 ASSESS coating types and characteristics

Coating type	Coating characteristics
Fluoropolymer	<ul style="list-style-type: none"> - Chemically inert - Corrosion and chemically resistant - Low surface energy
Fluoro-composite	<ul style="list-style-type: none"> - Fluoropolymer matrix reinforced with ceramic particles - Non-stick properties and enhanced mechanical properties
Sol-Gel (inorganic)	<ul style="list-style-type: none"> - Low adhesion glass-like - Ultra-smooth non-stick - High surface energy
Sol-Gel (hybrid)	
Diamond-like carbon	<ul style="list-style-type: none"> - Low roughness, friction and adhesion - Excellent chemical resistance and mechanical properties
Inconel 718 (none)	<ul style="list-style-type: none"> - Industry standard material

The overarching aim of the ASSESS program was to take forward promising anti-fouling coatings for field trials, and ultimately determine the physiochemical characteristics that promote anti-scaling on surfaces and develop a surface that can prevent mineral scale build-up in oilfield systems over extended periods of time. The reduced workover frequency as a result of minimised scale build-up will ultimately save on operating expenditure.

The best performing coatings per the four requirements in Section 2.12.2 were selected for further testing and potential field trial applications. Hydrophobic fluoropolymers were found to be the standout coating and provided a useful counter-point to Inconel 718 reference steel for testing due to the stark contrast in characteristics.

2.12.4 Scale removal

If an undesirable build-up of scale occurs within the well, numerous remediation methods and tools can be utilised in order to remove it dependent on the mineral species.

Hydrochloric acid can be used to remove CaCO_3 scale thanks to fast reaction rates and low costs, though is associated with exacerbation of asphaltene deposition, corrosion, emulsion formation and sand production. Sulphate and sulphide scales are relatively insoluble in acids and hence physical removal techniques such as milling or jetting are required to remove them. As such, complete prevention of sulphate scales is generally preferable to attempted removal.(12)

2.13 Summary of Literature

Proliferation of sulphide scales downhole is specific to sour oilfield systems, with studies looking at the mechanics of deposition and adhesion of common carbonate and sulphate scales far more prevalent. Detailing the nature of initial deposition and adhesion of CaCO_3 and BaSO_4 upon surfaces is of great interest to the oil industry, where the build-up of scale downhole can severely hamper production. Carbonate and sulphate scales generally precipitate heterogeneously, though homogeneous adhesion is also feasible in systems with higher SR values. This leads to complex surface interactions and adhesion of crystals to the substrate, not only through intermolecular forces e.g. vdW, but chemical bonding of crystals to the substrate surface in addition to anchoring of the crystals in surface defects.(190) PbS however, owing partly to its low solubility, precipitates as nanoparticles spontaneously within the aqueous phase of produced fluids in oilfield systems. Though the AFM force curve interaction of mineral PbS at the [001] face and AFM tips has been measured previously (151), this work is the first to observe and quantify the magnitude of change in interfacial attraction when AFM tip wettability has been modified under constant experimental conditions. As such, forces acting between bulk PbS particles and hydrophilic or hydrophobic surfaces respectively in oilfield scaling systems could be accurately represented through AFM measurements.

There have been numerous studies on the efficacy of anti-fouling surfaces in preventing deposition within single phase aqueous scaling systems where heterogeneous crystallisation is dominant.(16, 131, 191, 192) Whilst a light oil

phase has been shown to wet surfaces to different degrees based on wettability in a multiphase system,(193-195) its influence with respect to scale deposition in sulphide systems had not yet been considered before this work. The tendency of conventional CaCO_3 and BaSO_4 scales, as well as unconventional PbS to deposit and build-up on a range of anti-fouling surfaces in turbulent multiphase systems was therefore investigated.

Co-precipitation of scales in complex systems has been widely investigated in commonly occurring carbonate and sulphate scaling systems. CaSO_4 crystals have been shown to act as a precursor to heterogeneous seeding of CaCO_3 , where the energetic barrier is reduced leading to precipitation in calcite form.(196) Incorporation of ions into the lattice is common in CaCO_3 co-precipitation, where the adsorption of ions or compounds to the surface layer of growing calcite can result in changes to wettability and morphology.(197, 198). Whilst limited studies have considered co-precipitation of conventional carbonate and sulphide scales in single phase, (116) none have regarded the effects of co-precipitation in multiphase systems. This work assesses the role of the o-w interface on co-precipitation of CaCO_3 and PbS when a light oil phase is present and subsequent crystal complex formation, emulsion/droplet stabilisation and surface deposition.

The use of PAMPS and other sulphonated polyelectrolytes to prevent scale nucleation and growth has been previously investigated.(178, 199) Whilst high MW polyelectrolytes have shown promise with regards to the mitigation of low solubility sulphide scales e.g. FeS , their efficacy has not been trialled in either multiphase or complex scaling systems. In addition to the influence of PAMPS on emulsion stabilisation in PbS scaling systems, the effect of polyelectrolyte adsorption onto the PbS mineral and subsequent changes in both wettability and interfacial interactions with hydrophilic/hydrophobic surfaces was examined.

Chapter 3

Materials and Methods

A novel experimental set-up was designed to test the performance of a range of anti-fouling coatings in a range of scaling systems. The addition of an emulsified light oil phase to the reaction vessel was representative of flow in oil producing wells, where the interaction between precipitated mineral scale and the oil-water (o-w) interface was investigated.

To further probe the interfacial forces and interaction between PbS and surfaces of different wettability, force curve measurements using both hydrophilic and hydrophobic contacting tips on a cleaved galena surface were undertaken.

This methodology can be broken down into 4 sub-sections:

- a) characterisation of promising commercially available anti-fouling coatings used in experiments (Section 3.1 and 3.2)
- b) description of brine composition and scaling tests carried out in single and multiphase carbonate, sulphate and sulphide systems, as well as complex systems representative of oilfield brines (Section 3.3, 3.4, 3.5 and 3.6)
- c) post-experimental analysis of anti-fouling coupons, bulk scale and emulsions (Section 3.7)
- d) AFM force curve on galena [001] face: preparation and analysis (Section 3.8)

3.1 Anti-fouling surface characterisation

3.1.1 Water contact angle

Contact angle measurements were performed on all anti-fouling surfaces in order to establish the affinity of the oil and water phases to the respective surfaces. The likelihood of a stable oil film forming over the surface was associated with the displacement energy (DE), a thermodynamic measure of the ability of a surface to favour oil wetting via displacement of water molecules from the interface. DE is defined in Equation 3.1.(200)

Equation 3.1

$$DE = \gamma_{WA} \times (\cos\theta_{WS}) - \gamma_{OA} \times (\cos\theta_{OS})$$

Where γ_{WA} and γ_{OA} denotes respectively the water/air and oil/air surface tension while θ_{WS} and θ_{OS} denotes the contact angle of water and oil on the surface of interest. Equation 3.1 shows that the DE is the difference between the work of adhesion of oil and water, respectively, on the solid surface. An o/w emulsion with optimal tendency for oil to wet the surface should have a negative DE and the more negative the value of DE is, the more readily such displacement takes place. Fluoropolymer coatings are generally highly hydrophobic and favour the displacement of water and the formation of a stable oil layer that prevents scale forming at the surface of the sample.(201)

Analysis of the drop shape allowed determination of the contact angle of a sessile drop and its shadowed image in the substrate. A drop (~ 40 μ l) was metered from a syringe onto the solid substrate (anti-fouling coating) and an image of the drop was recorded with a camera in conjunction with Attension™ drop shape analysis software as shown in Figure 3.1.(202)

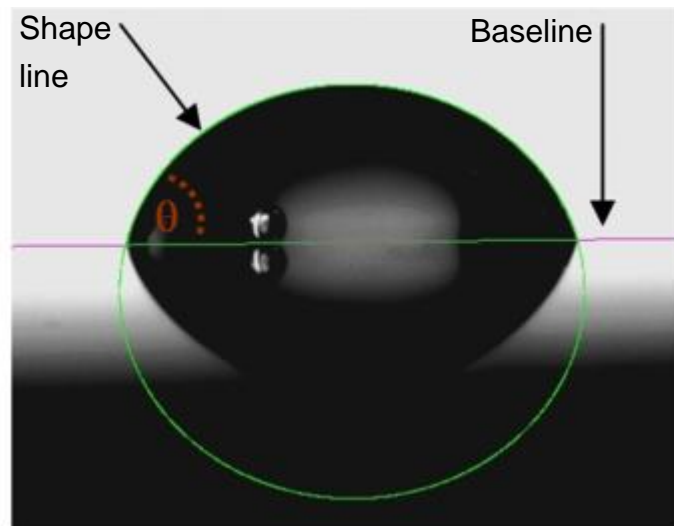


Figure 3.1 Sessile drop with fitted contour (202)

The Young-Laplace equation (Equation 3.2) was then applied to the curved liquid surface in order to measure the contact angle.(203)

Equation 3.2

$$p_c = \sigma \left(\frac{1}{R_1} + \frac{1}{R_2} \right)$$

Where p_c is capillary pressure, σ is the surface tension (mN/m) and the principal radii of curvature R_1 and R_2 .

3.1.2 Substrate hardness

Sufficient adherence of coatings to a substrate is of critical importance as it ensures full performance and reliability of the coatings during application. Scratch tests involved a stylus moved over a sample with a linearly increasing load until failure occurred at critical loads, as shown in Figure 3.2 (204). The failure events were then examined by optical microscopy.

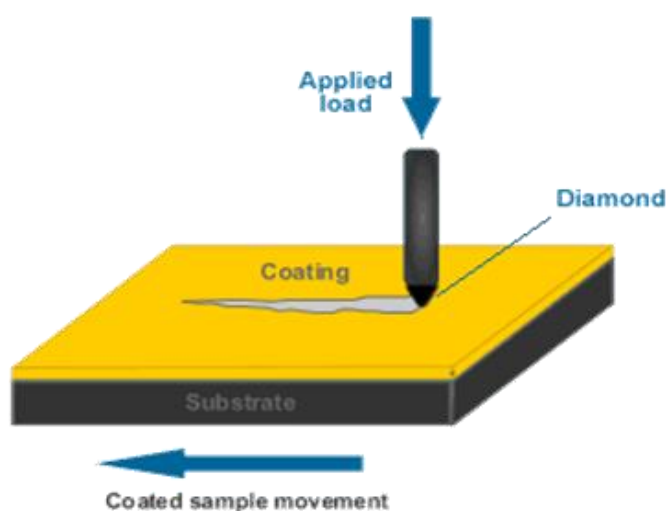


Figure 3.2 Schematic of a scratch test (204)

Scratch tests were completed using spherical tip (200 μm radius) with a loading rate of 10 N/mm, an initial load of 1 N and a final load of 90 N; 3 to 4 repeats were performed for each surface. A typical scratched sample observed under optical microscope is shown in Figure 3.3, where a) displays a hard DLC substrate, and d) a soft F3 surface. A TriboTechnic™ Scratch Tester Millennium 200 was the apparatus used in order to carry out the tests.

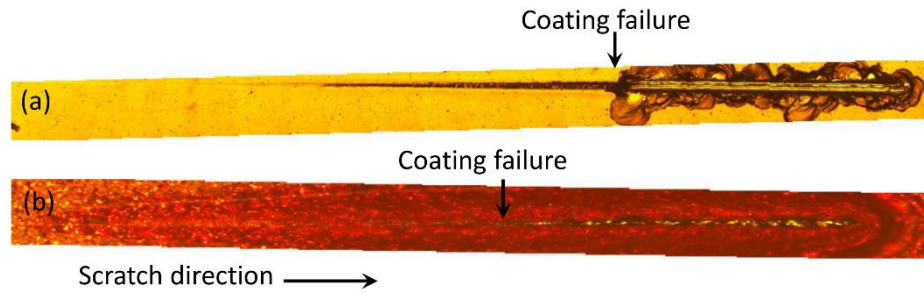


Figure 3.3 Substrates post-scratch test a) DLC; b) F3

3.1.3 Surface roughness

White light interferometry (WLI) analysis on FormTalysurf PG1800 equipment was used to determine the topographical parameters of each of the coatings, including average roughness (S_a), valley and peak intensity (S_{sk}) and sharpness (S_{ku}).

The coating was applied to a flat substrate and placed within the interferometer where a broadband ‘white-light’ source illuminated the test and reference surfaces. A condenser lens then collimated the light, before a beam splitter separated the light into reference and measurement beams. The reference beam is reflected by the reference mirror with the measurement beam being scattered from the test surface. Returning beams are relayed by the beam splitter to the image sensor where an interference pattern of the test surface topography was formed.(205)

3.2 Anti-fouling surfaces

A number of anti-fouling coatings with contrasting physiochemical characteristics were used for anti-fouling experiments. The wettability of anti-scaling surfaces, particularly in multiphase conditions, has been shown to be of importance with regard to the extent of inorganic scale deposition.(206) Table 3.1 lists the name and type of coatings evaluated. Coatings F1 and F2 are classified as hydrophobic (water contact angle $> 90^\circ$), whilst REF and DLC are classified as hydrophilic (water contact angle $< 90^\circ$).

Table 3.1 Anti-fouling coatings tested

Coating	Coating type	Water contact angle (°)	Displacement energy	Average Roughness (µm)	Hardness (GPa)
REF	UNS N07718 (none)	71	30	0.01	4.07 ± 0.28
DLC	Diamond-like carbon	68	11	0.01	1.43 ± 0.49
F1	Fluoro-polymer	101	-28	3.62	0.08 ± 0.02
F2		103	-31	0.93	0.09 ± 0.02
F3		105	-32	1.19	0.08 ± 0.01
F4		70	6	0.97	3.12 ± 0.4
SG1	Sol-Gel	42	33	0.08	0.37 ± 0.04
SG2		87	-9	0.2	1.45 ± 0.13
SG3		70	3	0.03	0.21 ± 0.03

3.2.1 Coating characteristics

This section describes the rudimentary characteristics of the three coating types selected and applied to Inconel steel due to their anti-scaling properties; diamond-like carbon (DLC), fluoropolymer (F) and sol-gel (SG).

3.2.1.1 Diamond-Like Carbon (DLC)

DLC coatings are amorphous carbon films comprising significantly of sp^3 -hybridized carbon atoms, sp^2 graphite and hydrogen, where the structure can be amorphous or contain diamond crystallites.(207, 208) This imbues them with high hardness, low friction coefficients against DLC and other materials, high temperature and corrosion resistance and low rates of wear.(209) A cross-section of a DLC coating and its structure can be seen in Figure 3.4.(210)

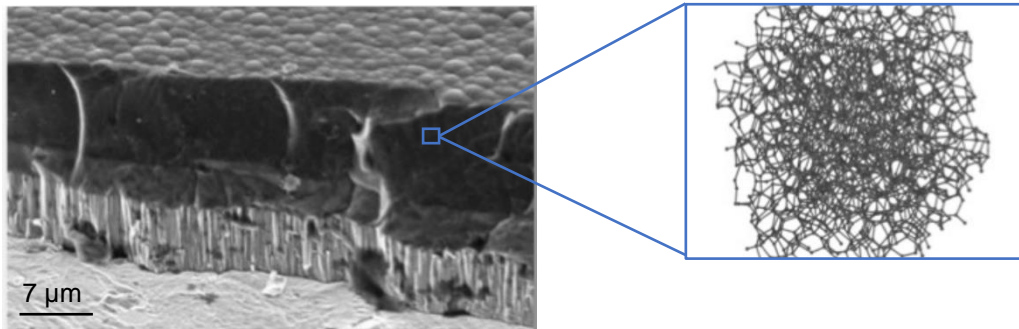


Figure 3.4 DLC film cross-section showing graphical representation of amorphous carbon structure (210)

3.2.1.2 Fluoropolymer (F)

Fluoropolymers in their most simple form consist of a carbon backbone with pendant groups that are C–F bonds, where polytetrafluoroethylene (PTFE) is an example of a linear fluoropolymer.(211)

It is from this fundamental carbon-fluorine structure that its properties are derived, including excellent temperature and corrosion resistance, chemical and organic resistance and a low friction, non-stick.(212) A cross-section of a PTFE coating and its structure can be seen in Figure 3.5.(213)

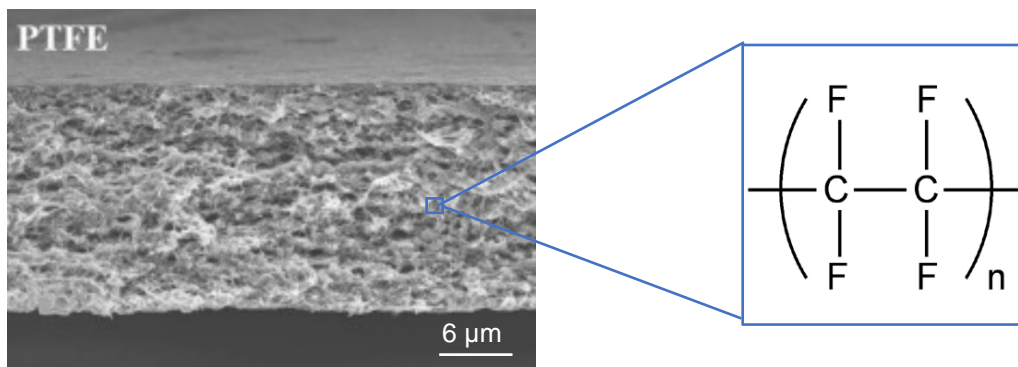


Figure 3.5 PTFE film cross-section and chemical representation of fluorocarbon structure (213)

3.2.1.3 Sol-gel (SG)

Sol-gel coatings are produced through the dispersion of colloidal particles and their consequent hydrolysis in liquid form a continuous network that can then be pyrolyzed through heat treatment to form an amorphous or crystalline structure. The process is commonly performed with silica oxides, but non-

silica oxides e.g. TiO_2 , ZrO_2 , Al_2O_3 have become widely used. Sol-gels are most commonly applied using dip-coating mechanisms where the substrate to be coated is immersed in liquid and then withdrawn at a well-defined speed before the drying process.(214, 215)

Sol-gels are generally thin and provide strong adhesive properties between the metallic substrate and top coat. They have good corrosive properties and can easily be applied to complex geometries whilst a gel. Additionally, the composition of sol-gel coatings are easily tuneable, with high purity products achievable due to the precursor of the desired ceramic oxide being able to be mixed and dissolved in a specialised solvent and hydrolysed into a sol.(216) A cross-section of a sol-gel coating and its structure can be seen in Figure 3.6.(217)

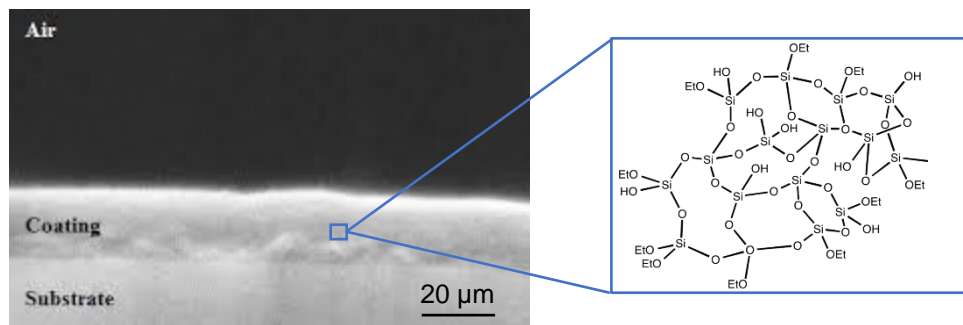


Figure 3.6 SEM cross-section of silica-based sol gel coating and chemical structure of typical branched network (217)

3.2.2 Coating selection

As this work was industrially motivated, coatings that did not meet specification were discarded throughout the experimental process, based on their performance, feasibility for application and supplier availability/cost. As such, the range of coatings tested was not necessarily consistent throughout the work. Coatings that had most promising characteristics and were selected for field trials, e.g. F1, F2 and DLC, were contrasted and compared throughout.

3.3 Mineral scaling tests

3.3.1 Carbonate and sulphate scaling tests

For both carbonate and sulphate experiments, mineral forming formation water (FW) and seawater (SW) brines were mixed in a 1:1 ratio within the 2.2 L reaction vessel. Experiments performed under multiphase conditions introduced light synthetic distillate or kerosene (C₁₁ - C₁₆ iso-alkanes) as the oil phase at varying o:w ratios specific to each test. Four cylindrical anti-fouling coupons (3.77 cm² each) were mounted upon a steel shaft and inserted into the vessel, alongside a bladed impeller, with both rotated at 400 rpm by overhead stirrers, where the dimensionless Reynolds number (*Re*) was calculated to be 3374 at the substrate interface. N₂ or CO₂ gas (specific to test type) was bubbled through the SW delivery vessel and the FW brine containing reaction vessel for one hour, ensuring anaerobic conditions in both incompatible brines before mixing, and was continuously fed into the reaction vessel throughout the experiment. Overpressure within the delivery vessel allowed flow of SW brine into the FW brine containing reaction vessel once a connecting valve was opened, initiating the experiment, before the valve was closed. The experiment run-time was 1 hour, after which the gas flow was stopped and the anti-fouling coupons carefully extracted. Samples were then dried under a gentle N₂ stream for a 24-hour period to evaporate excess water and/or oil on the coating surface, allowing any mineral deposits to dry without risk of crystal deformation associated with drying at temperature.

3.3.2 Modifications to equipment for sulphide tests

Due to the hazardous nature of H₂S gas, a number of considerations were taken into account during the design and operation of the scaling equipment for tests involving sulphide scales.

- Ultra-high molecular weight poly-ethylene (UHMWPE) plastic was used to fashion the reaction vessel, delivery vessel and solid scrubbing vessels. This was due to its low permeability and high resistance to H₂S related failure (218)
- Scrubbing vessels were filled with porous carbon/alumina-based scrubber in order to remove excess H₂S from the system. Pellets were generally easy to handle due to their inert nature and high capacity for H₂S adsorption
- O-rings and rotary valves were composed of H₂S resistant Viton in order to prevent long-term degradation and potential compromise

- All tests were carried out in a fume-hood where a slam-shut valve connected to a detector was rigged to cut off flow from the H₂S cylinder given a leak occurred and

3.3.3 Sulphide scaling tests

Sulphide scales are prevalent in sour systems where H₂S_(aq) is present within the produced flow-stream. The method and equipment used for sulphide tests was largely similar to carbonate and sulphate testing, though the introduction of gas into the vessel was carefully controlled due to high levels of toxicity. Once sealed, gas in a blend of 1% H₂S/99% N₂ was introduced into the air phase of the airtight reaction vessel at a constant pressure of 1.1-1.2 bar (absolute), controlled via a regulator connected to a pressurized cylinder. Unlike carbonate and sulphate tests, where the respective CO₃²⁻ and SO₄²⁻ anions were introduced via an incompatible seawater brine, H₂S in the gas phase dissociated from the gas into the aqueous phase over an extended period time before equilibrium was reached. This novel methodology was intended to be representative of downhole conditions, where as a result of gradually changing temperature, pH and chloride ion concentration, sulphide precipitation would occur at a slower rate than traditionally seen in sulphide scaling laboratory tests, where metal sulphides are often derived from the introduction of two aqueous solutions, resulting in spontaneous precipitation.(19, 22)

All scaling tests were buffered to pH 5.2 using 50 ml of 5 M acetate buffer (Table 3.2 and Table 3.3), monitored throughout the experiment using a H₂S resistant pH probe. Unbuffered tests resulted in a sharp drop in pH due to the dissociation of H₂S gas into solution and consequent release of protons. A pH of 5.2 was representative of sour wells where sulphide scaling has occurred, and from Bjerrem plots in Figure 2.17, was high enough to prompt dissociation of gaseous H₂S into bi-sulphide ions (HS⁻). Phosphate buffer (PBS) was considered but not used to control solution pH as it chelated with divalent Pb²⁺ ions in solution, forming an unwanted precipitate that would have compromised the accuracy of the experimental mass gain measurements.

Table 3.2 Solution composition

Solution	Compound	g/L
A	Acetic acid (CH ₃ COOH)	287.5
B	Sodium acetate (CH ₃ COONa)	410

Table 3.3 Proportion of solution mixed to form acetate buffer

Buffer	Solutions mixed	mL/L
Acetate (pH 5.2)	A	48
	B	452

Nitrogen (N₂) sparging of brines was performed for 1 h before the experiment was initiated to ensure a completely anaerobic environment, preventing the formation of sulphates. The H₂S blend was introduced into the airspace of the reaction vessel in a 1% H₂S/99% N₂ ratio for 1 h. For co-precipitation experiments, two deaerated incompatible brines were introduced using the seawater (SW) delivery vessel and injected through overpressure into the reaction vessel immediately before the H₂S blend stream was activated, initiating the test. Once the test was complete, the flow of H₂S from the gas cylinder was halted and inert N₂ gas flowed through the system to ensure that no residual H₂S was present within the system. This was achieved by placing a H₂S detector at the reaction vessel outlet before offsetting a small amount of gas until the system had reached safe levels (< 1 ppm).

As in standard carbonate and sulphate scaling tests, anti-fouling surfaces were extracted from the reaction vessel and removed individually into a petri-dish before drying under a N₂ stream.

Co-precipitation experiments incorporated PbS and CaCO₃ scaling brines, where seawater brine was introduced into a formation brine from the delivery vessel directly before activation of the 1% H₂S/99% N₂ blend into the reaction vessel. This prompted the simultaneous precipitation of carbonate and sulphide scales, replicating the proportion of solids that would be expected to form in actual producing systems.

3.3.4 Scaling rig

Figure 3.7 displays an image of the rig used for all scaling experiments, with Figure 3.8 showing a basic schematic of the same system.



Figure 3.7 Photograph of multiphase scaling rig with H₂S injection capability and seawater (SW) delivery vessel

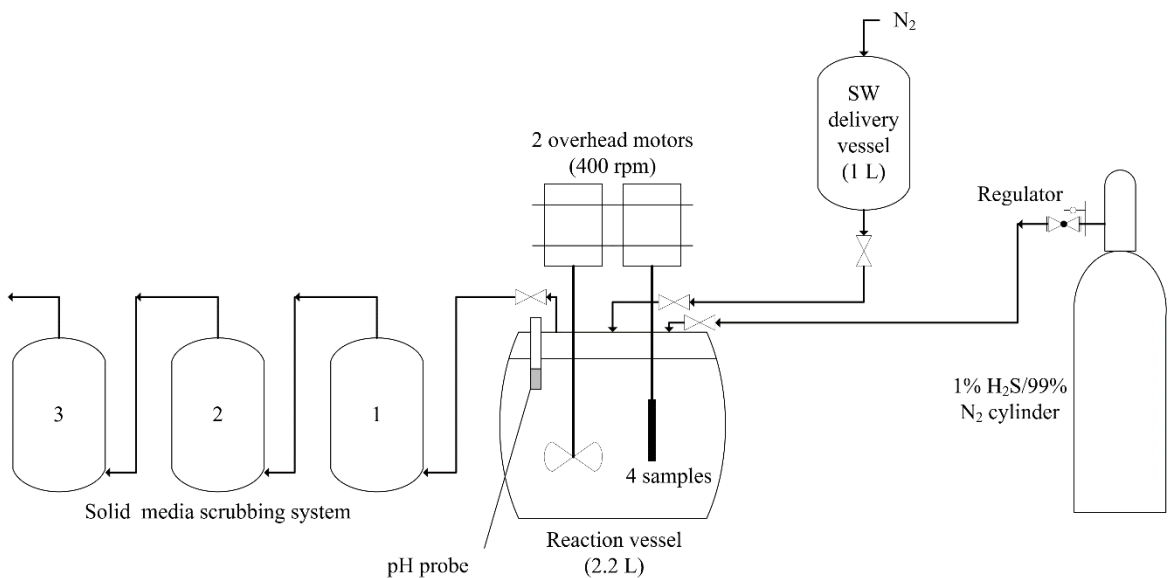


Figure 3.8 Schematic of multiphase scaling rig with H₂S injection capability and seawater (SW) delivery vessel

The rig was designed and constructed based on conventional multiphase scaling set-ups, where a 2-litre glass beaker containing brine has two overhanging motors enabling samples to be immersed and the solution to be vigorously stirred. Due to the hazardous nature of work carried out when H₂S is present, previous experiments investigating sulphide precipitation have been static, with little to no control over the level of turbulence at the sample interface or within the vessel. The new design allowed turbulence at the sample interface and within solution to be controlled, enabling the formation of multiphase emulsions. As part of our design, materials were selected based on their H₂S resistance, machinability, cost and durability. The new reaction vessel was airtight to prevent the escape of toxic H₂S gas injected at pressure into the air phase before dissociation into the solution. This required careful design and application of rotary seals around rotating shafts, where the likelihood of gas leak was heightened, in order to prevent escape of H₂S.

A H₂S resistant pH probe was integrated into reaction vessel lid to ensure solution pH was consistent to the value at which it had been buffered. For the safe removal of excess unreacted H₂S gas, a series of scrubbers were used. Porous carbon/alumina pellets were sourced that had a high adsorption rate of H₂S, that once fully saturated were able to be disposed of safely without special consideration.

Figure 3.9 shows the Solidworks™ design of components that comprised the reaction vessel, with Figure 3.9a & b displaying the lid from the top and bottom respectively, with Figure 3.9c the main 2.2 L reaction vessel. A 158 mm diameter/3 mm thick ethylene propylene (EPDM) H₂S resistant o-ring was inserted into the circular groove on the top face of the reaction vessel (Figure 3.9c) before 40 mm screws were secured into the 10 holes on the periphery of the lid in order to create an airtight seal between the lid and the vessel.

Custom-made EPDM rotary seals were inserted into the 2 circular grooves positioned towards the top of Figure 3.9a, before being secured in place by a screwed-in cap. They prevented escape of gas from the pressurised vessel where motor-driven rotating stainless-steel shafts supporting a bladed stirrer and anti-fouling coupons within the vessel, where the likelihood of a gas leak was increased.

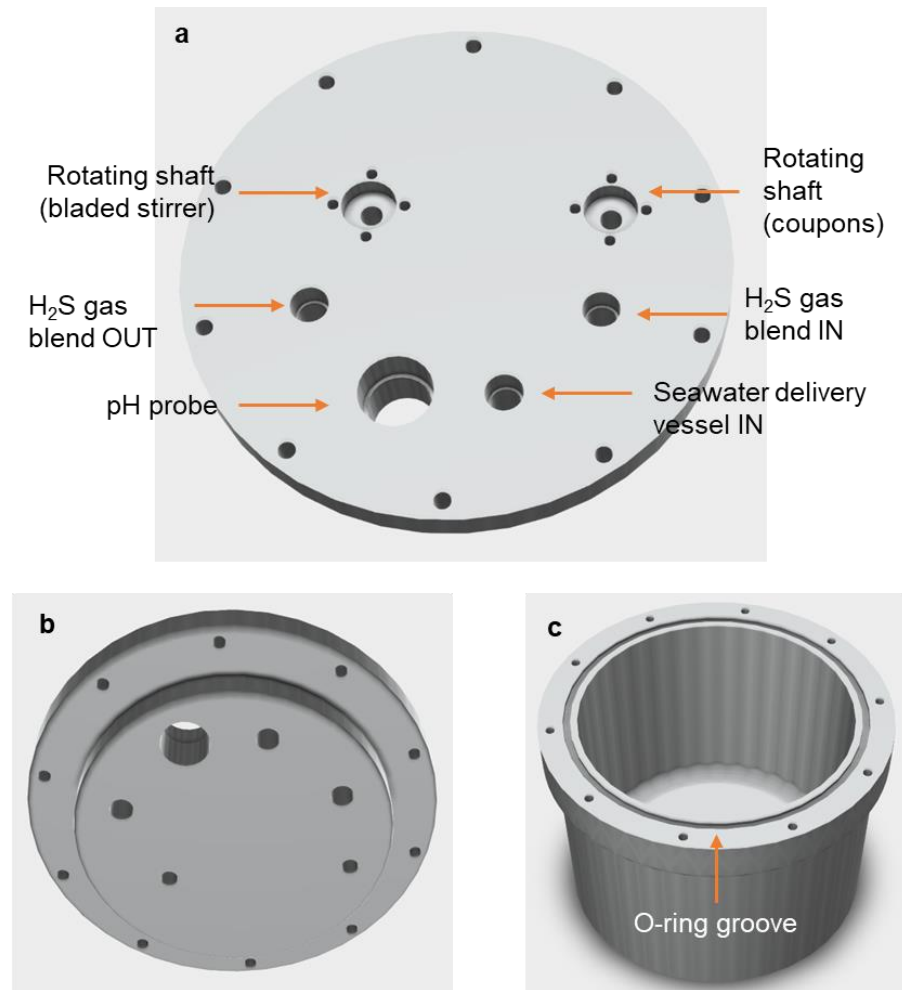


Figure 3.9 Solidworks™ images of main reaction vessel a) lid top; b) lid bottom; main vessel

3.3.5 Hydrodynamic conditions

A bladed impeller was rotated at 400 rpm, necessary to create an emulsion within the reaction vessel when a second immiscible phase e.g. oil was present. To propagate turbulence at the surface of the anti-fouling coupons, the shaft was rotated at 400 rpm, with hydrodynamic conditions represented in Table 3.4 representative of flow conditions within a single phase system. Rotating cylinder (RC) equipment, used extensively in corrosion and scaling research was implemented as flow becomes turbulent at relatively low rotational velocities, with ($Re > 300$) sufficient to create turbulence at the coupon surfaces.(219)

Table 3.4 Hydrodynamic conditions at coupon interface in single phase conditions

Parameter	Value
Reynolds number (Re)	3374
Wall shear stress τ (Pa)	0.17
Surface velocity U_{cyl} (cm.s-1)	25.13

3.3.6 System limitations

As the reaction vessel was primarily designed to promote turbulent emulsion forming conditions, it was constructed from UHMWPE. Whilst this versatile material was resistant to H₂S and relatively machinable, it could not withstand high temperatures and pressures that would be representative of downhole oilfield conditions. A custom-made autoclave would be required to create similar conditions at raised temperatures and pressures. Whilst the thermodynamics of crystallisation would change given exposure to extreme external conditions, it is predicted that the mechanism for deposition would be unchanged under ambient conditions.

Turbulent flow in producing oilfield systems can potentially reach Re values of >200,000 in pipe flow.(220) The experimental value at the coupon interface (Re = 3374) in these experiments was limited by the speed at which the shaft housing the coupons could be rotated due to the long-term tolerances of rotary valves ensuring the vessel was airtight.

3.4 Brine compositions

All brines were made up in MilliQ water (18.2 M Ω ·cm) and filtered through 0.45 μ m filters before experiments were carried out. The composition and resulting SR_{initial} of the brines can be seen in Table 3.5 to Table 3.8, with a CaCO₃ forming brine (Brine A), BaSO₄ forming brine (Brine B), PbS forming brine (Brine C) and PbS/CaCO₃ forming brine (Brine D) respectively. All brines were mixed in a 50:50 FW:SW ratio.

Table 3.5 Brine A - CaCO₃ forming brine composition and SR_{initial}

Ion	Ionic concentration (mg/L)		SR _{initial}
	Formation water	Sea water	
Na ⁺	10000	11744	CaCO ₃ = 76
Ca ²⁺	8000	-	
K ⁺	468	-	
Mg ²⁺	1118	-	
HCO ₃ ⁻	-	6102	
Cl ⁻	36629		

Table 3.6 Brine B - BaSO₄ forming brine composition and SR_{initial}

Ion	Ionic concentration (mg/L)		SR _{initial}
	Formation water	Sea water	
Na ⁺	31275	10890	BaSO ₄ = 1888 SrSO ₄ = 4
Ca ²⁺	2000	428	
K ⁺	654	1368	
Mg ²⁺	739	460	
Ba ²⁺	268	-	
Sr ²⁺	771	-	
SO ₄ ²⁻	-	2960	
Cl ⁻	74306		

For calculation of SR_{initial} of PbS, in Brine C, solubility and IAP was adjusted to account for a saline brine and pH 5.2 solution.(29) A high concentration of 1000 Pb²⁺ was used to accentuate the differences in scaling severity upon different anti-fouling surfaces, with KCl electrolyte at 0.5 M introduced to provide a high salinity system.

Table 3.7 Brine C - PbS forming brine composition and $SR_{initial}$

Ion	Ionic concentration (mg/L)		$SR_{initial}$
	<i>Formation water</i>	<i>H₂S injection</i>	
Pb ²⁺	1000	-	PbS = 1.7×10^{19}
K ⁺	19405	-	
Cl ⁻	17938	-	
HS ⁻	-	30 (at equilibrium)	

For Brine D, the two dominant precipitating species were PbS and CaCO₃, with $SR_{initial}$ calculated using both the process detailed in Section 3.5.1 and Multiscale software (Section 3.5.2) respectively.

Table 3.8 Brine D - PbS and CaCO₃ forming brine concentration and $SR_{initial}$

Ion	Ionic concentration (mg/L)		$SR_{initial}$
	<i>Formation water</i>	<i>Sea water</i>	
Na ⁺	10000	11744	PbS = 1.3×10^{17} CaCO ₃ = 76
Ca ²⁺	8000	-	
K ⁺	468	-	
Mg ²⁺	1118	-	
Pb ²⁺	100		
HCO ₃ ⁻	-	7002	
HS ⁻	-	30 (at equilibrium)	
Cl ⁻	38196		

3.5 Saturation ratio (SR) calculation

3.5.1 PbS

Initial saturation ratio ($SR_{initial}$) of brine solutions are shown in Table 3.5 to Table 3.8, where $SR_{initial}$ for PbS was calculated and from the ion activity product (IAP) and solubility product (K_{sp}) as seen in Equation 3.4.(35, 221, 222) The effect of decreased pH and Cl^- presence (salinity) was taken into consideration during calculations for PbS solubility.(29)

Table 3.9 shows the changing PbS solubility with NaCl concentration at reduced sulphur concentrations and pH values used in scaling experiments from Section 3.3. (Adapted from Barrett and Anderson).(29)

Table 3.9 Variation in PbS solubility with NaCl concentration and pH
* $m_{S(r)}$ is total reduced sulphide concentration

NaCl strength (M)	Pb molar solubility (log M)		Molar solubility of PbS (M) @ pH 5.2	PbS solubility product (K_{sp}) @ pH 5.2
	pH 4 and $0.001 m_{S(r)}$	pH 5.2 and $0.0001 m_{S(r)}$		
1	-11.2	-12.6	2.5×10^{-13}	6.3×10^{-26}
2	-10.7	-12.1	7.9×10^{-13}	6.3×10^{-25}
3	-10.3	-11.7	2.0×10^{-12}	4.0×10^{-24}
4	-9.92	-11.3	4.8×10^{-12}	2.3×10^{-23}
5	-9.63	-11	9.3×10^{-12}	8.7×10^{-23}

To calculate the molar solubility of PbS at pH 5.2 and $0.0001 m_{S(r)}$, Equation 3.3 was employed. (29)

Equation 3.3

$$\log M_{Pb} = (\text{Pb log M value in Table 3.9}) - (3 + \log M_{S(r)}) + 2(4 - \text{pH})$$

For Brine C, the Cl^- presence was deemed negligible with regards to the overall PbS solubility e.g. < 0.01 M, where it was inferred from the linear relationship ($R^2 = 0.991$) in Table 3.9 that K_{sp} of PbS at solution pH 5.2 in Brine

C was 1×10^{-26} . Brine D was calculated to have a Cl^- concentration of 1.07 M, prompting an increase in PbS solubility, resulting in a K_{sp} value of 6.9×10^{-26} .

The ionic activity product (IAP) of Pb^{2+} and S^{2-} was calculated for all PbS containing brines from species concentration and the respective activity coefficient (α). (29, 223) For brine C, where ionic activity was 0.01 M, the IAP was calculated to be 3.56×10^{-3} and 6.98×10^{-4} for Pb^{2+} and S^{2-} respectively. Brine D, with an ionic activity of 1 M, had IAP values of 4.1×10^{-5} and 2.25×10^{-4} for Pb^{2+} and S^{2-} respectively.

The $\text{SR}_{\text{Initial}}$ for PbS in brines C and D could then be calculated using Equation 3.4.

Equation 3.4
$$\text{SR}_{\text{Initial}} = \frac{(\text{IAP Pb})(\text{IAP S})}{(K_{sp} \text{ PbS})}$$

Table 3.10 shows the species activity and final $\text{SR}_{\text{Initial}}$ for PbS containing brines.(29, 223)

Table 3.10 Calculation of Brine C and D saturation ratio

Brine	Ionic activity (M)	Activity coefficient (α)		Ionic activity prod. (IAP)		$\text{SR}_{\text{Initial}}$
		Pb^{2+}	S^{2-}	Pb^{2+}	S^{2-}	
C	0.5	0.29	0.31	1.4×10^{-3}	2.9×10^{-4}	1.7×10^{19}
D	1.07	0.17	0.24	4.1×10^{-5}	2.3×10^{-4}	1.3×10^{17}

3.5.2 CaCO_3 and BaSO_4

The concentration of scaling ions in brines were based off case studies in the North Sea, with Forties formation water (FFW) and North Sea seawater (NSSW) providing the template for CaCO_3 and BaSO_4 forming brines.

Multiscale™ software was used to calculate the SR of minerals that had the potential to form within solution after input of chemical concentrations and physical conditions of the system, seen for CaCO_3 and BaSO_4 in Brine A and B respectively. In order to determine $\text{SR}_{\text{Initial}}$, the software calculated activity

coefficients of precipitating salts that were extrapolated using the Pitzer model calculated as a function of molality (Equation 3.5).(224)

Equation 3.5
$$a_i = m_i \gamma_i$$

Where a_i is the activity (dimensionless), m_i the molality (mole/kg H₂O) and γ_i the activity coefficient (dimensionless).

The solubility product for calcium carbonate in MultiScale™ is given by Equation 3.6.(224)

Equation 3.6
$$K_{sp}(\text{CaCO}_3) = m_{\text{Ca}^{2+}} \times m_{\text{CO}_3^{2-}}$$

With $m_{\text{Ca}^{2+}}$ and $m_{\text{CO}_3^{2-}}$ being the molality of the species.

3.6 Multiphase experiments

For o/w emulsions, kerosene (C₁₁ - C₁₆, ACS reagent grade, Fisher Scientific), as the light oil phase was introduced to the reaction vessel at an o:w ratio of 5:95 in CaCO₃, BaSO₄, PbS and PbS/CaCO₃ o/w emulsion multiphase scaling experiments.

3.6.1 PbS and PbS/CaCO₃ emulsion inversion

The o:w ratio at which catastrophic inversion of the Pickering emulsion occurred was determined by way of dropwise addition of oil to recovered emulsions, as described in Section 3.7.3.7. Once the o/w ratios had been extrapolated, experiments were run with an excess of continuous oil phase to ensure emulsion type was consistently maintained as w/o throughout the experiment.

PbS forming experiments in w/o emulsion were run at an 80:20 o:w ratio, and PbS/CaCO₃ forming solutions at a 60:40 o:w ratio (Table 3.11).

Table 3.11 Emulsion type and o:w ratios for scaling systems

Scaling system	Emulsion type	o:w ratio
CaCO ₃	o/w	5:95
BaSO ₄	o/w	5:95
PbS	o/w	5:95
	w/o	80:20
PbS/CaCO ₃	o/w	5:95
	w/o	60:40

3.6.2 PbS and PbS/CaCO₃ w/ polymeric inhibitor

Polymeric sulphonated inhibitor (PAMPS) was introduced into PbS and PbS/CaCO₃ the brine phase of multiphase o/w systems prior to scaling experiments at concentrations of 50, 500 and 5000 mg/L.

15% active PAMPS solution was used to formulate 10,000 and 100,000 mg/L active stock solutions (w/v) that were then dosed accordingly using a digital pipette into the brine solution in order to reach the required concentration pre-experiment.(179)

3.6.3 PbS pre-precipitation

3.6.3.1 PbS system

Pre-precipitation experiments were performed whereby approximately 1000 mg/L of pre-precipitated PbS nano-crystals were introduced into Brine C, where a light oil phase was present in an o:w ratio of 5:95. Further precipitation did not occur as reacting anions derived from the dissociation of H₂S were not introduced into the reaction vessel. It was hypothesised that PbS nanoparticles (previously collected and kept in a desiccator to prevent oxidation) would migrate to the o-w interface to form a Pickering emulsion and deposit via oil droplet impaction, similarly to PbS nanoparticles that had precipitated within the brine phase during scaling experiments.

With the exception of introduction of pre-precipitated PbS nanoparticle introduction and the bubbling of 100% N₂ as opposed to 1% H₂S and 99% N₂, all other experimental conditions were kept the same, as detailed in Section 3.3.3.

3.6.3.2 PbS/CaCO₃ system

Approximately 50 mg/L of pre-precipitated PbS nanoparticles were introduced to a CaCO₃ forming brine (Brine D), where a light oil phase was present in an o:w ratio of 5:95. Further PbS precipitation was not expected due to the H₂S containing gas stream being replaced with pure N₂. The experiment aimed to observe whether PbS nanoparticles still acted as the seeding point for calcite growth at the o-w interface in multiphase systems.

With the exception of introduction of pre-precipitated PbS nanoparticle introduction and the bubbling of 100% N₂ as opposed to 1% H₂S and 99% N₂, all other experimental conditions were kept the same, as detailed in Section 3.3.3.

3.7 Post-experimental analysis

Post-experimental analysis occurred in three strands dependent on experiment type:

- a) Surface scaling – *Single and multiphase*
- b) Bulk particle characterisation – *Single phase*
- c) Emulsion characterisation – *Multiphase*

3.7.1 Surface scaling

Deposition upon the surface of anti-fouling coupons was used as the primary metric in determining the efficacy of different coatings with regards to scale prevention.

3.7.1.1 Visual analysis

Immediately after removal from the post-experimental solution, photographs of the extracted anti-fouling coupons were taken to provide a rudimentary analysis of the scaling tendency. Whilst certainly not a definitive gauge of scaling severity, the effect of substrate type was well highlighted in systems where there was a large contrast in scaling tendency between surfaces.

3.7.1.2 Mass gain

Mass gain analysis, whereby cylindrical anti-fouling coupons were weighed before and after scaling experiments was used to determine the degree to

which crystallisation and deposition had occurred upon a specific substrate using a Mettler Toledo XS64 analytical balance (Ohio, USA). Coupons were removed from the scaled solution post-experiment and placed under a gentle N₂ stream for 24 hours/until dry from oil and/or water before weighing. Measurements were carried out in a temperature regulated laboratory, with up to 5 readings of each coupon taken to ensure consistency. Mass gain results were plotted against the water contact angle of the coating, regarded the most important parameter in terms of scale prevention, particularly in multiphase systems.(206)

3.7.1.3 Microscopy

Scanning Electron Microscopy (SEM) was used in conjunction with Energy Dispersive X-Ray (EDX) analysis to assess scaling severity and coverage, the scaled species, morphology and size of the deposited crystals and any pattern related to nucleation type in various conditions on anti-fouling substrates. The size of emulsified oil droplets was determined after analysis of the size of the impacted region clear of scale. After mass gain analysis, scaled coupons were spray coated with iridium (Ir) to inhibit charging and reduce thermal damage before being imaged on the microscope.

The SEM used was a Carl Zeiss EVO MA15® (Oxford Instruments), with the EDX system by AZtecEnergy. It incorporated an 80mm X-Max SDD detector with secondary and backscattered imaging utilised. A high-energy beam (20keV) interacted with the atoms of samples to generate images of surfaces and associated deposits. For EDX analysis, two different energies were used to assess the composition of substrate and deposit layers, where a high-energy beam penetrated the coating deeper. X-rays emitted by the samples after bombardment with the beam can be detected and the composition subsequently assessed.

3.7.1.4 X-Ray Diffraction (XRD)

XRD analysis using a Bruker D8 X-Ray Powder Diffractometer (Billerica, Massachusetts) allowed identification of the precipitated species collected post-experiment from single phase PbS forming brines. Solution containing a high concentration of particles, extracted using a pipette from the bottom of the reaction vessel where agglomerates had settled, were left to dry on a silicon zero diffraction plate under an N₂ stream before being placed in a desiccator.

Once dry, the sample was placed in the XRD where spectra were recorded in the 2θ range between $20-90^\circ$ with a step size of $0.033^\circ/s$, resulting in a 38 min runtime. DIFFRAC.SUITE™ software was then used to analyse the crystalline compounds present in detected peaks.

Crystal type and morphology is identified in XRD analysis whereby emitted x-ray waves are scattered after striking the crystal atoms' electrons, resulting in a phenomenon known as elastic scattering. Bragg's law can then be used to determine the specific direction in which constructive waves travel, ultimately leading to the formation of a diffraction pattern used to discern crystal species.

3.7.2 Bulk particle characterisation

Analysis of bulk phase particle behaviour was critical in establishing depositional mechanisms in single and multiphase systems.

3.7.2.1 Microscopy

Whilst SEM was a valid tool for conventional carbonate and sulphate crystal characterisation, higher magnifications were needed to properly assess the size and structure of nano-sized PbS particles. Transmission Electron Microscopy (TEM) allowed visualisation of individual PbS nanoparticles collected from the brine solution post-experiment and dried before analysis using a FEI Tecnai TF20 TEM (Oregon, USA).

For TEM measurements, a 200keV beam was shone through a thin sample upon which PbS nanoparticles were mounted, allowing ultra high-resolution imaging of the crystal structure. Parts of the beam are transmitted based upon specimen thickness or transparency, with the remainder of the transmitted beam then focused by the objective lens onto a charge coupled device camera.

3.7.2.2 Particle charge (zeta-potential)

After single phase experiments, zeta-potential measurements were taken of collected PbS precipitate using a zeta-sizer (Malvern Instruments, UK), establishing electro-kinetic potential at the shear plane and hence probability of agglomeration as a result of reduced electrostatic repulsion. Prior to zeta-potential measurements being taken, PbS particles suspended in the recovered brine phase were sonicated within an ultrasonic bath for a 2-hour

period in order to minimise agglomeration. This enabled more accurate analysis of the electrophoretic mobility between individual PbS particles.

Zeta-potential measurements were performed on systems with 0 and 50 mg/L of PAMPS present in pre-experiment single phase PbS forming solutions.

3.7.2.3 Particle size distribution (PSD)

Using a zeta-sizer (Malvern Instruments, UK) as in Section 3.7.2.2, particle size distribution (PSD) measurements allowed the agglomeration tendency and consequent average size of PbS agglomerates to be determined. Solutions containing PbS particles were sonicated for a 2-hour period within an ultrasonic bath in order to break up agglomerates to establish their minimum size after dispersion. As with zeta-potential measurements in Section 3.7.2.2, PSD readings were performed on systems with 0 and 50 mg/L of PAMPS present in pre-experiment single phase PbS forming solutions.

3.7.3 Emulsion characterisation

3.7.3.1 Visual analysis

Both simple and complex multiphase sulphide scaling systems containing as little as 50 mg/L Pb^{2+} ions could result in the formation of stable PbS-based Pickering emulsions. Post-experiment, a pipette was used to siphon and extract the emulsion that was partially-wetted between the excess oil and water phases, before addition into a clear 30 ml vial.

Photographs were taken of the recovered emulsion, where approximately 15 ml of the aqueous phase, 10 ml of the o/w emulsion and 5 ml of oil were recovered; maintaining the o/w emulsion after collection that was present in the system where the o:w ratio was 5:95. For w/o emulsions, a higher proportion of oil was recovered in order to preserve the emulsion type that was representative of the experiment e.g. 15 ml oil, 10 ml emulsion and 5 ml brine. Extraction of the Pickering emulsion using a digital pipette is shown in Figure 3.10.

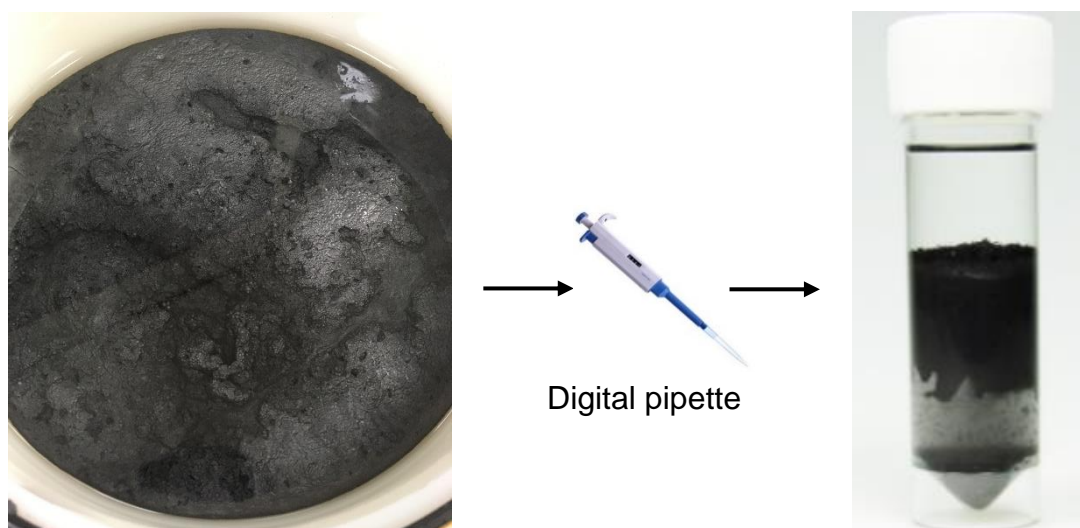


Figure 3.10 Extraction of PbS Pickering emulsion from post-experiment reaction vessel to vial using a digital pipette

3.7.3.2 Emulsion stability

Whilst the presence of PbS nanoparticles resulted in the permanent emulsification of a fraction of the water and oil present to form a Winsor type III emulsion, emulsion stability and particle phase affinity could be gauged through agitation of the vial, and analysis of the time taken for the respective free oil and water phases to separate and emulsion stabilisation to occur.(159) Photographs of the Pickering emulsion and excess oil and water phases were taken before agitation and at regular intervals (e.g. 1 min), until complete emulsion settling occurred (Figure 3.11).

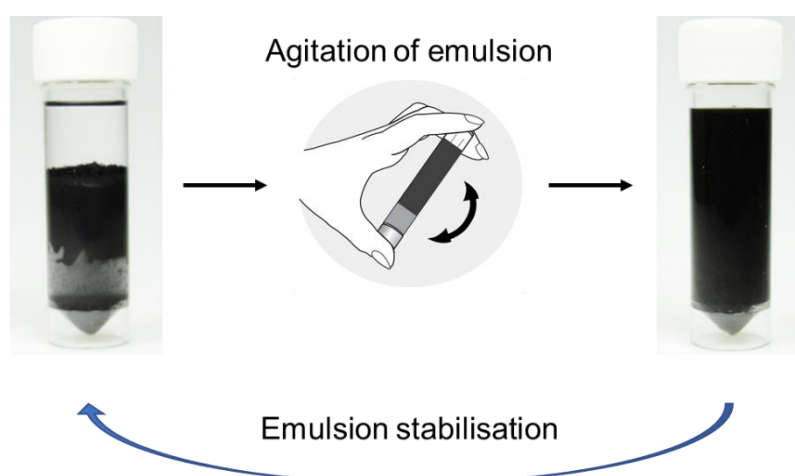


Figure 3.11 Agitation of recovered emulsion in 30 ml vial before recording of emulsion stabilisation time

3.7.3.3 PbS emulsion thermal stability and conductivity

25 ml of o/w PbS Pickering emulsion was collected into 30 ml vials and gradually heated within a water filled beaker upon a hot-plate, with a temperature and conductivity probe within the emulsion used to monitor any changes in emulsion conductivity and appearance with temperature.

Emulsions were heated up to 95°C, with photographs and conductivity readings taken for every 5°C rise in temperature.

3.7.3.4 Microscopy

To analyse the stabilising colloids in the Pickering emulsion, optical and cryo-SEM microscopy were performed, the latter using a Hitachi SU8230 SEM (Tokyo, Japan). Optical microscopy allowed visualisation of the oil droplet size, polydispersity and particle agglomerate arrangement at the droplet interface, whilst cryo-SEM allowed more detailed analysis of particle distribution and wetting at the emulsion interface. Preparation for cryo-SEM imaging involved rapid cooling of the specimen before transfer under vacuum to the cold preparation chamber. Back-Scatter Electron (BSE) techniques using a 10 keV beam were able to distinguish and highlight PbS arrangement at liquid interfaces in both simple and co-precipitating systems.

Images were taken using a Brunel SP300 Phase Contrast optical microscope (Brunel Microscopes, Wiltshire) to analyse oil droplets stabilised by CaCO₃ and BaSO₄ particles after multiphase experiments despite their large diameter.

3.7.3.5 Pickering emulsion viscosity

Measurements using a Malvern Bohlin Gemini rheometer (Malvern Instruments, UK) with cone and plate geometry of CP 1°/40mm measured the viscosity of the three o/w emulsions formed at different polymer concentrations across a ramping range of shears from 0.01 Pa to 2 Pa at 25°C.

3 ml of collected PbS-based Pickering emulsion was extracted from the vial using a pipette and placed below the cone and plate geometry, which was then lowered into position. Shear was ramped up to 2 Pa as viscosity was recorded. Viscosity measurements were performed on PbS o/w Pickering emulsions at PAMPS concentrations of 0, 500 and 5000 mg/L respectively.

3.7.3.6 X-Ray Diffraction (XRD)

XRD of PbS/CaCO₃ Pickering emulsions was carried out using the methodology described in Section 3.7.1.4, where the emulsion was extracted and left to dry on a silicon zero diffraction plate under an N₂ stream before spectroscopy measurements.

3.7.3.7 Emulsion inversion phase ratio

Formed PbS and PbS/CaCO₃ Pickering emulsions were siphoned and collected in 20 mL vials, where a proportion of oil and water was also collected from the reaction vessel. Starting with approximately 5 mL of recovered brine containing 1 mL of particle stabilised o/w emulsion and 1 mL of light phase oil, 0.5 mL of oil was added drop-wise. The vial was shaken and agitated, with an image taken after each oil addition until the point of emulsion inversion from o/w to w/o was observed.

3.8 Interfacial forces governing PbS adhesion

Atomic force microscopy (AFM) techniques were used to highlight the impact of substrate wettability on interfacial forces controlling the adhesion of partially-hydrophobic PbS. Force curve analysis of untreated (hydrophilic) and octadecyltrichlorosilane (OTS) functionalised (hydrophobic) silicon nitride (Si₃N₄) tips against a nanometrically smooth galena substrate was carried out. The influence of the hydrophobic force was examined, in addition to electrostatic interactions, with long-range forces increasing attraction between two hydrophobic surfaces, potentially as a result of OH bonds or a deficiency of water molecules from surfaces.⁽²²⁵⁾ The extended DLVO model including the effects of electrostatic interactions and hydrophobic attraction was applied to encompass the influence of all acting interfacial forces.⁽²²⁶⁾

Additionally, the adsorption of PAMPS onto the cleaved galena [001 face] was characterised, before force curve measurements were recorded using both hydrophilic and hydrophobic tips against the PAMPS functionalised surface.

An MFP-3D AFM instrument (Asylum Research, Santa Barbara, CA, USA) was used for all measurements.

3.8.1 Atomic Force Microscopy

Atomic Force Microscopy (AFM) measures the dependence of an interaction based on the distance between two surfaces at a given location. The force curve is established at a particular point on a sample surface where the deflection of a cantilever (force) is plotted against the extension of a piezoelectric scanner, calculating force upon approach and retraction away of a probe from the surface (F vs. D). The deflection of the cantilever, measured through use of a laser beam reflected from the cantilever to a detector, was converted to force using Hooke's law. The intermolecular and surface forces acting between two solids within an aqueous medium can then be extrapolated.(103) Figure 3.12 shows a schematic of AFM equipment.(227)

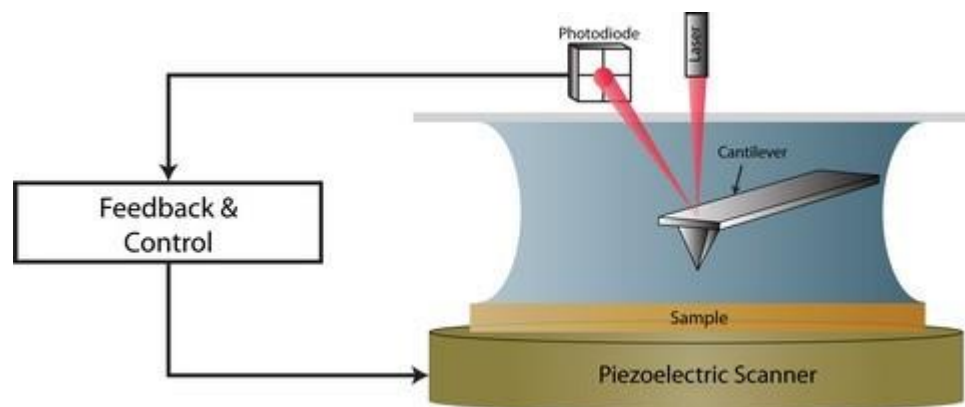


Figure 3.12 Schematic of AFM equipment (227)

Figure 3.13 represents a force curve measurement cycle, from approach of the tip to the substrate surface, to the retraction where pull-on and pull-off forces are measured in segments a - d and d - h respectively. The approach curve elucidates the effect of acting attractive (vdW or hydrophobic force) or repulsive forces (EDL, hydration or steric forces) acting before contact. Pull-on force measurement occurs through the forward deflection of the cantilever, multiplied by the effective spring constant. Pull-off force can be obtained by analysis of the jump-off contact, occurring when the spring of the cantilever spring constant is greater than the gradient of the tip-substrate adhesion force. The maximum backward deflection of the cantilever is referred to as the pull-off force.(104, 228)

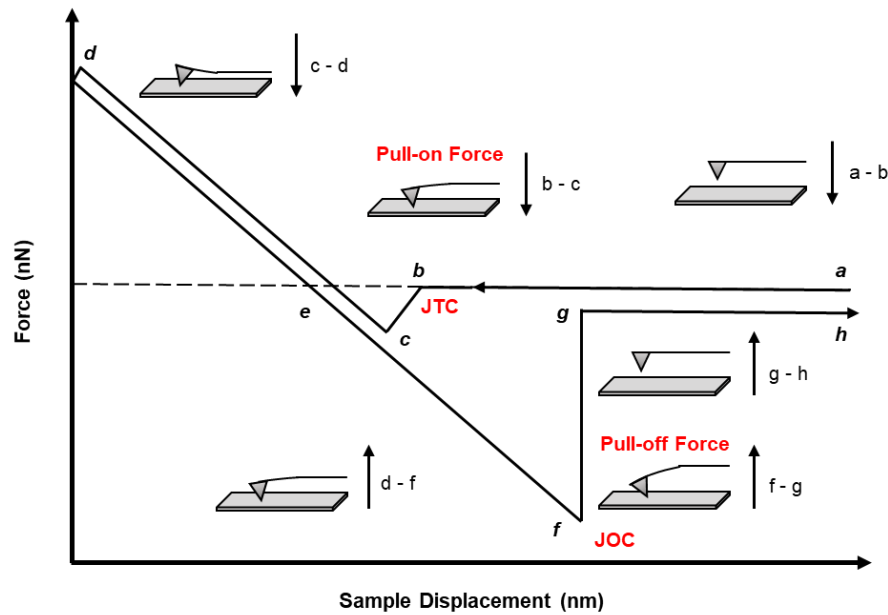


Figure 3.13 Illustration of force curve example sample displacement vs. force (104)

From Figure 3.13, points a – b show the approach of the tip to the substrate sample where distance is reduced at a constant velocity until it is brought into contact with the surface. When the force acting on the tip exceeds the stiffness of the cantilever the tip jumps to contact (JTC) the surface of the substrate (b – c). This attraction can result from interfacial forces such as van-der-Waals (vdW), capillary and hydrophobic forces, based on the interaction of the two surfaces in aqueous media. When the tip is contacted to the substrate (c – d) deflection is dominated by electronic repulsions between overlapping orbitals of the tip and sample atoms. The gradient of the curve within the contact region is a function of tip geometry and elastic modulus. Retraction of the tip from the substrate shown at d – e is the opposite of c – d, parallel when no deformation of the substrate occurs. Segment d – f shows the full retraction of the tip with adhesive bonds keeping the tip adhered to the substrate. As the tip continues to retract from the sample (f – g), the spring force of the cantilever overcomes the adhesive force and pulls off sharply, where several short and long-range attractive forces can influence adhesion.(151) At g – h the cantilever is not in contact or influenced by forces induced by the substrate.(104)

3.8.2 Mineral galena characterisation

Galena (Ward's Science, NY, USA) was fractured using a rock hammer along its naturally cleavage surface and cleaned with a N₂ stream. The cubic [001] face was identified using a hand lens prior fracture and selection of a flat fragment. Figure 3.14 shows a mineral galena specimen before fracture.(229)



Figure 3.14 Mineral galena (229)

3.8.2.1 Galena topography

Tapping mode was used to produce a topographical image of the [001] galena surface through oscillation of a Si₃N₄ AFM tip, contacting the surface intermittently in an air medium. A 2 x 2 μm image was produced through maintenance of constant tapping amplitude over the surface, whilst a second 'phase' image was recorded based on changes in the phase angle of oscillation. It was a viable means of both characterising surface roughness and topography (Figure 3.15), as well as assessing deposition of attaching PAMPS polyelectrolyte deposition.(230)

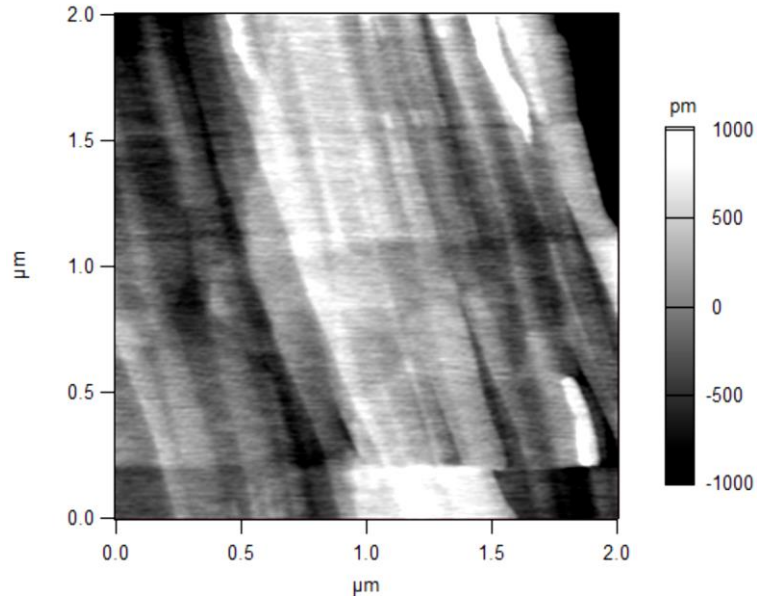


Figure 3.15 2 x 2 μm tapping mode image of cleaved galena [001] face to determine topography and RMS roughness

3.8.2.2 PAMPS adsorption

In order to assess degree of PAMPS adsorption and coverage, a soft AC240TS-R3 silicon AFM tip was used in tapping mode on the galena surface after adsorption had occurred. It was found that there was no significant change in PAMPS coverage after a time of approximately 30 minutes from a 0.5 M KCl w/ 50 mg/L PAMPS v/v solution, when compared to substrates that had been immersed in similar solution for a period of 60 and 120 minutes. Figure 3.16 and Figure 3.17 show PAMPS adsorption on the galena surface after 30 and 120 minutes respectively.

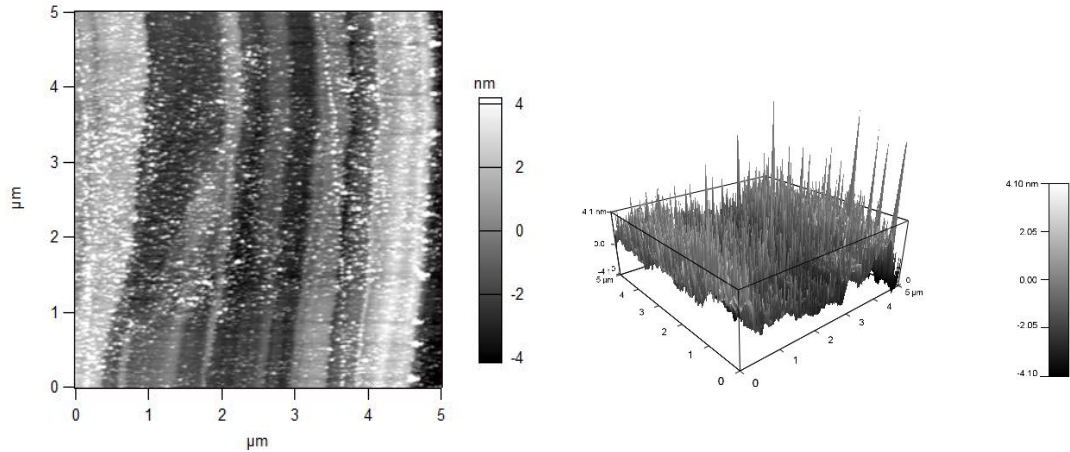


Figure 3.16 PAMPS coverage on galena after 30 min adsorption time in 50 mg/L PAMPS 0.5 M KCl solution

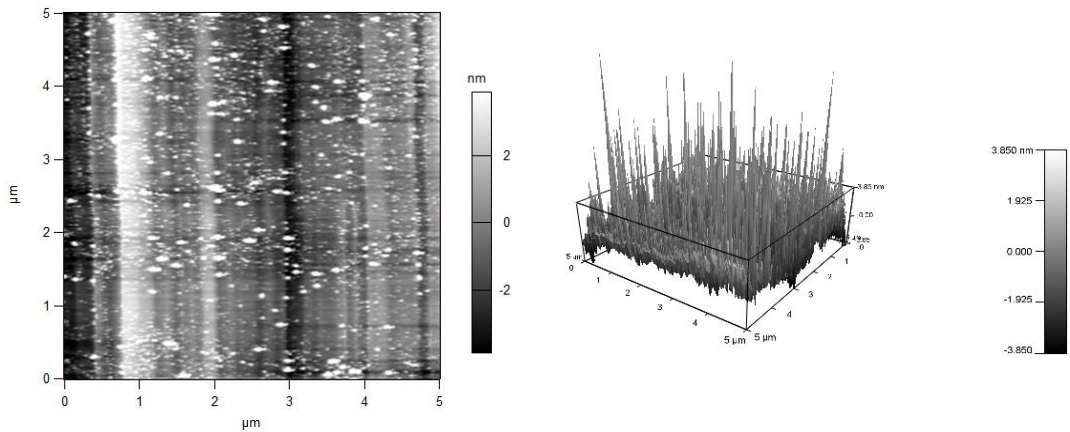


Figure 3.17 PAMPS coverage on galena after 120 min adsorption time in 50 mg/L PAMPS 0.5 M KCl solution

3.8.2.3 Galena (PbS) wettability

3.8.2.3.1 Oil-galena-water contact angle

A sealed quartz cell and an inverted sessile drop set up with an oil droplet injected into an aqueous electrolyte phase was used to study the oil droplet contact angle on a galena surface in solution, shown in the Figure 3.18. Galena (Ward's Science, NY, USA) was cleaved along the [001] plane and polished until smooth and flat along the face before being set within resin. To ensure a reduction in oxidation product formation (e.g. PbO), (231) the sample was polished using fine grade silicon carbide sandpaper to reveal an unoxidised surface, rinsed and N₂ dried before being placed immediately

within the cell containing N_2 sparged 0.5 M KCl solution (MilliQ water). The electrolyte solution pH was adjusted to 5.2, corresponding to pH used in scaling experiments and representative of sour oilfield brines, resulting in a galena surface charge of approximately -9 mV.(232)

An oil filled syringe was stoppered and inserted into the cell in such a way that ejected oil droplets would rise to the flat mineral galena surface where the oil contact angle could be imaged and analysed by the camera and software. For each measurement, oil droplet contact angles at ten different positions on the galena substrate was recorded and imaged using a camera with Attension™ software. To reduce the error attributed to variation in oil droplet volume, similar pressure was applied to the syringe when ejecting the droplet, with average contact angle extrapolated from three measurements where droplet volume was within a narrow deviation of approximately $40 \pm 2 \mu\text{l}$.

Synthetic kerosene was used as the light oil phase.

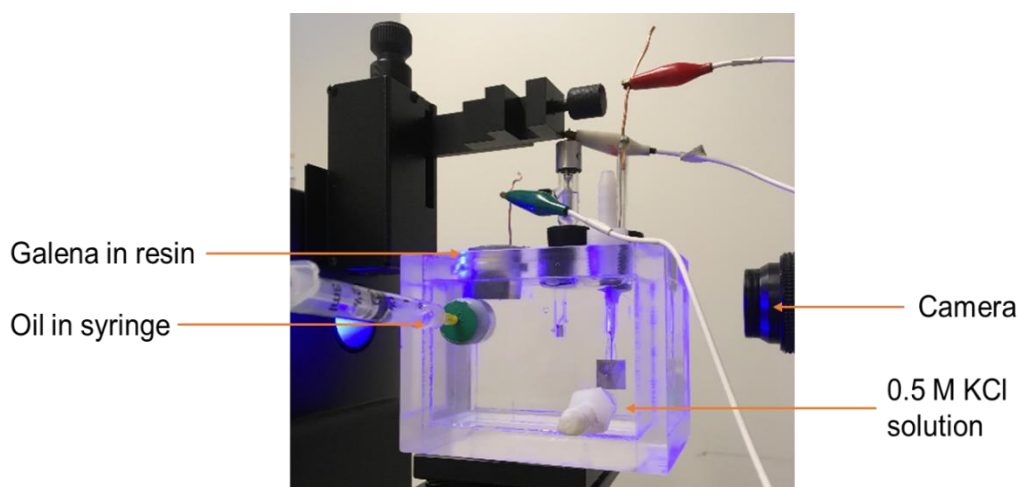


Figure 3.18 Inverse goniometer cell for oil-galena-water contact angle measurements

The cell was then filled with 0.5 M KCl w/ 50 mg/L PAMPS v/v solution and the freshly polished galena surface inserted promptly into the solution to minimise oxidation. After being immersed for 30 minutes within the solution to allow adsorption of PAMPS upon the galena surface, an $\sim 40 \mu\text{l}$ oil droplet was released from the syringe and a series of ten measurements were taken to establish the influence on average oil-galena-water contact angle.

3.8.2.3.2 Water-galena-air contact angle

Simple water-galena-air contact angle measurements were prepared using the method detailed for oil-galena-water in Section 3.8.2.3.1. Directly following polishing of the galena surface, a 40 μl droplet of 0.5 M KCl solution was placed on the surface in air and the contact angle recorded using AttensionTM software. For PAMPS functionalised galena, immersion of the resin-contained mineral for 30 minutes in N_2 sparged 0.5 M KCl w/ 50 mg/L PAMPS v/v solution was performed before removal, N_2 drying and application of a 0.5 KCl solution droplet onto the flat surface.

3.8.3 AFM tip hydrophobisation

Octadecyltrichlorosilane (OTS, $\text{C}_{18}\text{H}_{37}\text{Cl}_3\text{Si}$, 95%, ACROS organics) and toluene (C_6H_{14} , ACS reagent grade, Fisher Scientific) were used as received without further purification AFM tips were hydrophobised by way of OTS functionalization, where treatment resulted in a water contact angle of 95° .⁽¹⁵¹⁾ Tip preparation required cleaning of the Si_3N_4 tip in UV-ozone for 120 min, 30 min immersion in a 1% OTS and 99% toluene v/v solution, before rinsing with toluene/ethanol solution; sonication in MilliQ water and drying with N_2 prior to force curve measurements. Water contact angle of the treated tip was established after simultaneous OTS functionalization and sessile drop analysis of a glass slide treated in conjunction with the above method.

3.8.4 AFM solution preparation

Potassium chloride (KCl, ACS reagent grade, Fisher Scientific), was heated to 400°C to achieve complete purification before use. 0.5 M KCl electrolyte solution was then prepared in MilliQ water and pH adjusted to 5.2 using HCl and KOH as buffer solutions. A high electrolyte concentration was required to compress the electrical double layer (EDL) barrier, thus enabling attractive forces i) vdW; and ii) hydrophobic; to become dominant between the AFM tip and PbS substrate. Use of electrolyte solution was necessary due to the nature of the scaling work that simulated particle deposition in high salinity oilfield brines. For experiments where the cleaved galena surface was functionalised with PAMPS polyelectrolyte, freshly cleaved galena was cleaned with an N_2 stream and attached to the bottom of a sterile petri-dish with nail varnish before 0.5 M KCl w/ 50 mg/L PAMPS solution was introduced into the dish in order to fully submerge the mineral. Allowing 30 min for the [001] galena face to become fully covered with polyelectrolyte before

adsorption onto the surface started to plateau as equilibrium was reached, a syringe was used to extract the polyelectrolyte solution before 0.5 M KCl solution (no PAMPS) was re-introduced into the petri-dish immediately after. This enabled irreversible PAMPS adsorption upon the galena surface before force curve measurements were carried out, but removed high MW polyelectrolyte from the solution that could have adversely affected the accurate measurement of interfacial forces e.g. trapping and compression of polymer chains between tip and substrate.

3.8.5 AFM force curve measurements

Experiments were performed on a freshly cleaved galena substrate immersed in 0.5 M KCl using a MFP-3D AFM instrument (Asylum Research, Santa Barbara, CA, USA). AFM tips of pyramidal geometry were assumed to be conical in shape with a spherical cap at the apex.⁽²³³⁾ The geometry of Si₃N₄ AFM tips was determined by Field Emission - Scanning Electron Microscopy (FE-SEM) on a JAMP-9500F Field Emission Auger Microprobe (JEOL, MA, USA). ImageJ software was used to determine the radius of spherical cap R and the geometry angle of the spherical cap α . R was determined to be 32.5 ± 10 nm, and α was measured as $\sim 65 \pm 1^\circ$, based on Figure 3.19.

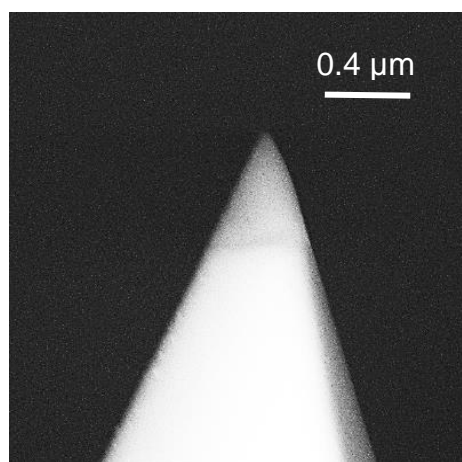


Figure 3.19 FE-SEM image of Si₃N₄ tip where R was determined to be 32.5 ± 10 nm

Constant velocity and loading force of $0.1 \mu\text{m/s}$ and 10 nN respectively were used for force measurements, with the tip driven to approach and then retract from the surface, with the 'jump-in' force measured on the tip approach. The

spring constants of the cantilevers used were determined to be 0.1 - 0.2 N/m using the Hutter and Bechhoefer method.(234) Measurements were recorded in 10 different areas upon each galena substrate, with 2 separate surfaces tested for each condition. Calculations for both attractive vdW and hydrophobic force (F_{HB}) can be seen in Equation 3.7 and Equation 3.9 respectively.(151)

Equation 3.7

$$F_{vdW} = \frac{A_H}{6} \left[\frac{R+D-2L_1}{L_1^2} - \frac{R-D}{D^2} \right] - \frac{A_H}{3 \tan^2 \alpha} \left(\frac{1}{L_1} + \frac{R \sin \alpha \tan \alpha - D - R(1 - \cos \alpha)}{2L_1^2} \right)$$

Equation 3.8

$$L_1 = D + R(1 - \cos \alpha)$$

Equation 3.9

$$F_{HB} = -CRe^{-D/D_0}$$

Equation 3.10

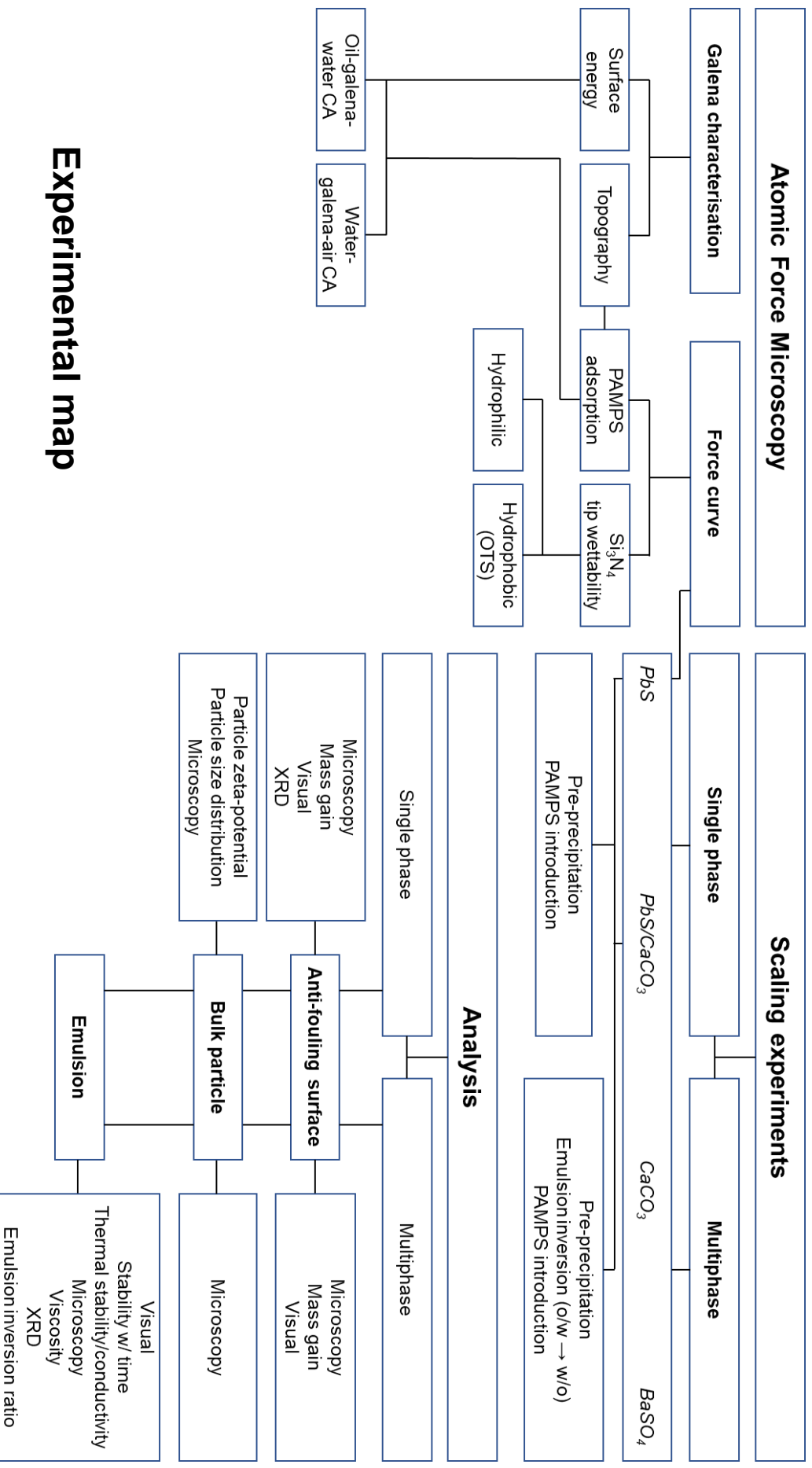
$$C = 2\pi\gamma(1 - \cos \theta)$$

The attractive vdW force between AFM tip and galena substrate (F_{vdW}), given by Equation 3.7, where the non-retarded Hamaker constant (A_H), used to analyse the measured forces between an Si_3N_4 tip and a galena surface was 6.3×10^{-20} J for Si_3N_4 -water-PbS.(151) D is the separation distance (m) from the tip to the substrate and L the distance (m) between a differential surface section of the tip and substrate (Equation 3.8).(235) Hydrophobic force (F_{HB}) followed an exponential equation (Equation 3.9), where D_0 is the decay length (nm) of hydrophobic interaction and C (N/m) is a constant (Equation 3.10).(146, 236-238) γ is the interfacial energy (mJ/m^2) and θ is static water contact angle ($^\circ$). From recorded adhesion force (nN) upon tip retraction, the measured adhesion could be calculated (Equation 3.11). F_{adh} is adhesion force and R is the AFM tip radius.

Equation 3.11

$$\text{Measured adhesion} = F_{adh}/R$$

Force (nN) vs. distance (m) data was then plotted, from experimental data and theoretical values based on vdW and hydrophobic forces.



Experimental map

Chapter 4

Scale Behaviour and Deposition in Single Phase Flow: Calcium Carbonate (CaCO₃), Barium Sulphate (BaSO₄) and Lead Sulphide (PbS) Systems

The proliferation of inorganic mineral scale is a cause for concern in a number of industries, with anti-fouling surfaces now being more routinely applied in conjunction with chemical treatments in order to control the initial nucleation of crystals upon substrates. Whilst single phase conditions where no oil is present are rare in producing oilfield wells (though can occur potentially as the result of cross-flow from a high pressured wet region that can be remedied by a cement squeeze job), these tests help to identify and compare the nucleation mechanisms of different scale species under simple conditions.(239) The scaling tendency of simple CaCO₃, BaSO₄ and PbS forming brines and their nucleation both in the bulk phase and onto substrates of varying wettability was explored. PbS particle adhesion was of particular interest, with AFM force curve analysis of hydrophilic and hydrophobic AFM tips (representative of anti-fouling surfaces) contacting a freshly cleaved galena (mineral form of PbS) surface to assess the role of attractive interfacial interactions in scale adhesion. PbS and CaCO₃, scales that often occur in tandem in oilfield wells where sulphides are present were precipitated simultaneously to assess the effects of co-precipitation on nucleation and deposition.(45) Eight coatings were tested preliminarily in simple scaling tests to establish a correlation between coating characteristics and deposition. Testing in complex solutions, e.g. PbS/CaCO₃ systems, was undertaken later in the process with coatings that had already been selected for field trials.

4.1 CaCO₃ deposition

In simple carbonate systems (Brine A), calcite crystals can be seen to precipitate heterogeneously upon anti-fouling surfaces, characterised by clearly defined rhombohedral morphologies up to 20 µm in diameter emanating from the substrate. Large halite (NaCl) crystal deposits acted as nucleation sites for secondary calcite precipitation, as seen on coupon F2 in Figure 4.2. Homogeneous nucleation in the bulk and consequent adhesion was assumed to have been negligible due to the relatively low CaCO₃ SR_{initial} of 76, where surfaces induced nucleation at degrees of super-cooling lower

than those required for spontaneous nucleation. SEM images in Figure 4.2 show little evidence of homogeneous deposition, where calcite crystals appear to have nucleated either directly on the substrate or as a result of secondary nucleation where amorphous shaped deposits appear to over. Whilst rhombohedral calcite is clearly present on all surfaces, there is a large degree of amorphous calcium carbonate (ACC) on the surface that has no defined shape. ACC is a metastable precursor to calcite that frequently forms in highly supersaturated solutions, its presence indicative of CaCO_3 in which physisorbed H_2S is below the critical level. As such, removal from solution and drying under a N_2 stream before desiccation and SEM imaging may well have enabled the maintenance of ACC on the coupon surface.(240, 241)

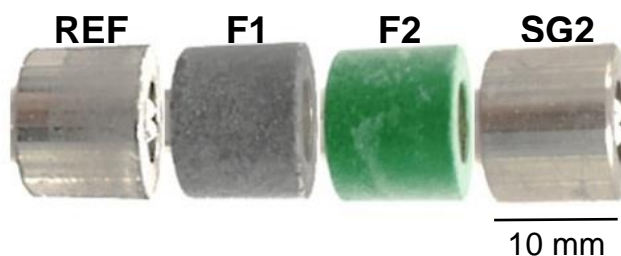


Figure 4.1 Photographs of samples – CaCO_3 single phase conditions

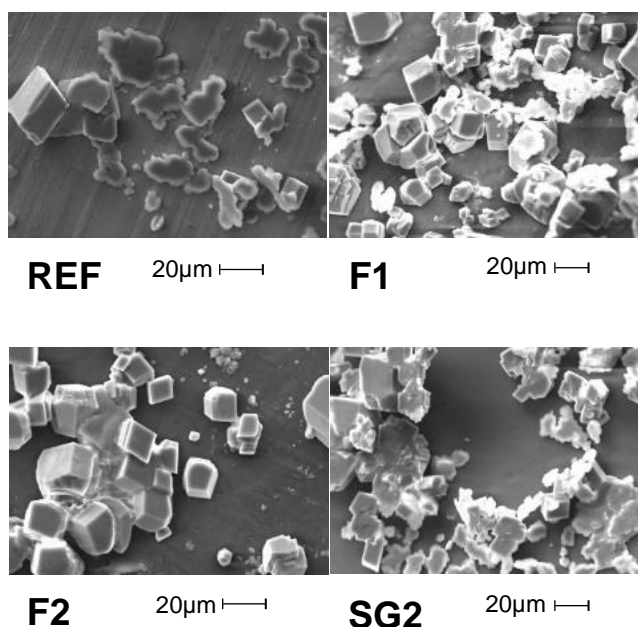


Figure 4.2 SEM images – CaCO_3 single phase conditions

From Figure 4.3, it can be seen there is no correlation ($R^2 = 0.19$) between water contact angle and mass gain upon surfaces, with fluoropolymer

surfaces showing a higher degree of surface scaling density. Fluoropolymers tend to have rougher surfaces as a consequence of application and finishing procedures, providing an increased number of potential nucleation sites, resulting in higher surface scale coverage in single phase systems. The smoothest fluoropolymer F2 had an average roughness (S_a) of $0.93\ \mu\text{m}$, whereas REF and DLC coatings had and S_a of $0.01\ \mu\text{m}$. This can be seen in work by Charpentier et al. (16), where fluoropolymer surfaces undergo significant scaling in turbulent, single phase carbonate and sulphate systems. The hydrophobic surface may encourage the formation of CaCO_3 -substrate bonds over that of solution-substrate bonds due to a reduction in wettability, and hence decreased net surface free energy of the CaCO_3 solution-substrate system, as demonstrated by Equation 2.28.(132)

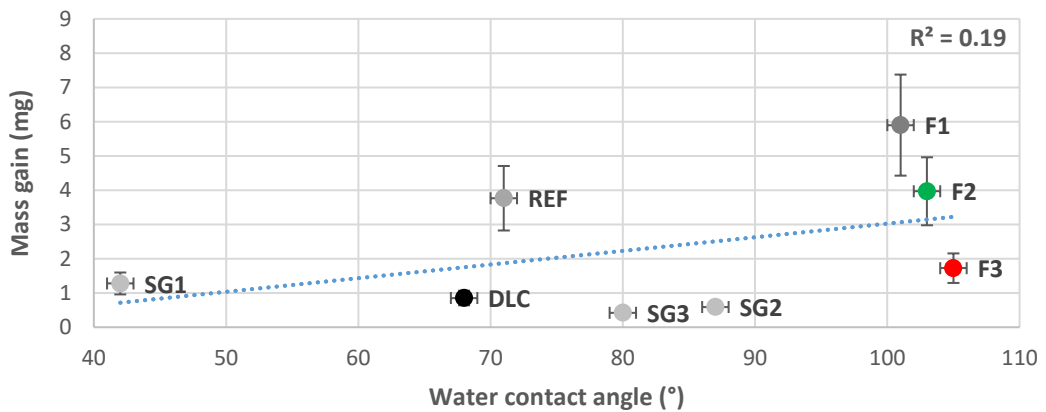


Figure 4.3 Water contact angle vs. mass gain – CaCO_3 single phase conditions

4.2 BaSO_4 deposition

In simple sulphate forming systems (Brine B), EDX analysis (Figure 4.6) showed barium (Ba) and strontium (Sr) containing species had precipitated heterogeneously upon the surface, measuring approximately $1\ \mu\text{m}$ diameter with surface coverage close to 100% in single phase systems (Figure 4.5). It has been reported in numerous field studies that Sr co-precipitates with Ba to form BaSO_4 and SrSO_4 scale, where SrSO_4 contents were between 1.2 and 15.9 percent and BaSO_4 varied from 63.7 to 97.5 percent. The $\text{SR}_{\text{initial}}$ of BaSO_4 in experiments described in Table 3.6 based off field water chemistry data is usually a few degrees of magnitude higher than that of SrSO_4 (1888 and 5 in tests described in this section respectively). Consequently, the

frequent precipitation of BaSO_4 is far more feasible thermodynamically, with tests by Weintritt and Cowan (242) showing that the Sr ion co-precipitated into the BaSO_4 lattice and was not found as SrSO_4 as a distinct crystal species.(242, 243)The high $\text{SR}_{\text{initial}}$ of BaSO_4 compared to CaCO_3 (1888 and 76 respectively) resulted in smaller stable crystal size and a higher degree of homogeneous nucleation and adhesion, where spontaneous bulk nucleation was more thermodynamically viable than in CaCO_3 forming systems. Overlying clustered homogeneously precipitated BaSO_4 and SrSO_4 of snowflake-like appearance were visible upon REF, F1 and F2 coupons from SEM images in Figure 4.4. Though barite is the only polymorph of the BaSO_4 crystal, it can exist in a number of morphologies that are highly dependent on saturation ratio and temperature.(31) Low SR (< 50) typically resulted in rectangular platelets that exhibited clear pyramidal growth, with increasing supersaturation (> 2500) resulting in a loss of preferential growth direction and irregular plate-like shape, as seen clearly in Figure 4.5.(31)

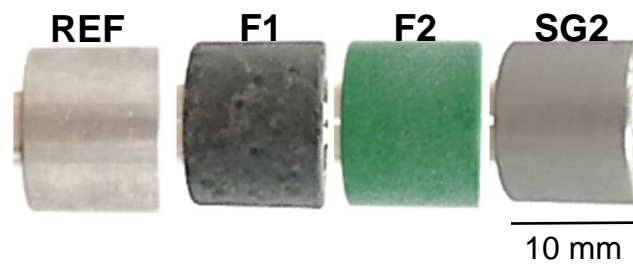


Figure 4.4 Photographs of samples – BaSO_4 single phase conditions

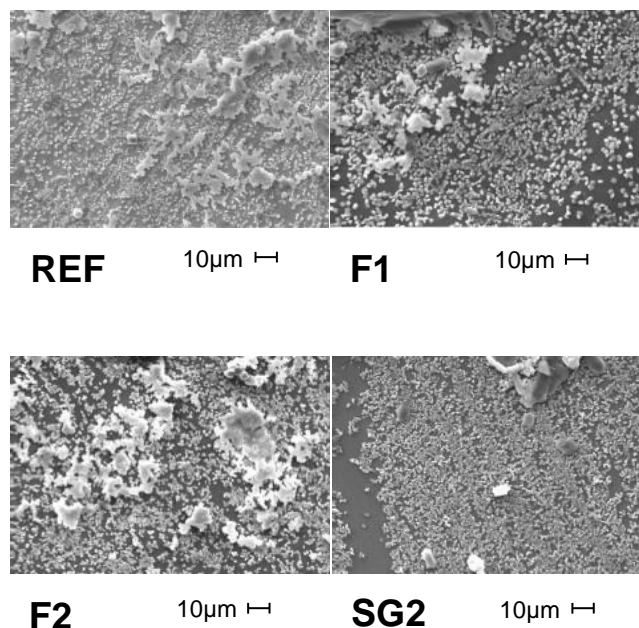


Figure 4.5 SEM images – BaSO_4 single phase conditions

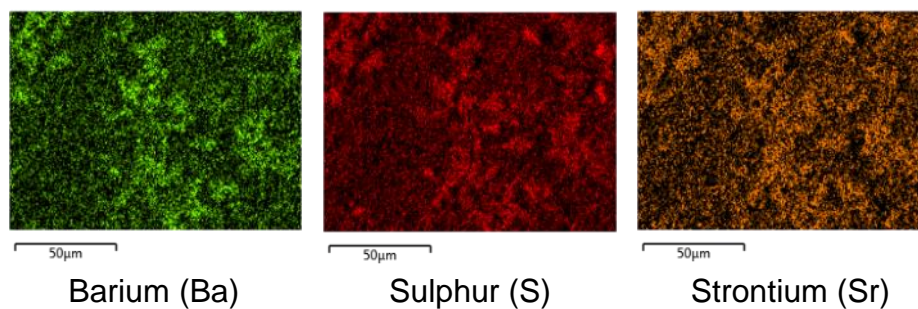


Figure 4.6 EDX analysis of REF coupon showing extensive presence of Sr, likely incorporated into the BaSO₄ lattice

From Figure 4.7, there is no real correlation between coating water contact angle and mass gain ($R^2 = 0.12$). All surfaces show near total surface coverage, though due to small crystal size the mass gain seen on surfaces is comparatively lower than with CaCO₃ deposits. The anti-fouling characteristics of surfaces e.g. wettability, are negated after formation of a single layer of sulphate crystals on the substrate, resulting in homogeneous deposits adhering from the bulk solution on all surfaces. As such, mass gain on all substrates was recorded to be between 0.13 and 0.4 mg/cm².

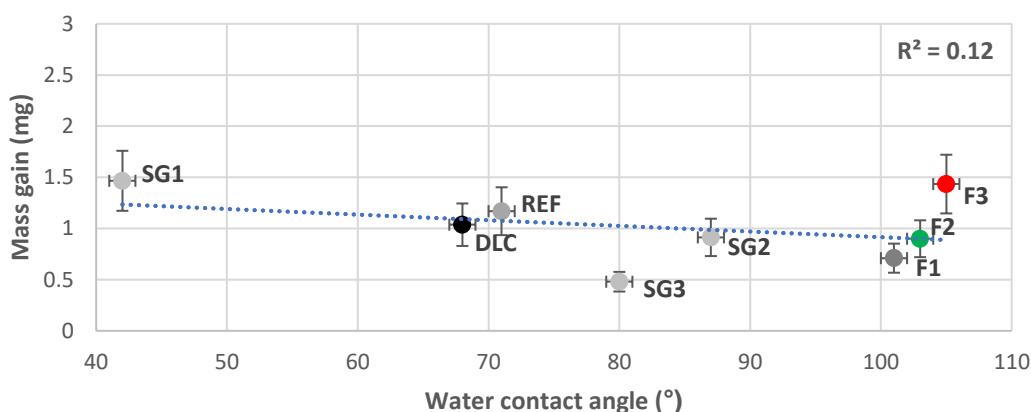


Figure 4.7 Water contact angle vs. mass gain – BaSO₄ single phase conditions

4.3 PbS deposition

As a consequence of the exceedingly high $SR_{initial}$ of 1.7×10^{19} for PbS in the system, scale precipitation occurred spontaneously within the homogeneous phase, with the rate-limiting step the gradual absorption into the aqueous

phase and consequent dissociation of H_2S to form aqueous HS^- anions. The rate of PbS precipitation could be gauged through the darkening of the reaction solution over the course of the experimental run time, becoming an opaque black color after approximately 15 minutes over the course of 1 hour as a result of the dark black appearance of the precipitating PbS nanoparticles. Any homogeneously precipitated PbS scale that therefore deposited onto a surface did so by way of adhesion as opposed to direct heterogeneous nucleation, with agglomerates attaching to surfaces through turbulent and gravitational deposition.(244) Loose deposits of PbS formed through aggregation of individual particles within the bulk phase are associated with lower adhesion rates to the surface than individual nanoparticles due to the reduction of contact area to volume ratio and consequent removal in turbulent flow.(140) Agglomerates show increased detachment rates from the substrate, likely due to turbulence and high shear flow at the interface, where the dimensionless Reynolds number (Re) is 3374 at rotary speeds of 400 rpm.(129) Figure 4.8 displays images of the anti-fouling coatings after removal from the reaction vessel post-experiment, with negligible PbS deposition on all surfaces, as seen on SEM images in Figure 4.9.

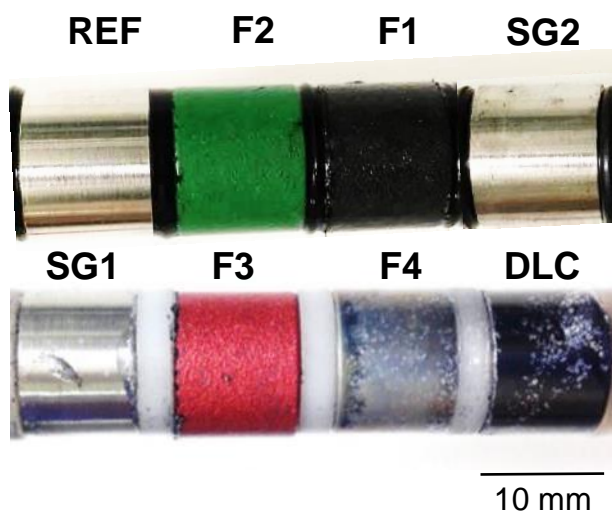


Figure 4.8 Photographs of samples – PbS single phase conditions

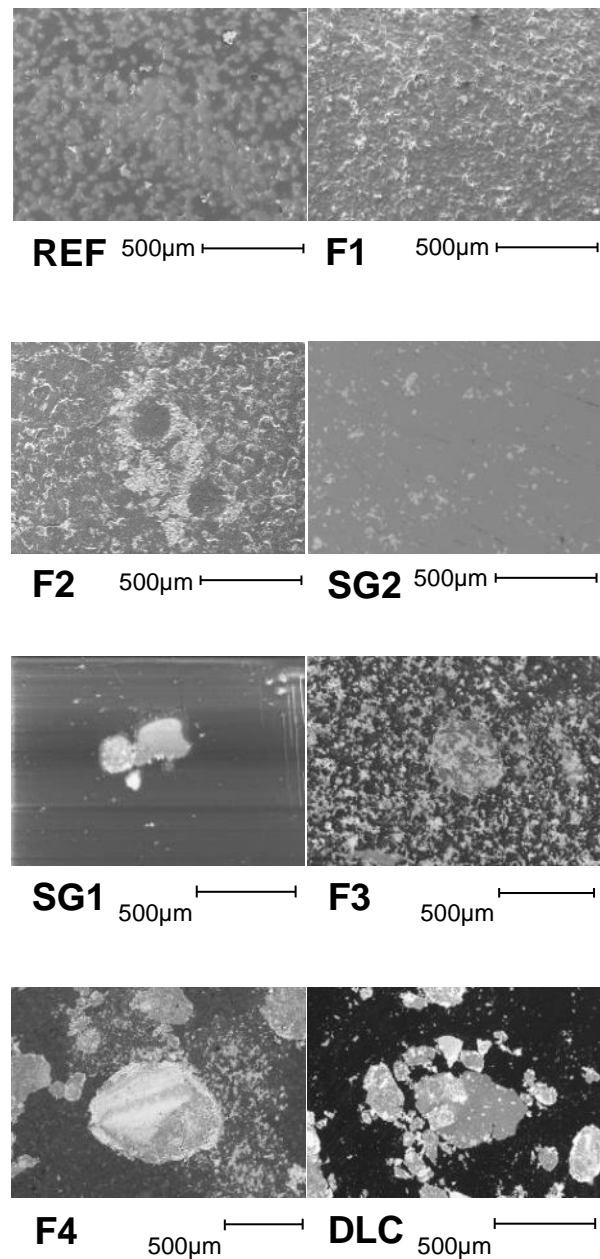


Figure 4.9 SEM images – PbS single phase conditions

From Figure 4.10 it can be seen there is a degree of correlation between mass gain and wetting properties of the anti-fouling surfaces, though very little overall deposition was seen. As deposition within the PbS system is adhesion driven, surface wettability has less influence in a single-phase system due to the low adherence of loose agglomerates; with topographical parameters such as average roughness (S_a) likely to have greater significance. Hydrophobic fluoropolymers see a higher degree of adhesion, thanks in part to the effect of attractive interfacial forces stemming from the hydrophobic interaction between the substrate and the partially hydrophobic PbS. Work by Charpentier et al. (16) shows that whilst turbulent flow conditions on a surface

significantly increase scale build-up in precipitating carbonate and sulphate systems, primarily due to the increased transport and availability of solute ion embryos at the sample surface and heterogeneous crystal interface; anti-fouling surfaces immersed in pre-precipitated carbonate and sulphate scaling brines under identical flow conditions show comparably negligible mass gain. Additionally, when adhesion of particles precipitated in the bulk phase is the sole mechanism for deposition, it has been shown that laminar flow ($Re < 300$) results in higher surface mass gain due to a reduction of the critical shear stress required for removal of loose agglomerates at the adhering surface.(16) Hydrophilic substrates were shown to accumulate $< 0.05 \text{ mg/cm}^2$ of PbS scale, whilst hydrophobic surfaces typically saw $0.11 - 0.16 \text{ mg/cm}^2$ of scale deposit.

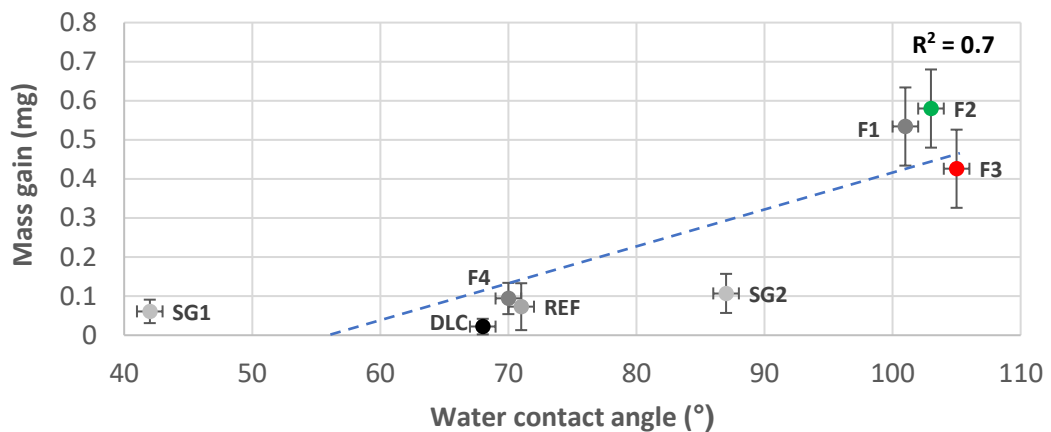


Figure 4.10 Water contact angle vs. mass gain – PbS single phase conditions

4.4 PbS characterisation

PbS nanocrystals were prone to agglomeration in aqueous solutions as a consequence of attractive vdW forces coupled with limited electrical double layer (EDL) repulsion, where the zeta potential (ZP) of nanoparticles at pH 5.2 was measured to be -9 mV .(232) Figure 4.11 shows the post-experimental brine, where loose PbS agglomerates formed within the bulk phase have settled at the bottom of the vial through gravitational deposition.(54)

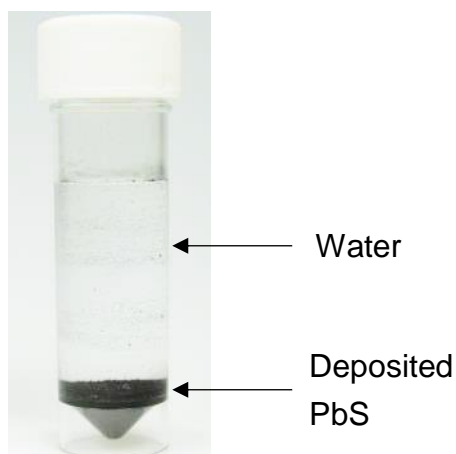


Figure 4.11 Post-experiment – PbS single phase conditions

Analysis of precipitated PbS nanocrystals revealed the formation of large agglomerates, ranging from 0.5 – 3 μm in diameter (Figure 4.12a & b). Individual crystals of galena precipitated in the homogeneous single aqueous phase were of cubic morphology and ranged from 30 – 60 nm in diameter, as represented in Figure 4.12c & d. The PbS particles formed were therefore within the range of 20 – 100 nm, as reported by Andritsos and Karabelas for spontaneous nucleation.⁽⁶⁵⁾ The very high saturation ratio of PbS in the experimental system described in Section 3.5.1 where SR_{Initial} is 1.7×10^{19} , likely results in different growth velocities at crystal faces. This leads to curving of crystal edges and the formation of rounded rectangle to spherically shaped crystals, in contrast to CaCO_3 crystals and PbS crystals grown at lower supersaturations that are characterised by sharp, clearly defined edges due to significantly slower growth rates at lower supersaturation.⁽³¹⁾

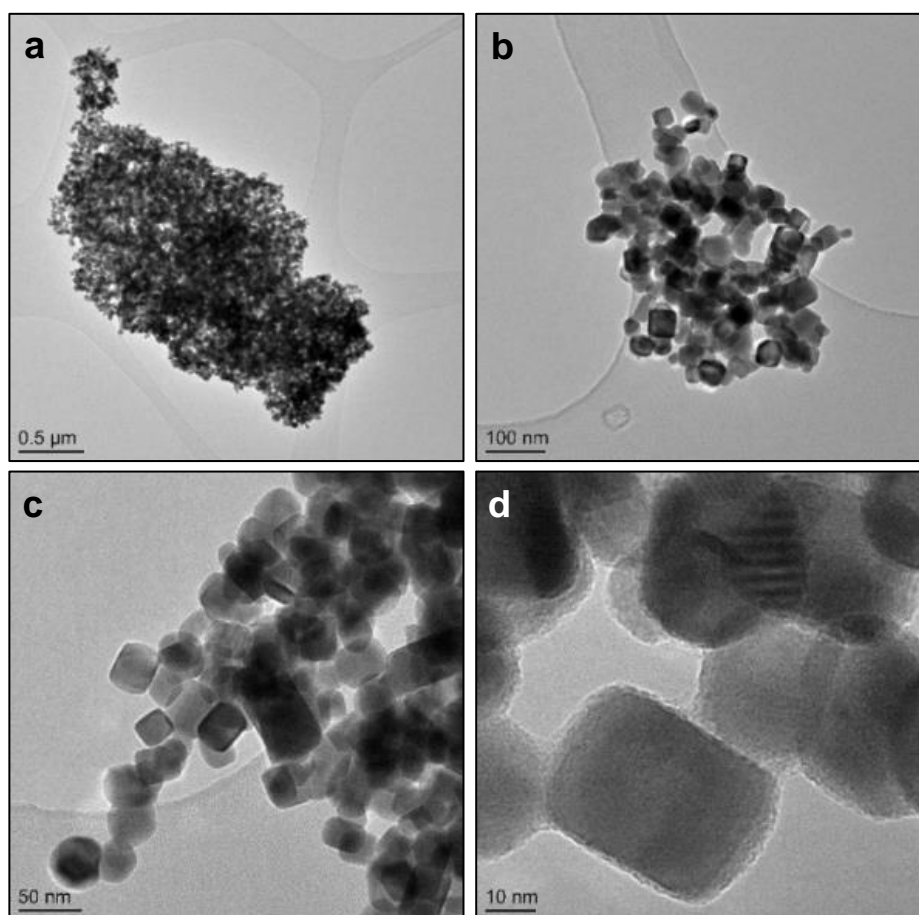


Figure 4.12 TEM images of precipitated PbS crystals

XRD analysis of PbS nanoparticles revealed that no undesirable oxidation products were present, indicating negligible oxidation had occurred, where spectra for PbS corresponding well with those found in literature for unoxidised PbS surfaces (Figure 4.13).⁽²⁴⁵⁾ Anglesite (PbSO_4), one of the primary oxidation products that has the potential to form upon the galena surface in weakly acidic conditions, though was not present in Figure 4.13.

Under downhole conditions there is usually a negligible concentration of dissolved oxygen, with injected seawaters used as part of secondary recovery techniques being treated thoroughly to ensure there is less than 0.01 ppm O_2 where H_2S is present.⁽²⁴⁶⁾ As such, precipitated PbS nanoparticles were kept in a desiccator after extraction from the reaction vessel, and galena used in AFM force curve experiments was freshly cleaved and immersed in solution.

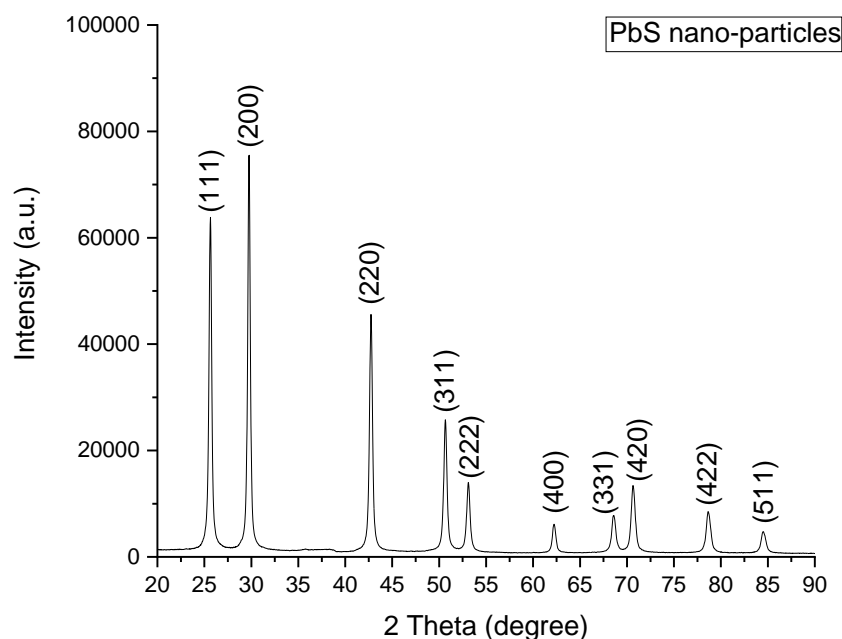


Figure 4.13 X-Ray Diffraction spectra of PbS nanoparticles

4.4.1 Mineral galena and synthetic PbS differences

Leiro et al.(247), after conducting XPS and AFM experiments on natural and synthetic galena samples, found negligible difference in surface oxidation behaviour, where both surfaces are relatively inert in air at short exposure times. Small differences were shown in the surface core level shift, i.e. the difference in electron binding energy between the surface and bulk atoms, between the two specimens. These were attributed to the deviation in relaxation and reconstruction of the surface, due to the influence of impurity atoms in the mineral galena.(247) Results and conclusions derived from analysis of mineral galena could therefore justifiably be used to explain phenomena observed from experiments with synthetic galena, due to their near identical properties and characteristics.

4.5 PbS adhesion

4.5.1 AFM force curve analysis

Force curve analysis of a freshly cleaved galena surface in 0.5 M KCl solution against untreated and OTS treated Si_3N_4 AFM tips, where water contact angle

was 5 and 95° respectively, provided insight into the various interfacial forces present upon interaction of PbS nanoparticles with various anti-fouling substrates. As a consequence of the partial hydrophobicity of PbS, hydrophobic force was expected to be the primary contributor to the higher degree of attraction and hence mass gain seen on hydrophobic surfaces F1, F2 and F3 in Figure 4.10.

4.5.2 Topography of galena

From tapping mode analysis of a freshly cleaved galena surface (Figure 4.14), the RMS roughness over a 2 x 2 μm area was determined to be 503 picometres (pm), smooth enough to ensure that force curve measurements were not affected by uneven topography that would likely disrupt molecular ordering at the interface.(248)

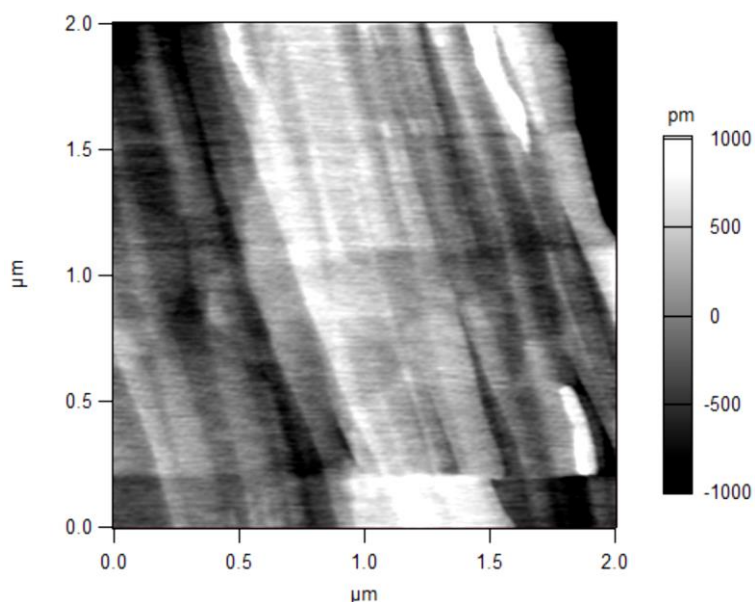


Figure 4.14 AFM contact mode image of cleaved galena [001] face – RMS roughness of 503 pm

4.5.3 Interfacial forces in PbS deposition

Figure 4.15a displays the approach of a hydrophilic tip on the galena substrate, where small but observable Si₃N₄ tip ‘jump-in’ was measured. Force at a distance of 4 nm becomes slightly negative, a result of vdW attraction on AFM tip approach to the substrate (calculated using Equation 3.7), fitting well with theoretical DLVO predictions (highlighted green) where the tip is strongly hydrophilic, representative of a hydrophilic coating e.g. REF, DLC. Jump-in was recorded at a separation distance of ~4 nm, with measured

adhesion upon retraction (pull-off force) of 26.7 ± 2.4 mN/m. No hydrophobic attraction force is present due to the highly hydrophilic Si_3N_4 tip.(249)

Figure 4.15b shows the effect of both vdW attraction and hydrophobic force (F_{HB}) after OTS hydrophobisation of the Si_3N_4 tip, representative of a hydrophobic surface e.g. F1 or F2, where experimental results are shown in open symbols, and extended DLVO calculations by the red curve (calculated using Equation 3.9). Based on galena surface energy of 38.03 mJ/m² and measured static water contact angle of unoxidised galena 49° , constant C was calculated to be 0.268 Nm/N.(250) As such, the decay length was approximated at 0.9 nm in 0.5 M KCl solution, corresponding well with the available literature.(151) Experimental data matches well with theoretical extended DLVO predictions where jump-in occurs at a separation distance of 9 nm and measured adhesion (F_{adh}/R) upon retraction was 62.1 ± 4.7 mN/m.

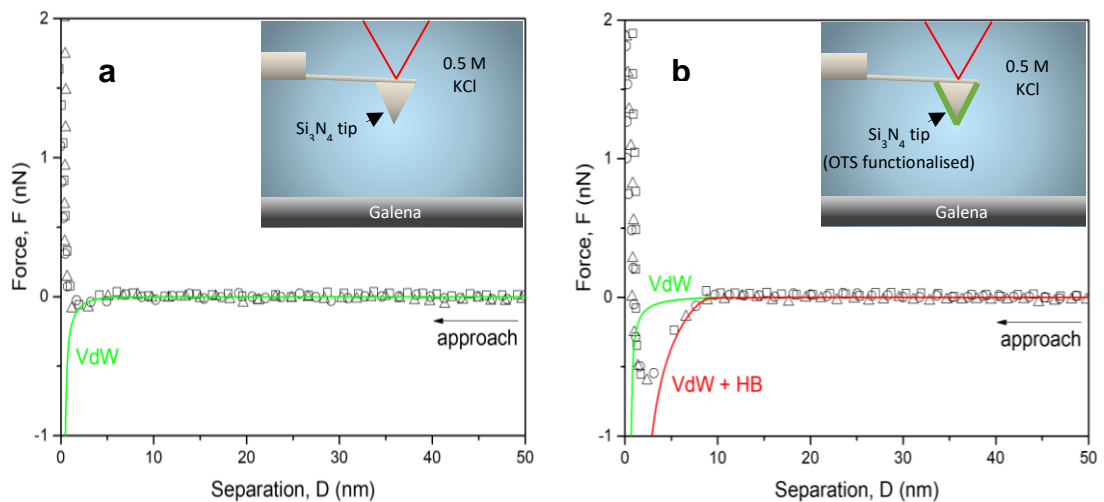


Figure 4.15 Force curve approach – a) Untreated Si_3N_4 tip - hydrophilic and galena substrate; b) Si_3N_4 (OTS treated) tip - hydrophobic and galena substrate

Both jump-in and pull-off force for the hydrophilic and hydrophobic surface condition are good indicators of the degree of attractive forces between galena and substrates of varying wettability. It can be inferred that adhesion of deposited partially-hydrophobic PbS particles to a hydrophobic substrate will be significantly higher than that on a hydrophilic substrate of identical smoothness. Measured adhesion was 26.7 ± 2.4 mN/m and 62.1 ± 4.7 mN/m on hydrophilic and hydrophobic surfaces respectively (Equation 3.11).

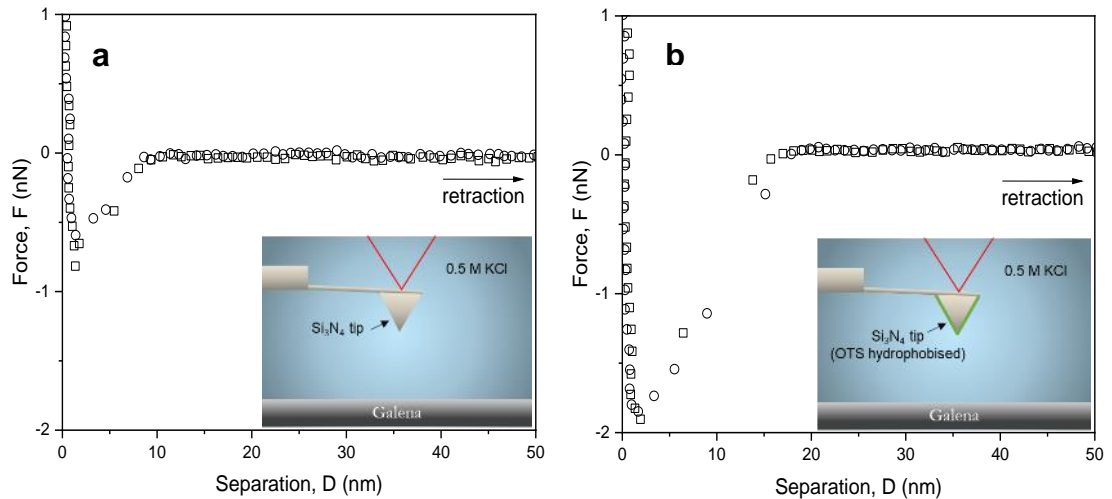


Figure 4.16 Force curve retraction – a) Untreated Si_3N_4 tip - hydrophilic and galena substrate; b) Si_3N_4 (OTS treated) tip - hydrophobic and galena substrate

Through force curve measurements, it can be shown that partially hydrophobic PbS exhibits a higher degree of interfacial attraction towards hydrophobic surfaces due to the additional effect of the hydrophobic force. Though literature exploring the nature of the hydrophobic force has not reached a definitive consensus, recent studies support the influence of gas molecules near the hydrophobic surfaces instantaneously forming a gaseous capillary where the barrier to nucleation was low.(225) This is demonstrated empirically in Figure 4.10 where hydrophobic fluoropolymers F1 and F2 see a higher degree of scaling than the hydrophilic coupons REF and DLC.

Whilst fundamentally the effect of hydrophobic force between PbS particles and the hydrophobic substrate is expected to result in higher degrees of homogeneous deposition on surfaces, the complex influence of substrate roughness for different anti-fouling surfaces is more difficult to quantify. Roughness parameters, such as asperity kurtosis, height, skewness, spacing etc. can contribute to the density of hooking sites that promote mechanical interlocking of particles on the substrate and ultimately adhesion.(142)

4.6 PbS/ CaCO_3 single phase

Figure 4.17 shows the deposition of CaCO_3 and PbS upon the anti-fouling coupons in single phase conditions. From Figure 4.18 it can be seen that calcite deposits of truncated octahedron morphology have nucleated heterogeneously upon substrates, with PbS agglomerates dispersed across

the surface of the substrate and upon calcite crystals, having adhered from the bulk solution after calcite growth.(251)

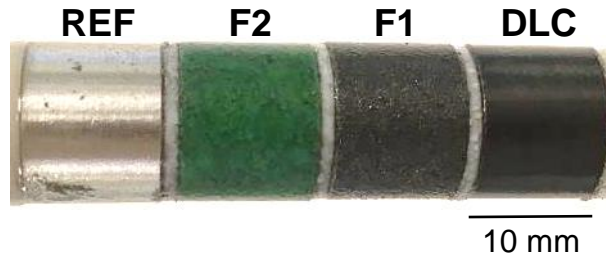


Figure 4.17 Photographs of samples – PbS/CaCO₃ single phase conditions

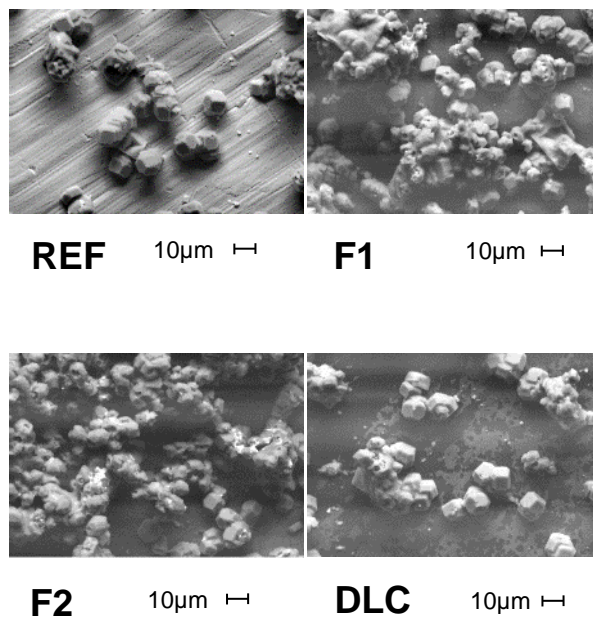


Figure 4.18 SEM images – PbS/CaCO₃ single phase conditions

Similar observations were made by Okocha et al.(19), where Pb²⁺ and CaCO₃ co-precipitation resulted in the formation of truncated octahedron shaped calcite, with no indication that the precipitated PbS acted as a point of seeding for nucleation in the bulk phase when CaCO₃ was later co-precipitated with PbS particles. In this system, as a result of the rate-limiting dissociation of the H₂S gas into the aqueous phase, unreacted free Pb²⁺ ions were initially present in solution during calcite precipitation. It is likely that Pb²⁺ ions incorporate into the forming calcite lattice, inhibiting the growth of rhombohedral crystals that were observed in solely CaCO₃ forming systems.(197)

Figure 4.19 shows a reasonable correlation between water contact angle and mass gain where $R^2 = 0.88$. The nature of CaCO_3 scaling results in high mass gain where heterogeneous growth can occur on substrates regardless of wettability. More extensive scaling occurs on fluoropolymer coatings due to the higher roughness and hence frequency of nucleation points, as well as the favouring of formation of CaCO_3 -substrate bonds over solution-substrate bonds as a result of increased net surface energy with decreased substrate wettability.(132)

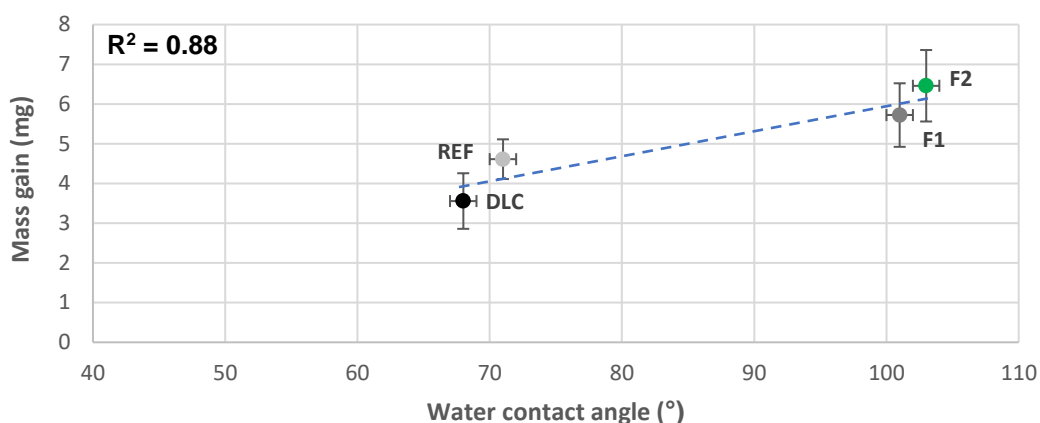


Figure 4.19 Water contact angle vs. mass gain – PbS/CaCO_3 single phase conditions

4.7 Chapter Summary

Whilst single phase conditions are rarely representative of down hole conditions due to the absence of a produced oil phase, these tests illuminated the mechanism by which different scale species form and grow upon different anti-fouling substrates.

Upon mixing of CaCO_3 forming carbonate brines, where SR_{initial} was 76, crystallisation occurred heterogeneously upon substrates, where surfaces provided a lower energy path to nucleation than that of the bulk phase. As such, heterogeneous calcite nucleation was observed on all substrates regardless of wettability. High solution cloudiness and measured turbidity of >500 NTU after 1 min indicated that while heterogeneous crystallisation was the primary driving force for deposition, homogeneous nucleation of CaCO_3 occurred readily within the bulk phase. This was either caused by spontaneous nucleation and formation of CaCO_3 solutes above the critical

radius, or by seeding from calcite nuclei that would otherwise have incorporated into a heterogeneously precipitated calcite crystal displaced as a result of high shear flow.(35)

There was no correlation between coating water contact angle and mass gain from Figure 4.3, where the disparity in surface mass gain between hydrophobic coatings of similar wettability was 1.6, 1.1, 0.5 mg/cm² on F1, F2 and F3 coatings respectively, highlighting the importance of surface roughness in calcite crystallisation. Additionally, hydrophobic surfaces may have encouraged the heterogeneous nucleation of calcite when compared to hydrophilic surfaces, where formation of CaCO₃-substrate bonds were favoured over that of solution-substrate bonds.(132)

Sulphate scale forming solutions resulted in heterogeneous crystallisation on all anti-fouling surfaces, where surface coverage was > 95% and no correlation seen between water contact angle and mass gain ($R^2 = 0.12$). Whilst the high $SR_{initial}$ of BaSO₄ (1888) resulted in significant homogeneous bulk nucleation as determined by turbidity measurements of > 500 NTU, the presence of a foreign substrate prompted nucleation of a monolayer of small barite crystals, approximately 1 µm in diameter. The limited growth of surface nucleated barite resulted in less mass gain upon substrates when compared to calcite, where the mass of deposit on the REF coupon was 0.32 mg/cm² and 1.0 mg/cm² for a BaSO₄ and CaCO₃ respectively.

The mechanism of mineral deposition in PbS scaling systems was generally easier to characterise due to the absence of heterogeneous nucleation and growth of crystals directly onto anti-fouling substrates. The level of PbS supersaturation ($SR_{initial} = 1.7 \times 10^{19}$) resulted exclusively in spontaneous nucleation within the bulk phase of the solution. As such, any PbS adhesion that occurred did so by way of adhesion of agglomerates from the bulk phase, often a result of turbulent activity at the solid-liquid interface and the influence of interfacial forces binding the deposit to the substrate. From Figure 4.10, it could be seen that though deposition was generally negligible (0.02 mg/cm²), slightly higher levels of deposition were observed on fluoropolymer surfaces, where deposition on F2 was, resulting in a reasonable correlation where $R^2 = 0.7$.

AFM analysis showed the action of interfacial forces on PbS adhesion, where the influence of hydrophobic force when galena was in contact with a hydrophobic OTS functionalised surface revealed the presence of an additional long-range attraction (Figure 4.15). Measured adhesion from AFM tip retraction was determined to be 62.1 ± 4.7 mN/m and 26.7 ± 2.4 mN/m for

galena surfaces in contact with hydrophobic and hydrophilic AFM tips respectively. This explained higher levels of mass gain on hydrophobic surfaces where PbS agglomerates were both more likely to impact low surface energy substrates and strongly adhere due to the presence of the long-range hydrophobic force. Though a correlation between PbS deposition recorded and surface wettability was present, the effect of substrate roughness for various coating anti-fouling surfaces was difficult to quantify.

CaCO₃ forming systems generally resulted in the highest levels of deposition, where the REF coupon saw 1.0 mg/cm² of scaling upon its surface, with BaSO₄ and PbS showing 0.32 mg/cm² and 0.02 mg/cm² on the coupon respectively. Lower crystal supersaturation of 76 favoured heterogeneous nucleation upon foreign surfaces, where rates of CaCO₃ crystal growth on calcite were of the second-order, indicating that a surface-diffusion-controlled mechanism existed, resulting in significant mass gain after the 1 h experimental run-time.(252) Though supersaturation strongly influenced crystal size and growth rate for various species, work by Bracco (253) compared the step velocities of calcite and barite under similar conditions, where variables such as saturation index, pH, temperature, anion-cation ratio were unchanged, showing that the growth rate of calcite was comparatively faster. Calcium was shown to have a much faster attachment rate at 25°C based on activation energies, resulting in increased crystal face growth velocity.(253)

Due to very high SR of PbS under experimental conditions, crystal embryos form readily, and nanoparticles precipitate spontaneously within the bulk phase in simple systems resulting in no further growth of nucleated crystals due to a lack of Pb²⁺ or S²⁻ ion availability at the PbS crystal interface. An absence of heterogeneous PbS crystallisation accompanied with negligible deposition from the bulk phase, where surface adhered agglomerates are not prone to further growth in solution, results in limited mass gain. As such, any crystals or agglomerates that had adhered on anti-fouling substrates from the bulk phase were not prone to further growth in solution, with free Pb²⁺ ions reacting with HS⁻ anions upon dissociation into the aqueous phase.

In complex PbS/CaCO₃ systems, presence of Pb²⁺ ions appeared to alter calcite morphology, where rhombohedral and truncated octahedron morphologies formed when Pb²⁺ ions were not present and present at 100 mg/L concentration in SEM images (REF coupon) from Figure 4.2 and Figure 4.18 respectively.

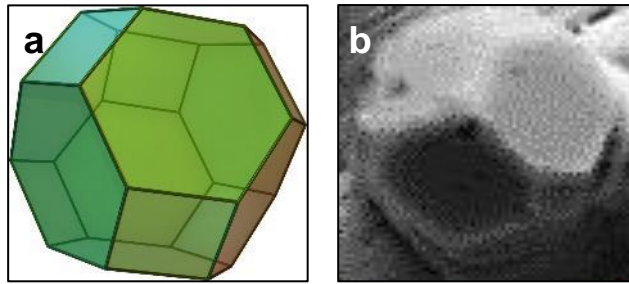


Figure 4.20 Truncated octahedron crystal morphology; a) Illustration; b) Imaged from PbS/CaCO₃ single phase systems

From Figure 4.20, two hexagonal faces can be clearly identified, with a square face in the top left of Figure 4.20b, indicating a truncated octahedron morphology.(251) Pb²⁺ ions have previously been shown to incorporate into the calcite lattice, with the presence of cations such as lithium (Li⁺) influencing the typical rhombohedral morphology to form a hexagonal lattice.(197, 254) Pastero et al.(254) observed that the growth mechanisms forming hexagonal patterns on the [0001] form of calcite crystals were driven by temporary adsorption of Li₂CO₃ onto the surface structure of the [1014] face, where step ledges are hindered by the presence of these islands.(254) Since the dissociation of H₂S_(g) into the aqueous solution is the rate-limiting step in the experiment described in Section 3.3.3, unreacted Pb²⁺ ions are present in solution for a period of time before becoming fully exhausted as barely soluble PbS nanoparticles are formed. Consequently, Pb²⁺ ions free in solution as calcite precipitates may result in the temporary formation of PbCO₃, prompting the change in morphology seen between rhombohedral and truncated octahedral in CaCO₃ and PbS/CaCO₃ systems respectively.

PbS agglomerates did not appear to act as seeding points for calcite, where heterogeneous nucleation of CaCO₃ occurred on the surface, with homogeneous deposition and adhesion of PbS likely enhanced by the presence of calcite crystals due to a significant increase in the frequency of hooking and attachment sites on the substrate. From comparison of Figure 4.3 and Figure 4.19, it could be seen that mass gain rose from 1.0 to 1.2 mg/cm² for CaCO₃ and PbS/CaCO₃ forming systems respectively. Higher mass gain on hydrophobic F1 and F2 compared to the REF coupon occurred as a combined result of preferential CaCO₃ nucleation from high net surface energy between CaCO₃ and the substrate, and the additional influence of the hydrophobic attraction between PbS agglomerates and the substrate.

4.7.1 Chapter Highlights

- In single phase conditions, hydrophobic surfaces encourage CaCO_3 -substrate bond formation.
- Surface Ra was significant in single phase as the increased density of nucleation points on rough surfaces drove heterogeneous crystallisation.
- Heterogeneous nucleation is the dominant mechanism in both CaCO_3 and BaSO_4 systems. The high SR of PbS resulted in precipitation exclusively within the bulk phase under given conditions.
- Particle deposition occurred through adhesion of PbS from the bulk phase to the surface, with higher rates of deposition on hydrophobic surfaces due to increased interfacial attractive forces (predominantly hydrophobic attraction) and rough surfaces of the fluoropolymer.
- In complex PbS/ CaCO_3 systems, presence of calcite where Pb^{2+} has been incorporated into the crystal lattice, altering the morphology from rhombohedral to a truncated octahedron.
- Seeding/occlusion of PbS agglomerates into the calcite crystal did not occur, with heterogeneous precipitation of calcite on the substrate promoting attachment of PbS agglomerates from the bulk phase

Chapter 5

Scale Behaviour and Deposition in Multiphase Flow: Simple Calcium Carbonate (CaCO_3), Barium Sulphate (BaSO_4) and Lead Sulphide (PbS) Systems

Single phase experiments in Chapter 4 demonstrated the precipitation mechanisms and nucleation tendency of several scale species found in oilfield systems. In practice, all oil and gas producing systems will exhibit two-phase flow, where water-oil-ratio (WOR) increases during the lifetime of a field.(255) Turbulent, multiphase flow conditions were generated in order to assess the role of the o-w interface in simple CaCO_3 , BaSO_4 and PbS scaling systems. Experiments aimed to contrast the precipitation and deposition mechanisms of conventional carbonates and sulphates with sulphide scale, proposing an alternative mechanism of deposition whereby scale particle stabilised Pickering emulsions impacted surfaces, as opposed to nucleating directly on substrates from solution.(23, 50) Influence of the multiphase on deposition was considered for anti-fouling coatings where wettability was the key parameter. The nature of the PbS Pickering emulsion in relation to surface fouling was investigated, with interfacial particle arrangement and emulsion stability providing insight into the mechanism by which PbS scale deposited, the role of the oil phase and the viability of this mechanism occurring under actual field scenarios. Eight coatings were tested preliminarily in simple scaling tests to establish a correlation between coating characteristics and deposition. Testing in complex solutions e.g. PbS/ CaCO_3 systems was undertaken later in the process with coatings that had been selected for field trials.

5.1 CaCO_3 in a multiphase (o/w) emulsion

Introduction of a light oil phase into a single-phase scaling system (Section 3.6), at an o:w ratio of 5:95 was able to demonstrate the effect of an oil phase on scale deposition upon surfaces of varying wettability. A carbonate scaling brine prompted the formation of CaCO_3 crystals that increased deposition and growth upon all anti-fouling surfaces when compared to single phase results in Chapter 4. The formation of an o/w emulsion resulted in stabilisation of CaCO_3 crystals at the interface, with the depositional pattern on the REF coupon in Figure 5.1 showing circular areas free of scale where oil droplets

had impacted the surface, resulting in deposition of CaCO_3 scale in the surrounding aqueous phase and on the substrate. This effect was not visible on hydrophobic coatings F1 and F2, where the oil wetted surface largely prevented contact of the substrate with the scale-forming aqueous phase. As a result of the turbulent nature of the system, localised heterogeneous crystallisation occurred on F1 and F2, with precipitated calcite acting as a nucleation site for secondary nucleation. This prompted homogeneous deposition from the emulsified bulk after the hydrophobic effects of that region of the substrate was compromised by scale presence. Secondary nucleation and growth was seen to be more extensive than in single phase, demonstrated through comparison of scaling on REF coupons in SEM images from Figure 4.2 and Figure 5.2, where well-defined, rhombohedral calcite crystals at the surface are overlain by large undefined calcite crystals. This trend, replicated on other anti-fouling surfaces, can be explained by enhanced attraction between oppositely charged Ca^{2+} and CO_3^{2-} ions near the o/w interface relative to that of the bulk, and the interface providing a thermodynamically favourable nucleation barrier for calcite precipitation. (256, 257) Agglomeration of ionic clusters and calcite of pre-critical radii at the o/w interface in multiphase systems increased the mass of conglomerates and therefore kinetic energy of collision; a similar phenomenon to that seen in single phase, whereby growth rate of crystals as a result of secondary nucleation has been shown to increase with rising shear rate. (258-260) The nature of the interlocking calcite structures, particularly apparent on the surface of the F2 coupon in Figure 5.2 indicate that a degree of the deposited calcite may have formed at the o-w interface before depositing through droplet impaction and rupture. This observation is also founded based on the depositional pattern on the coupon photographs, where circular areas free of scale on the REF and F1 coupons suggest o/w emulsion impaction as the mode of deposition.

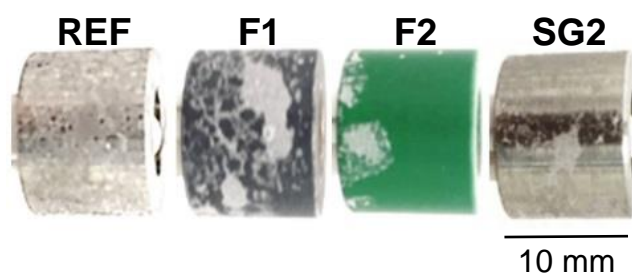


Figure 5.1 Photographs of samples – CaCO_3 multiphase conditions

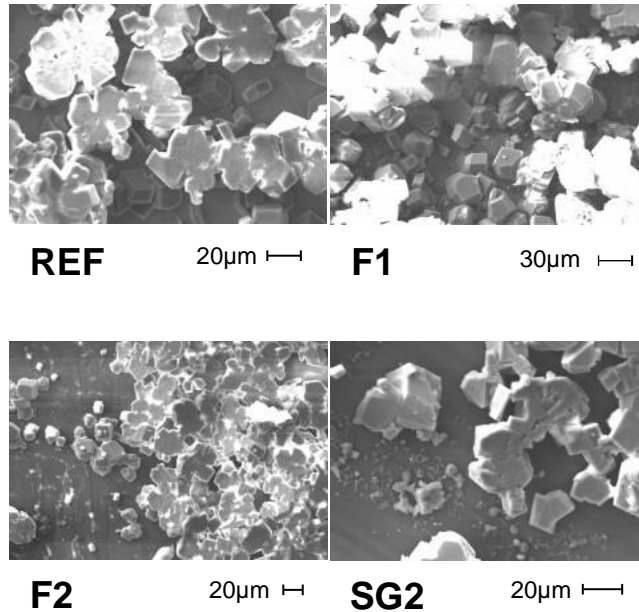


Figure 5.2 SEM images – CaCO₃ multiphase conditions

From Figure 5.3, the influence of presence of a light oil phase on depositional mass gain led to reversal of the trend seen in single phase CaCO₃ systems, though correlation was still very weak ($R^2 = 0.19$). Envelopment of the oil phase around fluoropolymer coatings reduced overall surface coverage of scale, an example of isolated nucleation seen on coupon F2 in Figure 5.1. Whilst scaling was for the most part prevented upon the F2 coupon surface, it is possible that imperfections acted as nucleation sites, prompting heterogeneous nucleation that then culminates in an increasing rate of secondary nucleation and homogeneous deposition confined to a specific site.

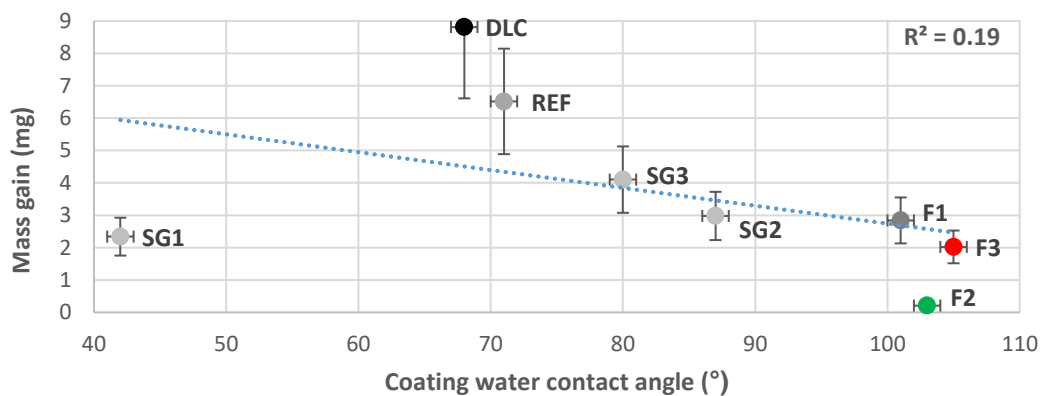


Figure 5.3 Water contact angle vs. mass gain – CaCO₃ multiphase conditions

5.2 BaSO₄ deposition in a multiphase (o/w) emulsion

In multiphase sulphate systems where o:w ratio was 5:95, BaSO₄ crystals had a tendency to stabilise and assemble at the o-w interface, leading to the snowflake-like deposits seen in SEM images in Figure 5.5. In o/w systems, oil droplets around which BaSO₄ particles have assembled from the bulk phase impact the anti-fouling substrate, resulting in the depositional pattern of scale on coupons in Figure 5.4, a similar pattern observed to that in CaCO₃ forming systems. Hydrophilic surfaces (REF; SG2) showed uniform scale coverage, with circular areas visibly free of scale where oil droplets had impacted the surface. Analysis of circular impact regions showed they were similar in diameter to BaSO₄ stabilised oil droplets, confirming the mechanism of deposition through droplet impaction.

Hydrophobic surfaces (F1; F2) however, had isolated regions where deposition had occurred; with homogeneously precipitated scale adsorbed at the o-w interface building up and adhering on to pre-scaled areas through collision of BaSO₄ and SrSO₄ scale particle-encapsulated oil droplets. Figure 5.5 shows SEM images of homogeneously precipitated 'snowflake' shaped deposits that have precipitated homogeneously within the bulk phase before depositing on the surface under the turbulent flow regime at the sample interface.

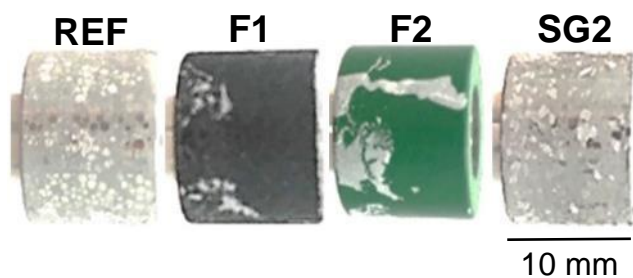


Figure 5.4 Photographs of samples – BaSO₄ multiphase conditions

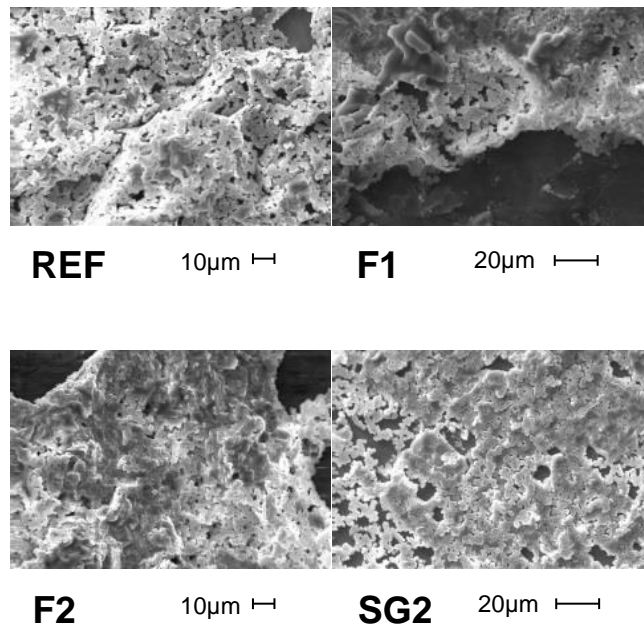


Figure 5.5 SEM images – BaSO₄ multiphase conditions

A similarly poor correlation ($R^2 = 0.42$) was observed for water contact angle vs. mass gain in sulphate systems (Figure 5.6), when compared to a CaCO₃ based multiphase system (Figure 5.3); though fluoropolymers showed more limited mass gain in general than hydrophilic surfaces. The higher the $SR_{initial}$ of a mineral salt, the more probable it is that stable crystal nuclei will precipitate homogeneously within the bulk phase.(35) The mass gain on surfaces through adhesion of scale particles from within the bulk phase is more heavily influenced by the presence of a light oil phase than those that nucleate directly for two reasons. Firstly, fluoropolymer surfaces are wetted by oil within an o/w emulsion as a result of their hydrophobicity, forming an oil wetting enveloping layer that shields the surface from scale within the brine phase. Secondly, the adsorption of particles at the o/w interface of oil droplets (given that the particle is partially wetted where barite water contact angle is 28°) increases transport and deposition of homogeneously precipitated scale onto surfaces via droplet impaction.(261) Due to the lack of an enveloping oil layer on hydrophilic surfaces, they are more prone to adhesion of partially-wetted particles under a turbulent regime.

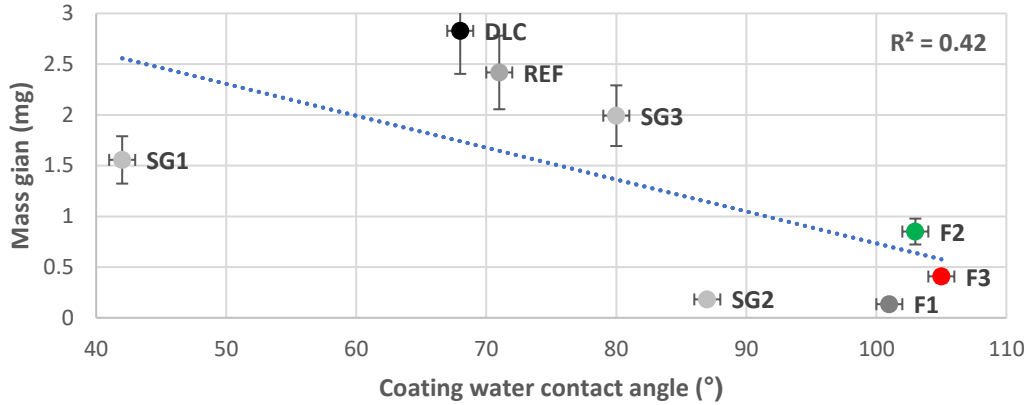


Figure 5.6 Water contact angle vs. mass gain – BaSO₄ multiphase conditions

5.3 PbS deposition in a multiphase (o/w) emulsion

As in single phase systems, homogeneous precipitation of PbS scale within the bulk phase of the system occurred spontaneously, with the rate-limiting step the diffusion and dissociation of H₂S to form reactive HS⁻ anions, as seen in Equation 2.22. As such, darkening of the solution occurs at a similar rate to that seen in single phase, turning an opaque black color after approximately 15 minutes. pH measurements demonstrated that the presence of an artificial oil phase at an o:w ratio of 5:95 did not affect the pH of the solution, which was recorded at pH 5.2. Consequently, the SR_{initial} of PbS and the rate of hydrolysis of H₂S into the brine phase was unchanged. Additionally, as in a single-phase system, transport and adhesion from the bulk was the sole mechanism driving the deposition of PbS scale when an oil phase was introduced at an o:w ratio of 5:95. It can be seen from Figure 5.7 that a thick, black deposit has adhered to all anti-fouling surfaces, with the exception of fluoropolymer coatings F1, F2 and F3. The behavior of PbS particles changes dramatically with the addition of a light oil phase, with adsorption of PbS at the o/w interface under turbulent conditions, whereby oil droplets within the water phase are encapsulated and stabilised by solid nanoparticles. As a result, PbS particles anchored at the o/w droplet interface become adherent upon impaction of surfaces, forming circular deposits around the point of collision; as seen in Figure 5.9 on hydrophilic REF, SG2, SG1, F4 and DLC surfaces.

Similarly, in multiphase BaSO₄ systems, circular scale-free areas were formed as a result of oil droplet impaction upon anti-fouling substrates. From SEM images in Figure 5.9, these scale-free areas upon hydrophilic surfaces ranged

in diameter from 100 – 500 μm , representative of the diameter of PbS stabilised oil droplets as seen in Figure 5.14.

The SG3 coating was replaced with F4 for these experiments. This enabled assessment as to whether there were characteristics of the fluoropolymer surface that enabled limited deposition of scale, or surface wettability was the dominant variable. The water contact angle for SG3 and F4 was identical at 70°.

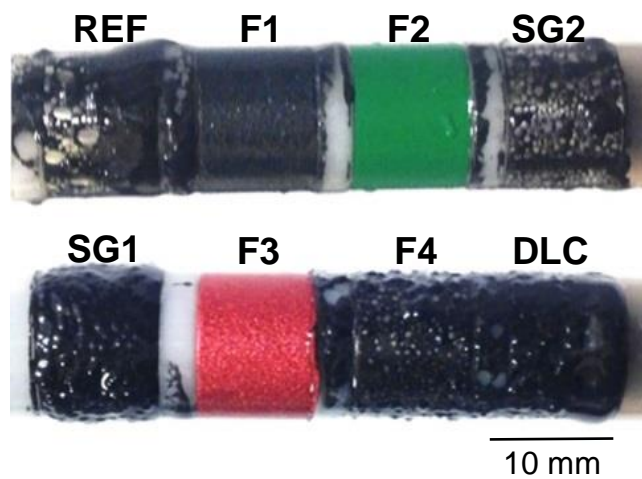


Figure 5.7 Photographs of samples – PbS multiphase conditions

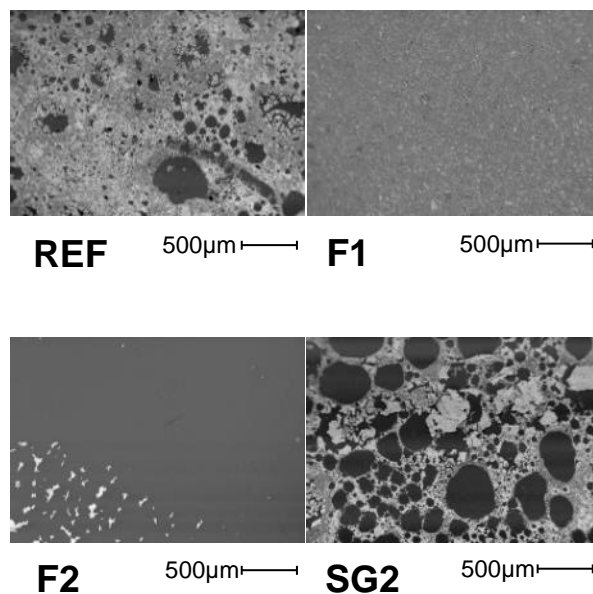


Figure 5.8 SEM images – PbS multiphase conditions

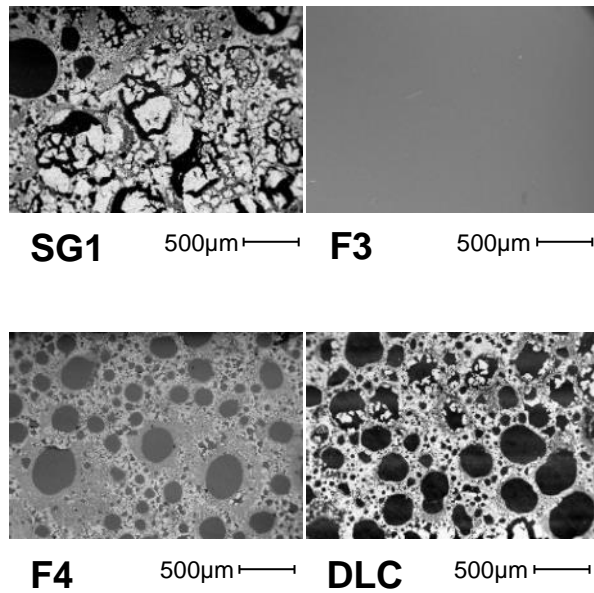


Figure 5.9 SEM images – PbS multiphase conditions

From Figure 5.10 it can be observed that there is a strong negative correlation between the water contact angle of an anti-fouling surface and the degree of mass gain through PbS scale deposition. Hydrophilic surfaces with a low contact angle see significant scale build-up, with the degree of PbS deposition decreasing as water contact angle increases. Coatings with a water contact angle over 90° that can be described as hydrophobic, such as fluoropolymer samples F1, F2 and F3, show little to no PbS deposition upon their surface.

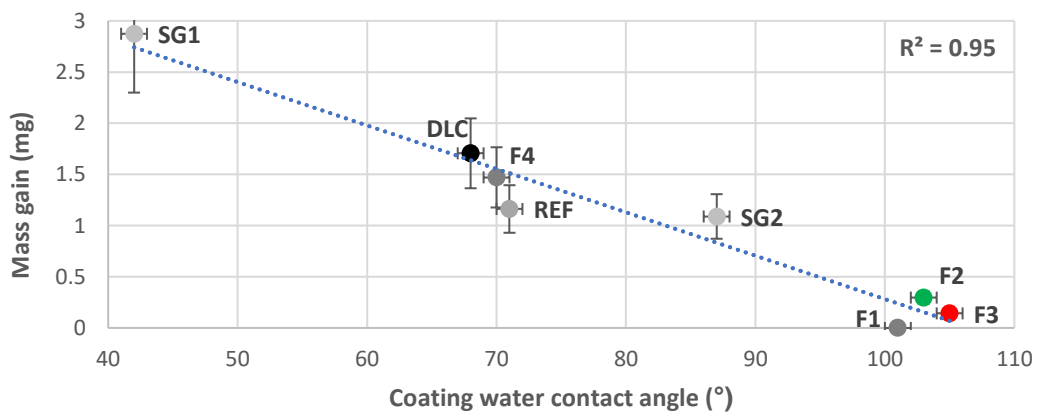


Figure 5.10 Water contact angle vs. mass gain – PbS multiphase conditions

5.4 PbS pre-precipitation

Pre-precipitation experiments showed that homogeneous adhesion was the mechanism by which PbS stabilised Pickering emulsions and their associated particles deposited, when the possibility of direct heterogeneous crystallisation upon surfaces was removed. Adhesion was predicted to be the sole mechanism by which PbS scale deposited on to surfaces within the scaling system, due to the spontaneous homogenous precipitation of scale within the bulk phase. Figure 5.11 shows the degree of PbS deposition through mass gain measurements described in (Section 3.6.3.1) when new anti-fouling surfaces were inserted into a multiphase system post-experiment, and the experiment carried out in a pre-formed 5:95 o/w PbS Pickering emulsion.

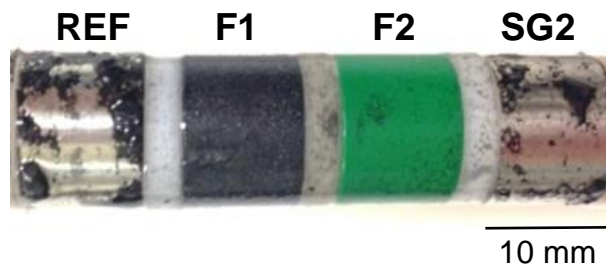


Figure 5.11 Photographs of samples – PbS multiphase conditions (pre-precipitated)

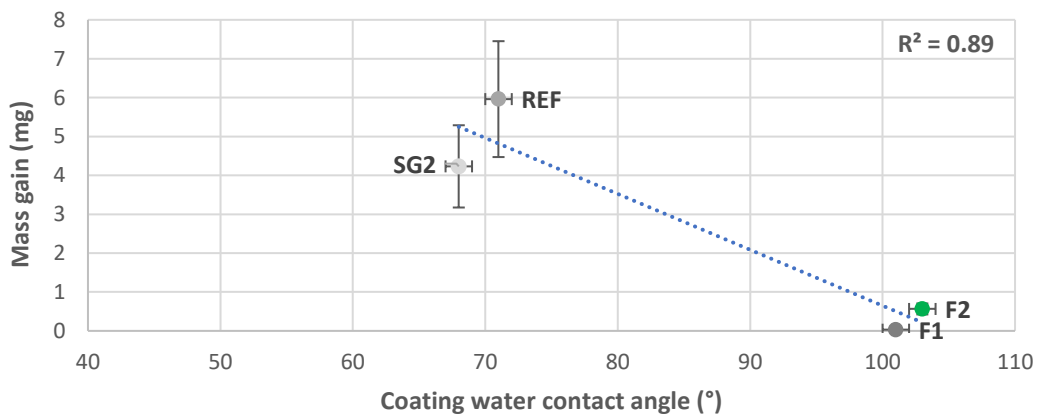


Figure 5.12 Water contact angle vs. mass gain – PbS multiphase conditions (pre-precipitated)

Deposition of PbS on anti-fouling surfaces in a pre-precipitated system follows a similar trend to that seen during initial multiphase scaling tests, where coating wettability strongly influenced degree of scale build-up ($R^2 = 0.96$).

Upon comparison of Figure 5.10 and Figure 5.12 however, it can be seen there was generally less deposition on all surfaces in pre-precipitated systems. This may be explained through a significant proportion of existing PbS scale precipitated in the initial test being deposited onto the reaction vessel and initial samples during the first experiment. Consequently, there is less PbS within the system after a second test is carried out in a pre-precipitated system, reducing the likelihood of scale particles contacting the anti-fouling surface and forming deposits.

5.5 PbS emulsion characterisation

Figure 5.13 shows a post-experimental o/w Pickering emulsion composed of oil, PbS nanoparticles and water, formed through vigorous shaking (a); with breaking of the oil and Pickering emulsion after 40 seconds; and significant migration of PbS particles from the water phase to the interface after a period of approximately 220 seconds (b). Phase separation after agitation gave an indication of PbS particle affinity within the emulsion and the oleophobic nature of the particles making up the Winsor type III emulsion.

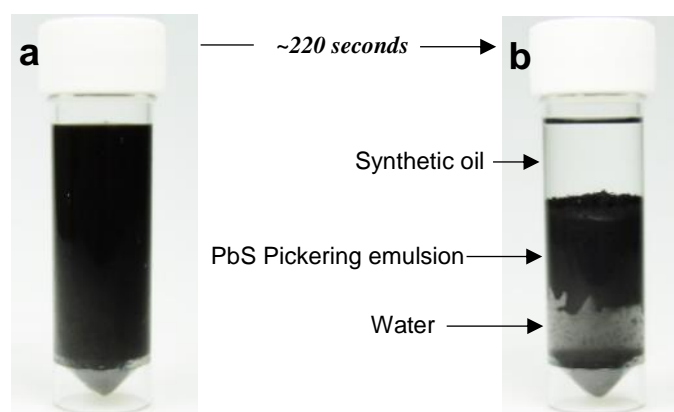


Figure 5.13 Oil, emulsion and brine phase separation: a) PbS emulsion after shaking; b) separation of oil phase (40 seconds) and significant migration of PbS particles from water to o/w interface after approximately 220 seconds

Optical microscope images of oil droplets stabilised by PbS that make up the emulsion can be seen in Figure 5.14a and b. At 1000 mg/L Pb²⁺ and oil volume fraction of approximately 0.3, the emulsion is relatively polydisperse, with oil droplet size ranging from 0.3 - 1 μ m. PbS agglomerates were shown in Figure

4.12 to range from 0.5 – 3 μm in diameter, and here are closely packed at the spherical interface.

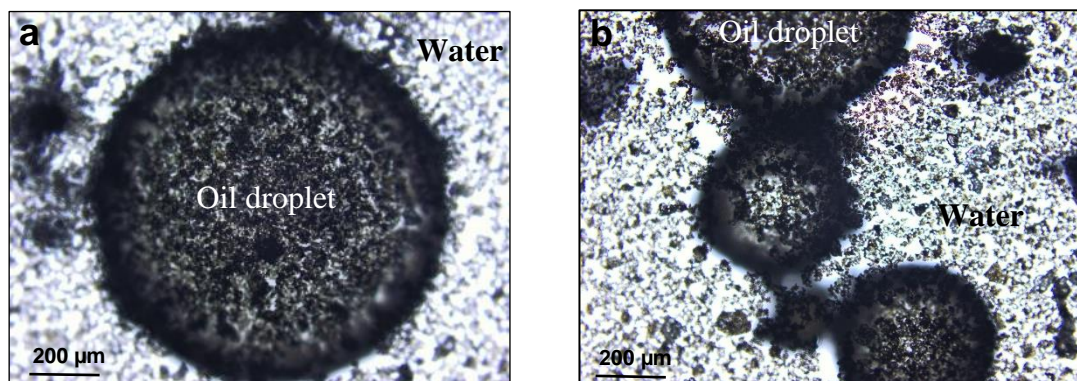


Figure 5.14 PbS stabilised oil droplets in o/w Pickering emulsion

Cryo-SEM imaging (Figure 5.15) displays the cross-section of an oil droplet encased and stabilised by a thin layer of PbS nanoparticles, highlighted as white dots through the use of BSE. EDX analysis further confirmed the role of PbS in stabilisation of the oil droplet, where yellow and pink highlighted areas show encompassing PbS nanoparticles at the o-w interface.

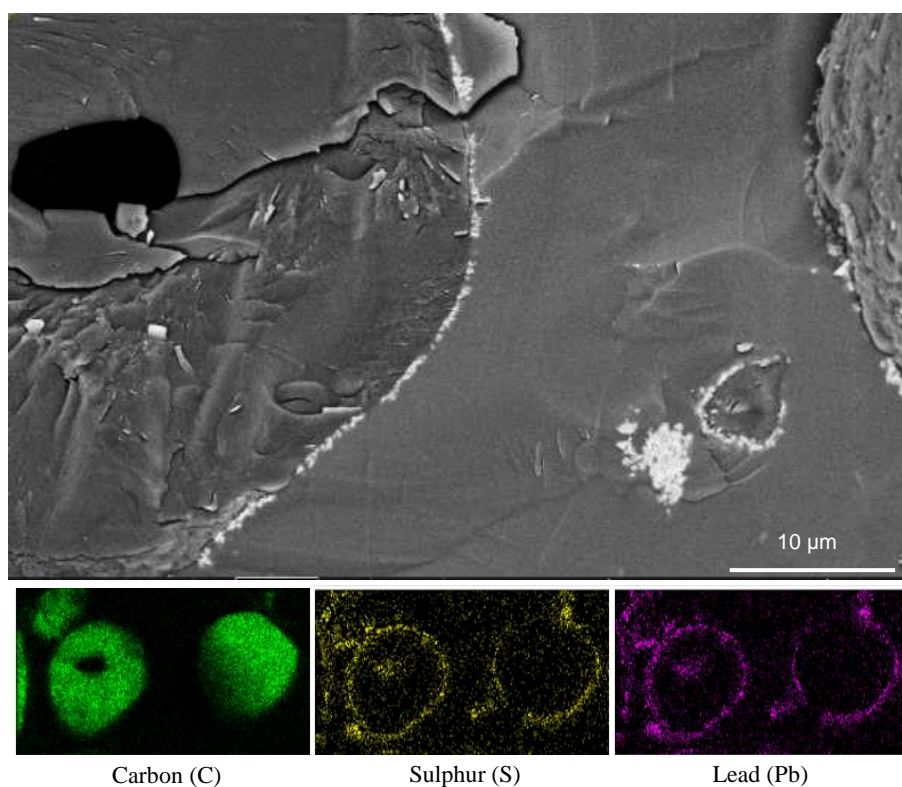


Figure 5.15 Cryo-SEM of oil droplet with PbS nanoparticles at o-w interface; EDX highlighting oil droplet and PbS species

PbS particle arrangement can be seen in greater detail in Figure 5.16, where it was revealed self-assembly of PbS agglomerates 6 - 10 nanoparticles deep form a network contained within the aqueous phase at the o-w interface. Transmission electron microscopy (TEM) embedded in the same image illustrates the appearance of the stabilising PbS particles.(262) PbS particle arrangement across the o-w interface is not entirely uniform however, with gaps appearing in-between agglomerates, Figure 5.16 showing one agglomerate around 3 μm in diameter with particle-free interface either side.

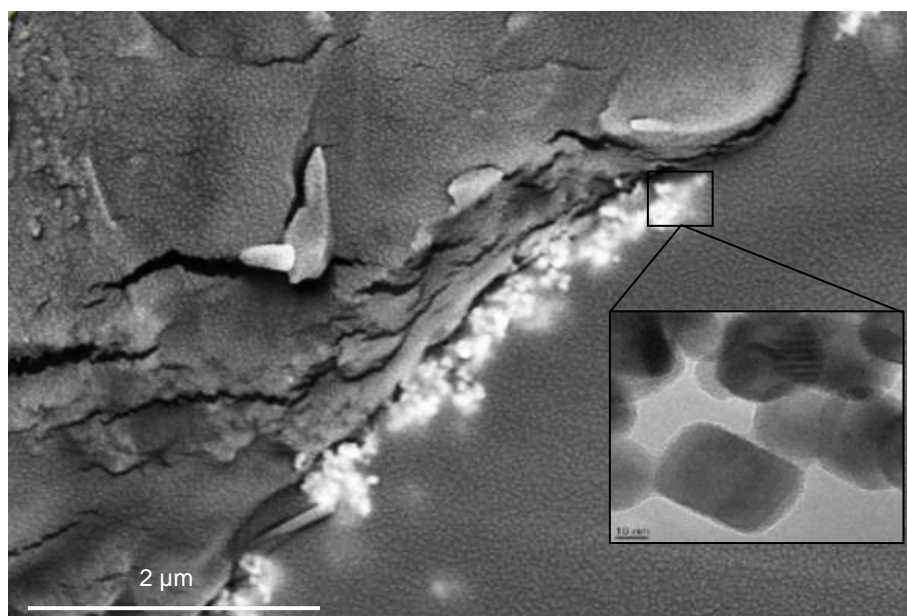


Figure 5.16 Cryo-SEM image of PbS arrangement at o-w interface; TEM image shows size and shape of PbS

Assembly of PbS nanoparticles in the aqueous phase at the o-w interface (Figure 5.16) can be explained by their hydrophilicity, with attachment to the interface rather than the bulk phase driven by partial hydrophobicity. Oil contact angle on unoxidised galena within an aqueous medium can be seen in Figure 5.17, where three-phase contact (TPC) angle at an oil-galena-water junction was $132.1 \pm 1.8^\circ$, and $47.9 \pm 0.6^\circ$ for a water-galena-air system.

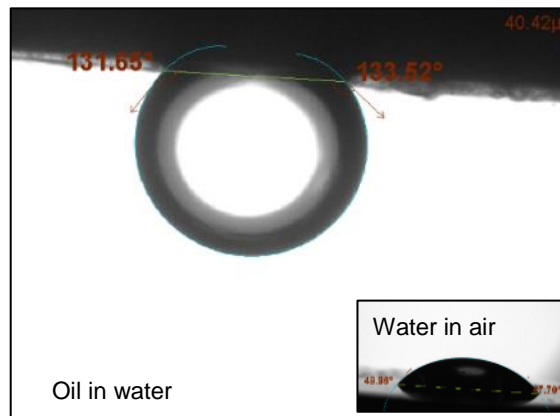


Figure 5.17 Main image shows inverted sessile drop of oil on galena in aqueous solution where oil CA was $132.1 \pm 1.8^\circ$; thumbnail displays water contact angle on galena in air where water CA was $47.9 \pm 0.6^\circ$

Natural mineral surfaces are typically heterogeneous due to the existence of impurities/functional groups on the surface, crystal orientation and hydrophilic/hydrophobic sites on the surface, therefore a single value for surface energy is not representative of the whole surface. Only through repeated water contact angle experiments could an average value could be established. Sulphide minerals have a low degree of surface polarity and hydrophobic characteristics, potentially as a result of surface oxidation and hydrolysis. Whilst sessile drop measurements provided a crude measure of PbS wettability, the heterogeneous distribution of hydrophobic sites upon the PbS [001] crystal plane results in the characterisation of PbS mineral throughout this work as 'partially hydrophobic'.(263)

5.6 PbS emulsion viscosity

A relative viscosity curve displaying ramping shear rate vs. apparent viscosity measurements (Figure 5.18) as described in Section 3.7.3.5, was able to predict the critical flow strength at which droplets within an 5:95 o/w emulsion ruptured.(264) Shear thinning, where the viscosity of the non-Newtonian emulsion drops under shear strain, was prompted by flocculation of oil droplets that lead to eventual coalescence and emulsion breaking.(265) This occurs at a shear rate of approximately 0.1 s^{-1} , where viscosity drops from $0.13 \text{ Pa}\cdot\text{s}$ to $0.01 \text{ Pa}\cdot\text{s}$ at a shear rate of 10 s^{-1} before stabilising, indicating that emulsion breaking and shear thinning had occurred. Large shear rates can prompt oil droplets within the emulsion to rupture and consequently destabilise.(266)

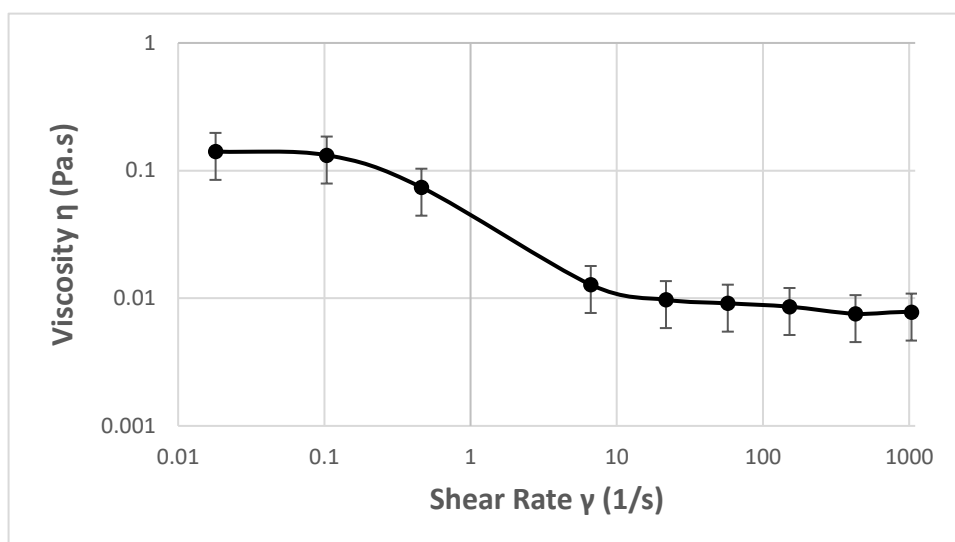


Figure 5.18 Shear rate vs. viscosity of o/w PbS Pickering emulsion at shear values of 0 - 2 Pa

Flocculation is potentially induced by the removal of stabilising PbS particles from the interface into the dispersed medium under high shear.(267) This subsequently reduces the packing fraction at the interface allowing oil droplet bridging to occur.

5.7 PbS emulsion thermal stability

The thermal stability of a PbS Pickering emulsion was investigated using the methodology in Section 3.7.3.3. From Figure 5.17, the oil-galena-water contact angle (θ_o) and water-galena-air contact angle (θ_w) were found to be $132.1 \pm 1.8^\circ$ and $47.9 \pm 0.6^\circ$ respectively that lead to partial-wetting at the interface and formation of an o/w emulsion at o:w ratio of 5:95. The conductivity of the emulsion (0.9 mS/cm) was found to be in agreement with that of a saline water, indicating water was the continuous phase. The adsorbed layer of PbS crystals formed a rigid coating around oil droplets that acted as a mechanical barrier, preventing oil droplet coalescence. Equation 2.36 shows the free energy of desorption (ΔG_w) required for desorption of a PbS particle into water phase. Even at high temperatures, the free energy of adsorption of a PbS particle of 50 nm radius (R) at the oil water interface ($\gamma_{o-w} = 50 \text{ mN m}^{-1}$), and exhibiting a water contact angle (θ_w) of 49° , the free energy required for desorption $\Delta G_w = 1.3 \times 10^{-16} \text{ J}$ is much larger than the thermal energy K_t ($5 \times 10^{-21} \text{ J}$ at 95° C), demonstrating the stability of such emulsions at high temperatures. Figure 5.19 shows the influence of

temperature on the conductivity of the emulsion and confirms its stability over the range of temperatures tested; the conductivity of the emulsion remains high and no visual breakage of the emulsion was observed up to temperatures of 95°C.

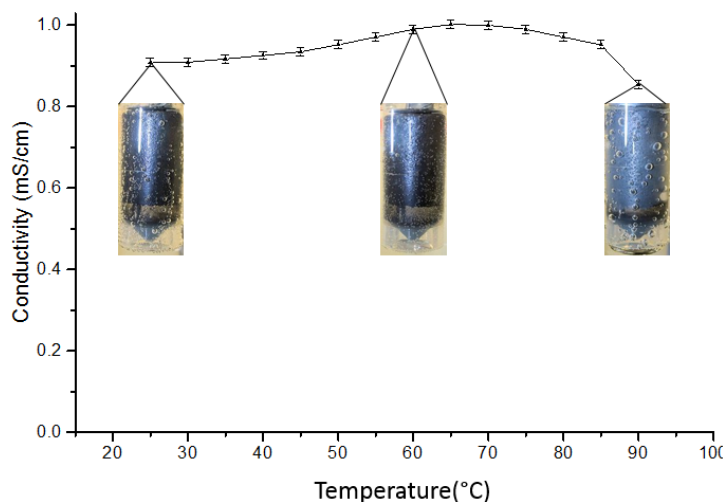


Figure 5.19 Thermal stability of a PbS Pickering emulsion – Conductivity vs. Temperature

5.8 PbS emulsion inversion

The phase ratio at which PbS Pickering emulsion inversion occurs (Section 3.6.1) can be observed in Figure 5.20, whereby an o/w emulsion formed above the aqueous phase when oil volume fraction was less than 0.75. Increasing of the oil volume fraction to over 0.75 resulted in destabilisation and sudden inversion of the continuous phase from water to oil, forming a w/o emulsion. This process was termed ‘catastrophic inversion’, as the system is responding to a change in drop volume fraction, where PbS particle concentration and water fraction are kept constant.(167)

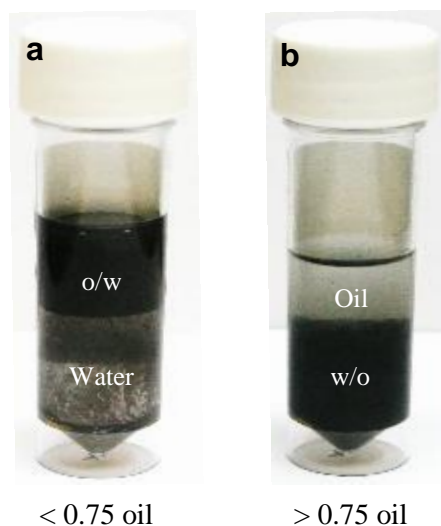


Figure 5.20 PbS multiphase system – a) o/w emulsion at < 0.75 oil phase fraction; b) w/o emulsion at > 0.75 oil phase fraction

Addition of oil resulted in Ostwald ripening, where molecules stabilising smaller oil droplets transferred and adsorbed onto larger drops as a result of the difference in Laplace pressure across the fluid interfaces.(167) The ripening process is hindered at constant phase fractions below 0.75 oil phase fraction as seen in Figure 5.20a, by the presence of PbS particles at the o-w interface of oil droplets. This rigid PbS particle layer resulted in the droplet interface possessing zero mean curvature, preventing coalescence as Laplace pressure dropped to zero.(268) Droplets flocculate and ripen, where swelling of drops resulted in insufficient PbS packing fraction at o-w droplet interfaces that eventually resulted in coalescence.(167) Ata (269) showed the sequence whereby a particle (silanised glass beads) stabilised air bubble and an uncoated bubble merge, that could be likened to light oil droplets (PbS coated/uncoated) within a continuous water phase (Figure 5.21). Oscillations created as a result of the merging bubbles drove the beads into the centre of the formed bridge, where amplitude of the oscillations gradually slowed until the merged bubbles stabilised.(167, 269)

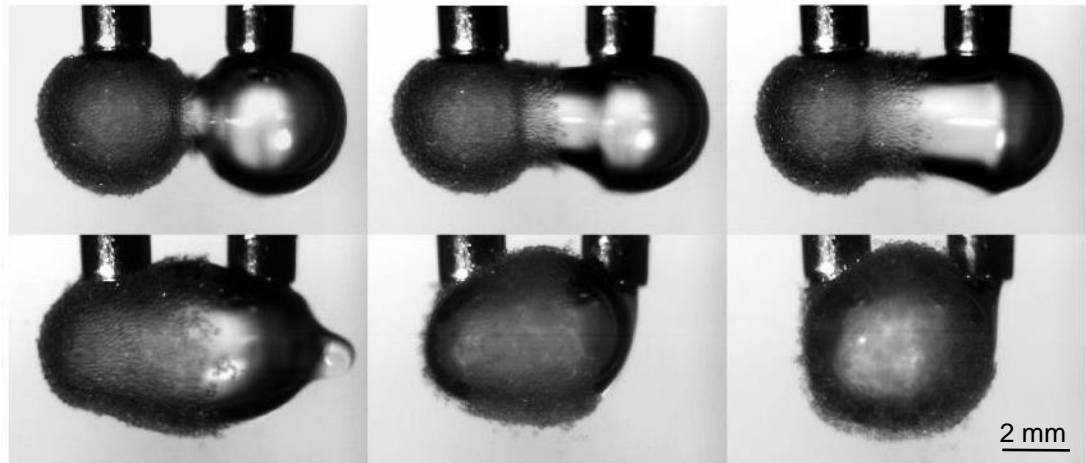


Figure 5.21 Particle laden droplet coalescing with uncoated droplet. The time between each photograph (top left to bottom right) was reported to be 0.5 ms (269)

Figure 5.22 displays PbS deposition upon anti-fouling coupons in a multiphase system with an o:w ratio of 80:20, where high oil volume fraction lead to a w/o emulsion in which PbS stabilised water droplets were the disperse phase. F1 and F2 remained clear of scale, while REF and DLC showed heavy deposition. Whilst excess oil present prevented fouling upon the hydrophobic fluoropolymer coatings, the low stability of the inverted emulsion lead to a high degree of surface deposition upon hydrophilic substrates, where the REF coupon saw 0.16 compared to 0.32 mg/cm² of PbS scaling in o/w and w/o emulsions respectively. This can be likely explained by the ease with which the unstable water droplets rupture having impacted the surface, resulting in a clear lack of persistent PbS-coated droplets residing on the substrate, unlike those seen in Figure 5.7 on the REF coupon.

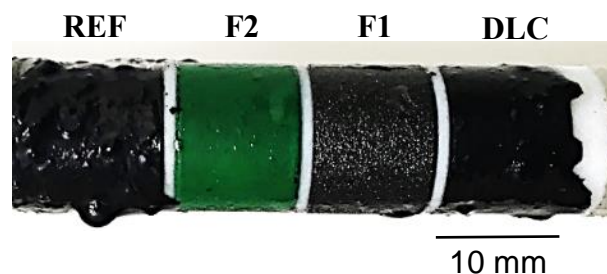


Figure 5.22 Anti-fouling coupons in a multiphase PbS system (80:20 o:w ratio)

Figure 5.23 plots the coating water contact angle against the mass gain for a multiphase PbS system with an o:w ratio of 80:20. As with o/w emulsion scaling in Figure 5.10, there was a reasonable correlation between coating wettability and mass deposited ($R^2 = 0.79$), with PbS fouling generally decreasing with increasing surface hydrophobicity.

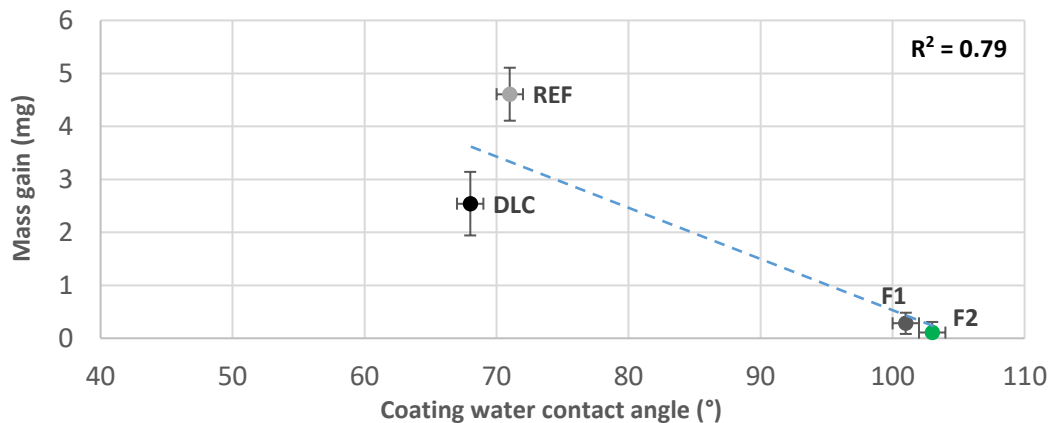


Figure 5.23 Water contact angle vs. mass gain in a multiphase PbS system (o:w 80:20 ratio)

5.9 Chapter summary

5.9.1 Deposition mechanisms in multiphase systems

The deposition of PbS Pickering emulsions occurred largely via mechanical means, whereby particle stabilised droplets impacted against surfaces within a high-energy turbulent o-w multiphase system and either ruptured or adhered.(262) Rupture of an oil or water droplet (dependent on emulsion type) after impacting a substrate can result in the deposition and adhesion of particles that previously contributed to droplet stabilisation.(206, 270, 271)

Similar depositional patterns upon the hydrophilic REF coupon can be seen in CaCO_3 , BaSO_4 and PbS systems, indicating that oil droplets had impacted the substrate within the turbulent regime, leaving a circular area scale-free. The lack of scale in areas impacted by oil droplets can be attributed to the hydrophilic nature of the formed scales, where water contact angle of calcite, barite and galena was recorded to be 6, 28 and 49° respectively.(261, 272) Analysis of average droplet size through optical microscopy confirmed commonalities between the size of imaged droplets and scale-free areas on substrate surfaces with respect to their specific systems. From analysis of the PbS emulsion and comparison with single phase results (Figure 4.10), it can

be seen that stabilisation of oil droplets through arrangement of PbS nanoparticles at the o/w interface enhanced transport of PbS scale to the hydrophilic substrate after droplet impaction.

Super-hydrophobic/super-oleophilic meshes are currently applied in the separation of diesel oil and water, where oil spreads quickly on the film and subsequently permeates the mesh.(273) The principle with regards to hydrophobic anti-fouling coatings is similar, where oil wet to a specific region is able to largely prevent undesirable contact with the aqueous phase that results in substrate fouling. This principle is demonstrated in Figure 5.24, where the excess free oil in solution is wetted to hydrophobic surfaces whilst PbS stabilised droplets are free to impact hydrophilic surfaces under turbulent conditions. The measure of a surface to become oil wet is described by the displacement energy (DE). Fluoropolymers F1, F2 and F3 had negative DE values of -28, -31 and -32 J respectively, prompting displacement of water molecules from the surface. The formation of a stable oil layer largely prevented the contact and precipitation of scaling ions within the aqueous phase upon the surface. Metal Inconel and other hydrophilic surfaces with positive DE were generally polar, possessing an affinity for water that drove contact with the aqueous phase and therefore precipitation and bulk adhesion.

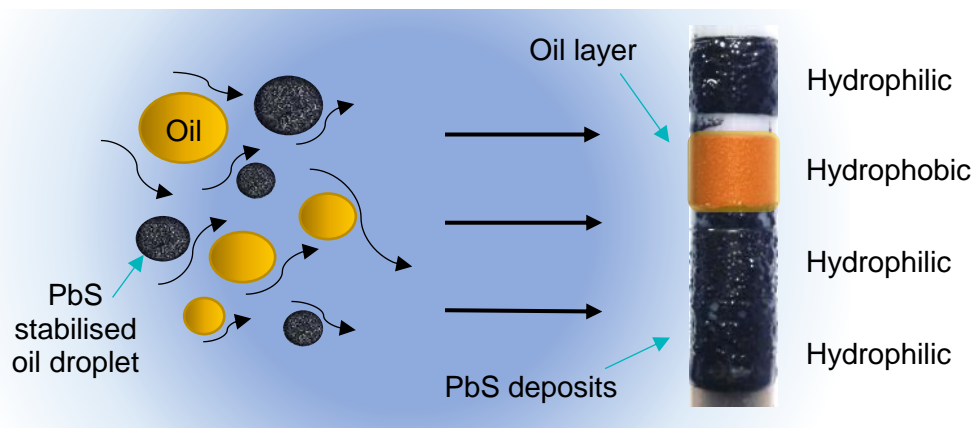


Figure 5.24 Oil droplet state in-situ within turbulent system. Oil wetting of hydrophobic surfaces by free excess oil and impaction of hydrophilic surfaces by PbS stabilised oil droplets

Impaction of the PbS particle stabilised oil droplets appears from SEM images (Figure 5.26) to occur via radial splashing, whereby a circular area of the substrate is left relatively scale-free, with particles splashing and emanating outward after contact. This is represented by Supakar et al. (274), where a

water droplet encased with hydrophobised glass beads is dropped upon a hydrophobic surface (Figure 5.25).(274)

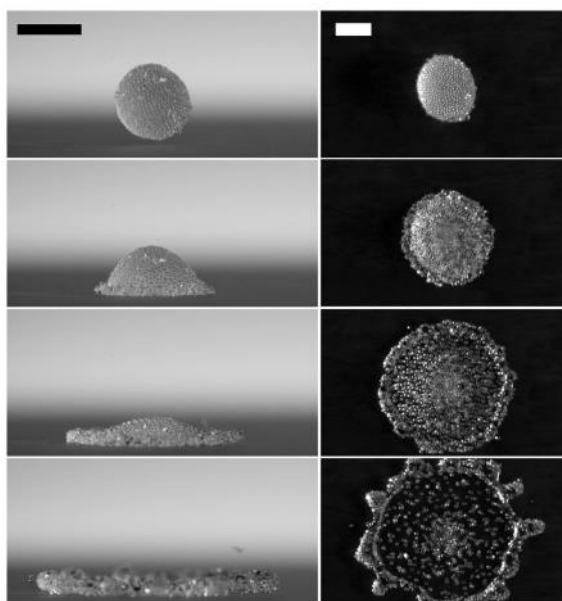


Figure 5.25 A liquid droplet coated with hydrophobised beads and impacted upon a hydrophobic surface where $t = -0.2, 1, 2.2, 4.8$. Scale bars in each image are 2 mm long (274)

Though similar in principle, the system described by Superkar et al. (274) is not wholly representative of the experimental mechanism for droplet deposition elucidated within this Chapter where an PbS coated oil droplet impacts a hydrophilic surface.(274) The process shown in Figure 5.25, whereby hydrophobic particles surrounding a water droplet impact a hydrophobic surface, likely results in reduced spreading of the water droplet across the surface and higher attachment of particles to the centre of the impacted area than PbS coated oil droplets due to the influence of attractive hydrophobic forces.

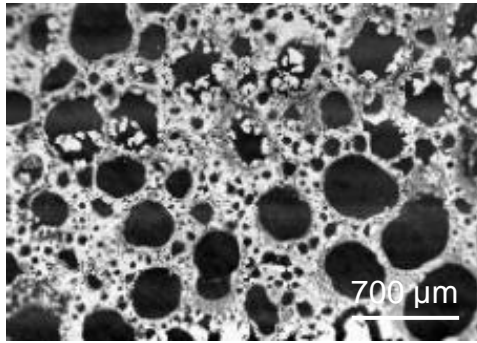


Figure 5.26 SEM of deposition pattern on DLC coupon in a o/w multiphase PbS system

The adhesive strength of particles once deposited has been shown to depend on the particle size and charge, in conjunction with the surface charge of the substrate.(104, 275)

The high stability of PbS particle-stabilised emulsions derived from a high energy requirement for the desorption of particles from the interface led to the attachment of intact oil droplets from the emulsion to the surface of hydrophilic substrates, as can be clearly seen from Figure 5.7. Initial deposition would in all probability have led to further build-up of PbS emulsion whereby the degree of emulsion attachment was reliant on the height of the turbulent boundary layer normal to the substrate, in addition to the increased effect of inertia acting on deposits further from the axis of rotation central to the RC sample.

The influence of water-cut has been shown to be substantial (Figure 5.20), where a water-cut <0.25 water phase fraction in a simple PbS multiphase system results in the formation of a w/o emulsion that is prone to catastrophic inversion as water-cut increases beyond this value. The emulsion type however had a limited effect on deposition of PbS upon surfaces of varying wettability, with hydrophobic surfaces seeing negligible PbS deposition when immersed within both regimes. Figure 5.27 displays a schematic of the scaling mechanism in w/o emulsion systems, where oil as the continuous phase still wets hydrophobic fluoropolymers and water droplets within which PbS particles are contained and stabilised at the interface are drawn to hydrophilic surfaces that they then impact.

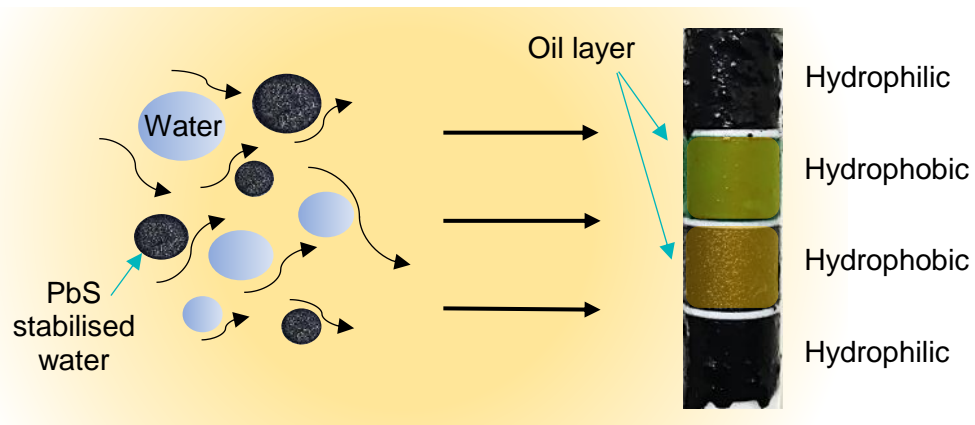


Figure 5.27 Water droplet state in-situ within turbulent system. Oil wetting of hydrophobic surfaces by bulk oil and impaction of hydrophilic surfaces by PbS stabilised water droplets

The low stability of the w/o emulsion results in the rupture of water droplets, where the 0.2 phase fraction of water used in the experiment (Section 3.6.1) is close to the inversion point at which catastrophic inversion will occur. As such, droplets rupture easily upon surfaces distributing their particles across the substrate in a manner similar to that seen in Figure 5.25. Kee et al. (155) showed that in turbulent w/o vertical pipe flow where velocity was 1 m/s, 10% water-cut was sufficient to ensure stable water-wetting of a hydrophilic steel surface. Consequently, it can be inferred that significant deposition on hydrophilic surfaces occurs due to the wetting of PbS particle-stabilised water droplets upon them before rupture.

5.9.2 Predicting scale deposition in multiphase flow

Despite conventional CaCO_3 and BaSO_4 scales being strongly hydrophilic with water contact angles of 6° (calcite) and 28° (barite) respectively, the wetting effect of the oil was not sufficient to completely prevent deposition on fluoropolymer surfaces. (261, 272) Figure 5.1 and Figure 5.4 show localised scale deposits on the F1 and F2 fluoropolymer substrates, with SEM images for CaCO_3 and BaSO_4 deposition from Figure 5.2 and Figure 5.5 respectively indicating that heterogeneous nucleation has occurred through limited exposure of the aqueous phase to the coating. Once calcite or barite crystals had nucleated upon the substrate, that anti-fouling attributes of that region are compromised, where the hydrophilic crystals and enhanced surface roughness reduced the wetting efficacy of the oil. Within PbS forming systems however, the exceedingly high SR at experimental conditions presented in Section 3.5.1 results exclusively in homogeneous precipitation within the bulk

phase and as a result, the integrity of hydrophobic fluoropolymer coatings was not compromised. Consequently, a relationship between the saturation ratio of a precipitating salt and the depositional tendency in multiphase systems on surfaces of varying wettability becomes apparent from the results, as seen in Table 5.1.

Table 5.1 Relationship between salt, SR and CA vs. mass gain correlation

Scale type	SR_{Initial}	R² value (coating CA vs. mass gain)
CaCO ₃	76	0.19
BaSO ₄	1888	0.42
PbS	1.7 x 10 ¹⁹	0.95

Inevitable and spontaneous crystallisation within the bulk aqueous phase at ambient temperatures eradicates uncertainty with regards to deposition often caused by heterogenous nucleation directly onto surfaces that results in the compromising of a substrate's anti-fouling attributes. The two key elements for deposition of bulk precipitated particles in turbulent multiphase systems include; i) particle or agglomerate wetting at the o-w interface and the formation of a Pickering emulsions; and ii) the hydrophobicity of the substrate.(262)

Pre-precipitation experiments in systems where a PbS Pickering o/w emulsion had been formed highlighted the role of the emulsion and excess free oil phase on deposition in PbS systems. Additionally, inversion of the emulsion type, where systems contained an 80:20 o:w ratio, prompted the formation of an w/o PbS Pickering emulsion that displayed similar depositional trends to o/w emulsions with excess oil wetted to hydrophobic surfaces preventing scaling.

Work presented in this Chapter lays the foundation for the development of a simple model of multiphase PbS deposition on surfaces based on their wettability. Its reliability was contingent upon a number of factors:

- Consistent multiphase flow dynamics at the substrate interface and in the emulsified bulk phase,

- Known interfacial tension between synthetic oil (kerosene) and brine in two-phase flow and the corresponding arrangement of unoxidised PbS at the o-w interface,
- PbS crystallisation was spontaneous and limited to the bulk phase,
- Constant pH, temperature and pressure (though temperature was shown to have little influence on emulsion stability up to 95°C)

Whilst laboratory studies demonstrate the highly predictable nature of simple PbS scaling in multiphase systems under the conditions described above, application of realistic downhole conditions would likely drastically influence system behaviour and complexity. In practicality, producing oilfield wells contain multiple scale forming species that nucleate heterogeneously, high levels of total dissolved solids (TDS), surfactants, inhibitors, and other colloidal particles e.g. clay fines, that can all contribute to emulsion stabilisation. Additionally, the saturation ratio of PbS can be driven down by low pH, high temperature and high free Cl⁻ ion concentration, where under extreme conditions, precipitation is no longer spontaneous.(29, 37, 38, 65) Despite this, the stability of PbS Pickering emulsions was unaffected up to temperatures of 95°C, as shown by observations and conductivity readings, due to the high energy of desorption of particles and agglomerates from the o-w interface.

5.9.3 Chapter Highlights

- Deposition of mineral scale under turbulent flow regimes in multiphase systems is enhanced through the formation and impaction of particle stabilised droplets onto substrates, as shown by the depositional patterns where radial splashing had occurred, resulting in splaying of particles
- Particle stabilisation at droplet interfaces leads to formation of highly stable Pickering emulsions, with the strength of particle attachment at the oil-water interface heavily influenced by wettability
- Through empirical deposition measurements, it was clear that substrate wettability was critical in determining the degree of scale deposition in multiphase systems
- Hydrophobic surfaces became oil-wet in multiphase systems, preventing impaction of particle-stabilised droplets (as part of a Pickering emulsion with an affinity to the aqueous phase) depositing upon surfaces

- A correlation between water contact angle and surface mass gain was therefore observed
- The strength of this correlation increases as the SR of the mineral within the system increases. PbS scale that crystallises exclusively within the bulk phase provides a very strong correlation between water contact angle and mass gain upon surfaces.
- Minerals at experimental SR's that are prone to heterogeneous nucleation e.g. CaCO_3 and BaSO_4 , show a weaker correlation between water contact angle and mass gain. This is due to the heterogeneous nucleation of crystals upon both hydrophilic and hydrophobic substrates, subsequently compromising their anti-fouling characteristics (ability to become oil-wetted).
- In both o/w and w/o systems, similar observations were made with regards to the relationship between water contact angle and mass gain. Oil wetting of hydrophobic surfaces prevented deposition, particularly in systems with high $\text{SR}_{\text{initial}}$ that precipitate spontaneously within the bulk phase.
- Emulsions were stable at elevated temperatures, due to the extremely high displacement energy required to remove particles and agglomerates from the o-w interface

Chapter 6

Scale Behaviour and Deposition in Multiphase Flow: Complex Lead Sulphide (PbS)/Calcium Carbonate (CaCO₃) Systems

As case studies have shown, precipitation of PbS and CaCO₃ species can occur both near the wellbore and higher up the production tubing. (37, 38) PbS precipitation tendency is significantly influenced by temperature, salinity and pH, and as such is analysed on a well-by-well basis through both custom modelling techniques and fouling analysis after equipment recovery. (38, 116) The likelihood therefore of co-precipitation occurring is high, where the spontaneous precipitation of barely soluble PbS towards the wellhead occurs in tandem with CaCO₃ crystallisation. Whilst previous studies have explored PbS and CaCO₃ co-precipitation under single phase conditions, this Chapter aims to explain the influence of the multiphase and presence of an oil-water interface, both on synergistic particle behaviour and interaction in addition to the depositional behaviour on various anti-fouling coatings. Coatings F1, F2 and DLC selected for field trials were tested within this Chapter.

6.1 PbS/CaCO₃ deposition (o/w) emulsion

Figure 6.1 shows PbS/CaCO₃ deposition upon anti-fouling coupons in a multiphase system with an o:w ratio of 5:95, leading to the formation of an o/w Pickering emulsion (Section 3.3.3). It can be seen that far heavier deposition occurred on the REF and DLC surfaces, as opposed to the largely scale-free F1 and F2 hydrophobic coatings. After droplet impaction and rupture however, interfacially stabilised particles remained interlinked, maintaining a persistent film after deposition upon a surface as seen on the REF coupon. Crystal arrangement at the o-w interface can have a significant influence on emulsion stability, where attraction and bridging of particles leads to the formation of a rigid layer or 'shell', cocooning the droplet that forms a film upon rupture. (276, 277) Figure 6.2 shows heavy deposition of PbS/CaCO₃ complexes upon hydrophilic REF and DLC coatings with the PbS/CaCO₃ complexes anchored and grown at the o-w interface deposit as flower-like structures recognisable from those observed from cryo-SEM analysis of the emulsion (Figure 6.6). Underlying heterogenous calcite deposits nucleated directly upon the surface may act as points of attachment for the homogeneously deposited PbS/CaCO₃

complexes, where droplet rupture results in the radial splashing of co-precipitated particles upon hydrophilic surfaces.(270, 271) Bridging and interlocking of the arrangement of PbS/CaCO₃ complexes at the o-w interface (Figure 6.6) prompted formation of a persistent film as described by Douaire et al.,(276) resulting in significant deposition after droplet impaction, best represented on the REF coupon in Figure 6.1.

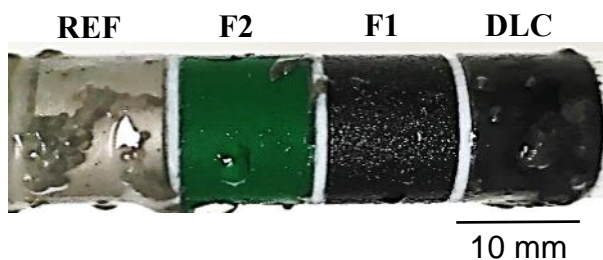


Figure 6.1 Anti-fouling coupons in a multiphase PbS/CaCO₃ system (5:95 o:w ratio)

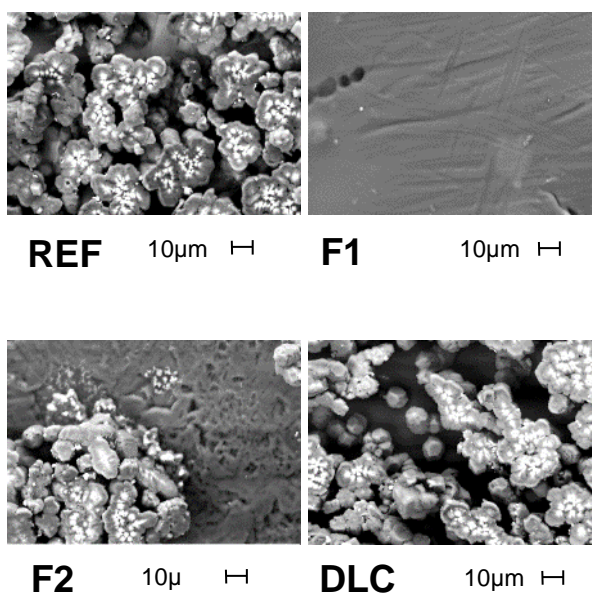


Figure 6.2 SEM of deposited PbS/CaCO₃ complexes on anti-fouling coupons (5:95 o:w ratio)

Figure 6.3 shows SEM and EDX imaging on the REF coupon respectively, where EDX analysis highlights the presence of incorporated PbS agglomerates (blue) within flower-shaped calcite structures (yellow/red).

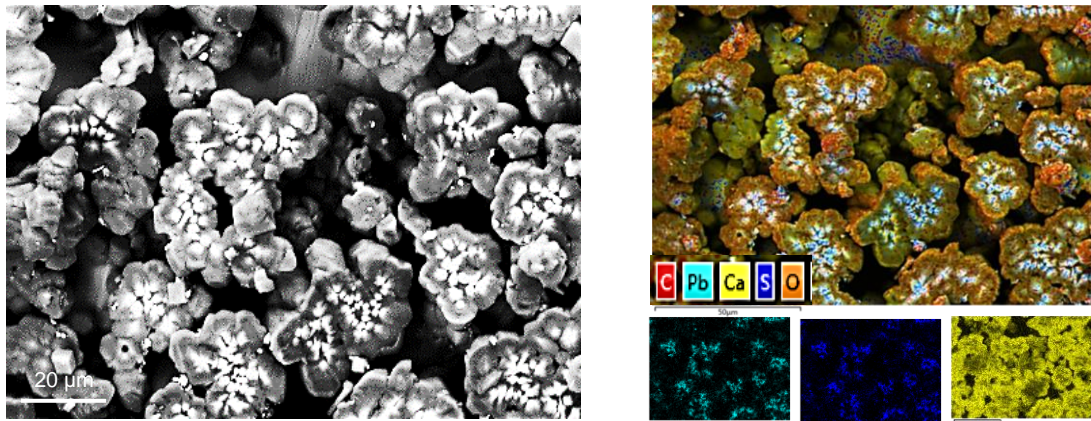


Figure 6.3 SEM and EDX of deposited PbS/CaCO₃ complexes (REF coupon) – o:w 5:95 ratio

As with simple PbS based multiphase systems, there was a particularly strong correlation between the water contact angle of the coating and the mass gain upon coatings (Figure 6.4) due to the tendency of the oil phase to envelop hydrophobic surfaces where $R^2 = 0.96$. This is counter to simple CaCO₃ systems, where heterogeneous nucleation occurs upon both hydrophobic and hydrophilic surfaces, negating the correlation caused by envelopment of the oil layer around F1 and F2 to prevent deposition.(262) The recorded mass gain upon the surfaces of hydrophilic coupons was significantly higher than in simple PbS systems, likely due to the large size and hence mass of the calcite crystal, with deposits on the REF coupon weighing 0.32 and 3.8 mg/cm² for a PbS and PbS/CaCO₃ o/w system respectively.

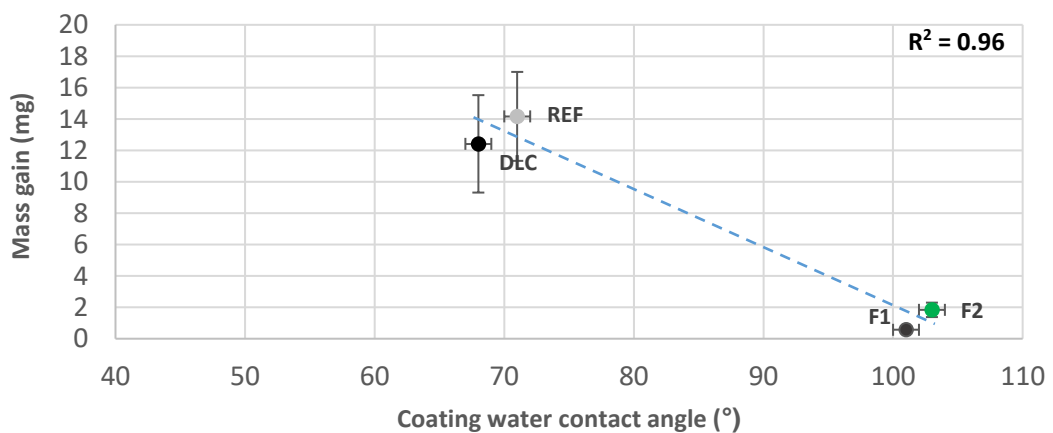


Figure 6.4 Water contact angle vs. mass gain in a multiphase PbS/CaCO₃ system (o:w 5:95 ratio)

6.2 PbS/CaCO₃ emulsion characterisation

Figure 6.5 shows optical microscope images of an oil droplet stabilised by PbS and CaCO₃ within an o/w emulsion. The emulsion at the brine concentration used was relatively polydisperse, with oil droplet size ranging from 0.2 - 1 mm. Images show clearly PbS agglomerates as black dots up to 5 µm in diameter embedded centrally within flower-like calcite structures around 30 - 80 µm in diameter.

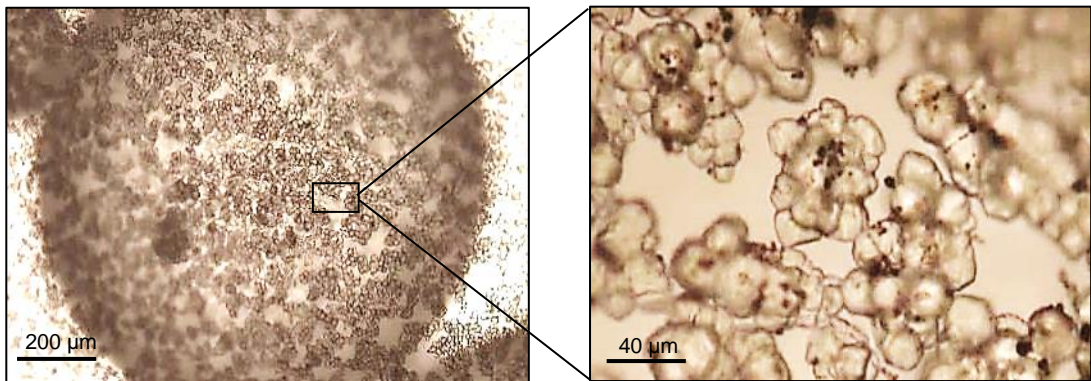


Figure 6.5 Optical microscope images of PbS/CaCO₃ stabilised oil droplet

From cryo-SEM imaging (Figure 6.6), a hemispherical indent from which an oil droplet from an o/w emulsion was dislodged after freezing was investigated (Section 3.7.3.4). PbS/calcite complexes were arranged along the droplet oil-water interface, with BSE revealing occluded PbS agglomerates acting as the centralised nucleation point for propagating calcite crystals. EDX confirmed that PbS agglomerates are incorporated into the calcite structure, with XRD analysis of the dried emulsion showing that PbS and CaCO₃ were the only species formed (Figure 6.9).

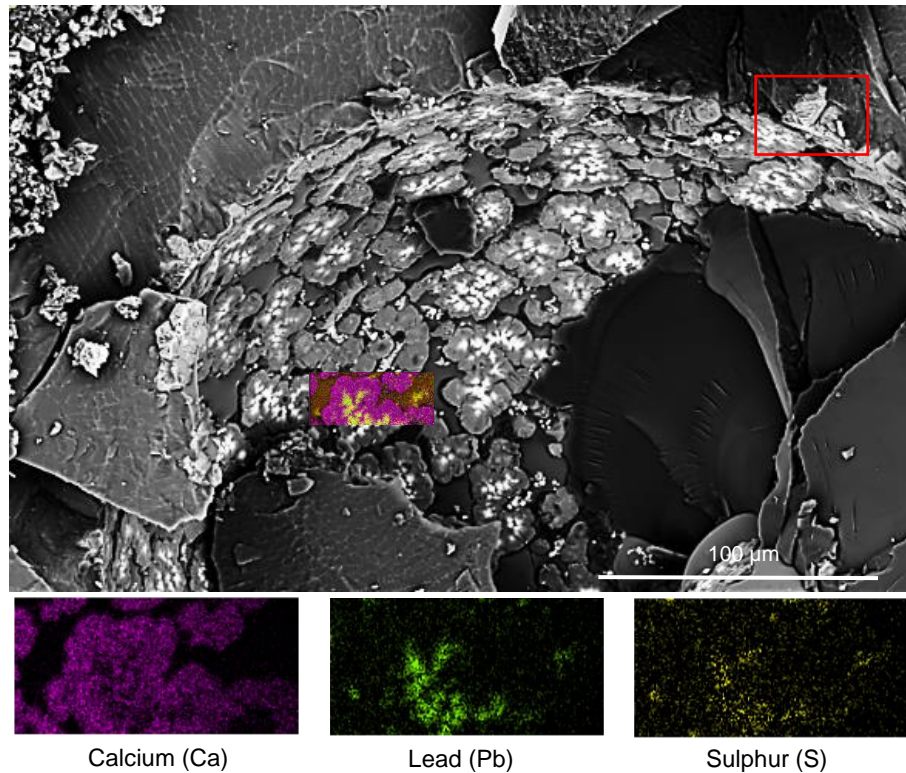


Figure 6.6 Cryo-SEM of PbS/CaCO₃ complexes at o-w interface; EDX shows centralised PbS within calcite structures

Further magnification at the o-w interface (Figure 6.7) showed the pyramidal structure of calcite growing outward from PbS agglomerates, known as 'hopper growth'.(278) Loose PbS agglomerates were also present at the interface that have not acted as seeding points for calcite crystallisation, indicating that self-assembly had occurred at the o-w interface prior to calcite growth. The area highlighted by the red box shows calcite that has grown at the o - w interface, extending around 20 µm and into the aqueous phase where CaCO₃ forming ions are available. Conversely, the PbS/CaCO₃ complex extends only 2 - 3 µm into the oil phase, suggesting that the free energy required for desorption from the interface is lower than that of pure PbS due to hydrophilic properties of calcite.

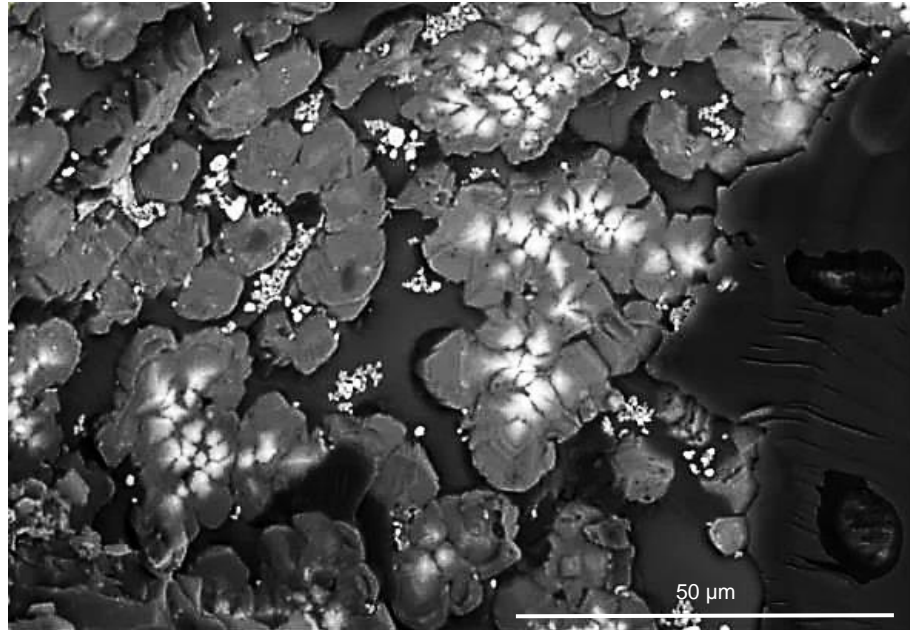


Figure 6.7 Cryo-SEM of PbS/CaCO₃ complexes at o-w interface

Calcite crystals are typically defined by a perfect rhombohedral shape with a dominant [104] face.(279) The transition between rhombohedral and hopper growth occurs at supersaturation where the growth rate of the rhombohedral crystal reaches a maximum. Above this threshold, the growth rate varies as the third power of supersaturation and is hence controlled by the maximum speed of surface integration of new ions, inducing hopper growth as seen centrally in (Figure 6.7). Rhombohedral growth is limited by the incorporation of ions into the calcite surface, with new surfaces being created in their place, where the position of the calcite likely limits ion availability due to the presence of the oil phase.(278) Both galena (cubic) and calcite (trigonal) are prone to hopper growth, indicating a degree of structural similarity that may prompt incorporation of PbS into the calcite structure during co-precipitation.(278, 280)

The exceedingly high $SR_{Initial}$ of PbS (1.3×10^{17}) resulted in spontaneous precipitation of nanoparticles that acted as seeding points for the crystallisation and growth of calcite by occlusion co-crystallisation.(121) Calcite is naturally hydrophilic, with a water contact angle of 6° and as such would not typically adsorb at the o-w interface.(272) The incorporation of PbS into the calcite structure enhanced the hydrophobicity of the PbS/calcite structure, leading to adsorption energy at the o-w interface. Andersson et al.(197) showed that incorporation of the weakly hydrated lead ion into the calcite lattice through cation substitution resulted in increased hydrophobicity of the calcite structure.

From Figure 6.8, where a cross-section of cryo-frozen oil droplet was viewed from the top down, the proportion of the PbS/CaCO₃ complex was immersed in the aqueous phase (lighter) relative to the oil phase (darker) could be gauged, where only a very small proportion of the structure was present in the organic phase due to the hydrophilic properties of calcite. Similarly, alongside Figure 6.6, the degree of calcite extrusion into the aqueous phase was determined to be approximately 20 µm. Occluded PbS agglomerates around which calcite has grown could be seen in Figure 6.8, highlighted in white, within the grey coloured PbS/CaCO₃ structure in the centre of the image.

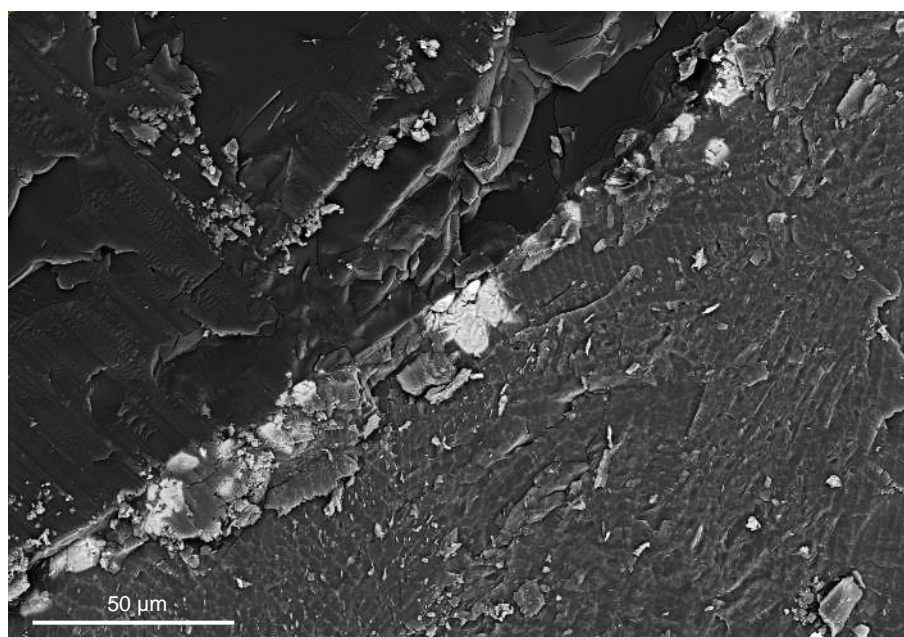


Figure 6.8 PbS/CaCO₃ complexes at the o-w droplet interface

XRD spectra for deposited PbS/CaCO₃ scale can be seen in Figure 6.9, where peaks for both calcite and PbS could be clearly identified and matched to standard reference patterns with high accuracy, where no unidentified species were present. The lack of any non-identifiable peaks indicated that negligible incorporation had occurred, where peaks for species such as PbCO₃ were not visible on spectra. Cryo-SEM with BSE imaging, in conjunction with EDX analysis in Figure 6.6 and Figure 6.7 therefore shows PbS agglomerates that have merely been occluded, rather than Pb²⁺ ions incorporated into the calcite lattice.

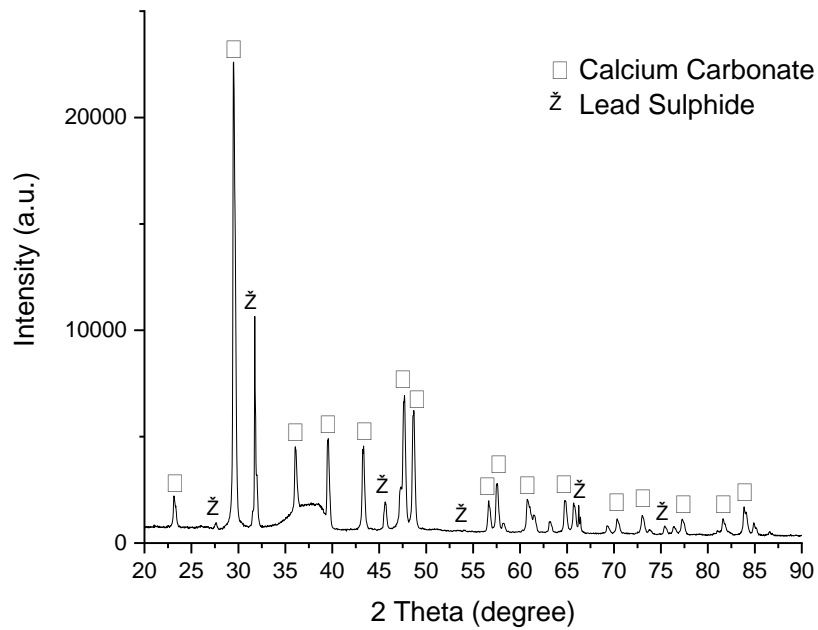


Figure 6.9 XRD of dried PbS/CaCO₃ co-precipitate emulsion

6.3 PbS pre-precipitation (o/w emulsion)

Pre-precipitation experiments where approximately 500 mg/L of PbS nanoparticles were introduced into the reaction vessel prior to the experiment demonstrated that agglomerates acted as seeding points at the o-w interface (Section 3.6.3.2), with deposited PbS/calcite structures are similar to those seen in co-precipitation tests (Figure 6.10).

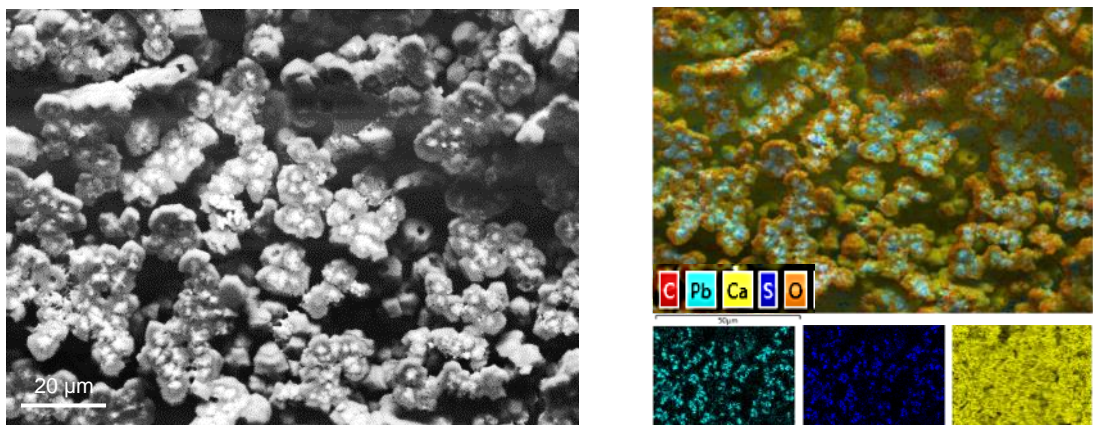


Figure 6.10 SEM and EDX of deposited PbS/CaCO₃ complexes after pre-precipitation and dosing of PbS agglomerates – o:w 5:95 ratio

6.4 PbS/CaCO₃ emulsion inversion

The phase distribution at which emulsion inversion occurs for a complex PbS/CaCO₃ system can be observed in Figure 6.11, whereby an o/w emulsion formed above the aqueous phase when oil volume fraction was less than 0.5 (Section 3.6.1). Increasing of the dispersed oil phase volume fraction to over 0.5 resulted in a catastrophic inversion, similar to that observed in PbS stabilised systems (Figure 5.20).(165)

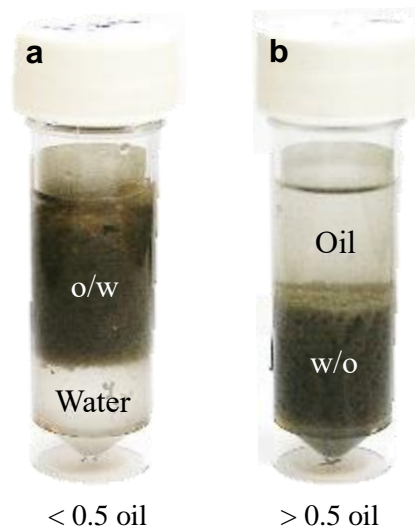


Figure 6.11 PbS/CaCO₃ system – a) o/w emulsion at < 0.5 oil phase fraction; b) w/o emulsion at > 0.5 oil phase fraction

Emulsion inversion at an oil volume fraction of 0.5 suggests that the PbS/CaCO₃ complex at the o-w interface has a water contact angle of approximately 90°, incongruent with the partially and strongly hydrophilic nature of PbS and calcite respectively.(272) It may be the case that the nature of calcite complex growth at the o-w interface, as opposed to typical bulk nucleation and adsorption observed with PbS, leads to interfacial growth and protrusion into the oil phase and seemingly higher hydrophobicity at the interface.

6.5 PbS/CaCO₃ deposition (w/o emulsion)

PbS/CaCO₃ deposition upon anti-fouling coupons in a w/o emulsion, where o:w ratio is 60:40, can be seen in Figure 6.12. As with scaling in the o/w

emulsion system, hydrophobic fluoropolymers F1 and F2 are scale-free, whilst the hydrophilic REF and DLC have a significant amount of deposition upon their surface (Figure 6.13). Excess oil, readily available to envelop the hydrophobic surfaces, prevents the deposition of PbS/CaCO₃ stabilised emulsion that is prone to impaction on surfaces contained within the aqueous phase.

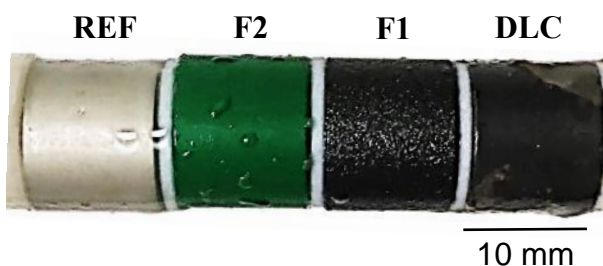


Figure 6.12 Anti-fouling coupons in a multiphase PbS/CaCO₃ system (60:40 o:w ratio)

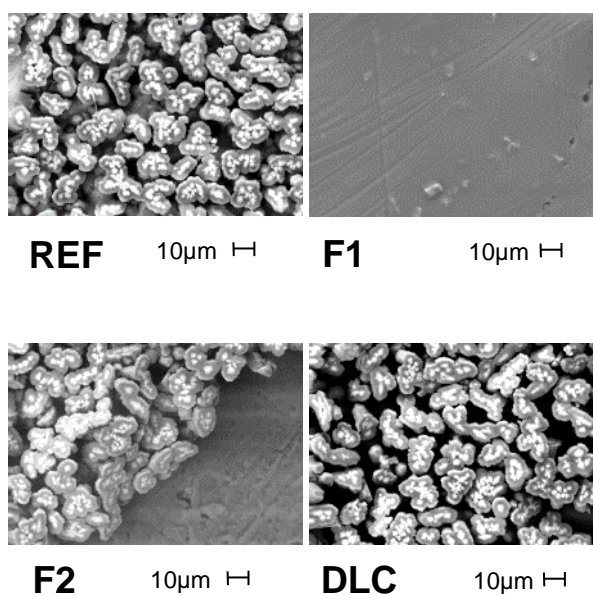


Figure 6.13 SEM of deposited PbS/CaCO₃ complexes on anti-fouling coupons (60:40 o:w ratio)

SEM and EDX imaging (Figure 6.14) revealed the familiar pattern whereby PbS agglomerates acted as seeds for calcite nucleation and growth before deposition through emulsion droplet impaction upon the REF coupon. The average size of the PbS/CaCO₃ complexes varied from 10 - 20 μm, smaller than in o/w systems where typical size of PbS/CaCO₃ complexes ranged from

20 - 30 μm . Reduction in the availability of scaling ions due to a drop in overall aqueous volume (0.95 to 0.4 volume fraction) was likely responsible for the limited growth of calcite structures around PbS agglomerate clusters.

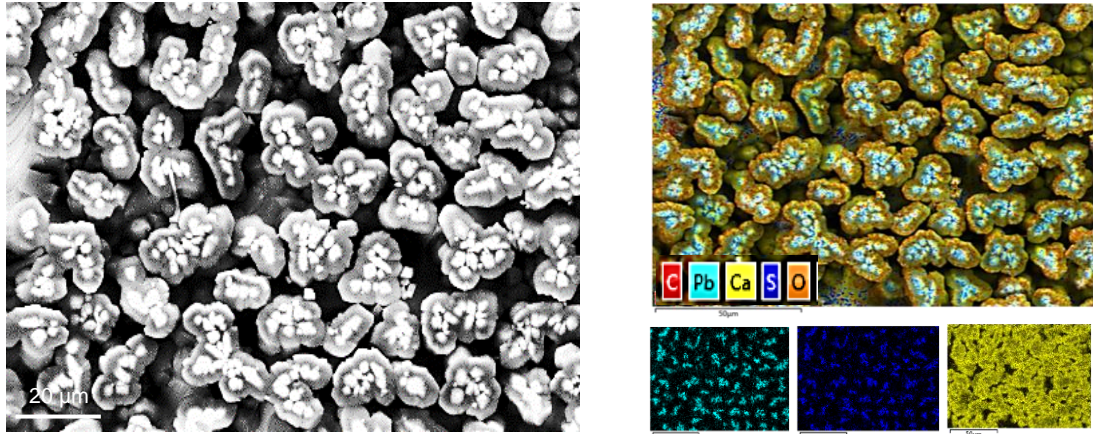


Figure 6.14 SEM and EDX of deposited PbS/CaCO₃ complexes (REF coupon) – o:w 60:40 ratio

Figure 6.15 showed that similarly to deposition in o/w PbS/CaCO₃ Pickering emulsion systems, hydrophilic coatings saw a proportionally high degree of mass gain due to the lack of an enveloping oil layer on the surface, whereas hydrophobic fluoropolymers F1 and F2 received less than 1 mg of scaling where $R^2 = 0.78$.

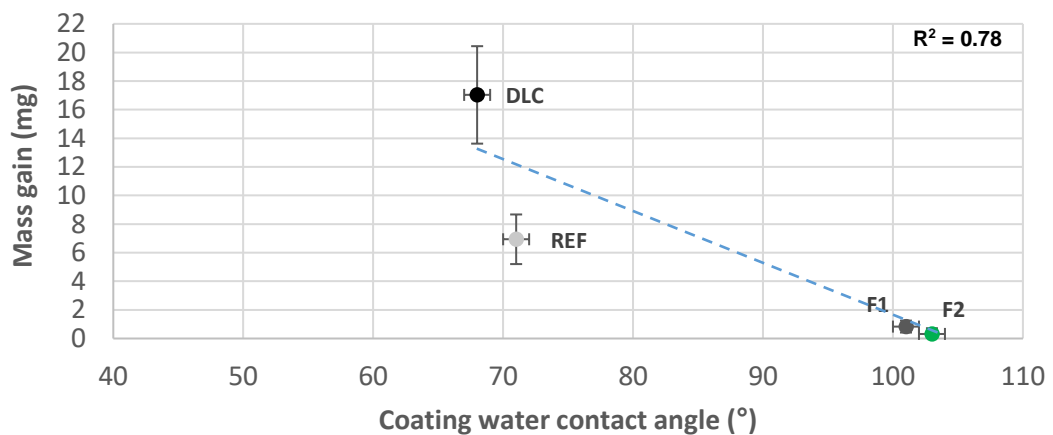


Figure 6.15 Water contact angle vs. mass gain in a multiphase PbS/CaCO₃ system (o:w 60:40 ratio)

6.6 Chapter summary

6.6.1 PbS occlusion in CaCO₃ at the o-w interface

Co-precipitation of PbS and CaCO₃ in a turbulent multiphase system resulted in the formation of a Pickering emulsion, stabilised by complexes in which PbS agglomerates were incorporated into a flower-shaped calcite structure through occlusion co-precipitation at the o-w interface. Spontaneous nucleation of PbS in the bulk aqueous phase as a result of an exceedingly high SR_{initial} of 1.3×10^{17} resulted in adsorption of particles and agglomerates to the o-w interface that then acted as seeding points for the secondary nucleation of slow growing calcite structures.(113-115)

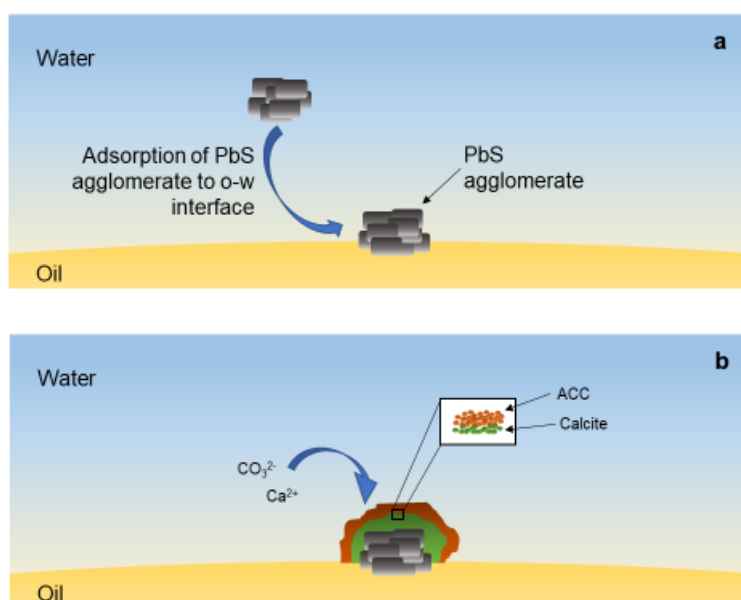
The role of the multiphase was of paramount importance in the formation of the partially-wetted PbS/CaCO₃ complex, as shown when compared to tests in single phase conditions, where truncated octahedral calcite was nucleated upon the substrate with negligible incorporation of PbS into the structure (Figure 4.18). The assembly of PbS particles at the interface is therefore integral with respect to growth of the incorporated PbS/CaCO₃ structure. In Pickering emulsions, the arrangement of emulsion stabilising particles adsorbed at the o-w interface can prompt creation of an encompassing PbS matrix that acts as a template for the interfacial heterogeneous nucleation of calcite in the aqueous phase, lowering the activation energy of calcite nucleation.(276) Such behaviour has been documented in the crystallisation of fat crystals in emulsified foods such as butter, where additives are included in the melt to act as seeding or crystallisation points.(276) For the stabilising particles to act as a template, the emulsifier (PbS) and the solidifying crystal (calcite) should exhibit some level of structural similarity. The propensity for both galena and calcite to exhibit cubic morphology enforces the notion that similarities in the crystal structure enabled occlusion of the PbS agglomerate within the calcite. In this case, the PbS stabilised at the interface enhances both the heterogeneous nucleation process and kinetics of calcite crystallisation.(281, 282)

pH values for formation waters will lie between approximately 4.6 and 8.9, a pH band at which sulphate groups form readily on the PbS surface given that conditions are anoxic.(153) This will, as with sulphate rich organic sites within an eggshell membrane that promote calcification (Section 2.9.3), create an area of elevated local supersaturation at the surface of the PbS agglomerate extending into the aqueous phase to which Ca²⁺ and CO₃²⁻ ions from solution migrate and nucleate. It is possible that, as a result of the high SR_{Initial} of CaCO₃, flat ACC accumulates on the PbS surface immersed within the

aqueous solution, forming substantial deposits. The CaCO_3 mineral deposits then transform through secondary nucleation into large calcite crystals, with disk-shaped ACC and smaller CaCO_3 on the surface dissolving and supplying ions for further calcite growth where flat surfaced morphologies are dominant. The flower-shape of the calcite that occluded the PbS agglomerate at the interface is likely a result of the secondary nucleation determining the calcite orientation, based on the initial calcite seeds that provided a template for propagation of the initial ACC front transforming to calcite at neutral pH values of < 7 .

The driving force behind the direct transformation of ACC to calcite may be the formation of pre-nucleation clusters with a proto-calcitic and poorly crystalline structure.(283-285) Turbulent multiphase flow results in the high mass transport of scale-forming ions and pre-nucleation clusters to interfaces, where they crystallise through secondary nucleation from ACC to calcite.(125) The presence of impurities such as Mg^{2+} ions has been shown to remove the intermediary transformation stage, where vaterite is formed as a pre-cursor to calcite under ambient conditions.(124, 286, 287)

Figure 6.16 shows the growth of calcite around occluded PbS agglomerates at an o-w interface, adapted from Navarro et al.(124)



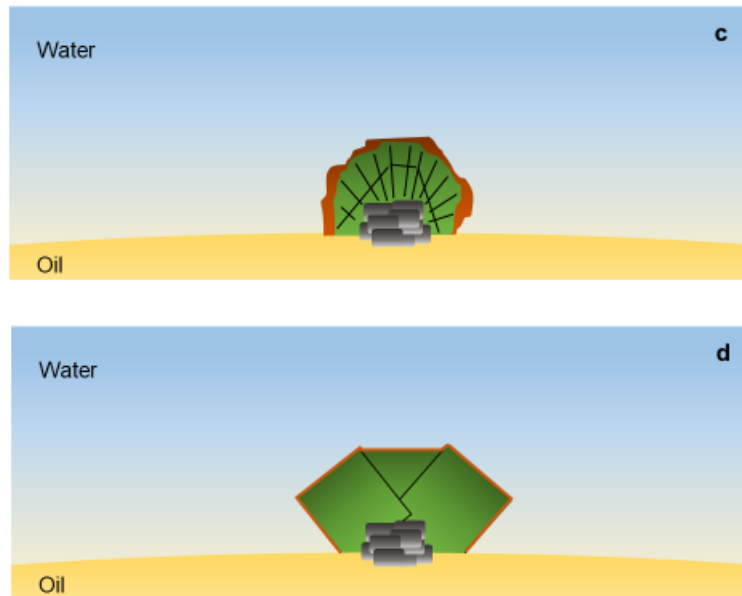


Figure 6.16 Growth of calcite around occluded PbS agglomerates at an o-w interface

6.6.2 PbS/CaCO₃ emulsion behaviour

Emulsion type was inverted from o/w to w/o at approximately 0.5 oil volume fraction. From (Figure 5.20) it can be seen that PbS only systems undergo emulsion inversion from o/w to w/o when the oil phase fraction is > 0.75 , demonstrating high kinetic stability. Particle arrangement at the o-w interface plays an important role in emulsion stabilisation, preventing the flocculation, ripening and coalescence of droplets due to high PbS packing fraction and subsequent particle jamming.(268) From comparison of oil droplet particle packing fraction in both PbS and PbS/CaCO₃ systems, it can be inferred that in PbS systems, the nature of the particle/agglomerate arrangement results in a higher packing fraction of adsorbed scale at the o-w interface. Highlighted areas in Figure 6.17, show $> 90\%$ and $\sim 60\%$ coverage for a PbS and PbS/CaCO₃ coated droplets respectively. In PbS/CaCO₃ systems this likely results in higher flocculation and Ostwald ripening due to the ability of oil droplets to form a bridge and ultimately coalesce at lower oil phase fractions.(167)

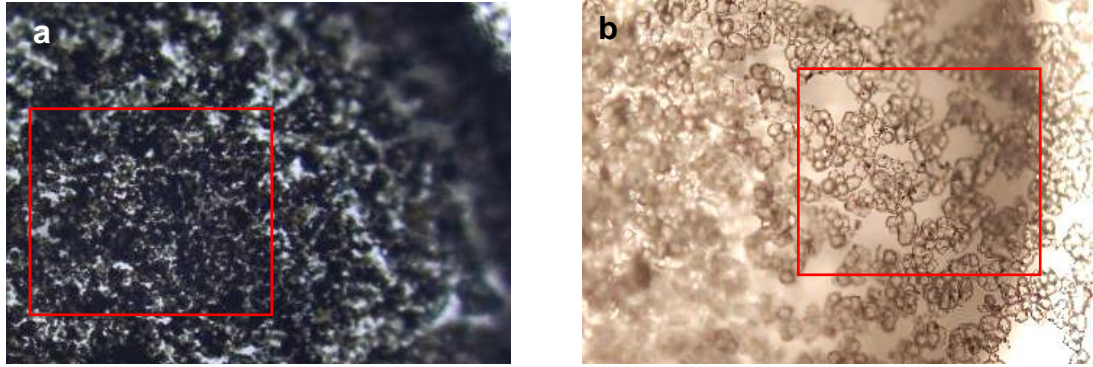


Figure 6.17 a) PbS arrangement at oil droplet interface – high packing fraction; b) PbS/CaCO₃ arrangement at oil droplet interface – low packing fraction

The presence of calcite likely reduced the energy required for desorption of the PbS/CaCO₃ complex from the o-w interface, where its hydrophilicity dictated a large portion of the crystal would be contained within the aqueous phase. This detachment in turn would have aided in the flocculation and ripening of droplets as oil phase fraction was increased.(288)

The deposition of PbS and CaCO₃ crystals upon the surface of anti-fouling substrates did not follow the deposition patterns seen in simple CaCO₃, BaSO₄ and PbS multiphase systems where impacting oil droplets left circular areas free of scale (Figure 5.9). In PbS/CaCO₃ systems, coverage was generally uniform on hydrophilic surfaces, where scale had nucleated directly onto the substrate, with large areas covered by homogeneously adhered ruptured film (Figure 6.1). Calcite of truncated octahedron morphology that had precipitated heterogeneously upon surfaces likely promoted the emulsion deposition of PbS/CaCO₃ complexes adsorbed at the o-w interface due to increased substrate roughness driving attachment. The lower stability of PbS/CaCO₃ droplets, as shown in Figure 6.17 as a consequence of the lower packing fraction at the interface, resulted in the probable rupture of any oil droplet impacting the substrate.

Whilst this system is clearly not entirely representative of downhole conditions due to obvious differences in temperature/pressure etc., the interaction between two different scale types and the influence of a multiphase interface on said interaction is both relevant and significant. Calcite, due to its high hydrophilicity, does not adsorb at the o-w interface as readily as PbS. The presence therefore of partially hydrophobic particles or agglomerates that can prompt nucleation at the droplet interface as opposed to on other foreign surfaces could be beneficial in reducing heterogeneous crystallisation and

further growth in oilfield systems. It was shown in Figure 6.1 however that hydrophilic REF and DLC surfaces were still prone to heavy deposition, due to the impaction of scale particle-coated droplets within a Pickering emulsion upon their surface and subsequent adhesion. As with PbS systems seen in Chapter 5, hydrophobic surfaces F1 and F2 were able to largely prevent contact and deposition of the scale-stabilised emulsions by way of excess oil wetting the surface, demonstrated by the minimal mass gain.

Comparison of the degree of scaling seen on hydrophobic fluoropolymers in CaCO_3 and PbS/CaCO_3 multiphase systems showed mass gain was 0.75 and 0.15 mg/cm^2 respectively on the F1 surface. It is therefore clear that the presence of PbS at the o-w interface impacted the ability of calcite to deposit and grow directly upon hydrophobic substrates.

6.6.3 Chapter Highlights

- During co-precipitation of PbS and CaCO_3 , PbS agglomerates can act as seeding points for calcite growth at the o-w interface in multiphase systems
- Entrapment of the PbS agglomerate in the growing calcite structure is characterised as 'occlusion co-precipitation'
- As with PbS deposition in multiphase systems (Chapter 5), oil wetting plays a critical role in determining surface deposition within complex multiphase systems
- The presence of PbS particles in CaCO_3 multiphase systems was shown to reduce calcite deposition upon hydrophobic surfaces, by providing an alternative nucleation point at droplet interfaces at which calcite could precipitate and grow. This ultimately limited the heterogeneous nucleation of calcite upon hydrophobic surfaces
- Sulphate groups at the PbS surface resulted in an increased flux of Ca^{2+} and CO_3^{2-} ions, with high SR leading to the growth of amorphous calcium carbonate (ACC) that then transforms into calcite, resulting in a flower-shaped structure
- Reduced packing fraction of mineral scale at the interface of PbS/CaCO_3 systems compared to PbS only systems (~60% to ~90% respectively) results in catastrophic phase inversion occurring at 0.5 oil volume fraction as opposed to 0.75 in PbS systems. When packing fraction at the o-w interface is reduced, flocculation and oil droplet bridging occurs more readily.

Chapter 7

Influence of Poly(2-acrylamido-2-methyl-1-propanesulfonic acid) (PAMPS) on PbS precipitation and deposition in single and multiphase systems

Sulphonic acid-based polymers such as poly(2-acrylamido-2-methyl-1-propanesulfonic acid) (PAMPS) are widely used in metal cation removal for wastewater applications. Consequently, they are of use in the oil and gas industry in both preventing the nucleation and growth of problematic scales. Chapter 7 aims to quantify the fundamental acting interfacial forces between PAMPS functionalised PbS and surfaces of varying wettability through force curve analysis, before demonstrating empirically that anti-fouling surface characteristics have an influence on PbS deposition in both single and multiphase systems. The effect of high PAMPS inhibitor concentration on PbS precipitation and emulsion behaviour was explored in multiphase experiments. Testing at elevated concentrations simulated batch injection methods or squeeze treatment, often used for scale inhibitor delivery in oilfield wells, whereby very high concentrations of inhibitor are pumped into the near-wellbore area that are then diluted by the produced water stream over time. The influence of additional scale-forming species was also probed, with the effect of PAMPS on scale formation in a PbS/CaCO₃ forming system investigated. Coatings F1, F2 and DLC selected for field trials were tested within this Chapter.

7.1 PAMPS adsorption on PbS/galena

From topographic and phase scanning measurements using AFM contact mode, it can be seen that PAMPS adsorbs onto the cleaved galena substrate on the [001] face, where white dots on Figure 7.1 represent deposited polymer acting as raised asperities. ImageJ analysis of Figure 7.1a showed that PAMPS surface coverage was approximately 80%, where the influence of electrostatic repulsion of the sulphonic acid head groups between adsorbing molecules prevented formation of a uniform film.(289) Adsorption of PAMPS was performed in 0.5 M KCl electrolyte solution to alleviate the influence of the EDL and provide a solution representative of high TDS oilfield brines. The net negative surface charge of the galena substrate at pH 5.2 (-8.8 mV) and respective contact angle of 49° when unoxidised, resulted in a partially

hydrophobic surface directly after cleaving. Oxidative dissolution of isolated cubic areas upon the freshly cleaved galena occurred with time after exposure, leading to the emergence of regions with increased hydrophobicity, prompted by the limited formation of anglesite, thiosulphates and sulphites under weakly acidic conditions of pH 5.2.(152, 290)

PAMPS, as an amphiphilic molecule with a hydrophobic backbone and hydrophilic sulphonic acid group, is able to adsorb onto both hydrophilic and hydrophobic areas. Long range attraction because of hydrophobic force has been shown to be responsible for higher levels of PAMPS adsorption onto areas of higher hydrophobicity.(177, 291) Consequently, it was expected that a significant proportion of adsorbed PAMPS molecules would have their negatively charged sulphonic acid group facing away normal to the substrate and into the solution, endowing the surface with a higher negative overall charge, as shown in Table 7.1. Areas of high and low PAMPS coverage in Figure 7.1 may be explained by the tendency of cleaved galena to form hydrophobic regions more susceptible to adsorption. As such, during AFM force curve measurements, contact mode analysis was performed on the galena substrate prior to force curve readings in order to identify areas of high PAMPS coverage.(177, 290)

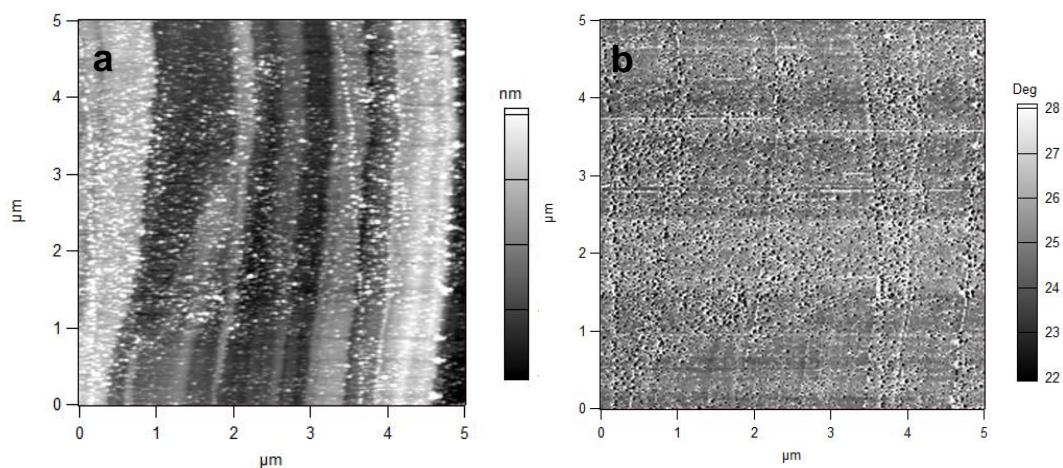


Figure 7.1 a) 2 x 2 μm area of PAMPS functionalised galena analysed through contact mode topography; b) respective phase image

Zeta-potential measurements of PbS particles synthesised in single phase systems in the presence of 0 and 50 mg/L PAMPS gave an indication as to

the influence of PAMPS functionalisation on surface charge. Table 7.1 shows the influence of PAMPS concentration on PbS particle zeta-potential.

Table 7.1 PbS zeta-potential at 0 and 50 mg/L concentration

PAMPS concentration (mg/L)	PbS zeta-potential (mV)
0	-8.8 ± 0.7
50	-24.8 ± 2.2

Wettability of the galena substrate as a result of increased net negative charge after PAMPS functionalisation is shown in Figure 7.2, where oil-galena-water TPC is $151.4 \pm 3.3^\circ$ compared to $132.1 \pm 1.8^\circ$ where no polyelectrolyte is present. Subsequently, water-galena-air contact angle is reduced to $29.5 \pm 2.4^\circ$ from $47.9 \pm 0.6^\circ$ on untreated galena substrate.

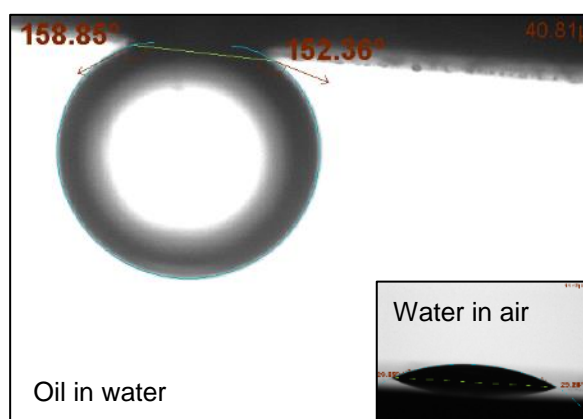


Figure 7.2 Main image - inverted sessile drop of oil on PAMPS functionalised galena in aqueous solution where oil CA is $151.4 \pm 3.3^\circ$; Thumbnail - water contact angle on PAMPS functionalised galena in air where water CA is $29.5 \pm 2.4^\circ$

7.2 PAMPS functionalised PbS adhesion

Figure 7.3a and b show the force curve approach results for an untreated (hydrophilic) and an OTS functionalised (hydrophobic) Si_3N_4 tip against a polymer functionalised galena surface respectively. Unlike on an untreated galena surface, there does not appear to be any jump-in as a result of

attractive forces in Figure 7.3a due to moderate electrostatic repulsion between two hydrophilic surfaces despite high system salinity. No obvious jump-in is detected in Figure 7.3b however, perhaps due to the compression of long chain polymers as the tip approaches the galena substrate. (292)

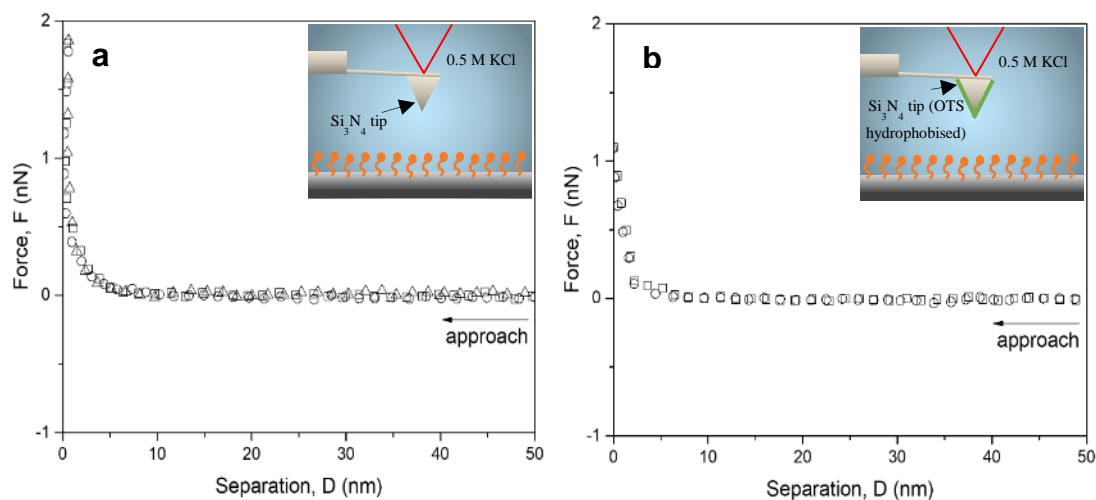


Figure 7.3 Force curve upon approach – a) Untreated Si₃N₄ tip and PAMPS functionalised galena substrate; b) Si₃N₄ (OTS treated) tip and PAMPS functionalised galena substrate

Despite no apparent jump-in recorded on approach for a hydrophobic tip on a polymer functionalised surface where vdW attraction was expected (Figure 7.3b), the measured adhesion force upon tip retraction was significantly higher for the OTS hydrophobised condition than for the untreated hydrophilic tip. This may indicate the presence of a net positive charge on the OTS functionalised tip due to preferential adsorption of hydronium ions (H₃O⁺), resulting in electrostatic attraction between the PAMPS functionalised substrate and the positively charged tip. (293) Figure 7.4 displays the adhesion force upon retraction of the tip, where measured adhesion force was 0 and 33.4 ± 4.6 mN/m for an untreated AFM tip and OTS treated AFM tip upon functionalised galena respectively.

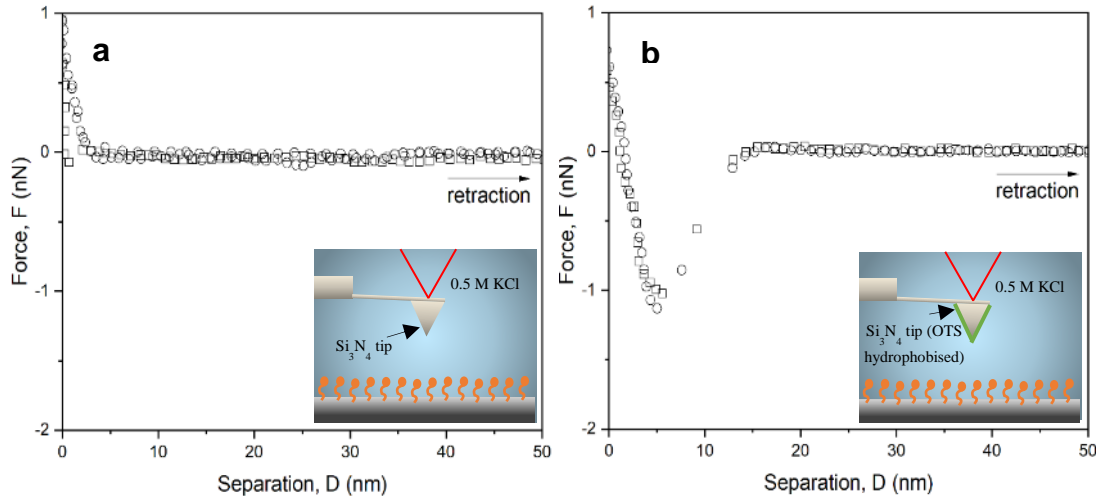


Figure 7.4 Force curve upon retraction – a) Untreated Si_3N_4 tip and PAMPS functionalised galena substrate; b) Si_3N_4 (OTS treated) tip and PAMPS functionalised galena substrate

The hydrophilic REF and DLC coupons show negligible PbS surface deposition due to the lack of attractive vdW and hydrophobic forces present between the substrate and polymer functionalised PbS particles, where zeta-potential was measured as -24.8 ± 2.2 .(104) The hydrophobic substrates F1 and F2 however prompted adhesion of functionalised PbS particles from the bulk phase, driven by the vdW electrostatic attraction. This is demonstrable from Figure 7.4b, where adhesion was measured as 33.4 ± 4.6 mN/m.

Force curve measurements on long-chain polymer functionalised surfaces can often lead to measured inaccuracies that stem from unwanted attachment of the branched polymer to the tip. This can result in pulling and peeling of the attached polymer from the substrate upon retraction of the AFM tip, distorting adhesion force measurements.(292) This phenomenon was not encountered in force curve measurements upon retraction of the AFM tip under either the hydrophilic or hydrophobic condition.

7.3 PbS deposition in single phase – 50 mg/L PAMPS

Figure 7.5 shows PbS deposition on anti-fouling surfaces when 50 mg/L of PAMPS polyelectrolyte was present in the initial KCl/PbCl_2 (Brine C) solution. Whilst visually the degree of PbS deposition on the black F1 and DLC surfaces was hard to determine, it can be seen that the REF coupon is virtually scale-

free, and the usually green F2 coupon has undergone significant PbS deposition.

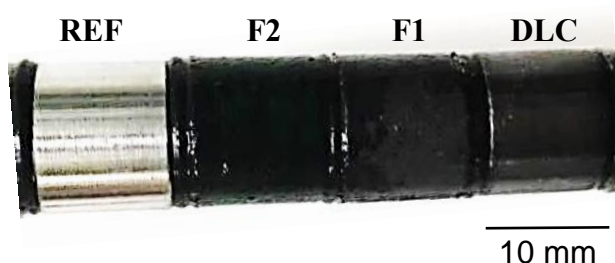


Figure 7.5 Photographs of samples – PbS single phase conditions - 50 mg/L PAMPS

From Figure 7.6, there is a reasonable trend ($R^2 = 0.83$) between coating water contact angle and mass gain upon surfaces, where hydrophobic surfaces are more prone to PbS deposition.

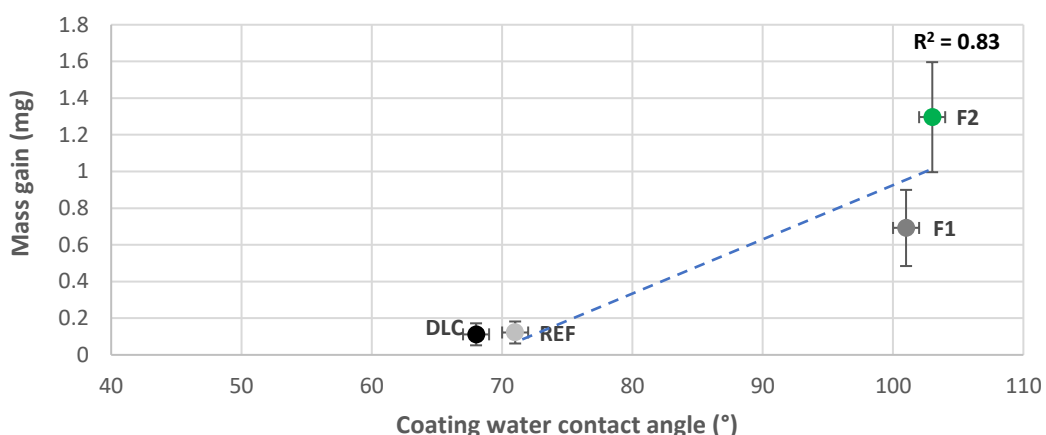


Figure 7.6 Water contact angle vs. mass gain in a single phase PbS system – 50 mg/L PAMPS

Increasing the negative surface potential (Table 7.1) of PbS particles from -8.8 to -24.8 mV through PAMPS polyelectrolyte functionalisation enhanced the strength of the electrostatic repulsive force of PbS against hydrophilic substrates such as REF and DLC. Interaction of functionalised PbS particles with hydrophobic substrates however increased the net surface charge and hence attractive vdW force.(294) The presence of interaction forces on a molecular level was subsequently confirmed through AFM analysis, as seen in Figure 7.3 and Figure 7.4.

As an amphiphilic molecule, PAMPS had the potential to adsorb primarily onto positively charged hydrophobic surfaces, as well as hydrophilic surfaces as a result of hydrophobic force and electrostatic attraction respectively.(177) Consequently, recorded mass gain could be partially attributed to polyelectrolyte attachment, with PAMPS adsorption upon both the scale particles and substrate likely to limit PbS deposition as a consequence of increased electrostatic repulsion.

The influence of PAMPS functionalisation on PbS particle size distribution and agglomeration tendency may also play a role in deposition, where PSD analysis showed average diameter of colloids was determined to be 4434 nm and 837 nm for systems with 0 and 50 mg/L of PAMPS respectively. Whilst adhesion force of a particle or agglomerate to a substrate increases with particle size, the influence of turbulent flow at the interface on particle removal in systems is dominant. Smaller particles or agglomerates, albeit with lower adhesion, have a higher substrate contact area to volume ratio and therefore are less likely to be removed from the substrate.(140) This may in part explain the increase in deposited mass gain on fluoropolymer surfaces F1 and F2 between PAMPS-containing and PAMPS-free systems, displayed in Figure 7.5 and Figure 4.8 respectively.

As discussed in Section 4.3, it is feasible that the increased roughness of fluoropolymers F1 and F2 compared to REF and DLC had an influence on PbS particle deposition. Due to the complex influence of the many substrate roughness parameters on deposition it was difficult to quantify how significant coating topography is on overall mass gain when compared to interacting forces.(140)

7.4 PbS deposition in o/w multiphase – 50 mg/L PAMPS

From Figure 7.7, it can be seen that there is very little effect on depositional pattern and appearance when compared to uninhibited systems (Figure 5.7), where a black emulsion is deposited on the REF coupon and hydrophobic fluoropolymers F1 and F2 see very low levels of mass gain on their surfaces. 50 mg/L of PAMPS within the initial brine was clearly not sufficient to remove all 1000 mg/L of Pb^{2+} ions within solution, with a large proportion left free to react with dissociated HS^- anions.

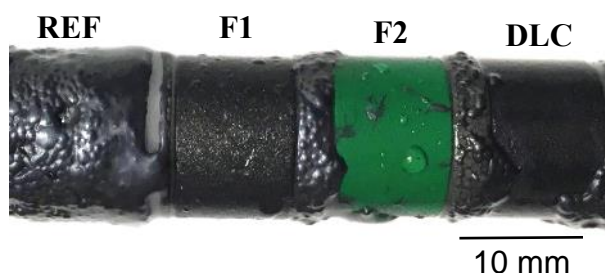


Figure 7.7 Photographs of samples – PbS multiphase conditions - 50 mg/L PAMPS

Analysis of the PbS emulsion formed at 50 mg/L PAMPS showed little difference from the uninhibited emulsion seen in Figure 7.8 in terms of appearance. There was a slight difference in the time taken for the water phase to separate and form a stable Winsor type III emulsion, shifting from 40 to 60 seconds for uninhibited and 50 mg/L PAMPS solutions respectively. This was caused by the stabilising effect of the high MW polymer alongside the PbS particles, resulting in emulsion tightening where droplets range from 150 – 400 μm .

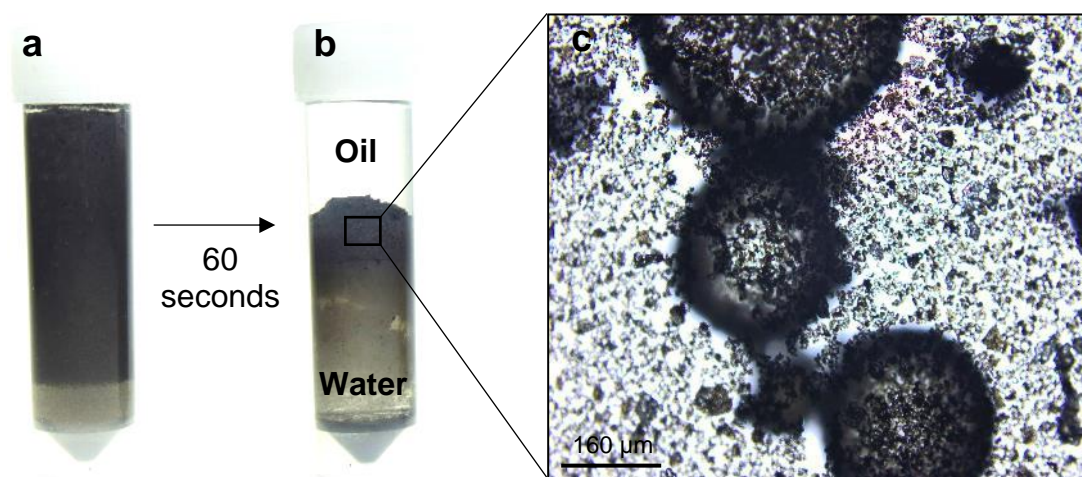


Figure 7.8 PbS multiphase system - 50 mg/L PAMPS a) Post-experimental emulsion after agitation; b) Separation into stable 3-phase emulsion after 60 seconds; c) Optical microscope image of oil droplet (x20 mag)

The presence of the excess oil phase wetted to the fluoropolymer substrates prevented deposition of the PbS emulsion, whilst hydrophilic surfaces saw significant mass gain upon their surfaces resulting in a strong correlation between water contact angle and mass gain where $R^2 = 0.89$.

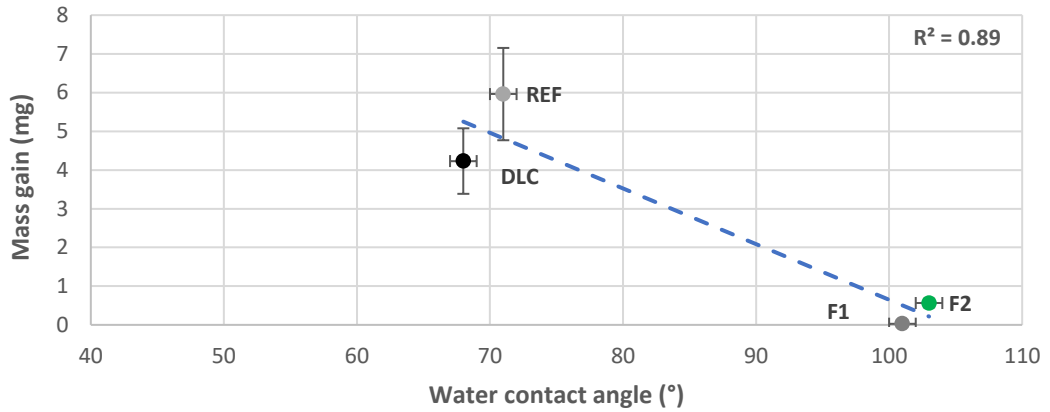


Figure 7.9 Water contact angle vs. mass gain in a multiphase PbS system – 50 mg/L PAMPS

7.5 PbS deposition in o/w multiphase – 500 mg/L PAMPS

Figure 7.10 shows deposition upon coupons of the PbS emulsion, where deposits can be seen on hydrophilic REF and DLC coupons, with hydrophobic surfaces F1 and F2 remaining relatively scale-free. PbS presence has been clearly reduced, with the emulsified deposit a translucent brown colour as opposed to the opaque black emulsion present when no inhibitor is present (Figure 5.7).

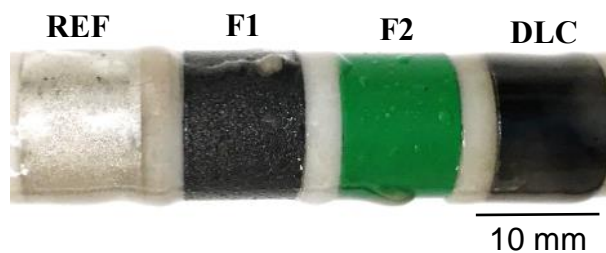


Figure 7.10 Photographs of samples – PbS multiphase conditions - 500 mg/L PAMPS

As in other multiphase systems where no inhibitor is present, emulsion deposition is limited on the surfaces of hydrophobic fluoropolymers where an excess, un-emulsified oil phase is present. This results in a good correlation between coating water contact angle and depositional mass gain, where $R^2 = 0.92$.

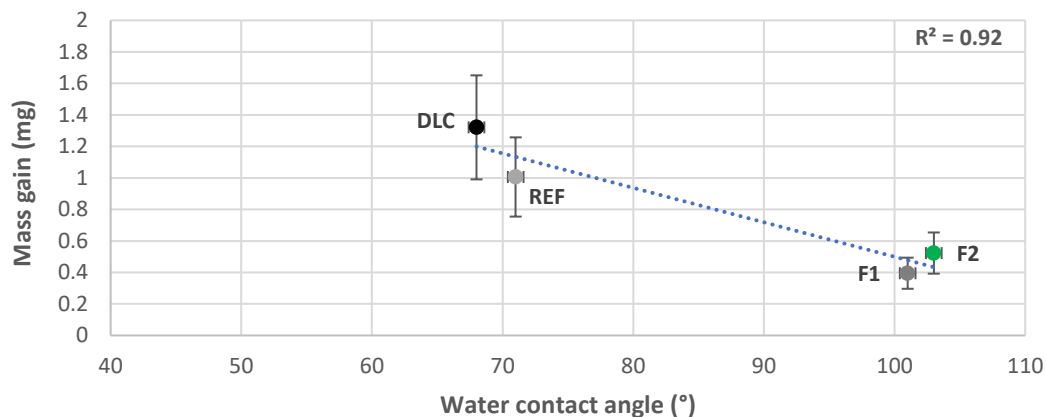


Figure 7.11 Water contact angle vs. mass gain in a multiphase PbS system – 500 mg/L PAMPS

The appearance of the emulsion changes drastically based on PAMPS concentration, whereby the precipitation and growth of PbS particles is reduced through both nucleation inhibition and growth retardation respectively.(178) From Figure 7.12a, the brown appearance of the emulsion indicates a reduction in the presence of PbS.

When no PAMPS was present, the Pickering emulsion separated and stabilised into a Winsor type III emulsion where three distinct phases (oil/emulsion/water) were visible approximately 40 seconds after agitation (Figure 5.13). Addition of PAMPS at 500 mg/L however significantly increased the time taken for the emulsion to become demulsified, where individual phases separated out, as seen in (Figure 7.12a & b) respectively. At 500 mg/L PAMPS concentration, though more stable, the oil phase was not fully emulsified, with a distinct layer present above the o/w emulsion (Figure 7.12b).

The size of oil droplets within the emulsion were generally reduced, with a rise in mono-dispersity as polymer concentration was increased. Maximum oil droplet sizes of 700 and 160 microns were recorded at PAMPS concentrations of 0 and 500 mg/L respectively, from optical microscope images (Figure 5.14 and Figure 7.12c). When no PAMPS was present, agglomerates of PbS nanoparticles were seen to stabilise oil droplets, forming a Pickering emulsion. When PAMPS was introduced to the system however, negligible PbS agglomerates were visible at droplet interfaces due to complexation of the free Pb^{2+} ions in solution and inhibitory effect of the PAMPS polyelectrolyte. Tightening of the emulsion occurred however due to the surfactant-like properties of the long-chain PAMPS molecule leading to increased stabilisation.

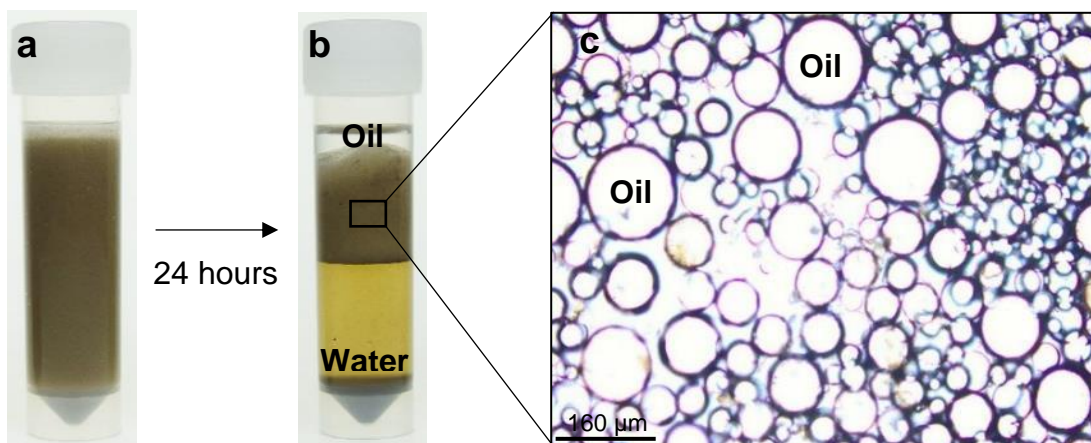


Figure 7.12 500 mg/L PAMPS inhibitor a) Post-experimental emulsion after agitation; b) Separation into stable Winsor type III emulsion after 24 hours; c) Optical microscope image of oil droplets (x20 mag)

7.6 PbS deposition in o/w multiphase – 5000 mg/L PAMPS

From Figure 7.13, it can be seen at heightened concentrations of 5000 mg/L PAMPS that emulsion deposition is uniform over all anti-fouling surfaces regardless of wettability, with the formed emulsion cream coloured in appearance indicating negligible presence of precipitated PbS.

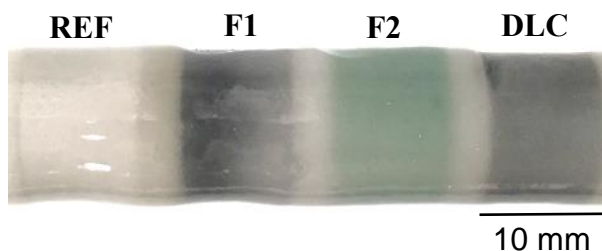


Figure 7.13 Photographs of samples – PbS multiphase conditions - 5000 mg/L PAMPS

As a result of the uniform scale coverage over all anti-fouling coatings, there was no clear correlation between coating water contact angle and mass gain where $R^2 = 0.48$ (Figure 7.14).

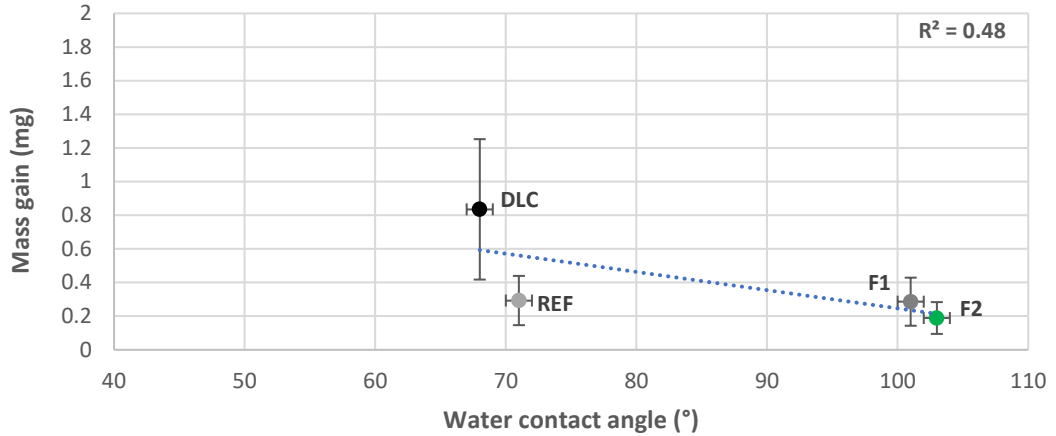


Figure 7.14 Water contact angle vs. mass gain in a multiphase PbS system – 5000 mg/L PAMPS

Scaling of fluoropolymers F1 and F2 occurs at 5000 mg/L PAMPS inhibitor concentration due to the complete emulsification of the oil phase in systems where the o:w ratio is 5:95. As with systems that contain 500 mg/L PAMPS, high emulsion stability results in emulsion tightening, where oil droplets within the stabilised emulsion reached a maximum diameter of 120 μm (Figure 7.15c). 24 hours after agitation of the recovered brine it can be seen that, while the emulsion has separated from the aqueous phase, there is no excess oil (Figure 7.15b).

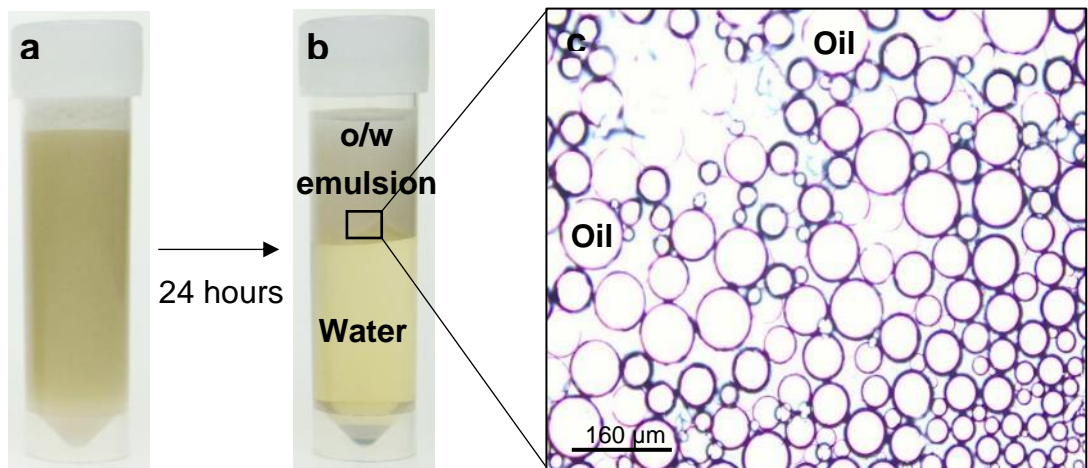


Figure 7.15 5000 mg/L PAMPS a) Post-experimental emulsion after agitation; b) Separation into stable Winsor type III emulsion after 24 hours; c) Optical microscope image of oil droplets (x20 mag)

7.6.1 PbS/PAMPS emulsion rheology

Influence of emulsion viscosity on the presence of excess free oil at the substrate interface was assessed using rheometric techniques, where a decrease in viscosity with ramping shear rate from the geometry could be equated to breaking of the emulsion and consequent shear thinning.

Relative viscosity curves were plotted for PbS emulsions at PAMPS inhibitor concentrations of 0, 500 and 5000 mg/L. At 0 and 500 mg/L PAMPS concentrations, emulsions displayed shear thinning between shear rates of $0.1 - 10 \text{ s}^{-1}$ before viscosity became relatively stable, indicating emulsion breaking had occurred and the oil and water phases had separated. When 5000 mg/L PAMPS was present in solution, shear thinning occurred, with the gradient remaining relatively linear up to 1000 s^{-1} . This showed that emulsion breaking did not occur at high shear rates. The viscous and stable nature of the emulsion formed at 5000 mg/L PAMPS resulted in uniform deposition of a persistent coating on all surfaces at experimental shear values. (265)

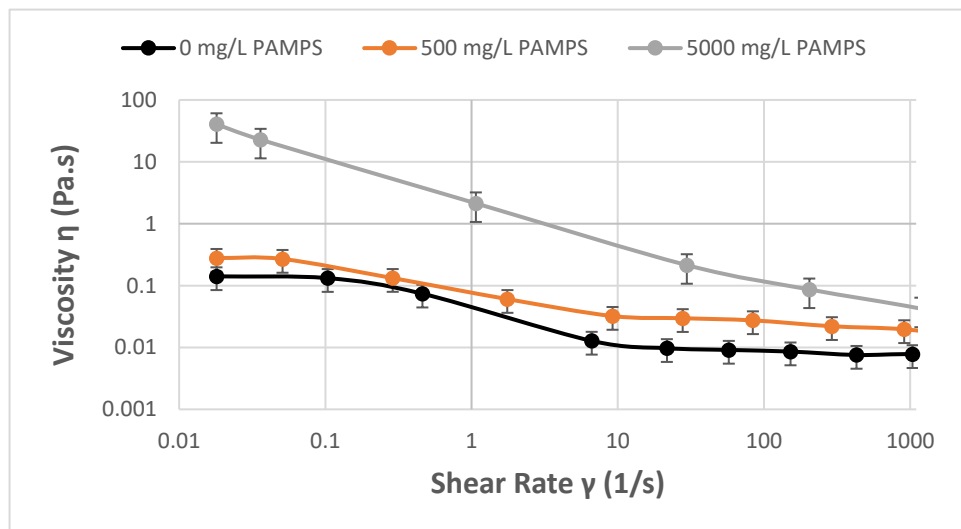


Figure 7.16 Viscosity of PbS Pickering emulsions with concentrations of 0, 500 and 5000 mg/L under ramping shear rate

At 0 and 500 mg/L PAMPS inhibitor, the 5% oil phase was not completely emulsified and the presence of excess free oil resulted in a strong correlation between coating water contact angle and surface mass gain for scaling experiments. Complete emulsification of the oil phase at 5000 mg/L PAMPS and the subsequent departure of the oil partitioning layer present at concentrations of 0 and 500 mg/L led to uniform deposition of viscous emulsion upon surfaces, irrespective of wettability (Figure 7.13). Excess free

PAMPS in solution migrated from solution to the o-w interface to form a stable o/w emulsion, and hence had a significant effect on viscosity and depositional behaviour.

7.6.2 Emulsion behaviour at the coating interface

In two-phase flow regimes, a phenomenon known as the ‘wall depletion effect’ can occur upon surfaces, contingent on o:w phase ratio, phase composition, flow rate and surface characteristics. Particles dispersed in the continuous phase migrate to the central region of the fluid and away from the wall (high shear region). Subsequently, a thin fluid layer close to the wall containing a low concentration of particles allows the central core to effectively slip. (265)

7.7 Influence of PAMPS on PbS deposition

7.7.1 Multiphase system - 0 mg/L PAMPS

Figure 7.17a displays an SEM image of a PbS deposited when no PAMPS was present in the initial solution, with agglomerates amassing on the REF substrate after PbS stabilised oil droplet impaction to form a continuous ‘cake’ that almost completely covers the surface. EDX analysis revealed that Pb and S elements constituted the visible deposits (Figure 7.17b & c).

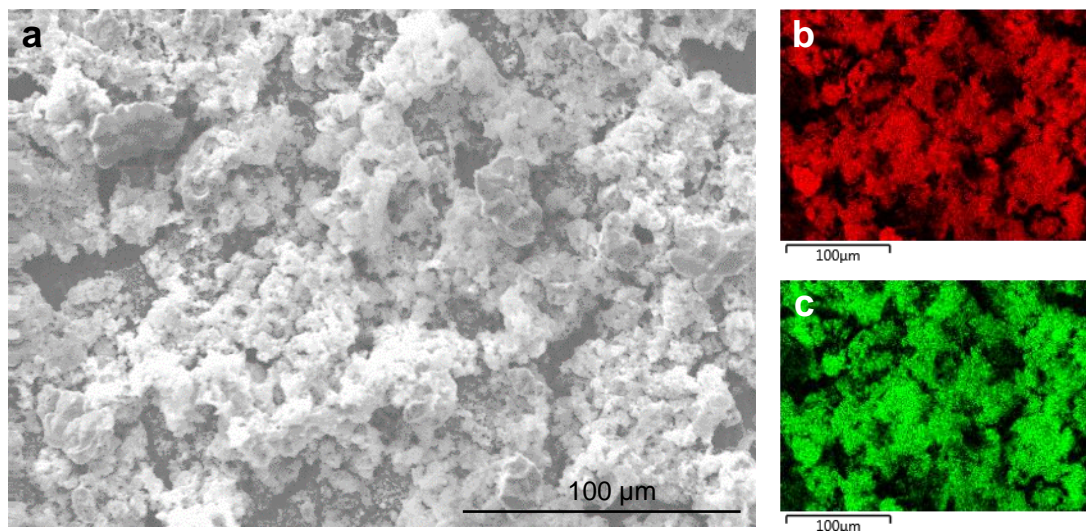


Figure 7.17 PbS multiphase systems - 0 mg/L PAMPS a) SEM image of PbS deposition on REF coupon; b and c) EDX images of Pb and S

7.7.2 Multiphase system - 500 mg/L PAMPS

From the SEM image in Figure 7.18a, it can be seen that the presence of PbS has been significantly reduced in systems where PAMPS is present when compared to deposition in uninhibited systems. Areas covering most of the substrate that show cobweb-like transparent deposits are likely PAMPS films formed at the o-w interface of droplets that have ruptured under drying. EDX analysis in Figure 7.18b & c displays a circular deposit of PbS, showing the role of PbS stabilisation at the oil droplet interface and impact on the mechanism of PbS scale deposition. From EDX spectra measuring the intensity of present elements within a scanned area, it was shown that the intensity of the Pb element, indicating PbS presence on the surface, was 188 and 4 cps/eV for PbS scaling systems containing 0 and 500 mg/L of PAMPS respectively (Figure 7.19).

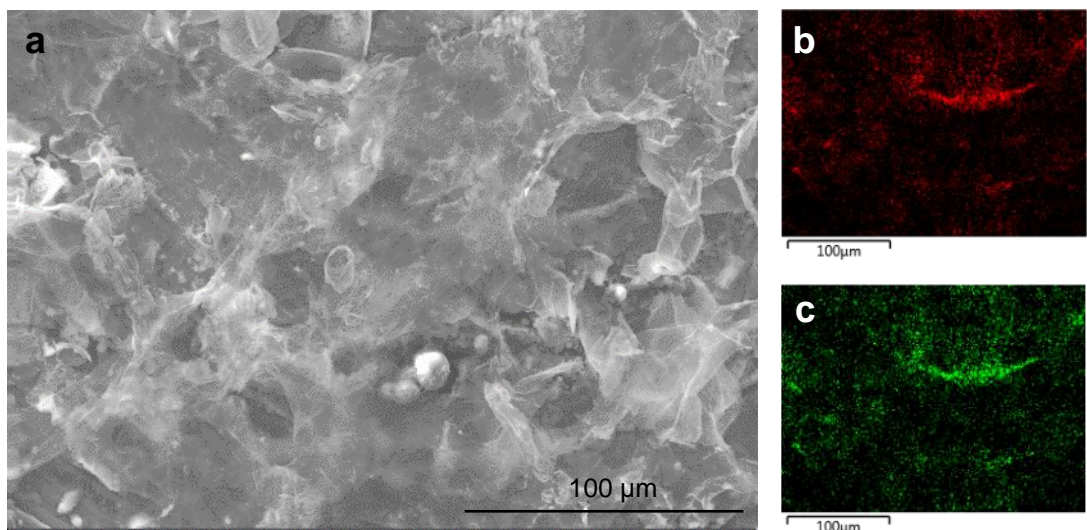


Figure 7.18 PbS multiphase systems - 500 mg/L PAMPS a) SEM image of PbS deposition on REF coupon; b and c) EDX images of Pb and S

PAMPS based inhibitor is used widely in the removal of heavy metal ions from solution, where the affinity to bind metal ions results from electrostatic interactions between divalent lead cations and sulphonic acid groups on the PAMPS molecule.(295) As PAMPS is introduced into the experimental brine prior to the dissociation of $H_2S_{(g)}$, the polyelectrolyte is able to remove a large proportion of free Pb^{2+} ions from solution before reaction with the PbS forming HS^- anion can occur, as well as bind and retard the growth of solutes forming in solution.(178, 295)

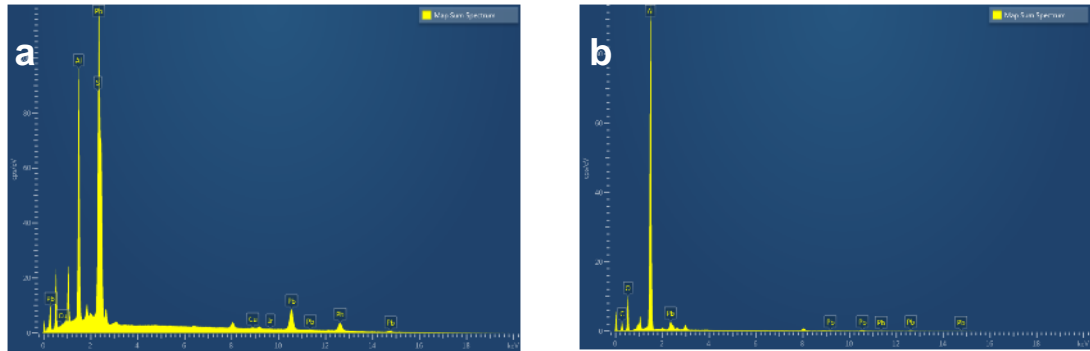


Figure 7.19 a) EDX spectra of PbS deposit on REF coupon - 0 mg/L PAMPS; b) EDX spectra of PbS deposit on REF coupon - 500 mg/L PAMPS

PAMPS was introduced to the PbS/CaCO₃ forming system at concentrations (50 mg/L) seen in oilfield systems that might be typically encountered towards the end of a squeeze treatment cycle when further scale injection treatment is impending. From Figure 7.20, it can be seen that deposition had still occurred upon surfaces, though not as extensively as when no PAMPS was present given otherwise identical conditions (Figure 6.1).

Inhibitor presence resulted in deformation and rounding of the calcite crystal (Figure 7.21). A heterogeneously precipitated layer of CaCO₃ can be seen to form directly upon the substrate, most apparent on the DLC coating. On hydrophobic surfaces, heterogeneous CaCO₃ growth likely offsets the local anti-fouling attributes by negating the influence of the enveloping oil layer that prevents homogeneous deposition of PbS/CaCO₃ stabilised at the interface.

It can clearly be seen from SEM images in Figure 7.21 that the PbS/CaCO₃ complexes are hemispherical in shape, where the rounded side is largely facing the substrate and the flat side exposing the PbS clusters faces away from the substrate. After stabilisation of PbS agglomerates at the o-w interface, solute Ca²⁺ and CO₃²⁻ ions from the aqueous phase adsorb into the forming calcite lattice surrounding the PbS structure, prompting growth of calcite exclusively into the aqueous phase. This gives an indication into the scale deposition mechanism, whereby oil droplets impact the substrate and consequently rupture, with the once spherical particle-stabilised interface now a film splayed and adhered onto the substrate.

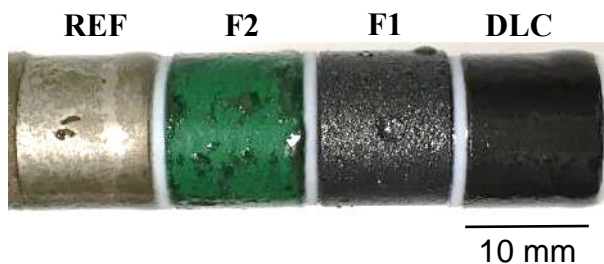


Figure 7.20 Photographs of samples - multiphase PbS/CaCO₃ system (5:95 o:w ratio) - 50 mg/L PAMPS inhibitor

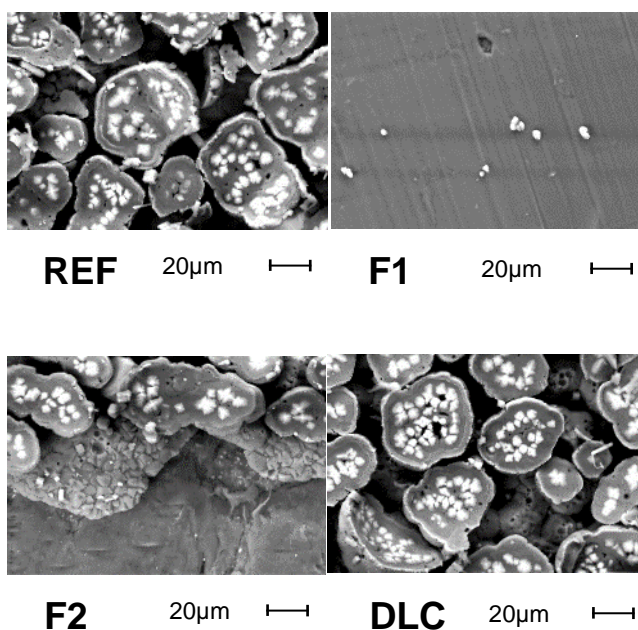


Figure 7.21 SEM images of deposits on anti-fouling surfaces in a multiphase PbS/CaCO₃ system (o:w 5:95 ratio) - 50 mg/L PAMPS

Figure 7.22 shows SEM and EDX imaging of the DLC coupon from Figure 7.21, where occluded white areas highlighted by BSE imaging are shown to be elementally composed of Pb and S, with Ca, C and O constituting the calcite crystal highlighted in red/yellow, as well as the heterogeneously precipitated base layer.

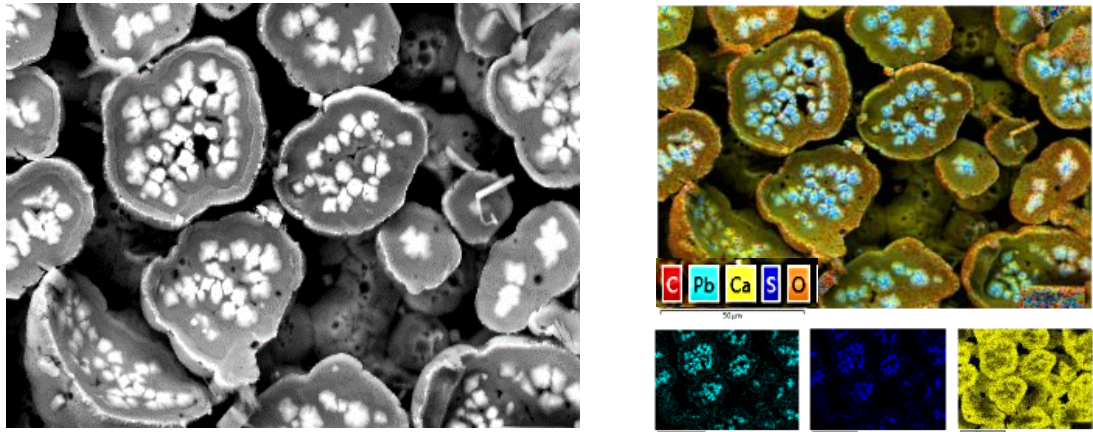


Figure 7.22 SEM and EDX of deposited PbS/CaCO₃ complexes - 50 mg/L PAMPS inhibitor (DLC coupon) – o:w 5:95 ratio

From Figure 7.23, there is a strong correlation ($R^2 = 0.78$) due to the presence of the excess light oil phase that envelops hydrophobic fluoropolymers F1 and F2. Calcite however can be seen to have precipitated heterogeneously on the F2 coupon, compromising the local hydrophobic characteristics and promoting the adhesion of the PbS/CaCO₃ complex from the bulk phase.

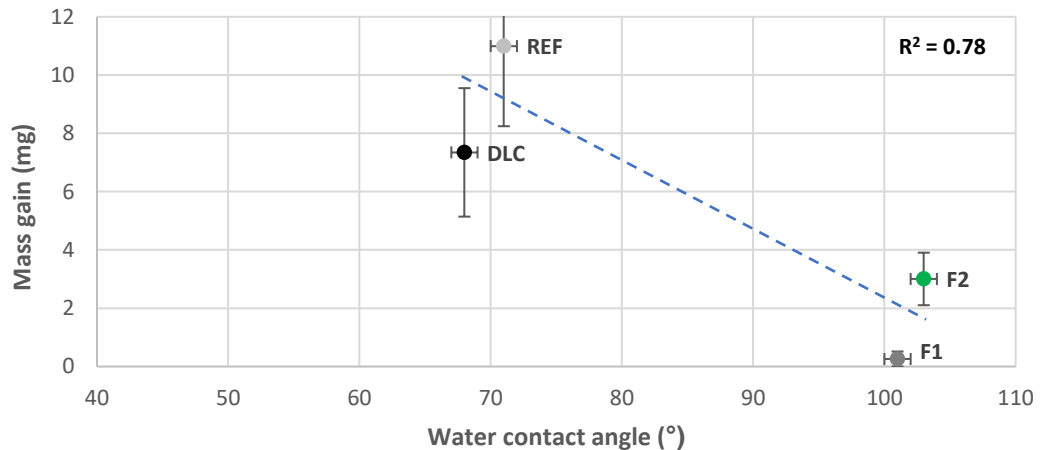


Figure 7.23 Water contact angle vs. mass gain in a multiphase PbS/CaCO₃ system (o:w 5:95 ratio) - 50 mg/L PAMPS

PAMPS has been reported to act as both a nucleation inhibitor and a growth retardant and as such, step-growth of calcite crystals was disrupted, with rhombohedral structures replaced by more rounded calcite that encapsulates clusters of PbS agglomerates, as seen in Figure 7.22. (178, 295)

The affinity of divalent Pb^{2+} and Ca^{2+} cations to a sulphonic acid group is similar due to their equal valency, though the size of the Pb^{2+} ion increases adsorption potential of the PAMPS molecule, subsequently reducing nucleation potential of free metal ions.(296) The presence of numerous additional cations such as K^+ , Na^+ , Mg^{2+} within the complex brine contribute to adsorption by the polyelectrolyte, hence a more significant concentration of PAMPS would be required to prevent nucleation and growth of mineral scales in complex systems.

7.9 Chapter Summary

The partially hydrophobic nature of the [001] face of unoxidised cleaved galena (WCA of 49°) invited the adsorption of amphiphilic PAMPS polyelectrolyte due to the interaction of the hydrophobic backbone with the substrate.(177) It can be inferred through contact angle measurements in Figure 7.2 that orientation of the PAMPS electrolyte is with the sulphonic acid head group towards solution, prompting a more negatively charged and hence hydrophilic surface. This was reflected by zeta-potential measurements, where PAMPS functionalisation of sonicated PbS nanoparticles resulted in a surface charge shift from -8.8 to -24.8 mV.

From Figure 7.1 it can be seen that surface coverage was ~80%, with electrostatic repulsion between the sulphonic acid heads of the amphiphilic PAMPS molecules likely to prevent the formation of a closely packed, uniform film.(289) Isolated oxidation of surface was also likely to have influenced adsorption density, with adsorbing PAMPS favouring oxidised areas due to their hydrophobic tendency.

From force curve measurements between a PAMPS functionalised cleaved galena substrate and an AFM tip, it could be seen that no attractive or adhesive force was recorded upon approach or retraction when the tip was hydrophilic. This was due to the arrangement and orientation of the PAMPS molecule on the galena substrate, where the hydrophobic tail was attracted to the partially hydrophobic substrate resulting in the sulphonic acid group bringing about a strongly negative charge. The absence of hydrophobic forces and negligible vdW attraction resulted in relatively neutral contact between the tip and the substrate. Upon retraction of the OTS functionalised hydrophobic AFM tip however, a degree of measured adhesion (33.4 ± 4.6 mN/m) of the tip to the substrate was recorded due to the influence of electrostatic vdW

attraction. No attraction was detected upon approach as long-range hydrophobic force was not present due to the negative charge of the PAMPS functionalised galena substrate.

Empirical measurements in a single-phase system, whereby the deposition of PAMPS functionalised PbS nanoparticles in solution on anti-fouling surfaces of both hydrophilic and hydrophobic wettability, enforced AFM findings that hydrophobic surfaces are more susceptible to deposition via adhesion Figure 7.6. The influence of electrostatic attraction between the net positively charged substrate and negatively charged PAMPS functionalised PbS prompts attachment to the surface. Additionally, reduced average agglomerate size of 873 nm, compared to uninhibited systems where PSD analysis showed the average to be 4434 nm, resulted in increased attachment of PbS agglomerates to substrates due to the lesser influence of turbulent flow at the interface in prompting removal.(140)

Introduction of PAMPS to multiphase systems played a role not only in reducing the precipitation of PbS particles in solution but altering emulsion behaviour through stabilisation of the long-chain PAMPS amphiphile at the o-w interface. Whilst introduction of 50 mg/L PAMPS had little inhibitory effect Figure 7.7, from Figure 7.10 and Figure 7.14 it can be seen the influence of 500 and 5000 mg/L is significant, with the emulsion tightened and more stable. Heightened PAMPS polymer concentration at 5000 mg/L, exaggerated to represent near-wellbore concentrations directly after a scale inhibitor squeeze treatment, resulted in the complete emulsification of the 5% oil phase that in turn lead to complete coverage of all anti-fouling surfaces regardless of wettability. Despite removal of unreacted Pb^{2+} ions from solution through adsorption onto the PAMPS molecules, the excess PAMPS in solution migrates to the o-w interface from the aqueous phase to prompt formation of a persistent emulsion. The high stability of the PAMPS stabilised emulsion at 5000 mg/L PAMPS is apparent through viscosity measurements (Figure 7.16), where viscosity remains high even at raised shear stresses. EDX imaging and spectra of deposits on the surface of REF coupons post-experiment demonstrated that the degree of precipitated and adhered PbS can be estimated, based upon spectral intensity of 188 and 4 cps/eV for Pb in systems containing 0 and 500 mg/L PAMPS respectively.

Introduction of a complex $PbS/CaCO_3$ scaling brine into a multiphase system showed that while 50 mg/L of PAMPS was insufficient to inhibit significant scaling (Figure 7.20), precipitated calcite crystals around the occluded PbS were no longer rhombohedral in morphology (Figure 7.22). In complex

systems containing significant monovalent and divalent cations, significant levels of inhibitor would likely be required to reduce the precipitation of problematic mineral scales.(296)

7.9.1 Chapter Highlights

- High molecular weight PAMPS polyelectrolyte adsorbed onto galena/PbS surfaces through interaction of its hydrophobic backbone to the partially hydrophobic substrate. This resulted in increased negative surface charge of PbS particles, increasing the electrostatic repulsion between particles in solution, consequently reducing agglomeration.
- The influence of PAMPS functionalisation of PbS upon interaction of surfaces with varying hydrophobicity was measured via AFM force curve analysis. PAMPS presence on the PbS surface removed the influence of the long-range hydrophobic force that was detected with untreated PbS surfaces (Chapter 4).
- Higher electrostatic attraction between PAMPS functionalised PbS agglomerates and hydrophobic surfaces when compared to hydrophilic surfaces, led to increased deposition on hydrophobic substrates in single phase conditions.
- In multiphase systems, high concentration of PAMPS resulted in emulsion tightening and stabilisation of the excess oil phase in 5:95 o:w emulsions. Emulsion deposition therefore occurred on all surfaces uniformly, regardless of their wettability. This phenomenon could conceivably occur within oilfield systems where a combination of high water-cut and high polymer/solids concentration around the near-wellbore region could cause viscosity of the o/w emulsion to rise. E.g. after scale inhibitor squeeze treatments.
- Under complex PbS/CaCO₃ water chemistries representative of those found in sour North-sea systems, 50 mg/L PAMPS failed to inhibit the formation and deposition of PbS, with the polymer binding preferentially to calcite crystals, affecting their morphology.

Chapter 8

Conclusion

This Chapter aims to summarise the results and findings from this work on the mechanisms of lead sulphide (PbS) formation and precipitation through a range of conditions and onto various anti-fouling surfaces, with a wider scope of preventing mineral scale deposition on downhole production equipment.

This study achieved:

- Design and construction of a sulphide scaling rig that had the capacity to allow gradual formation of metal sulphides in turbulent multiphase conditions
- Evaluation of the performance of a number of anti-fouling substrates in single and multiphase conditions within both simple and complex scaling systems
- Probing acting interfacial forces between cleaved galena and surfaces of opposing wettability, in conjunction with the effect of sulphonated polyelectrolyte (PAMPS) on interfacial behaviour, emulsion characteristics and deposition

8.1 Attachment and adhesion of PbS to anti-fouling surfaces

The complex combination of parameters that determine surface crystallisation and adhesion renders it impossible to identify one single property that either enhances or prevents nucleation on surfaces with an array of physiochemical characteristics.(32, 297) Individually, substrate roughness, surface energy and chemical composition are unable to define the scaling tendency of a surface as alteration of one can inextricably influence the other.

Scale crystals that nucleate heterogeneously are generally more susceptible to influence from surface chemistry and topography, where local supersaturation around surface asperities can lead to crystal formation. Homogeneously precipitated crystals e.g. PbS, that have a tendency to adhere to surfaces from the bulk phase are less prone to the influence of surface chemistry and roughness, where interfacial interactions determine the likelihood of initial deposition and adhesion.(131)

The degree of attractive force and therefore adhesion likelihood of PbS nanoparticles from the bulk onto surfaces was heavily dependent on attractive

interactions at the nanoscale such as van-der-Waals (vdW), and dependent on the substrate, long-range hydrophobic force. AFM force curve analysis was used to highlight the additional attraction that arose between a galena (PbS mineral) substrate and a plane functionalised with hydrophobic OTS, where hydrophobic forces prompt strong jump-in of the AFM tip ~9 nm from the surface. For interaction between galena and an untreated Si₃N₄ tip that was highly hydrophilic, vdW was predicted to be the dominant force, where theoretical predictions matched up with experimental readings at which weak jump-in was detected at approximately 4 nm from the galena substrate. Consequently, it was determined that the degree of adhesion upon AFM tip retraction was significantly higher between galena and a hydrophobic surface, owing to the effect of the long-range hydrophobic force. It can be inferred that adhesion of deposited partially-hydrophobic PbS particles to a hydrophobic substrate will be significantly higher than that on a hydrophilic substrate of identical smoothness, where measured adhesion was 62.1 ± 4.7 mN/m and 26.7 ± 2.4 mN/m respectively.

This study was able to therefore address the strength of adhesive forces between PbS particles and surfaces of different wettability located in producing sour oilfield streams, and ultimately the intensity of scale deposition and build-up. Andritsos and Karabelas (298) showed that hydrophobic Teflon™ promotes a higher rate of PbS deposition when compared to untreated hydrophilic steel surfaces. AFM analysis in this work demonstrated the role of the attractive hydrophobic force in promoting higher PbS deposition rate and enhanced homogeneous scaling upon hydrophobic fluoropolymer surfaces.

8.2 Light oil phase influence on mineral scale behaviour and Pickering emulsion formation

In the presence of an oil-water boundary, it has been shown that colloids will bind to a liquid-liquid interface under equilibrium conditions in order to minimise system energy, with their position determined by the contact angle that is described by Young's law.(164) PbS nanoparticles are partially hydrophobic with a water contact angle of 48° and consequently they adsorb strongly and irreversibly to the o-w interface.(151) The free energy of desorption (ΔG_w) required for desorption of a PbS particle into water phase was determined to be $\Delta G_w = 1.3 \times 10^{-16}$ J given that the PbS particle had a 50 nm radius (R) at the oil water interface ($\gamma_{o-w} = 50$ mN m⁻¹). Adsorption strength of the PbS particle to the interface was significant enough to not be affected

by high temperatures, where the thermal energy (K_t) at 95°C (5×10^{-21} J) was not sufficient for removal. Calcite and barite crystals are more hydrophilic than galena, with water contact angles of 6 and 28° respectively, where adsorption of bulk-formed particles to the interface was feasible, but the energy required for desorption (ΔG_w) was significantly lower.

As PbS nanoparticles in turbulent multiphase solution migrate to the interface of formed droplets, stabilisation occurs, leading to the formation of a stable Pickering emulsion. Dependent on particle concentration and phase ratio, excess water and oil phases reside below and above the PbS-stabilised emulsion. Whilst o/w emulsions form when the water fraction is > 0.25 , catastrophic inversion occurs as the phase ratio of water is < 0.25 , prompting the formation of an w/o emulsion. As primary production in oil wells progresses, this threshold of > 0.25 brine is likely to be reached as water-cut increases with reservoir life and aquifer expansion.

It was shown through co-precipitation of PbS and CaCO_3 in complex scaling systems, based on North Sea water chemistries, that the presence of an o-w interface significantly affects scaling mechanisms. The spontaneous precipitation of PbS nanoparticles and their subsequent migration to the o-w interface not only forms a stable Pickering emulsion, but provides a seeding point for the co-precipitation of PbS and CaCO_3 whereby PbS is occluded at the interface. As such, PbS/ CaCO_3 complexes are anchored at the droplet interface. Inversion of the emulsion from o/w to w/o, unlike in solely PbS forming systems, was shown to occur when water phase fraction was < 0.5 .

The adsorption of solids at liquid-liquid interfaces is not a new phenomenon, with Pickering (299) describing the formation of solid-stabilised emulsions as early as 1907. The mechanism of Pickering emulsions as a mode to deposit scale in multiphase systems however has not been previously described. The transport of mineral scales at the interface of the continuous and disperse phase in oil producing systems has large implications with regards to scale deposition and prevention, as well as scale inhibitor utility.

The co-precipitation of multiple crystal species in complex solutions has been widely documented.(114, 196, 198, 243, 300) The formation of crystal complexes and films as a consequence of occlusion co-precipitation, otherwise known as mechanical entrapment has not previously been shown to occur in the context of mineral scaling. The gulf in SR value between PbS and CaCO_3 under the scaling conditions described in Chapter 3, and the subsequent adsorption of spontaneously precipitated PbS at the interface results in PbS occlusion within growing calcite structures. This previously

unknown mechanism likely has implications with regards to both PbS and CaCO₃ deposition, emulsion inversion and o/w separation.

8.3 PbS deposition in multiphase systems

The nucleation and deposition of mineral scales in single phase systems has been widely investigated. Precipitation of common oilfield scales e.g. calcite and barite typically occurs via heterogeneous nucleation, where the low saturation ratio of calcite and barite results in the energetically favourable crystallisation of minerals directly onto surfaces and equipment. Given that bulk nucleation of crystals occurs in single phase brine systems where flow is turbulent, deposition occurs by a combination of gravitational deposition and interfacial attraction, resulting in a far lower rate of surface mass gain than that seen with heterogeneous crystallisation.(129)

Upon introduction of the light oil phase, migration of crystals to a o-w droplet interface and formation of a Pickering emulsion however changes the mechanism of scale deposition. Particle coated droplets within a turbulent flow stream impact surfaces with a higher velocity and frequency than individual particles or agglomerates within the bulk phase due to their higher mass. Impaction of droplets leads to rupture that results in splaying of the particles onto the substrate as part of an interfacial film, as well as attachment of intact solid-coated droplets from the emulsified phase to the substrate. This ultimately leads to increased mass transport of scale particles to surfaces, given that they had been adsorbed at the o-w interface in turbulent flow. Whilst the enhancement of deposition was clear with regards to bulk-precipitated particles such as PbS, scales such as CaCO₃ and BaSO₄ that had a tendency to precipitate on surfaces heterogeneously also saw increased mass gain. In addition to the deposition of interfacially stabilised particles from oil droplets, it was hypothesised that the dispersed phase enhanced the mass transport of ions and solutes to crystals on the substrate surface, resulting in secondary nucleation and faster growth rate.

In single phase systems, a complex combination of physiochemical characteristics determined the scaling tendency of a substrate, rendering fouling prediction difficult.(131) In multiphase systems however, the wettability and displacement energy of anti-fouling substrates was of paramount importance in determining the degree of scaling, particularly in systems where homogeneous bulk precipitation was predominant. Hydrophobic surfaces with a negative displacement energy e.g. F1, F2, became oil wetted in the

presence of a light oil phase, preventing the deposition and adhesion of hydrophilic mineral scales from the bulk brine phase or Pickering emulsions with an aqueous phase affinity. The influence of hydrophobic substrates on fouling mitigation in multiphase systems was not as pronounced in systems with scales prone to forming on surfaces heterogeneously e.g. CaCO_3 , where contact of the aqueous phase can lead to crystallisation directly upon surfaces, leading to compromise of local coating hydrophobicity. Saturation ratio, as the thermodynamic driving force for nucleation, is a reasonable metric for predicting the degree of homogeneous nucleation likely to occur for a particular scaling compound within a system.(301) Through this work an empirical relationship was discovered between the saturation ratio of a scaling compound, and the degree of correlation between coating water contact angle and mass gain. As such, the depositional tendency of PbS scales that precipitated exclusively in the bulk phase to form Pickering emulsions could be predicted with a very high degree of accuracy based on coating hydrophobicity.

The strong correlation between water contact angle and scale mass gain in multiphase PbS systems was apparent in both o/w and w/o emulsions, where the water-cut was 95% and 20% respectively, indicating that hydrophobic surfaces are a viable means of preventing scaling over the course of production well life. In complex PbS and CaCO_3 scaling systems, the presence of PbS that acted as a seeding point for CaCO_3 growth at the o-w interface enhanced the correlation strength between coating water contact angle and mass gain when compared to simple CaCO_3 multiphase scaling systems. This was in all likelihood due to a reduction of scaling ions within the bulk aqueous phase, limiting the potential for heterogeneous nucleation upon hydrophobic surfaces that would have in turn compromised the coating characteristics and led to scale build-up. As with simple PbS multiphase systems, the presence of an oil phase regardless of emulsion type (o/w or w/o) resulted in negligible deposition of PbS and CaCO_3 scale upon hydrophobic surfaces.

Whilst the deposition of PbS has been observed to occur by both heterogeneous crystallisation at low pH values and concentrations, and as a result of gravitational and intermolecular forces when precipitated homogeneously, the mechanics of PbS fouling in multiphase systems was not previously understood. Impaction of particle coated droplets has been described, where the radial dispersion of particles from the point of droplet impaction upon substrates results in scale deposition.(274) Systems in which

Pickering emulsions are present see repeated droplet impaction upon surfaces, resulting in either droplet rupture or attachment of droplets to the substrate. In multiphase systems deposition was mitigated upon hydrophobic surfaces, where free oil within the solution has been shown to oil wet and envelop surfaces exhibiting a negative displacement energy.(273)

8.4 Chemical inhibition of PbS scale

Sulphonated polymers are used as inhibitors in metal sulphide scaling systems to inhibit both the nucleation and growth crystals.(50, 185, 186) As a consequence of the low thermodynamic barrier for nucleation of metal sulphide compounds, it is difficult to successfully inhibit precipitation due to the spontaneous nature in which crystals are formed, requiring unrealistically high concentrations of inhibitor. The polyelectrolyte can be effective as it is able to bind to precipitated PbS particles, acting as a dispersant in order to prevent agglomeration and subsequent deposition from the bulk phase.

AFM analysis of PAMPS functionalised galena showed that the attractive force between both hydrophilic and hydrophobic AFM tips in contact with the substrate was reduced as a result of polyelectrolyte functionalisation. Negligible attraction was detected at both approach and retraction of the hydrophilic tip from the surface, where repulsive electrostatic forces dominated between the two hydrophilic surfaces. Hydrophobisation of the AFM tip did not register attraction due to vdW forces upon approach, perhaps due to compression of the polyelectrolyte adsorbed upon the surface. Retraction however recorded a measured adhesion force of 33.4 ± 4.6 mN/m, indicating that vdW forces were present. These results were shown empirically in single phase PbS scaling experiments where 50 mg/L of PAMPS was present. Comparatively high levels of mass gain occurred on hydrophobic surfaces F1 and F2 in relation to hydrophilic surfaces REF and DLC as a consequence of the attractive vdW present between the hydrophobic surface and functionalised PbS nanoparticles.

Introduction of PAMPS into systems containing a light oil phase was shown to have little inhibitory effect at low concentrations of 50 mg/L PAMPS and a limited effect at 500 mg/L, where hydrophobic surfaces were again relatively scale free due to the wetting effect of the oil phase upon their surface. There was therefore a correlation between coating water contact angle and mass gain seen upon surfaces due to the presence of an excess free oil phase, as seen in systems where no inhibitor was present.

The PAMPS polyelectrolyte, due to its high MW and amphiphilic nature acted as a surfactant, resulting in further stabilisation of the emulsion in addition to the emulsifying effect of solid PbS particles that had precipitated in solution. At high PAMPS concentrations where the water-cut was high e.g. 95%, emulsification of all free oil in the system occurred, leading to a 2-phase emulsion. As such, no oil was available to coat and envelop hydrophobic surface coatings leading to uniform deposition upon all anti-fouling coatings regardless of their displacement energy.

Whilst in simple PbS forming systems PAMPS is relatively effective at inhibiting scale formation when introduced at high concentrations, the presence of other co-precipitating minerals e.g. CaCO_3 , likely reduced inhibitor efficacy. PAMPS is used in CaCO_3 inhibition thanks to its low P_{ka} and strong hydration, where the sulphonate group can bind with particles in solution, whilst the carboxylate groups interact with free metal cations e.g. Ca^{2+} . In complex PbS/ CaCO_3 systems, the morphology of calcite was significantly affected by the presence of 50 mg/L PAMPS, where rhombohedral crystals became rounded. It is therefore likely in oilfield systems where multiple scale species are present, that the interference of other mineral scales and free cations retard the inhibitory effect of PAMPS on the metal sulphides for which it is intended.

Dietzsch et al. (178) explained the role of PAMPS-based co-polymers in controlling CaCO_3 scale formation and the mechanisms through which inhibition occurs. Control of insoluble sulphide scales in oilfield production has typically been addressed through the use of polymeric inhibitors, with varying degrees of success.(14, 22, 185) Literature specifically investigating the influence of PAMPS polyelectrolyte on sulphide scale precipitation has not been published previously, with inhibition efficacy assessed in both single and multiphase PbS systems in this work.

8.5 Ranking of surfaces for field application

Hydrophobic fluoropolymer surfaces were deemed to be the most promising in terms of overall scale prevention, where their anti-fouling attributes in systems where a light oil phase was present set them apart from hydrophilic coatings such as DLC. The additional benefits of durability and application practicality that were typical of PTFE-based coatings rendered them suitable for field trials and potential application on downhole equipment.

From the fluoropolymer surfaces tested, F1 and F2 were almost indistinguishable in terms of performance owing to their similar characteristics. Whilst F2 may have been marginally better in terms of preventing initial fouling due to its slightly lower average surface roughness (S_a), upcoming field trials will be able to determine the true efficacy when applied to actual scaling scenarios.

Chapter 9

Future work

This thesis ultimately aimed to establish the mechanism behind fouling in multiphase systems. Whilst a number of useful conclusions have been drawn on the nature of Pickering emulsions and their deposition upon different anti-fouling surfaces, further research is required to understand the fundamental mechanism governing droplet impaction and scaling of pertinent species in different conditions. Whilst the prospect of mechanical mitigation of metal sulphide scales through the application of anti-fouling surfaces appears promising, more work is required on their chemical inhibition in complex scaling systems. Any future studies must factor in the advantages of potential synergy between chemical and mechanical methods.

Future work will take place in two strands:

- 1) Continued laboratory-based testing and analysis
- 2) Field trial and sample analysis

9.1 Laboratory-based testing

Future tests will aim to characterise scale deposition mechanism in multiphase systems under increasingly realistic conditions and brines. The development of an experimental rig that can support high temperature and pressure tests, deposition on a number of surfaces and sulphide forming conditions, is critical in establishing the validity of the oilfield scaling mechanisms put forward in this work. For future lab tests:

- A custom-built autoclave that is capable of handling HT/HP, whilst integrating a mechanism that allows complete dispersion of oil or water within two-phase flow, whilst propagating turbulence on a series of surfaces. Testing of multiphase PbS deposition mechanisms as described in Chapter 5 within HT/HP systems is vital to establish the required thermal energy to destabilise emulsions. Whilst it has been shown PbS-stabilised emulsions are stable up to temperatures of 95°C under ambient conditions, pressures and temperatures in deep wells can far exceed that.(40, 49)

- Further study and eventual refinement of effective anti-fouling coatings, including development and testing of novel surfaces e.g. polymer brush. The scope of the project and application may extend beyond oilfield scale prevention, identifying other industries that could benefit from such work.
- While this study investigated the scaling behaviour of PbS in simple and complex systems, other metal sulphides e.g. ZnS, are often found in tandem. Future work will encompass the co-precipitation of multiple sulphide scales and examine their interaction with conventional carbonate and sulphate scales, closely mimicking brine compositions found in North Sea case studies (and beyond).
- Though the initial mechanism for deposition of scale in multiphase systems has been described in this work, the implications of build-up over long periods of time, as would be representative of actual systems, were not investigated. Future work should examine the long-term growth kinetics of CaCO_3 , BaSO_4 and PbS scales by running tests for extended periods.
- The multiphase experiments detailed in this work describe very dispersed bubble flow induced by high stirrer speeds. During production however, lower flow rate, higher oil viscosity and changing o:w ratio can prompt a reduction in dispersion that leads to annular, plug or churn flow. Through modification of the bladed-stirrer speed and investigation into the effects specific to this set-up, different types of flow in multiphase and the influence of deposition could be explored.
- Whilst the mechanism of particle deposition via droplet impaction in solid-stabilised emulsions was well established through post-experimental analysis, it has not been directly observed. Future work should aim to image the point of droplet impaction upon a substrate and assess the mode of particle attachment from the interface of both emulsified oil and water droplets. This will allow validation of the deposition model hypothesised in Chapter 5.
- There is limited literature on occlusion precipitation as observed in Chapter 6, with this work certainly the first observing this phenomenon occurring in crystalline scaling systems. Future work should encompass deeper investigation into complex PbS and CaCO_3 co-

precipitation, eventually introducing other combinations of scales that precipitate in the field. Ultimately, modelling techniques could elucidate the co-precipitation mechanism between insoluble sulphide scales and carbonate/sulphate species, ultimately predicting their behaviour under different downhole conditions.

- This work showed that high MW polymers and solids are prone to adsorption at the interface in oil-water systems, contributing to the stabilisation of droplets within emulsions. Future work should explore the effects of other solids found naturally in produced flow from reservoirs, (e.g. clays, sand, asphaltenes) on emulsion behaviour.

9.2 Assessment of field trial samples

Three upcoming North Sea field trials will establish the efficacy of F1, F2 and DLC coatings with regards to anti-fouling when inserted downhole. Samples will be placed near critical equipment e.g. sub-surface safety valves, in order to mimic conditions at surfaces to which they may ultimately be applied. REF (stainless steel) coupons will be inserted between each coated ring to provide a reference and ensure adjacent samples do not interfere with the degree of scale deposition.

The duration of the field trial will be determined by the operational needs of the drilling well, with recovery of the scaled samples likely contingent on the need to carry out a workover e.g. if scale inhibitor squeeze is required.

Analysis of coupons will provide a clearer picture as to whether certain commercially available anti-fouling coatings are able to significantly mitigate the deposition and build-up of scale in oilfield systems. Once samples are retrieved from the well post-field trial, they will be carefully transported back to the laboratory where a number of analytical techniques will be undertaken;

- **Mass gain** as a result of mineral scaling will provide a comparison of scaling tendency between different coatings and the standard reference material under downhole conditions
- **Inductively coupled plasma (ICP-MS)** will enable determination of elements present in scale build-up and at what concentration
- **SEM microscopy and EDX** will be integral in establishing the scale crystal type, size, coverage, morphology, and initial and secondary deposits
- **XRD analysis** will determine scale species and morphology

Scaling on coupons recovered from downhole field trials will be assessed, with both the anti-scaling efficacy of coatings and the degree to which lab-based tests were representative of downhole scaling analysed. Whilst short-term lab tests are unlikely to yield entirely similar results to samples exposed to real-life complex scaling scenarios for a period of months, the initial crystallisation can be surveyed and compared in both cases. Initial attachment and growth of mineral scale will compromise the coating characteristics and therefore act as a catalyst for further growth.

In order to compare more accurately the lab and field results, brine and oil compositions from the field in which the trial has taken place will be recorded and replicated in the lab. This will then give a good indication into the validity of lab-based tests in order to determine the performance of anti-fouling coatings intended for application downhole in producing oil and gas wells.

References

1. Geographic, C. *EnergyIQ*. [Online]. 2019. [Accessed].
2. Tissot, B.P. and Welte, D.H. *Petroleum formation and occurrence*. Springer Science & Business Media, 2013.
3. Pepper, A.S. and Corvi, P.J. Simple kinetic models of petroleum formation. Part I: oil and gas generation from kerogen. *Marine and Petroleum Geology*. 1995, **12**(3), pp.291-319.
4. Libes, S. *Introduction to marine biogeochemistry*. Academic Press, 2011.
5. Socha. *Fossil Fuel Formation*. [Online]. 2018. [Accessed].
6. Collins, A.G. Enhanced oil recovery injection waters. In: *Oil Field Subsurface Injection of Water*. ASTM International, 1977.
7. Al-Mutairi, S.M. and Kokal, S.L. EOR potential in the middle east: current and future trends. In: *SPE EUROPEC/EAGE Annual Conference and Exhibition: Society of Petroleum Engineers*, 2011.
8. Jordan, M.M., Collins, I.R. and Mackay, E.J. Low sulfate seawater injection for barium sulfate scale control: A life-of-field solution to a complex challenge. *SPE Production & Operations*. 2008, **23**(02), pp.192-209.
9. Langelier, W., Caldwell, D., Lawrence, W. and Spaulding, C. Scale control in sea water distillation equipment-contact stabilization. *Industrial & Engineering Chemistry*. 1950, **42**(1), pp.126-130.
10. Knudsen, J. and McCluer, H. Hard-water scaling of finned tubes at moderate temperatures. *Chem. Eng. Progr.* 1959, **55**.
11. Kelland, M.A. *Production Chemicals for the Oil and Gas Industry, Second Edition*. Taylor & Francis, 2014.
12. Bellarby, J. *Well completion design*. Elsevier, 2009.
13. Frenier, W.W. and Ziauddin, M. *Formation, Removal, and Inhibition of Inorganic Scale in the Oilfield Environment*. Society of Petroleum Engineers, 2008.
14. Collins, I. and Jordan, M. Occurance, Prediction And Prevention Of Zinc Sulfide Scale Within Gulf Coast And North Sea High Temperature/High Salinity Production Wells. In: *International Symposium on Oilfield Scale: Society of Petroleum Engineers*, 2001.
15. Dyer, S., Anderson, C. and Graham, G. Thermal stability of amine methyl phosphonate scale inhibitors. *Journal of Petroleum Science and Engineering*. 2004, **43**(3-4), pp.259-270.
16. Charpentier, T., Neville, A., Baraka-Lokmane, S., Hurtevent, C., Ordonez-Varela, J., Nielsen, F.M., Eroini, V., Olsen, J., Ellingsen, J. and Bache, Ø. Evaluation of Anti-fouling Surfaces for Prevention of Mineral Scaling in Sub-surface Safety Valves. In: *SPE International Oilfield Scale Conference and Exhibition: Society of Petroleum Engineers*, 2014.
17. Eroini, V., Kapur, N., Neville, A. and Euvrard, M. Preventing scale formation using modified surfaces. In: *CORROSION 2011: NACE International*, 2011.
18. Vazirian, M.M., Charpentier, T.V., de Oliveira Penna, M. and Neville, A. Surface inorganic scale formation in oil and gas industry: As adhesion and deposition processes. *Journal of Petroleum Science and Engineering*. 2016, **137**, pp.22-32.
19. Okocha, C. and Sorbie, K. Scale Prediction for Iron, Zinc and Lead Sulphides and Its Relation to Scale Test Design. In: *CORROSION 2014: NACE International*, 2014.
20. Wang, S. and Wylde, J. Scale Inhibitor Selection For Deepwater High Temperature Applications. In: *CORROSION 2009, 2009/1/1/, Atlanta, Georgia*. NACE: NACE International, 2009, p.13.
21. Sorbie, K. and Okocha, C. Scale Prediction for Iron, Zinc, and Lead Sulfides and Its Relation to Scale Test Design. In: *SPE International Symposium on Oilfield Chemistry: Society of Petroleum Engineers*, 2013.

22. Okocha, C., Sorbie, K. and Boak, L. *Novel Inhibition Mechanism for Sulfide Scales. Paper SPE 112538 presented at the SPE International Symposium and Exhibition on Formation Damage Control, Lafayette, Louisiana, USA, 13–15 February. 2008.*
23. Al-Harbi, B.G., Graham, A.J. and Sorbie, K.S. Zinc and Lead Interactions in Combined Sulphide Scales. In: *2017/4/3/. SPE: Society of Petroleum Engineers.*
24. Hansen, C.M. The three dimensional solubility parameter. *Danish Technical: Copenhagen.* 1967, **14**.
25. Crabtree, M., Eslinger, D., Fletcher, P., Miller, M., Johnson, A. and King, G. Fighting scale—removal and prevention. *Oilfield Review.* 1999, **11**(3), pp.30-45.
26. Cheung, C.S. and Beech, I.B. The use of biocides to control sulphate-reducing bacteria in biofilms on mild steel surfaces. *Biofouling.* 1996, **9**(3), pp.231-249.
27. Merdhan, A.B. and Yassin, A.A.M. Solubility of common oil field scales of injection water and high–barium concentration and high–salinity formation water. *Jurnal Teknologi.* 2009, **50**(1), pp.67-77.
28. Moghadasi, J., Sharif, A., Müller-Steinhagen, H. and Jamialahmadi, M. Prediction of Scale Formation Problems in Oil Reservoirs and Production Equipment due to Injection of Incompatible Waters. *Developments in Chemical Engineering and Mineral Processing.* 2006, **14**(3-4), pp.545-566.
29. Barrett, T. and Anderson, G.J.G.e.C.A. The solubility of sphalerite and galena in 1–5 m NaCl solutions to 300 C. 1988, **52**(4), pp.813-820.
30. Barite Specimen, L. *Barite Specimen Localities - Barite Photos, Localities.* [Online]. 2016. [Accessed]. Available from: <http://www.baritespecimenlocalities.org/>
31. Judat, B. and Kind, M. Morphology and internal structure of barium sulfate—derivation of a new growth mechanism. *Journal of Colloid and Interface Science.* 2004, **269**(2), pp.341-353.
32. Wang, Z. *Mineral scale formation-aspects of surface energy and adhesion.* thesis, University of Leeds, 2006.
33. Chen, J., Long, X. and Chen, Y. Comparison of Multilayer Water Adsorption on the Hydrophobic Galena (PbS) and Hydrophilic Pyrite (FeS₂) Surfaces: A DFT Study. *The Journal of Physical Chemistry C.* 2014, **118**(22), pp.11657-11665.
34. MERUS. *Calcium carbonate deposit.* MERUS, 2017.
35. Mullin, J.W. *Crystallization.* Butterworth-Heinemann, 2001.
36. Al-Anezi, K. and Hilal, N. Scale formation in desalination plants: effect of carbon dioxide solubility. *Desalination.* 2007, **204**(1-3), pp.385-402.
37. Frota, T., Silva, D., Aguiar, J., Anjos, R., Silva, I.J.B.J.o.P. and Gas. Assessment of scale formation in the column of an oil and natural gas producing well: A case study. 2013, **7**(1).
38. Baraka-Lokmane, S., Hurtevent, C., Zhou, H., Saha, P., Tots, N., Rieu, F., Lastennet, R. and Sugiarto, T. TOTAL's Experience on the Development and Implementation of a Scale Management Strategy in Central Graben Fields. In: *SPE International Oilfield Scale Conference and Exhibition: Society of Petroleum Engineers, 2014.*
39. Stack, A.G., Raiteri, P. and Gale, J.D. Accurate rates of the complex mechanisms for growth and dissolution of minerals using a combination of rare-event theories. *Journal of the American Chemical Society.* 2011, **134**(1), pp.11-14.
40. Shadravan, A. and Amani, M. HPHT 101: What every engineer or geoscientist should know about high pressure hightemperature wells. In: *SPE Kuwait International Petroleum Conference and Exhibition: Society of Petroleum Engineers, 2012.*
41. Schlumberger. Sulfate Removal System. *Schlumberger.* [Online]. 2016.
42. Stigliani, W.M. Changes in valued “capacities” of soils and sediments as indicators of nonlinear and time-delayed environmental effects. *Environmental Monitoring and Assessment.* 1988, **10**(3), pp.245-307.
43. Muyzer, G. and Stams, A.J. The ecology and biotechnology of sulphate-reducing bacteria. *Nature reviews microbiology.* 2008, **6**(6), p.441.

44. Widdel, F. and Hansen, T. *The dissimilatory sulphate and sulphur-reducing bacteria. The prokaryotes*. New York: Springer. 1991.
45. Jordan, M., Mackin, K., Johnston, C. and Feasey, N. Control of hydrogen sulphide scavenger induced scale and the associated challenge of sulphide scale formation within a North Sea high temperature/high salinity fields production wells. Laboratory evaluation to field application. In: *SPE International Symposium on Oilfield Scale*: Society of Petroleum Engineers, 2004.
46. Leach, D.L., Taylor, R.D., Fey, D.L., Diehl, S.F. and Saltus, R.W. *A deposit model for Mississippi Valley-Type lead-zinc ores: Chapter A in Mineral deposit models for resource assessment*. US Geological Survey, 2010.
47. Eden, B., Laycock, P.J. and Fielder, M. *OILFIELD RESERVOIR SOURING*. Department of Energy, 1993.
48. Ramachandran, S., Al-Muntasheri, G., Leal, J. and Wang, Q. Corrosion and Scale Formation in High Temperature Sour Gas Wells: Chemistry and Field Practice. In: *SPE International Symposium on Oilfield Chemistry*: Society of Petroleum Engineers, 2015.
49. Li, Y., She, C., Liu, N., Zhang, H., Zhang, L. and Zhu, D. Completion difficulties of HTHP and high-flowrate sour gas wells in the Longwangmiao Fm gas reservoir, Sichuan Basin, and corresponding countermeasures. *Natural Gas Industry B*. 2016.
50. Baraka-Lokmane, S., Hurtevent, C., Rossiter, M., Bryce, F., Lepoivre, F., Marais, A., Tillement, O., Simpson, C. and Graham, G. Design and Performance of Novel Sulphide Nanoparticle Scale Inhibitors for North Sea HP/HT Fields. In: *SPE International Oilfield Scale Conference and Exhibition*: Society of Petroleum Engineers, 2016.
51. Sadvnikov, S., Kozhevnikova, N., Pushin, V. and Rempel, A. Microstructure of nanocrystalline PbS powders and films. *Inorganic Materials*. 2012, **48**(1), pp.21-27.
52. Furukawa, Y. and Nada, H. *Advances in the Understanding of Crystal Growth Mechanisms*. 1997.
53. Ostwald, W. Über die vermeintliche Isomerie des roten und gelben Quecksilberoxyds und die Oberflächenspannung fester Körper. *Zeitschrift für physikalische Chemie*. 1900, **34**(1), pp.495-503.
54. Amjad, Z. and Demadis, K.D. *Mineral Scales and Deposits: Scientific and Technological Approaches*. Elsevier, 2015.
55. Papavinasam, S. *Corrosion control in the oil and gas industry*. Elsevier, 2013.
56. Chen, T., Neville, A. and Yuan, M. Calcium carbonate scale formation—assessing the initial stages of precipitation and deposition. *Journal of Petroleum Science and Engineering*. 2005, **46**(3), pp.185-194.
57. Söhnle, O. and Mullin, J. Precipitation of calcium carbonate. *Journal of crystal Growth*. 1982, **60**(2), pp.239-250.
58. Cejka, J., Corma, A. and Zones, S. *Zeolites and catalysis: synthesis, reactions and applications*. John Wiley & Sons, 2010.
59. Nancollas, G. and Reddy, M. The crystallization of calcium carbonate. II. Calcite growth mechanism. *Journal of Colloid and Interface Science*. 1971, **37**(4), pp.824-830.
60. Eroini, V. *Kinetic study of calcium carbonate formation and inhibition by using an in-situ flow cell*. thesis, University of Leeds, 2011.
61. Wyslouzil, B.E. and Wölk, J. Overview: Homogeneous nucleation from the vapor phase—The experimental science. *The Journal of chemical physics*. 2016, **145**(21), p.211702.
62. Volmer, M. and Weber, A. Keimbildung in übersättigten Gebilden. *Z. phys. Chem*. 1926, **119**(3/4), pp.277-301.
63. Vignes, A. *Extractive Metallurgy 1: Basic Thermodynamics and Kinetics*. Wiley, 2013.

64. Dong, L., Chu, Y., Zhuo, Y. and Zhang, W. Two-minute synthesis of PbS nanocubes with high yield and good dispersibility at room temperature. *Nanotechnology*. 2009, **20**(12), p.125301.
65. Andritsos, N. and Karabelas, A. Sulfide scale formation and control: the case of lead sulfide. *Geothermics*. 1991, **20**(5), pp.343-353.
66. Lewis, A.E.J.H. Review of metal sulphide precipitation. 2010, **104**(2), pp.222-234.
67. Nehrke, G. *Calcite precipitation from aqueous solution: transformation from vaterite and role of solution stoichiometry*. thesis, UU Dept. of Earth Sciences, 2007.
68. Kong, Y., Chen, J., Fang, H., Heath, G., Wo, Y., Wang, W., Li, Y., Guo, Y., Evans, S.D. and Chen, S. Highly Fluorescent Ribonuclease-A-Encapsulated Lead Sulfide Quantum Dots for Ultrasensitive Fluorescence in Vivo Imaging in the Second Near-Infrared Window. *Chemistry of Materials*. 2016, **28**(9), pp.3041-3050.
69. Parsons, S.A. and Jefferson, B. *Introduction to potable water treatment processes*. Blackwell publishing, 2006.
70. Myerson, A. *Handbook of industrial crystallization*. Butterworth-Heinemann, 2002.
71. Chianese, A., Di Bernardino, F. and Jones, A. On the effect of secondary nucleation on the crystal size distribution from a seeded batch crystallizer. *Chemical engineering science*. 1993, **48**(3), pp.551-560.
72. Agrawal, S. and Paterson, A. Secondary nucleation: Mechanisms and models. *Chemical Engineering Communications*. 2015, **202**(5), pp.698-706.
73. Rodriguez-Blanco, J.D., Shaw, S. and Benning, L.G. The kinetics and mechanisms of amorphous calcium carbonate (ACC) crystallization to calcite, via vaterite. *Nanoscale*. 2011, **3**(1), pp.265-271.
74. Addadi, L., Raz, S. and Weiner, S. Taking advantage of disorder: amorphous calcium carbonate and its roles in biomineralization. *Advanced Materials*. 2003, **15**(12), pp.959-970.
75. Gong, Y.U., Killian, C.E., Olson, I.C., Appathurai, N.P., Amasino, A.L., Martin, M.C., Holt, L.J., Wilt, F.H. and Gilbert, P. Phase transitions in biogenic amorphous calcium carbonate. *Proceedings of the National Academy of Sciences*. 2012, **109**(16), pp.6088-6093.
76. Uwaha, M. and Koyama, K. Transition from nucleation to ripening in the classical nucleation model. *Journal of crystal Growth*. 2010, **312**(7), pp.1046-1054.
77. Uwaha, M. 8 - Growth Kinetics: Basics of Crystal Growth Mechanisms. In: Nishinaga, T. ed. *Handbook of Crystal Growth (Second Edition)*. Boston: Elsevier, 2015, pp.359-399.
78. De Yoreo, J.J. and Vekilov, P.G. Principles of crystal nucleation and growth. *Reviews in mineralogy and geochemistry*. 2003, **54**(1), pp.57-93.
79. Polte, J.J.C. Fundamental growth principles of colloidal metal nanoparticles—a new perspective. 2015, **17**(36), pp.6809-6830.
80. MacAndrew, R.J.J.o.P.T. Technology Focus: HP/HT Challenges (April 2008). 2008, **60**(04), pp.88-88.
81. Vu, H.P., Black, J.R. and Haese, R.R.J.E.P. Changes in formation water composition during water storage at surface and post re-injection. 2017, **114**, pp.5732-5741.
82. Nehrke, G., Reichart, G.-J., Van Cappellen, P., Meile, C. and Bijma, J.J.G.e.C.A. Dependence of calcite growth rate and Sr partitioning on solution stoichiometry: non-Kossel crystal growth. 2007, **71**(9), pp.2240-2249.
83. De La Pierre, M., Raiteri, P., Stack, A.G. and Gale, J.D. Uncovering the atomistic mechanism for calcite step growth. *Angewandte Chemie International Edition*. 2017, **56**(29), pp.8464-8467.
84. Sancho-Tomás, M., Fermani, S., Durán-Olivencia, M.A., Otálora, F., Gómez-Morales, J., Falini, G. and García-Ruiz, J. Influence of charged polypeptides on nucleation and growth of CaCO₃ evaluated by counterdiffusion experiments. *Crystal Growth & Design*. 2013, **13**(9), pp.3884-3891.

85. Kowacz, M., Putnis, C. and Putnis, A. The effect of cation: anion ratio in solution on the mechanism of barite growth at constant supersaturation: role of the desolvation process on the growth kinetics. *Geochimica et Cosmochimica Acta*. 2007, **71**(21), pp.5168-5179.
86. Petres, J.J., Deželić, G. and Težak, B. Monodisperse sols of barium sulfate. III. Electron-microscopic study of internal structure of particles. *Croatica chemica acta*. 1969, **41**(3), pp.183-186.
87. Chang, J. and Waclawik, E.R. Colloidal semiconductor nanocrystals: controlled synthesis and surface chemistry in organic media. *RSC Advances*. 2014, **4**(45), pp.23505-23527.
88. Thanh, N.T., Maclean, N. and Mahiddine, S. Mechanisms of nucleation and growth of nanoparticles in solution. *Chemical reviews*. 2014, **114**(15), pp.7610-7630.
89. Shanmugapriya, T., Vinayakan, R., Thomas, K.G. and Ramamurthy, P. Synthesis of CdS nanorods and nanospheres: shape tuning by the controlled addition of a sulfide precursor at room temperature. *CrystEngComm*. 2011, **13**(7), pp.2340-2345.
90. Brazeau, A.L. and Jones, N.D. Growth Mechanisms in Nanocrystalline Lead Sulfide by Stopped-Flow Kinetic Analysis. *The Journal of Physical Chemistry C*. 2009, **113**(47), pp.20246-20251.
91. Rattanasak, U., Pankhet, K. and Chindaprasirt, P. Effect of chemical admixtures on properties of high-calcium fly ash geopolymer. *International Journal of Minerals, Metallurgy, and Materials*. 2011, **18**(3), pp.364-369.
92. Guyette, R.P. and Cutter, B.E. Barium and manganese trends in tree-rings as monitors of sulfur deposition. *Water, Air, & Soil Pollution*. 1994, **73**(1), pp.213-223.
93. Lee, K., Millero, F.J., Byrne, R.H., Feely, R.A. and Wanninkhof, R. The recommended dissociation constants for carbonic acid in seawater. *Geophysical Research Letters*. 2000, **27**(2), pp.229-232.
94. Barbero, J.A., McCurdy, K.G. and Tremaine, P.R. Apparent molal heat capacities and volumes of aqueous hydrogen sulfide and sodium hydrogen sulfide near 25 C: The temperature dependence of H₂S ionization. *Canadian Journal of Chemistry*. 1982, **60**(14), pp.1872-1880.
95. Migdisov, A.A., Williams-Jones, A., Lakshtanov, L. and Alekhin, Y.V. Estimates of the second dissociation constant of H₂S from the surface sulfidation of crystalline sulfur. *Geochimica et Cosmochimica Acta*. 2002, **66**(10), pp.1713-1725.
96. Al-Janabi, Y., Al-Jabran, A., Alsalem, M. and Al-Dossary, K. Downhole O₂-Corrosion Inhibitor Evaluation for Nitrogen Gas Lifting System—Part I: Rotating Cage & LPR. In: *15th Middle East Corrosion Conference, paper*.
97. Scarascia, G., Wang, T. and Hong, P.-Y. Quorum sensing and the use of quorum quenchers as natural biocides to inhibit sulfate-reducing bacteria. *Antibiotics*. 2016, **5**(4), p.39.
98. Sato, M. Oxidation of sulfide ore bodies; 1, Geochemical environments in terms of Eh and pH. *Economic Geology*. 1960, **55**(5), pp.928-961.
99. Gaudin, A. and Sun, S. Correlation between mineral behavior in cataphoresis and in flotation. *Trans. AIME*. 1946, **169**, pp.347-362.
100. Aplan, F. and Fuerstenau, D. Principles of nonmetallic mineral flotation. *Froth flotation*. 1962, **50**, p.170.
101. Wang, D., Jiao, F., Qin, W., Wang, X.J.S.S. and Technology. Effect of surface oxidation on the flotation separation of chalcopyrite and galena using sodium humate as depressant. 2018, **53**(6), pp.961-972.
102. Butt, H.-J. A technique for measuring the force between a colloidal particle in water and a bubble. *Journal of Colloid and Interface Science*. 1994, **166**(1), pp.109-117.
103. Xie, L. Probing Surface Heterogeneity, Electrochemical Properties and Bubble-Solid Interaction Mechanisms of Sulfide Minerals in Flotation. 2017.

104. Leite, F.L., Bueno, C.C., Da Róz, A.L., Ziemath, E.C. and Oliveira, O.N.J.I.j.o.m.s. Theoretical models for surface forces and adhesion and their measurement using atomic force microscopy. 2012, **13**(10), pp.12773-12856.
105. Brown, M.A., Goel, A. and Abbas, Z. Effect of electrolyte concentration on the stern layer thickness at a charged interface. *Angewandte Chemie International Edition*. 2016, **55**(11), pp.3790-3794.
106. Morse, J.W. and He, S. Influences of T, S and PCO₂ on the pseudo-homogeneous precipitation of CaCO₃ from seawater: implications for whiting formation. *Marine Chemistry*. 1993, **41**(4), pp.291-297.
107. Coto, B., Martos, C., Peña, J.L., Rodríguez, R. and Pastor, G. Effects in the solubility of CaCO₃: Experimental study and model description. *Fluid Phase Equilibria*. 2012, **324**, pp.1-7.
108. Yuan, M. Barium Sulfate Scale Inhibition in the Deepwater Cold Temperature Environment. In: *International Symposium on Oilfield Scale, 2001/1/1/, Aberdeen, United Kingdom*. SPE: Society of Petroleum Engineers, 2001, p.10.
109. Reed, M.H., Palandri, J.J.R.i.M. and Geochemistry. Sulfide mineral precipitation from hydrothermal fluids. 2006, **61**(1), pp.609-631.
110. Marchioretto, M.M., Bruning, H. and Rulkens, W. Heavy Metals Precipitation in Sewage Sludge. *Separation Science and Technology*. 2005, **40**(16), pp.3393-3405.
111. Wogelius, R.A. Adsorption and co-precipitation reactions at the mineral-fluid interface: natural and anthropogenic processes. *Crystal Research and Technology*. 2013, **48**(10), pp.877-902.
112. Kolthoff, I. Theory of coprecipitation. The formation and properties of crystalline precipitates. *The Journal of Physical Chemistry*. 1932, **36**(3), pp.860-881.
113. Dunitz, J.D.J.C. Crystal and co-crystal: a second opinion. 2003, **5**(91), pp.506-506.
114. Kumagai, T.J.R. Coprecipitation of cadmium with calcium carbonate from aqueous solutions at 15 to 50°C. 1992, **41**, pp.57-63.
115. Bard, A.J., Inzelt, G. and Scholz, F. *Electrochemical dictionary*. Springer Science & Business Media, 2008.
116. Okocha, C.E. *Mechanistic evaluation of sulphide scale formation in the oilfield*. thesis, Heriot-Watt University, 2011.
117. Chen, T., Neville, A. and Yuan, M. Influence of Mg²⁺ on CaCO₃ formation—bulk precipitation and surface deposition. *Chemical engineering science*. 2006, **61**(16), pp.5318-5327.
118. Compton, R.G. and Brown, C.A. The Inhibition of Calcite Dissolution/Precipitation: Mg²⁺ Cations. *Journal of Colloid and Interface Science*. 1994, **165**(2), pp.445-449.
119. de Leeuw, N.H. Molecular Dynamics Simulations of the Growth Inhibiting Effect of Fe²⁺, Mg²⁺, Cd²⁺, and Sr²⁺ on Calcite Crystal Growth. *The Journal of Physical Chemistry B*. 2002, **106**(20), pp.5241-5249.
120. Sangwal, K. Effects of impurities on crystal growth processes. *Progress in Crystal Growth and Characterization of Materials*. 1996, **32**(1), pp.3-43.
121. Mallampati, R. and Valiyaveetil, S.J.R.A. Co-precipitation with calcium carbonate—a fast and nontoxic method for removal of nanopollutants from water? 2015, **5**(15), pp.11023-11028.
122. Li, S.-S., Chang, C.-H., Wang, Y.-C., Lin, C.-W., Wang, D.-Y., Lin, J.-C., Chen, C.-C., Sheu, H.-S., Chia, H.-C., Wu, W.-R.J.E. and Science, E. Intermixing-seeded growth for high-performance planar heterojunction perovskite solar cells assisted by precursor-capped nanoparticles. 2016, **9**(4), pp.1282-1289.
123. Reddy, S., Rautaray, D., Sainkar, S.R. and Sastry, M. On the morphology of SrCO₃ crystals grown at the interface between two immiscible liquids. *Bulletin of Materials Science*. 2003, **26**(3), p.283.
124. Rodríguez-Navarro, A.B., Marie, P., Nys, Y., Hincke, M.T. and Gautron, J. Amorphous calcium carbonate controls avian eggshell mineralization: a new paradigm for

- understanding rapid eggshell calcification. *Journal of structural biology*. 2015, **190**(3), pp.291-303.
125. Quddus, A., Khokhar, M. and Allam, I. Effect of Hydrodynamics on Calcium Sulfate Scale Deposition. *SPE Paper*. 1993, **27417**.
 126. K. Friedlander, S. *Behavior of Suspended Particles in a Turbulent Fluid*. 1957.
 127. Kostoglou, M., Andritsos, N. and Karabelas, A. Flow of supersaturated solutions in pipes. Modeling bulk precipitation and scale formation. *Chemical Engineering Communications*. 1995, **133**(1), pp.107-131.
 128. Unni, H.N. and Yang, C. Brownian dynamics simulation and experimental study of colloidal particle deposition in a microchannel flow. *Journal of Colloid and Interface Science*. 2005, **291**(1), pp.28-36.
 129. Andritsos, N. and Karabelas, A. Crystallization and deposit formation of lead sulfide from aqueous solutions: II. Morphology of the deposits. *Journal of Colloid and Interface Science*. 1991, **145**(1), pp.170-181.
 130. Geddert, T., Kipp, S., Augustin, W. and Scholl, S. Influence of Different Surface Materials on Nucleation and Crystal Growth in Heat Exchangers. 2007.
 131. Cheong, W., Gaskell, P. and Neville, A. Substrate effect on surface adhesion/crystallisation of calcium carbonate. *Journal of crystal Growth*. 2013, **363**, pp.7-21.
 132. Chevalier, N.R. Do Surface Wetting Properties Affect Calcium Carbonate Heterogeneous Nucleation and Adhesion? *The Journal of Physical Chemistry C*. 2014, **118**(31), pp.17600-17607.
 133. Marion, G., Millero, F. and Feistel, R. Precipitation of solid phase calcium carbonates and their effect on application of seawater S A–T–P models. *Ocean Science*. 2009, **5**(3), pp.285-291.
 134. Wu, S. *Polymer interface and adhesion*. 1982.
 135. Brewis, D. and Briggs, D. *Industrial adhesion problems*. 1985.
 136. Oliveira, R. Understanding adhesion: A means for preventing fouling. *Experimental Thermal and Fluid Science*. 1997, **14**(4), pp.316-322.
 137. Grasso, D., Subramaniam, K., Butkus, M., Strevett, K. and Bergendahl, J. A review of non-DLVO interactions in environmental colloidal systems. *Reviews in Environmental Science and Biotechnology*. 2002, **1**(1), pp.17-38.
 138. Ebeling, D., van den Ende, D. and Mugele, F. Electrostatic interaction forces in aqueous salt solutions of variable concentration and valency. *Nanotechnology*. 2011, **22**(30), p.305706.
 139. Comyn, J. *Adhesion science*. Royal Society of Chemistry, 2007.
 140. Corn, M. The adhesion of solid particles to solid surfaces. I. A review. *J Air Pollut Control Assoc*. 1961, **11**, pp.523-528.
 141. Preočanin, T., Selmani, A., Lindqvist-Reis, P., Heberling, F., Kallay, N. and Lützenkirchen, J. Surface charge at Teflon/aqueous solution of potassium chloride interfaces. *Colloids and Surfaces A: Physicochemical and Engineering Aspects*. 2012, **412**, pp.120-128.
 142. Keysar, S., Semiat, R., Hasson, D. and Yahalom, J. Effect of surface roughness on the morphology of calcite crystallizing on mild steel. *Journal of Colloid and Interface Science*. 1994, **162**(2), pp.311-319.
 143. Butt, H.-J., Golovko, D.S. and Bonaccorso, E.J.T.J.o.P.C.B. On the derivation of Young's equation for sessile drops: nonequilibrium effects due to evaporation. 2007, **111**(19), pp.5277-5283.
 144. Rabinovich, Y.I., Adler, J.J., Ata, A., Singh, R.K. and Moudgil, B.M. Adhesion between Nanoscale Rough Surfaces. *J Colloid Interface Sci*. 2000, **232**(1), pp.10-16.
 145. Bukuaghangin, O., Sanni, O., Kapur, N., Huggan, M., Neville, A. and Charpentier, T. Kinetics study of barium sulphate surface scaling and inhibition with a once-through flow system. *Journal of Petroleum Science and Engineering*. 2016, **147**, pp.699-706.

146. Israelachvili, J.N. *Intermolecular and surface forces*. Academic press, 2011.
147. Adair, J.H., Suvaci, E. and Sindel, J. Surface and Colloid Chemistry. In: Buschow, K.H.J. et al. eds. *Encyclopedia of Materials: Science and Technology*. Oxford: Elsevier, 2001, pp.1-10.
148. Cevc, G. Hydration force and the interfacial structure of the polar surface. *Journal of the Chemical Society, Faraday Transactions*. 1991, **87**(17), pp.2733-2739.
149. Leikin, S., Parsegian, V.A., Rau, D.C. and Rand, R.P. Hydration forces. *Annual Review of Physical Chemistry*. 1993, **44**(1), pp.369-395.
150. Pashley, R.M. DLVO and hydration forces between mica surfaces in Li⁺, Na⁺, K⁺, and Cs⁺ electrolyte solutions: A correlation of double-layer and hydration forces with surface cation exchange properties. *Journal of Colloid and Interface Science*. 1981, **83**(2), pp.531-546.
151. Xie, L., Wang, J., Shi, C., Huang, J., Zhang, H., Liu, Q., Liu, Q. and Zeng, H.J.T.J.o.P.C.C. Probing surface interactions of electrochemically active galena mineral surface using atomic force microscopy. 2016, **120**(39), pp.22433-22442.
152. De Giudici, G., Ricci, P., Lattanzi, P. and Anedda, A. Dissolution of the (001) surface of galena: An in situ assessment of surface speciation by fluid-cell micro-Raman spectroscopy. *American Mineralogist*. 2007, **92**(4), pp.518-524.
153. De Giudici, G. and Zuddas, P. In situ investigation of galena dissolution in oxygen saturated solution: evolution of surface features and kinetic rate. *Geochimica et Cosmochimica Acta*. 2001, **65**(9), pp.1381-1389.
154. Flores, J.G., Chen, X.T. and Brill, J.P. Characterization of Oil-Water Flow Patterns in Vertical and Deviated Wells. In: *SPE Annual Technical Conference and Exhibition, 1997/1/1/, San Antonio, Texas*. SPE: Society of Petroleum Engineers, 1997, p.10.
155. Kee, K.E., Richter, S., Babic, M. and Nešić, S. Experimental Study of Oil-Water Flow Patterns in a Large Diameter Flow Loop—The Effect on Water Wetting and Corrosion. *CORROSION*. 2015, **72**(4), pp.569-582.
156. Rahmani, A.M., Wang, A., Manoharan, V.N. and Colosqui, C.E. Colloidal particle adsorption at liquid interfaces: capillary driven dynamics and thermally activated kinetics. *Soft Matter*. 2016, **12**(30), pp.6365-6372.
157. Chevalier, Y. and Bolzinger, M.-A. Emulsions stabilized with solid nanoparticles: Pickering emulsions. *Colloids and Surfaces A: Physicochemical and Engineering Aspects*. 2013, **439**, pp.23-34.
158. Bebie, J., Schoonen, M.A., Fuhrmann, M. and Strongin, D.R. Surface charge development on transition metal sulfides: an electrokinetic study. *Geochimica et Cosmochimica Acta*. 1998, **62**(4), pp.633-642.
159. Kim, I., Worthen, A.J., Johnston, K.P., DiCarlo, D.A. and Huh, C. Size-dependent properties of silica nanoparticles for Pickering stabilization of emulsions and foams. *Journal of Nanoparticle Research*. 2016, **18**(4), p.82.
160. Kirchberg, S., Abdin, Y. and Ziegmann, G. Influence of particle shape and size on the wetting behavior of soft magnetic micropowders. *Powder Technology*. 2011, **207**(1–3), pp.311-317.
161. Nonomura, Y., Kobayashi, N.J.J.o.c. and science, i. Phase inversion of the Pickering emulsions stabilized by plate-shaped clay particles. 2009, **330**(2), pp.463-466.
162. Pal, R. A Simple Model for the Viscosity of Pickering Emulsions. *Fluids*. 2018, **3**(1), p.2.
163. Keal, L. *Dynamics of hard and soft colloids at aqueous interfaces*. thesis, Université Pierre et Marie Curie-Paris VI, 2016.
164. Davies, G.B., Krüger, T., Coveney, P.V., Harting, J. and Bresme, F.J.A.m. Assembling ellipsoidal particles at fluid interfaces using switchable dipolar capillary interactions. 2014, **26**(39), pp.6715-6719.
165. Binks, B.P. and Lumsdon, S.J.L. Influence of particle wettability on the type and stability of surfactant-free emulsions. 2000, **16**(23), pp.8622-8631.

166. Speight, J.G. *Handbook of petroleum product analysis*. John Wiley & Sons, 2015.
167. Whitby, C.P. and Wanless, E.J. Controlling Pickering Emulsion Destabilisation: A Route to Fabricating New Materials by Phase Inversion. *Materials (Basel, Switzerland)*. 2016, **9**(8), p.626.
168. Arditty, S., Whitby, C.P., Binks, B.P., Schmitt, V. and Leal-Calderon, F. Some general features of limited coalescence in solid-stabilized emulsions. *The European physical journal. E, Soft matter*. 2003, **11**(3), pp.273-281.
169. Zhai, X. and Efrima, S. Chemical and Physical Aspects of Macroemulsions Stabilized by Interfacial Colloids. *The Journal of Physical Chemistry*. 1996, **100**(26), pp.11019-11028.
170. Strey, R. Microemulsion microstructure and interfacial curvature. *Colloid and Polymer Science*. 1994, **272**(8), pp.1005-1019.
171. Park, B.J., Brugarolas, T. and Lee, D. Janus particles at an oil–water interface. *Soft Matter*. 2011, **7**(14), pp.6413-6417.
172. Perro, A., Reculosa, S., Ravaine, S., Bourgeat-Lami, E. and Duguet, E. Design and synthesis of Janus micro- and nanoparticles. *Journal of Materials Chemistry*. 2005, **15**(35-36), pp.3745-3760.
173. Graham, G., Boak, L. and Hobden, C. Examination of the Effect of Generically Different Scale Inhibitor Species (PPCA and DETPMP) on the Adherence and Growth of Barium Sulphate Scale on Metal Surfaces. In: *International Symposium on Oilfield Scale*: Society of Petroleum Engineers, 2001.
174. Barakat, M.A. and Schmidt, E. Polymer-enhanced ultrafiltration process for heavy metals removal from industrial wastewater. *Desalination*. 2010, **256**(1), pp.90-93.
175. Ilevbare, G.A., Liu, H., Edgar, K.J. and Taylor, L.S. Understanding Polymer Properties Important for Crystal Growth Inhibition—Impact of Chemically Diverse Polymers on Solution Crystal Growth of Ritonavir. *Crystal Growth & Design*. 2012, **12**(6), pp.3133-3143.
176. Raffa, P., Wever, D.A.Z., Picchioni, F. and Broekhuis, A.A. Polymeric Surfactants: Synthesis, Properties, and Links to Applications. *Chemical reviews*. 2015, **115**(16), pp.8504-8563.
177. Cui, S., Liu, C., Wang, Z., Zhang, X., Strandman, S. and Tenhu, H. Single Molecule Force Spectroscopy on Polyelectrolytes: Effect of Spacer on Adhesion Force and Linear Charge Density on Rigidity. *Macromolecules*. 2004, **37**(3), pp.946-953.
178. Dietzsch, M., Barz, M., Schüler, T., Klassen, S., Schreiber, M., Susewind, M., Loges, N., Lang, M., Hellmann, N., Fritz, M., Fischer, K., Theato, P., Kühnle, A., Schmidt, M., Zentel, R. and Tremel, W. PAA-PAMPS Copolymers as an Efficient Tool to Control CaCO₃ Scale Formation. *Langmuir*. 2013, **29**(9), pp.3080-3088.
179. Sigma-Aldrich. *Poly(2-acrylamido-2-methyl-1-propanesulfonic acid) solution*, [Exhibition catalogue]. 2019.
180. Boivin, J. Oil industry biocides. 1995.
181. Cheung, C.W.S. and Beech, I.B. The use of biocides to control sulphate-reducing bacteria in biofilms on mild steel surfaces. *Biofouling*. 1996, **9**(3), pp.231-249.
182. Whitham, T.S. and Gilbert, P.D. Evaluation of a model biofilm for the ranking of biocide performance against sulphate-reducing bacteria. *Journal of Applied Bacteriology*. 1993, **75**(6), pp.529-535.
183. Gardner, L.R. and Stewart, P.S. Action of glutaraldehyde and nitrite against sulfate-reducing bacterial biofilms. *Journal of Industrial Microbiology and Biotechnology*. 2002, **29**(6), pp.354-360.
184. Arensdorf, J.J., Miner, K., Ertmoed, R., Clay, W.K., Stadnicki, P. and Voordouw, G. Mitigation of Reservoir Souring by Nitrate in a Produced-Water Reinjection System in Alberta. In: *SPE International Symposium on Oilfield Chemistry, 2009/1/1/, The Woodlands. Texas*. SPE: Society of Petroleum Engineers, 2009, p.8.

185. Lopez, T.H., Yuan, M., Williamson, D.A. and Przybylinski, J.L. Comparing efficacy of scale inhibitors for inhibition of zinc sulfide and lead sulfide scales. In: *SPE International Symposium on Oilfield Scale*: Society of Petroleum Engineers, 2005.
186. Chen, T., Chen, P., Montgomerie, H., Hagen, T.H. and Jeffrey, C. Development of Test Method and Inhibitors for Lead Sulfide. In: *SPE International Conference on Oilfield Scale*: Society of Petroleum Engineers, 2010.
187. Bukuaghangin, O., Neville, A. and Charpentier, T.V. Scale Formation in Multiphase Conditions.
188. Patankar, N.A. Mimicking the Lotus Effect: Influence of Double Roughness Structures and Slender Pillars. *Langmuir*. 2004, **20**(19), pp.8209-8213.
189. Vazirian, M.M., Charpentier, T.V.J., de Oliveira Penna, M. and Neville, A. Surface inorganic scale formation in oil and gas industry: As adhesion and deposition processes. *Journal of Petroleum Science and Engineering*. 2016, **137**, pp.22-32.
190. Mayer, M., Augustin, W. and Scholl, S. Adhesion of single crystals on modified surfaces in crystallization fouling. *Journal of crystal Growth*. 2012, **361**, pp.152-158.
191. Mayer, M., Augustin, W. and Scholl, S. Experimental study on the adhesion of single crystals on modified surfaces in crystallization fouling. In: *Proceedings of the International Conference on Heat Exchanger Fouling and Cleaning IX–2011*, 2011.
192. Baraka-Lokmane, S., Charpentier, J., Thibaut, V., Neville, A., Hurtevent, C., Ordonez-Varela, J.R., Moeller Nielsen, F., Eroini, V., Olsen, J.H. and Ellingsen, J.A. Comparison of characteristic of anti-scaling coating for subsurface safety valve for use in oil and gas industry. In: *International Petroleum Technology Conference*: International Petroleum Technology Conference, 2014.
193. Zhang, Z.-h., Wang, H.-j., Liang, Y.-h., Li, X.-j., Ren, L.-q., Cui, Z.-q. and Luo, C. One-step fabrication of robust superhydrophobic and superoleophilic surfaces with self-cleaning and oil/water separation function. *Scientific Reports*. 2018, **8**(1), p.3869.
194. Crick, C.R., Ozkan, F.T. and Parkin, I.P. Fabrication of optimized oil-water separation devices through the targeted treatment of silica meshes. *Science and technology of advanced materials*. 2015, **16**(5), pp.055006-055006.
195. Karimnezhad, H. Fabrication of Hydrophobic Membrane for the Separation of n-Hexane/Water Mixture Using Novel Oleophilic Nanoparticle and Kevlar Fabric, as a Superior Support. *Journal of Water and Environmental Nanotechnology*. 2017, **2**(3), pp.145-156.
196. Zarga, Y., Boubaker, H.B., Ghaffour, N. and Elfil, H. Study of calcium carbonate and sulfate co-precipitation. *Chemical engineering science*. 2013, **96**, pp.33-41.
197. Andersson, M.P., Dideriksen, K., Sakuma, H. and Stipp, S.L.S.J.S.r. Modelling how incorporation of divalent cations affects calcite wettability—implications for biomineralisation and oil recovery. 2016, **6**, p.28854.
198. Hua, B., Deng, B., Thornton, E.C., Yang, J. and Amonette, J.E. Incorporation of Chromate into Calcium Carbonate Structure During Coprecipitation. *Water, Air, and Soil Pollution*. 2007, **179**(1), pp.381-390.
199. Li, W., Ruan, G., Bhandari, N., Wang, X., Liu, Y., Dushane, H., Sriyathne, M., Harouaka, K., Lu, Y.-T., Deng, G., Zhao, Y., Kan, A.T. and Tomson, M. Development of Novel Iron Sulfide Scale Control Chemicals. In: *SPE International Oilfield Scale Conference and Exhibition, 2018/6/20/, Aberdeen, Scotland, UK*. SPE: Society of Petroleum Engineers, 2018, p.12.
200. Tian, X., Jokinen, V., Li, J., Sainio, J. and Ras, R.H.A. Unusual Dual Superlyophobic Surfaces in Oil–Water Systems: The Design Principles. *Advanced Materials*. 2016, **28**(48), pp.10652-10658.
201. Teng, H. Overview of the Development of the Fluoropolymer Industry. *Applied Sciences*. 2012, **2**(2), pp.496-512.

202. Kruss. *Drop Shape Analysis*. [Online]. 2019. [Accessed 03/03/2019]. Available from: <https://www.kruss-scientific.com/services/education-theory/glossary/drop-shape-analysis/>
203. Siqveland, L.M. and Skjaeveland, S. Derivations of the Young–Laplace equation. *Unpublished research*. [https://doi.org/10.13140/RG.2014, 2\(4485.5768\)](https://doi.org/10.13140/RG.2014.2(4485.5768)).
204. Savkova, J. and Blahova, O. Scratch resistance of TiAlSiN coatings. *Chem. Listy*. 2011, **105**, pp.214-217.
205. Wyant, J.C. *White light interferometry*. SPIE, 2002.
206. Keogh, W., Charpentier, T., Neville, A., O'Brien, A., Eroini, V., Olsen, J.H., Nielsen, F.M., Ellingsen, J.A., Bache, O. and Baraka-Lokmane, S. Evaluation of Anti-Fouling Surfaces for Prevention of Lead Sulfide Scaling in Single and Multiphase Conditions. In: *CORROSION 2017, 2017/4/27/, New Orleans, Louisiana, USA*. NACE: NACE International, 2017, p.15.
207. Yang, L. *Nanotechnology-enhanced orthopedic materials: fabrications, applications and future trends*. Woodhead Publishing, 2015.
208. Robertson, J. Diamond-like carbon. *Pure and applied chemistry*. 1994, **66**(9), pp.1789-1796.
209. Hutchings, I. and Shipway, P. *Tribology: friction and wear of engineering materials*. Butterworth-Heinemann, 2017.
210. USA, h. *HEF Overview Slide Presentation*. [Online]. 2015. [Accessed]. Available from: http://www.hefusa.net/HEF_overview.html
211. McKeen, L.W. *The effect of creep and other time related factors on plastics and elastomers*. Elsevier, 2009.
212. Deflorian, F., Fedrizzi, L., Locaspi, A. and Bonora, P. Testing of corrosion resistant fluoropolymer coatings. *Electrochimica Acta*. 1993, **38**(14), pp.1945-1950.
213. Park, B.-H., Sohn, J.-Y. and Shin, J. Radiolytic preparation and characterization of hydrophilic poly(acrylonitrile-co-vinylsulfonate)-grafted porous poly(tetrafluoroethylene) substrates. *Radiation Physics and Chemistry*. 2016, **118**, pp.42-47.
214. Saji, V.S. and Cook, R. *Corrosion protection and control using nanomaterials*. Elsevier, 2012.
215. Sakka, S. *Handbook of Advanced Ceramics: Chapter 11.1. 2. Sol–Gel Process and Applications*. Elsevier Inc. Chapters, 2013.
216. Pierre, A. Porous sol-gel ceramics. *Ceramics international*. 1997, **23**(3), pp.229-238.
217. Kócs, L., Albert, E., Tegze, B., Kabai-Faix, M., Major, C., Szalai, A., Basa, P. and Hórvölgyi, Z. Silica Sol-gel Coatings with Improved Light Transmittance and Stability. *Periodica Polytechnica Chemical Engineering*. 2018, **62**(1), pp.21-31.
218. Graco. *Chemical Compatibility*. [Online]. 2013. [Accessed]. Available from: <https://www.graco.com/gb/en/products/ad/chemical-compatibility.html>
219. Palomar-Pardave, M., Gonzales, I., Romero-Romo, M., Oropez, T. and Palomar-Pardave, M. *MES 23: Electrochemistry, Nanotechnology, and Biomaterials*. Electrochemical Society: Pennington, NJ, USA. 2008.
220. Podryabinkin, E., Rudyak, V., Gavrilov, A. and May, R. Detailed modeling of drilling fluid flow in a wellbore annulus while drilling. In: *ASME 2013 32nd International Conference on Ocean, Offshore and Arctic Engineering: American Society of Mechanical Engineers Digital Collection*, 2013.
221. Kielland, J.J.J.o.t.A.C.S. Individual activity coefficients of ions in aqueous solutions. 1937, **59**(9), pp.1675-1678.
222. Kong, Y., Chen, J., Fang, H., Heath, G., Wo, Y., Wang, W., Li, Y., Guo, Y., Evans, S.D. and Chen, S.J.C.o.M. Highly fluorescent ribonuclease-A-encapsulated lead sulfide quantum dots for ultrasensitive fluorescence in vivo imaging in the second near-infrared window. 2016, **28**(9), pp.3041-3050.

223. Kielland, J. Individual activity coefficients of ions in aqueous solutions. *Journal of the American Chemical Society*. 1937, **59**(9), pp.1675-1678.
224. Pitzer, K.S. Thermodynamics of electrolytes. I. Theoretical basis and general equations. *The Journal of Physical Chemistry*. 1973, **77**(2), pp.268-277.
225. Schlesinger, I. and Sivan, U.J.L. New information on the hydrophobic interaction revealed by frequency modulation AFM. 2017, **33**(10), pp.2485-2496.
226. Yoon, R.-H., Mao, L.J.J.o.C. and Science, I. Application of extended DLVO theory, IV: derivation of flotation rate equation from first principles. 1996, **181**(2), pp.613-626.
227. Group, N.F. *Commercial AFMs*. [Online]. 2019. [Accessed]. Available from: <https://www.nanofunction.org/commercial-afms/>
228. Burnham, N.A., Colton, R.J. and Pollock, H.M. Interpretation of force curves in force microscopy. *Nanotechnology*. 1993, **4**(2), pp.64-80.
229. CanStockPhoto. *Natural Galena Stone Isolated*. [Online]. 2019. [Accessed]. Available from: <https://www.canstockphoto.com/natural-galena-stone-isolated-44682745.html>
230. Gu, X., Raghavan, D., Nguyen, T., VanLandingham, M.R. and Yebassa, D. Characterization of polyester degradation using tapping mode atomic force microscopy: exposure to alkaline solution at room temperature. *Polymer Degradation and Stability*. 2001, **74**(1), pp.139-149.
231. Manocha, A. and Park, R.L.J.A.o.S.S. Flotation related ESCA studies on PbS surfaces. 1977, **1**(1), pp.129-141.
232. Keogh, W., Boakye, G.O., Neville, A., Charpentier, T., Olsen, J.H., Eroini, V., Nielsen, F., Ellingsen, J., Bache, O. and Baraka-Lokmane, S. Lead Sulfide (PbS) Scale Behavior and Deposition as a Function of Polymeric Sulfide Inhibitor Concentration in Multiphase. In: *NACE 2018: Proceedings of the International Corrosion Conference and Expo Series: National Association of Corrosion Engineers*, 2018.
233. Sen, S., Subramanian, S. and Discher, D.E. Indentation and Adhesive Probing of a Cell Membrane with AFM: Theoretical Model and Experiments. *Biophysical Journal*. 2005, **89**(5), pp.3203-3213.
234. Hutter, J.L. and Bechhoefer, J.J.R.o.S.I. Calibration of atomic-force microscope tips. 1993, **64**(7), pp.1868-1873.
235. Liu, J., Sandaklie-Nikolova, L., Wang, X., Miller, J.D.J.J.o.c. and science, i. Surface force measurements at kaolinite edge surfaces using atomic force microscopy. 2014, **420**, pp.35-40.
236. Tabor, R.F., Wu, C., Grieser, F., Chan, D.Y. and Dagastine, R.R.J.S.M. Non-linear and cyclical collisions between drops and bubbles: using AFM to understand droplet interactions in micro-scale flows. 2013, **9**(8), pp.2426-2433.
237. Shi, C., Chan, D.Y., Liu, Q. and Zeng, H. Probing the hydrophobic interaction between air bubbles and partially hydrophobic surfaces using atomic force microscopy. *The Journal of Physical Chemistry C*. 2014, **118**(43), pp.25000-25008.
238. Xie, L., Shi, C., Wang, J., Huang, J., Lu, Q., Liu, Q. and Zeng, H. Probing the interaction between air bubble and sphalerite mineral surface using atomic force microscope. *Langmuir*. 2015, **31**(8), pp.2438-2446.
239. Abu El Ela, M., Mahgoub, I., Mahmoud, K.J.O. and journal, g. Approach diagnoses, reduces water cut. 2007, **105**(7), pp.39-39.
240. Konrad, F., Gallien, F., Gerard, D.E. and Dietzel, M. Transformation of Amorphous Calcium Carbonate in Air. *Crystal Growth & Design*. 2016, **16**(11), pp.6310-6317.
241. Tobler, D.J., Rodriguez Blanco, J.D., Sørensen, H.O., Stipp, S.L.S. and Dideriksen, K. Effect of pH on Amorphous Calcium Carbonate Structure and Transformation. *Crystal Growth & Design*. 2016, **16**(8), pp.4500-4508.
242. Weintritt, D. and Cowan, J.J.J.o.P.T. Unique characteristics of barium sulfate scale deposition. 1967, **19**(10), pp.1,381-381,394.

243. Li, Y.-H., Crane, S.D. and Coleman, J.R. A Novel Approach to Predict the Co-Precipitation of BaSO₄ and SrSO₄. In: *SPE Production Operations Symposium*: Society of Petroleum Engineers, 1995.
244. Soo, S.L. and Tung, S.K. Deposition and entrainment in pipe flow of a suspension. *Powder Technology*. 1972, **6**(5), pp.283-294.
245. Kumar, D., Agarwal, G., Tripathi, B., Vyas, D. and Kulshrestha, V. Characterization of PbS nanoparticles synthesized by chemical bath deposition. *Journal of Alloys and Compounds*. 2009, **484**(1), pp.463-466.
246. Alsaadi, H.A.A.J.J.o.E. Corrosion Study of the Injection Equipments in Water in Al-Ahdeb Wells-Iraq. 2015, **21**(1), pp.15-28.
247. Leiro, J.A., Laajalehto, K., Peltoniemi, M.S., Torhola, M. and Szczerbakow, A. Surface core-level shift and AFM study of the galena (100) surface. *Surface and Interface Analysis*. 2002, **33**(12), pp.964-967.
248. Kaggwa, G.B., Nalam, P.C., Kilpatrick, J.I., Spencer, N.D. and Jarvis, S.P. Impact of Hydrophilic/Hydrophobic Surface Chemistry on Hydration Forces in the Absence of Confinement. *Langmuir*. 2012, **28**(16), pp.6589-6594.
249. Sokolov, I., Ong, Q.K., Shodiev, H., Chechik, N., James, D. and Oliver, M. AFM study of forces between silica, silicon nitride and polyurethane pads. *Journal of Colloid and Interface Science*. 2006, **300**(2), pp.475-481.
250. Jańczuk, B., Chibowski, E., Wójcik, W., Guindo, M., González-Caballero, F.J.M.c. and physics. Surface free energy of some lead compounds compared to galena. 1994, **37**(1), pp.64-67.
251. Cao, H. *Synthesis and Applications of Inorganic Nanostructures*. John Wiley & Sons, 2017.
252. Lioliou, M.G., Paraskeva, C.A., Koutsoukos, P.G. and Payatakes, A.C. Heterogeneous nucleation and growth of calcium carbonate on calcite and quartz. *Journal of Colloid and Interface Science*. 2007, **308**(2), pp.421-428.
253. Bracco, J.N. *Growth of Sparingly-Soluble AB-type Minerals as a Function of their A: B Ratio*. thesis, Wright State University, 2015.
254. Pastero, L., Costa, E., Bruno, M., Rubbo, M., Sgualdino, G., Aquilano, D.J.C.g. and design. Morphology of calcite (CaCO₃) crystals growing from aqueous solutions in the presence of Li⁺ ions. Surface behavior of the {0001} form. 2004, **4**(3), pp.485-490.
255. Scanlon, B.R., Reedy, R.C., Male, F., Walsh, M.J.E.s. and technology. Water issues related to transitioning from conventional to unconventional oil production in the Permian Basin. 2017, **51**(18), pp.10903-10912.
256. Venkateshwaran, V., Vembanur, S. and Garde, S. Water-mediated ion-ion interactions are enhanced at the water vapor-liquid interface. *Proceedings of the National Academy of Sciences*. 2014, **111**(24), p.8729.
257. Chevalier, N.R. and Guenoun, P. Surface Tension Drives the Orientation of Crystals at the Air-Water Interface. *The journal of physical chemistry letters*. 2016, **7**(14), pp.2809-2813.
258. Forsyth, C., Mulheran, P.A., Forsyth, C., Haw, M.D., Burns, I.S. and Sefcik, J. Influence of Controlled Fluid Shear on Nucleation Rates in Glycine Aqueous Solutions. *Crystal Growth & Design*. 2015, **15**(1), pp.94-102.
259. Agrawal, S.G. *Evaporative crystallization of alpha-lactose monohydrate: a thesis presented in partial fulfilment of the requirements for the degree of Doctor of Philosophy in Chemical Engineering at Massey University, Manawatu, New Zealand*. thesis, Massey University, 2012.
260. Smeets, P.J.M., Finney, A.R., Habraken, W.J.E.M., Nudelman, F., Friedrich, H., Laven, J., De Yoreo, J.J., Rodger, P.M. and Sommerdijk, N.A.J.M. A classical view on nonclassical nucleation. *Proceedings of the National Academy of Sciences*. 2017, **114**(38), p.E7882.

261. Ulusoy, U. and Yekeler, M. Floatability of barite particles with different shape and roughness. 2007.
262. Keogh, W., Neville, A., Huggan, M., Eroini, V., Olsen, J.H., Nielsen, F.M., Baraka-Lokmane, S., Bourdelet, E., Ellingsen, J.A., Bache, O.J.E. and Fuels. Deposition of Inorganic Carbonate, Sulfate, and Sulfide Scales on Antifouling Surfaces in Multiphase Flow. 2017, **31**(11), pp.11838-11851.
263. Khodakarami, M., Alagha, L. and Burnett, D.J. Probing Surface Characteristics of Rare Earth Minerals Using Contact Angle Measurements, Atomic Force Microscopy, and Inverse Gas Chromatography. *ACS omega*. 2019, **4**(8), pp.13319-13329.
264. Jansen, K., Agterof, W. and Mellema, J. Droplet breakup in concentrated emulsions. *Journal of rheology*. 2001, **45**(1), pp.227-236.
265. dos Santos, R.G., Bannwart, A.C. and Loh, W. Phase segregation, shear thinning and rheological behavior of crude oil-in-water emulsions. *Chemical engineering research and design*. 2014, **92**(9), pp.1629-1636.
266. Whitby, C.P. and Krebsz, M. Coalescence in concentrated Pickering emulsions under shear. *Soft Matter*. 2014, **10**(27), pp.4848-4854.
267. Pal, R. Dynamics of flocculated emulsions. *Chemical engineering science*. 1997, **52**(7), pp.1177-1187.
268. Cates, M.J.S.I.L.N.o.t.L.H.S.S.V., July. Complex fluids: the physics of emulsions. 2017, **98**, p.317.
269. Ata, S. Coalescence of Bubbles Covered by Particles. *Langmuir*. 2008, **24**(12), pp.6085-6091.
270. Ok, H., Park, H., Carr, W.W., Morris, J.F., Zhu, J.J.J.o.d.s. and technology. Particle-Laden Drop Impacting on Solid Surfaces. 2005, **25**(4), pp.449-456.
271. Grishaev, V., Iorio, C.S., Dubois, F. and Amirfazli, A.J.L. Complex drop impact morphology. 2015, **31**(36), pp.9833-9844.
272. Kowalczyk, P.B., Akkaya, C., Ergun, M., Janicki, M., Sahbaz, O. and Drzymala, J.J.P.o.M.P. Water contact angle on corresponding surfaces of freshly fractured fluorite, calcite and mica. 2017, **53**.
273. Feng, L., Zhang, Z., Mai, Z., Ma, Y., Liu, B., Jiang, L. and Zhu, D.J.A.C. A super-hydrophobic and super-oleophilic coating mesh film for the separation of oil and water. 2004, **116**(15), pp.2046-2048.
274. Supakar, T., Kumar, A. and Marston, J.O. Impact dynamics of particle-coated droplets. *Physical Review E*. 2017, **95**(1), p.013106.
275. Jarzabek, D.M., Chmielewski, M., Dulnik, J., Strojny-Nedza, A.J.J.o.M.E. and Performance. The influence of the particle size on the adhesion between ceramic particles and metal matrix in MMC composites. 2016, **25**(8), pp.3139-3145.
276. Douaire, M., Di Bari, V., Norton, J., Sullo, A., Lillford, P., Norton, I.J.A.i.c. and science, i. Fat crystallisation at oil–water interfaces. 2014, **203**, pp.1-10.
277. Chacon, L. and Baret, J.J.J.o.P.D.A.P. Microfluidic angle of repose test for Pickering emulsions. 2017, **50**(39), p.39LT04.
278. Desarnaud, J., Derluyn, H., Carmeliet, J., Bonn, D. and Shahidzadeh, N.J.T.j.o.p.c.l. Hopper Growth of Salt Crystals. 2018.
279. Ritchie, A.W., Watson, M.I., Turnbull, R., Lu, Z.Z., Telfer, M., Gano, J.E., Self, K., Greer, H.F. and Zhou, W.J.C. Reversed crystal growth of rhombohedral calcite in the presence of chitosan and gum arabic. 2013, **15**(47), pp.10266-10271.
280. Bonev, I.K. and Rice, C.M.J.M.M. Single crystal galena pillars as highly anisometric dissolution forms. 1997, **61**(3), pp.377-386.
281. Ueno, S., Hamada, Y., Sato, K.J.C.g. and design. Controlling polymorphic crystallization of n-alkane crystals in emulsion droplets through interfacial heterogeneous nucleation. 2003, **3**(6), pp.935-939.

282. Awad, T., Sato, K.J.C. and Bionterfaces, S.B. Acceleration of crystallisation of palm kernel oil in oil-in-water emulsion by hydrophobic emulsifier additives. 2002, **25**(1), pp.45-53.
283. Gebauer, D., Völkel, A. and Cölfen, H. Stable Prenucleation Calcium Carbonate Clusters. *Science*. 2008, **322**(5909), p.1819.
284. Pouget, E.M., Bomans, P.H.H., Goos, J.A.C.M., Frederik, P.M., de With, G. and Sommerdijk, N.A.J.M. The Initial Stages of Template-Controlled CaCO₃ Formation Revealed by Cryo-TEM. *Science*. 2009, **323**(5920), p.1455.
285. Kellermeier, M., Picker, A., Kempster, A., Cölfen, H. and Gebauer, D. A Straightforward Treatment of Activity in Aqueous CaCO₃ Solutions and the Consequences for Nucleation Theory. *Advanced Materials*. 2014, **26**(5), pp.752-757.
286. Weiner, S. and Addadi, L. Crystallization Pathways in Biomineralization. *Annual Review of Materials Research*. 2011, **41**(1), pp.21-40.
287. Rodriguez-Blanco, J., Shaw, S., Bots, P., Roncal-Herrero, T. and Benning, L. The role of pH and Mg on the stability and crystallization of amorphous calcium carbonate. *Journal of Alloys and Compounds*. 2012, **536**, pp.S477-S479.
288. KOWALCZUK, P.B., AKKAYA, C., ERGUN, M., JANICKI, M.J., SAHBAZ, O. and DRZYMALA, J. WATER CONTACT ANGLE ON CORRESPONDING SURFACES OF FRESHLY FRACTURED FLUORITE, CALCITE AND MICA. *Physicochem. Probl. Miner. Process*. 2017, **53**(1), pp.192-201.
289. Holappa, S., Kontturi, K.S., Salminen, A., Seppälä, J. and Laine, J. Adsorption of Hydrophobically End-Capped Poly(ethylene glycol) on Cellulose. *Langmuir*. 2013, **29**(45), pp.13750-13759.
290. Prestidge, C.A. and Ralston, J. Contact Angle Studies of Galena Particles. *Journal of Colloid and Interface Science*. 1995, **172**(2), pp.302-310.
291. Hempenius, M.A., Péter, M., Robins, N.S., Kooij, E.S. and Vancso, G.J. Water-Soluble Poly(ferrocenylsilanes) for Supramolecular Assemblies by Layer-by-Layer Deposition. *Langmuir*. 2002, **18**(20), pp.7629-7634.
292. Szilagyi, I., Trefalt, G., Tiraferri, A., Maroni, P. and Borkovec, M. Polyelectrolyte adsorption, interparticle forces, and colloidal aggregation. *Soft Matter*. 2014, **10**(15), pp.2479-2502.
293. Tian, C.S. and Shen, Y.R. Structure and charging of hydrophobic material/water interfaces studied by phase-sensitive sum-frequency vibrational spectroscopy. *Proceedings of the National Academy of Sciences*. 2009, **106**(36), p.15148.
294. Singh, G., Bremmell, K.E., Griesser, H.J. and Kingshott, P.J.S.m. Colloid-probe AFM studies of the interaction forces of proteins adsorbed on colloidal crystals. 2015, **11**(16), pp.3188-3197.
295. Çavuş, S. and Gürdağ, G. Noncompetitive Removal of Heavy Metal Ions from Aqueous Solutions by Poly[2-(acrylamido)-2-methyl-1-propanesulfonic acid-co-itaconic acid] Hydrogel. *Industrial & Engineering Chemistry Research*. 2009, **48**(5), pp.2652-2658.
296. Dąbrowski, A., Hubicki, Z., Podkościelny, P. and Robens, E. Selective removal of the heavy metal ions from waters and industrial wastewaters by ion-exchange method. *Chemosphere*. 2004, **56**(2), pp.91-106.
297. Packham, D.E. Surface energy, surface topography and adhesion. *International Journal of Adhesion and Adhesives*. 2003, **23**(6), pp.437-448.
298. Andritsos, N. and Karabelas, A. Laboratory studies of PbS scale formation in steel pipes. *Geothermics*. 1989, **18**(1-2), pp.17-24.
299. Pickering, S.U. CXCVI.—emulsions. *Journal of the Chemical Society, Transactions*. 1907, **91**, pp.2001-2021.
300. Sudmalis, M. and Sheikholeslami, R. Coprecipitation of CaCO₃ and CaSO₄. *The Canadian Journal of Chemical Engineering*. 2000, **78**(1), pp.21-31.

301. Kucher, M., Babic, D. and Kind, M. Precipitation of barium sulfate: experimental investigation about the influence of supersaturation and free lattice ion ratio on particle formation. *Chemical Engineering and Processing: Process Intensification*. 2006, **45**(10), pp.900-907.